


# PREPARATION, CHARACTERISATION AND APPLICATION OF SINGLE AND MULTILAYER MIXED-MATRIX MEMBRANES

by

**AHMED IBRAHIM**

A thesis submitted to the University of Birmingham for the degree of

**DOCTOR OF PHILOSOPHY**

Centre of Doctoral Training in Fuel Cells and their Fuels

School of Chemical Engineering

College of Engineering and Physical Sciences

University of Birmingham

September 2024

UNIVERSITY OF
BIRMINGHAM

## University of Birmingham Research Archive

### e-theses repository

This unpublished thesis/dissertation is copyright of the author and/or third parties. The intellectual property rights of the author or third parties in respect of this work are as defined by The Copyright Designs and Patents Act 1988 or as modified by any successor legislation.

Any use made of information contained in this thesis/dissertation must be in accordance with that legislation and must be properly acknowledged. Further distribution or reproduction in any format is prohibited without the permission of the copyright holder.

# ABSTRACT

Single layer and multilayer Nafion membranes incorporated with graphene oxide (GO) were investigated for application in polymer electrolyte fuel cells operating at intermediate temperatures (IT-PEFCs). The intermediate temperature regime has been utilised as a method to improve the power density output of fuel cells used in transport applications and graphene oxide was identified as the filler of choice due to its oxygen containing functional groups.

An experimental approach was taken, with membranes prepared with a variety of parameters such as graphene oxide weight loading, number of membrane layers, and membrane thickness. A variety of characterisation techniques were utilised to confirm successful incorporation of graphene oxide within the membrane, and subsequent samples were tested in a fuel cell at elevated temperatures.

Introducing graphene oxide suppressed the hydrogen crossover current density experienced during fuel cell operation in comparison to the reference Nafion sample. The multilayer membranes had even more pronounced hydrogen crossover barrier properties because of their three individual layers. Additionally, decreasing the membrane thickness led to improved fuel cell performance. The use of a Nafion/cerium oxide composite layer was found to maintain hydrogen crossover levels under 10 mA $cm^{-2}$ for over a week at 100°C during accelerated stress tests (AST).

However, some challenges in producing multilayer membranes pertained due to frequent interruption of the interfaces of the separate layers, which was further emphasised when fabricating thinner membranes. The development of thinner membranes, the improvement of interlayer contact, and the optimisation of cerium oxide fillers are topics that should be further explored in future work.

# ACKNOWLEDGEMENTS

I would like to give my appreciation to everyone who I met during my PhD, including the group members I spent many hours with in the lab and office. Thank you Naser, Abdul, and Liam for your friendship and for making my experience memorable. I wish you all the best.

I want to express my deepest gratitude to my supervisors, Ahmad and Robert. Ahmad, for his guidance and encouragement, and Robert, who helped me cross the finish line. I'm also sincerely grateful to Elvin, who went above and beyond to help, and Kun for his advice. Special thanks to John, whose kindness I have not forgotten.

I would like to acknowledge the CDT and EPSRC for funding my PhD. I am also grateful to the Leverhulme Trust for sponsoring my year abroad, and I would like to thank Stephen and his group for kindly hosting me.

Finally, this would not have been possible without the endless support of my sisters, Hodan, Hibaq and Saynab, and my dear parents, Anab and Salah.

# TABLE OF CONTENTS

**ABSTRACT** ..... **i**

**ACKNOWLEDGEMENTS** ..... **ii**

**TABLE OF CONTENTS** ..... **iii**

**LIST OF FIGURES** ..... **x**

**LIST OF TABLES** ..... **xvii**

**GLOSSARY OF TERMS AND ABBREVIATIONS** ..... **xix**

**1 Introduction** ..... **1**

1.1 Decarbonisation and the role of hydrogen ..... 1

1.2 Fuel cell technology ..... 4

1.2.1 Components of a working fuel cell ..... 8

1.3 Challenges of integrating PEFCs technologies ..... 10

1.4 Aims and Objectives ..... 11

1.5 Outline of the thesis ..... 12

**2 Literature Review** ..... **13**

2.1 Membranes for fuel cells ..... 13

2.2 Fuel cell operating temperatures ..... 17

2.2.1 Low, intermediate and high temperature fuel cells ..... 18

2.3 Degradation of Nafion ..... 20

2.4 Research strategies for membrane development at intermediate temperatures ..... 22
2.5 Use of filler materials ..... 22
2.5.1 Graphene oxide fillers ..... 23
2.5.1.1 Functionalisation ..... 25
2.5.1.2 More than one filler ..... 30
2.5.1.3 Localisation of filler ..... 34
2.5.2 Inorganic materials ..... 40
2.5.2.1 Filler morphology ..... 46
2.5.2.2 Inorganic fillers for high temperature fuel cells ..... 53
2.5.2.3 Cerium oxide ..... 55
2.5.3 Acids and ionic liquids ..... 59
2.6 Trends and perspectives ..... 64
2.7 Purpose of thesis and next steps ..... 74
**3 Materials and Methods ..... 76**
3.1 Materials ..... 76
3.2 Methods ..... 77
3.2.1 Graphene oxide synthesis ..... 77
3.2.2 Sulphonated graphene oxide synthesis ..... 77
3.2.3 Graphene oxide usage in this thesis ..... 77
3.3 Membrane preparation and characterisation ..... 78
3.3.1 Single layer Nafion membrane fabrication ..... 79

3.3.2 Single layer mixed matrix membrane fabrication ..... 79
3.3.3 Multilayer mixed matrix membrane fabrication ..... 80
3.3.4 Membrane activation ..... 83
3.3.5 Ex-situ characterisation ..... 84
3.3.5.1 Water uptake ..... 84
3.3.5.2 Ion exchange capacity ..... 84
3.3.5.3 Environmental scanning electron microscopy ..... 85
3.3.5.4 Thermogravimetric analysis ..... 86
3.3.5.5 Tensile strength analysis ..... 87
3.3.5.6 Fourier transform infrared spectroscopy ..... 88
3.3.5.7 Raman spectroscopy ..... 88
3.3.5.8 X-ray diffraction ..... 89
3.3.5.9 X-ray photoelectron spectroscopy ..... 89
3.4 In-situ performance testing ..... 90
3.4.1 MEA fabrication ..... 90
3.4.2 Assembly of fuel cell and activation ..... 92
3.4.3 Polarisation curves ..... 95
3.4.4 Electrochemical impedance spectroscopy ..... 96
3.4.5 Hydrogen crossover ..... 97
3.5 Lifetime testing ..... 98
3.5.1 24-hour OCV holding test ..... 98

3.5.2 Accelerated stress tests (AST) ..... 99

**4 Characterisation and fabrication ..... 101**

4.1 Graphene oxide characterisation ..... 101

4.1.1 X-ray photoelectron spectroscopy ..... 101

4.1.2 Raman spectroscopy ..... 103

4.1.3 Fourier transform infrared spectroscopy ..... 104

4.1.4 X-ray diffraction ..... 105

4.1.5 Thermogravimetric analysis ..... 106

4.1.6 Summary ..... 107

4.2 Fabrication of mixed matrix composite membranes ..... 108

4.2.1 Influence of probe sonication ..... 108

4.2.2 Influence of desiccation ..... 110

4.2.3 Influence of oven level ..... 111

4.2.4 Summary ..... 112

4.3 Single layer membrane characterisation ..... 113

4.3.1 Environmental scanning electron microscopy ..... 113

4.3.2 Thermogravimetric analysis ..... 117

4.3.3 X-ray diffraction and Fourier transform infrared spectroscopy ..... 118

4.3.4 Water uptake and Ion exchange capacity ..... 120

4.3.5 Summary ..... 121

4.4 Fabrication of multilayer membranes ..... 122

4.4.1 Influence of casting solvent ..... 123
4.4.2 Influence of activation ..... 126
4.4.3 Summary ..... 127
4.5 Multilayer membrane characterisation ..... 128
4.5.1 Environmental scanning electron microscopy ..... 128
4.5.2 Thermogravimetric analysis ..... 133
4.5.3 X-ray diffraction and Fourier transform infrared spectroscopy ..... 134
4.5.4 Water uptake and ion exchange capacity ..... 135
4.5.5 Summary ..... 137
4.6 Optimised membrane fabrication ..... 137
4.7 Optimised membranes characterisation ..... 140
4.7.1 Environmental scanning electron microscopy ..... 140
4.7.2 Raman spectroscopy ..... 141
4.7.3 Mechanical testing ..... 144
4.7.4 Summary ..... 145
4.7.5 Progress assessment and best practices ..... 145
4.8 Conclusions ..... 146
**5 In-situ performance testing ..... 147**
5.1 Single layer Nafion-GO membrane ..... 147
5.1.1 Influence of GO loading and temperature ..... 148
5.1.1.1 Polarisation curves ..... 148

5.1.1.2 HFR ..... 152
5.1.1.3 Hydrogen crossover ..... 154
5.1.1.4 Summary ..... 158
5.1.2 Influence of membrane thickness ..... 159
5.1.2.1 Current and power density ..... 159
5.1.2.2 HFR ..... 161
5.1.2.3 OCV ..... 162
5.1.2.4 Summary ..... 163
5.2 Multilayer membranes ..... 164
5.2.1 Influence of GO loading and temperature ..... 164
5.2.1.1 Polarisation curves ..... 165
5.2.1.2 HFR ..... 168
5.2.1.3 Hydrogen crossover ..... 169
5.2.1.4 Summary ..... 170
5.2.2 Influence of membrane thickness ..... 171
5.2.2.1 Current and power density ..... 171
5.2.2.2 HFR ..... 173
5.2.2.3 Hydrogen crossover ..... 174
5.2.2.4 Summary ..... 176
5.2.3 Progress assessment and best practices ..... 176
5.3 Comparison with literature ..... 177

5.4 Conclusion ..... 178

**6 Durability studies ..... 181**

6.1 24-hour OCV hold test ..... 181

6.1.1 Polarisation curves ..... 182

6.1.2 OCV and Hydrogen crossover ..... 183

6.1.3 Post-mortem SEM ..... 185

6.1.4 Summary ..... 188

6.2 Optimised membrane tests ..... 188

6.2.1 Single and multilayer membranes with synthesised GO ..... 189

6.2.2 Single and multilayer membrane with synthesised sulphonated GO ..... 196

6.2.3 Single and multilayer membranes with synthesised sulphonated GO with a Nafion/Cerium oxide interlayer ..... 201

6.2.4 Progress assessment and best practices ..... 210

6.3 Conclusion ..... 210

**7 Conclusion and future directions ..... 212**

**LIST OF REFERENCES ..... 215**

# LIST OF FIGURES

Figure 1-1: Schematic representation of a fuel cell ..... 5

Figure 1-2: Fuel cell expanded image of components. ..... 8

Figure 2-1: Structure of Nafion and the structure of a water channel. The blue lines are the backbone of Nafion and the blue filled circles are the sulphonic side groups. ..... 14

Figure 2-2: Grotthus (a) and vehicle (b) mechanisms. ..... 16

Figure 2-3: Membrane conductivity operating windows. ..... 18

Figure 2-4: Structure of graphene and graphene oxide. ..... 23

Figure 2-5: MEA polarisation and power density curves for 10 wt.% functionalised GO/Nafion and recast Nafion. ..... 26

Figure 2-6: Single cell performances of the membranes with anhydrous $H_2/O_2$ operated at 120°C, under anhydrous conditions. ..... 28

Figure 2-7: SEM images of a) GO (0.5 wt.%) multilayer b) GO (2.5 wt.%) multilayer[180] ..... 35

Figure 2-8: Cross-sectional SEM image of the multilayer DMD MEA showing the catalyst layer (CL), the sprayed ionomer layers (PEM), and the GO/cerium oxide interlayer in the middle. ..... 39

Figure 2-9: Polarisation curves for the: (a,b) titania nanoparticles TP25, (c,d) mesoporous particles TMP, and (e,f) titanium oxide nanotube (TNT) composites measured at 80 and 130°C. ..... 48

Figure 2-10: Pre- and post-500 h test performance curves. ..... 57

Figure 2-11: Polarisation curves of a $H_2/O_2$ fuel cell using a SPI-1.51(50) composite membrane without humidification at gas utilisation ratios of 30% for $H_2$ and 15% for $O_2$ operation at 30°C, and operation at 80°C. ..... 62

Figure 3-1: Diagrams of: A) single layer Nafion, B) single layer mixed matrix membrane with graphene oxide filler, and C) multilayer mixed matrix membrane with an inner composite layer with graphene oxide filler. ..... 82
Figure 3-2: ESEM sample preparation. ..... 86
Figure 3-3: Hot-pressing method assembly and method. ..... 91
Figure 3-4: Nafion (left) and Nafion-GO(4.5) (right) MEAs. ..... 91
Figure 3-5: Set up of fuel cell station, from top to bottom: A) Insulation to keep fuel cell at elevated temperatures, B) fuel cell station, C) external potentiostat, D) thermocouple, E) fuel inlet, F) four probe electrode system, G) current collector cables, H) fuel cell, I) heating bars, and J) outlet leading to back pressure system. ..... 93
Figure 3-6: Polarisation curve with identified losses. ..... 96
Figure 4-1: a) Survey spectra, b) C1s spectrum of synthesised GO, and c) S2p spectra. ..... 102
Figure 4-2: Raman microscopy images of a) synthesised GO, b) synthesised sulphonated GO, c) commercial GO, and d) Raman spectra of the GO samples. ..... 104
Figure 4-3: FT-IR spectra of the GO samples. ..... 105
Figure 4-4: XRD spectrum of commercial GO. ..... 106
Figure 4-5: TGA of graphite and GO samples. ..... 107
Figure 4-6: Fabrication challenges: a) Phase separation, b) cracks, and c) cracks prior to removal. ..... 109
Figure 4-7: Nafion-GO(4.5) membranes. ..... 111
Figure 4-8: Membrane thickness deviation (not to scale). ..... 112
Figure 4-9: ESEM images of recast Nafion at a magnification of A) 1000, B) 2500, and C) 5000. ..... 113

Figure 4-10: ESEM images of Nafion-GO(1.5) at a magnification of A) 1000, and B) 2000. ..... 114
Figure 4-11: ESEM images of Nafion-GO(3) at a magnification of A) 2000, B) 5000, C) 10,000, D) 20,000, E) 25,000, and F) 50,000. ..... 114
Figure 4-12: ESEM images of Nafion-GO(4.5) at a magnification of A) 1000, B) 5000, and C) 25,000. ..... 115
Figure 4-13: ESEM images of Nafion-GO(6) at magnification of A) 1000, B) 5000, and C) 25,000. ..... 115
Figure 4-14: ESEM images of a) Nafion-GO(1.5), and b) Nafion-GO(6). ..... 116
Figure 4-15: a) TGA and b) DTG of mixed matrix membrane samples. ..... 117
Figure 4-16: Degree of conversion of mixed matrix membranes. ..... 118
Figure 4-17: XRD patterns of mixed matrix membranes. ..... 119
Figure 4-18: FT-IR spectra of mixed matrix membranes. ..... 119
Figure 4-19: a) Water uptake, and b) IEC of mixed matrix membranes. ..... 121
Figure 4-20: Multilayer membrane with a) wells of GO, b) lines of GO, c) multilayer membranes prepared with ethanol and d) isopropyl alcohol, e) inside of oven with metal trays. ..... 125
Figure 4-21: A Multilayer membrane after activation. ..... 126
Figure 4-22: Multilayer membranes with varying GO loading. ..... 127
Figure 4-23: ESEM images of ML-GO(0.26) at a magnification of A) 1000, B) 5000, and C) 15,000. ..... 129
Figure 4-24: ESEM images of ML-GO(0.53) at a magnification of A) 1000, B) 5000, and C) 10,000. ..... 129

Figure 4-25: ESEM images of ML-GO(0.79) at a magnification of A) 1000, B) 5000, and C) 20,000. ..... 129
Figure 4-26: ESEM images of ML-GO(1.05) at a magnification of A) 1000, B) 5000, and C) 15,000. ..... 130
Figure 4-27: Attempted spot and line scan on ML-GO(1.05). ..... 130
Figure 4-28: ESEM images of ML-GO(4.5) at a magnification of A) 5000, B) 10,000, and C) 15,000. ..... 131
Figure 4-29: Bending in ML-GO(4.5), and no bending in ML-GO(0.79). ..... 132
Figure 4-30: a) TGA and b) DTG of multilayer mixed matrix membrane samples..... 133
Figure 4-31: Degree of conversion of multilayer mixed matrix membranes. ..... 134
Figure 4-32: XRD patterns of multilayer mixed matrix membranes..... 135
Figure 4-33: FT-IR spectra of multilayer mixed matrix membranes. ..... 135
Figure 4-34: a) Water uptake and b) IEC of multilayer membranes. ..... 136
Figure 4-35: Membrane fabrication process: a) SynGO, b) SynGO, Nafion and ethanol dispersions and c) Nafion-SynGO(1.5) membrane. ..... 138
Figure 4-36: a) Cracked membranes and b) Subsequent membranes removed from petri dishes. ..... 138
Figure 4-37: Membranes prepared with synthesised GO. ..... 139
Figure 4-38: ESEM images of Nafion-SynGO(1.5) at a magnification of A) 2000, B) 5000, and C) 15,000. ..... 140
Figure 4-39: ESEM images of ML-SynGO(0.26) at a magnification of A) 1000, B) 5000, and C) 20,000. ..... 141

Figure 4-40: a-g) Raman microscopy images of Recast Nafion, Nafion-GO(1.5), Nafion-GO(3), Nafion-GO(4.5), Nafion-GO(6), Nafion-SynGO(1.5) and Nafion-SynSGO(1.5), and h) Raman spectra. ..... 142
Figure 4-41: a-h) Raman microscopy images of Recast Nafion, ML-GO(0.26), ML-GO(0.53), ML-GO(0.79), ML-GO(1.05), ML-GO(4.5), ML-SynGO(0.26) and ML-SynSGO(0.26), and i) Raman spectra. ..... 143
Figure 4-42: Stress-strain curves of single layer mixed-matrix membranes. ..... 145
Figure 5-1: Polarisation and power curves of single layer membranes at 80, 100, and 120°C. ..... 150
Figure 5-2: a) Current density, and b) power density at 400 mV achieved by single layer membranes at 80, 100 and 120°C. ..... 151
Figure 5-3: a) Nyquist plot, and b) high frequency resistance of single layer membranes at 80, 100 and 120°C. ..... 153
Figure 5-4: Hydrogen crossover current densities produced by single layer membranes at 80, 100 and 120°C. ..... 155
Figure 5-5: A) Hydrogen transport through a dense Nafion membrane, and B) Hydrogen transport between Nafion chains. ..... 156
Figure 5-6: A) Hydrogen transport through Nafion-GO and B) Hydrogen transport between hydrated Nafion-GO chains. ..... 157
Figure 5-7: a) Current density, and b) power density achieved at 400 mV by recast Nafion and Nafion-GO(4.5) membranes of 50, 40 and 30 μm thickness ..... 160
Figure 5-8: HFR values achieved by recast Nafion and Nafion-GO(4.5) membranes of 50, 40 and 30 μm thickness. ..... 162

Figure 5-9: OCV of recast Nafion and Nafion-GO(4.5) membranes of 50, 40 and 30 μm thickness. ..... 163
Figure 5-10: Polarisation and power curves of multilayer membranes at 80, 100, and 120°C. ..... 166
Figure 5-11: a) Current density, and b) power density at 400 mV achieved by recast Nafion and multilayer membranes at 80, 100 and 120°C. ..... 167
Figure 5-12: High frequency resistance values of recast Nafion and multilayer membranes at 80, 100 and 120°C. ..... 169
Figure 5-13: Hydrogen crossover current densities of recast Nafion and multilayer membranes at 80, 100 and 120°C. ..... 170
Figure 5-14: a) Current density, and b) power density achieved at 400 mV by multilayer membranes of varying thickness at 80, 100 and 120°C. ..... 172
Figure 5-15: High frequency resistance values of ML-GO(0.79) membranes of varying thickness at 80, 100 and 120°C. ..... 173
Figure 5-16: OCV and hydrogen crossover current densities of ML-GO(0.79) membranes of varying thickness at 80, 100 and 120°C. ..... 175
Figure 6-1: Polarisation and power curves of a) Nafion at 80°C, b) Nafion at 120°C, c) Nafion-GO(4.5) at 80°C and d) Nafion-GO(4.5) at 120°C. ..... 183
Figure 6-2: A) OCV, and B) hydrogen crossover current densities of Nafion and Nafion-GO(4.5) at 80°C and 120°C ..... 184
Figure 6-3: SEM cross sections of Nafion, and post OCV hold test Nafion MEAs after testing at 80°C and 120°C. ..... 186
Figure 6-4: SEM cross sections of Nafion-GO(4.5), and post OCV hold test Nafion-GO(4.5) MEAs after testing at 80°C and 120°C ..... 187

Figure 6-5: Polarisation and power curves of Nafion-GO(1.5) at 80, 100, and 120°C. ..... 190
Figure 6-6: Results of Nafion-GO(1.5): a) current density at 400 mV, b) power density at 400 mV, c) HFR and, d) hydrogen crossover current density at 80°C, 100°C and 120°C. ..... 191
Figure 6-7: Polarisation and power curves of ML-GO(0.26) at 80, 100, and 120°C. ..... 192
Figure 6-8: Results of ML-GO(0.26): a) current density at 400 mV, b) power density at 400 mV, c) HFR and, d) hydrogen crossover current density at 80°C, 100°C and 120°C. ..... 193
Figure 6-9: Structure of: A) Nafion-GO and B) Nafion-SynGO..... 195
Figure 6-10: Polarisation and power curves of Nafion-SGO(1.5) during accelerated stress testing. ..... 196
Figure 6-11: Results of Nafion-SGO(1.5): a) current density at 400 mV, b) power density at 400 mV, c) HFR and, d) hydrogen crossover current density and OCV during accelerated stress testing..... 197
Figure 6-12: Polarisation and power curves of ML-SGO(0.26) during accelerated stress testing. ..... 198
Figure 6-13: Results of ML-SGO(0.26): a) current density at 400 mV, b) power density at 400 mV, c) HFR and, d) hydrogen crossover current density and OCV during accelerated stress testing..... 199
Figure 6-14: Polarisation and power curves of Nafion-SGO(1.5) with cerium oxide during accelerated stress testing..... 202
Figure 6-15: Results of Nafion-SGO(1.5) with cerium oxide: a) current density at 400 mV, b) power density at 400 mV, c) HFR and, d) hydrogen crossover current density and OCV during accelerated stress testing. ..... 203
Figure 6-16: Polarisation and power curves of ML-SGO(0.26) with cerium oxide during accelerated stress testing..... 205

Figure 6-17: Results of ML-SGO(0.26) with cerium oxide: a) current density at 400 mV, b) power density at 400 mV, c) HFR and, d) hydrogen crossover current density and OCV during accelerated stress testing. ..... 206
Figure 7-1: Schematic of an alternative multilayer design, with GO in the middle layer and cerium oxide nanoparticles in the cathode side layer. ..... 214

# LIST OF TABLES

Table 1-1: Summary of fuel cell types. ..... 6

Table 2-1: Membrane and conductive species involved at different temperatures. ..... 20

Table 2-2: Summary of membrane performance. X is data that was not presented in referenced journal article. ..... 70

Table 2-3: Summary of membrane characteristics. ..... 72

Table 3-1: Materials used in thesis. ..... 76

Table 3-2: Nafion membrane fabrication parameters, values correspond to Nafion D1021 EW 1100 (10% in water) with a 9 cm diameter petri dish. ..... 79

Table 3-3: Nafion-GO membrane fabrication parameters, values correspond to Nafion D1021 EW 1100 (10% in water) with a 9 cm diameter petri dish and 4.5 wt.% of GO. ..... 80

Table 3-4: Multilayer-GO membrane fabrication parameters; values correspond to Nafion D1021 EW 1100 (10% in water) with a 9 cm diameter petri dish and 0.79 wt.% of GO. ..... 81

Table 3-5: Multilayer membrane naming convention with GO weight loadings. ..... 81

Table 3-6: Summary of membranes prepared. ..... 82

Table 3-7: Fuel cell activation parameters ..... 94

Table 3-8: Hydrogen crossover parameters. ..... 97

Table 3-9: 24-hour OCV hold test parameters ..... 99

Table 3-10: AST test parameters ..... 99

Table 3-11: Optimised samples tested. ..... 100

Table 4-1: Summary characterisation results for the GO samples. ..... 108

Table 4-2: Mass loss percentages during different temperature regions for mixed matrix membrane samples. ..... 117

Table 4-3: Mass loss percentages during different temperature regions for mixed matrix multilayer membrane samples. ..... 133
Table 5-1: Summary of single layer composite membranes tested. ..... 147
Table 5-2: Summary of multilayer membranes tested..... 164
Table 5-3: Comparison of fuel cell results with literature. ..... 177
Table 5-4: Summary of fuel cell testing: current and power density at 400 mV, hydrogen crossover current density and hydrogen permeability. ..... 179
Table 5-5: Summary of fuel cell testing: Peak current and peak power density, high frequency resistance and OCV. ..... 180
Table 6-1: Table of OCV hold test samples. ..... 181
Table 6-2: Summary of 24-hour OCV hold test, membranes have an initial thickness of 50µm ..... 188
Table 6-3: Comparison between Nafion and Nafion-SynGO(1.5) membranes. ..... 193
Table 6-4: Influence of sulphonation on membrane performance. ..... 200
Table 6-5: Summary of AST testing; current density..... 207
Table 6-6: Summary of AST testing; power density. ..... 207
Table 6-7: Summary of AST testing; HFR. ..... 208
Table 6-8: Summary of AST testing; hydrogen crossover current density. ..... 208
Table 6-9: Summary of AST testing; OCV. ..... 209

# GLOSSARY OF TERMS AND ABBREVIATIONS

| | |
|---|---|
| AST | Accelerated stress test |
| BPP | Bipolar plates |
| CommGO | Commercial graphene oxide |
| EDX | Energy dispersive x-ray analysis |
| ESEM | Environmental scanning electron microscopy |
| EV | Electric vehicles |
| FC | Fuel cell |
| FCV | Fuel cell vehicle |
| FT-IR | Fourier transform infrared spectroscopy |
| GHG | Greenhouse gases |
| GDL | Gas diffusion layer |
| GO | Graphene oxide |
| HFR | High frequency resistance |
| HT-PEFC | High temperature polymer electrolyte fuel cell |
| IEC | Ion exchange capacity |
| IT-PEFC | Intermediate temperature polymer electrolyte fuel cell |
| MEA | Membrane electrode assembly |

| | |
|---|---|
| ML | Multilayer |
| OCV | Open circuit voltage |
| PEFC | Polymer electrolyte fuel cell/polymer electrolyte fuel cell |
| PTFE | Polytetrafluoroethylene |
| RH | Relative humidity |
| SEM | Scanning electron microscopy |
| SGO | Sulphonated graphene oxide |
| SynGO | Synthesised graphene oxide |
| TGA | Thermogravimetric analysis |
| WU | Water uptake |
| XPS | X-ray photon spectroscopy |
| XRD | X-ray diffraction |

This thesis includes work from two published journal articles:

Gabriele G.Gagliardi, **Ahmed Ibrahim**, Domenico Borello and Ahmad El-Kharouf. Composite Polymers Development and Application for Polymer Electrolyte Membrane Technologies—A Review. Molecules 25 (7) (2020) p.1712. Doi: 10.3390/molecules25071712.

This review paper summarised the use of composite membranes in polymer electrolyte fuel cells, methanol fuel cells and electrolysers. The section on composite membranes in polymer electrolyte fuel cells was written by Ahmed Ibrahim, and the section on composite membranes for methanol fuel cells and electrolysers by Gabriele G.Gagliardi. Ahmad El-Kharouf and Domenico Borello supervised the project. The literature review in this thesis (Chapter 2) only includes work written by Ahmed Ibrahim in the review paper, and was extensively edited.

**Ahmed Ibrahim**, Oheen Hossain, Jagjit Chaggar, Robert Steinberger-Wilckens and Ahmad El-Kharouf. GO-Nafion composite membrane development for enabling intermediate temperature operation of polymer electrolyte fuel cell. International Journal of Hydrogen Energy 45 (8) (2020) 5526-5534. Doi: 10.1016/j.ijhydene.2019.05.210.

This experimental paper presented composite membranes consisting of Nafion and graphene oxide, their fabrication, characterisation and testing in a polymer electrolyte fuel cell. Membrane fabrication, characterisation and fuel cell tests were performed by Ahmed Ibrahim, Oheen Hossain, and Jagjit Chaggar. Ahmad El-Kharouf and Robert Steinberger-Wilckens supervised the project. In this thesis, the preparation, characterisation and fuel cell experiments were repeated by Ahmed Ibrahim with graphene oxide weight loading included as an additional variable, and the subsequent experimental data was extensively reanalysed and reformatted.

# 1 Introduction

## 1.1 Decarbonisation and the role of hydrogen

Constant and continuous utilisation of fossil fuels in all energy system sectors has increased emissions of greenhouse gases (GHGs) such as carbon dioxide, methane, nitrogen oxides and sulphur oxides into the atmosphere[1,2]. Industrial energy use (24.2%), agriculture, forestry and land use (18.4%), energy use in buildings (17.5%) and transport (16.2%) are the greatest single sources of global greenhouse emmisions[3–6].

The main output of global political gatherings has been the goal of achieving "net-zero" and the long term mission of preventing average world temperature from exceeding a 2°C increase[7,8], preventing catastrophic consequences[9–13]. Hence reducing GHG emissions is of the upmost importance.

In order to tackle climate change caused by greenhouse gas emissions, non-technology-based mitigation strategies have been introduced to encourage consumers to adopt a more "sustainable lifestyle". Examples include the promotion of non-polluting fuels and technologies, taxing high polluting cars[14], introducing "ultra-low emission zones" in cities[15,16] or incentivising carpooling[17].

On the other hand, technology-based mitigation strategies to promote decarbonisation include the use of renewable technologies such as solar, wind and hydropower[18–20]. These technologies can produce electricity from light, wind, and the gravitational potential of water, respectively. However, they require the support of storage technologies, such as batteries, due to the fluctuating nature of the energy sources[21].

Electric battery technology has become a strong substitute for the traditional combustion engine as a method to reduce GHG emissions in the transport sector, and progress has been rapid[22]. In recent years, companies such as NIO, Tesla, General Motors, BMW, and Hyundai have launched electric vehicles (EVs) for the commercial market[23]. To add, there are even bicycles and scooters fitted with batteries, termed "E-Bikes" and "E-Scooters", respectively[24].

The EVs are entirely powered by electricity (termed all-electric vehicles) and therefore do not emit GHGs. However, there are some disadvantages:

- Currently, larger vehicle batteries lack sufficient energy density and take a long time to fully charge[25].
- The electricity that charges the battery will often have come from traditional power plants, essentially reducing part of the benefit of using them in the first place[26].

One answer is the use of "hybrid" vehicles that combine the use of a small battery with a combustion engine[27]. These are termed plug-in hybrid-electric vehicles.

An alternative energy vector and method to promote decarbonisation is the utilisation of hydrogen, whose conversion generates only heat and water. Therefore, hydrogen can play a key role and has begun to be incorporated in industry, transport, buildings and power generation[28]. The holistic concept of decarbonisation via hydrogen is named the "hydrogen economy".

As an example, hydrogen can be used in the transport industry through fuel cells (FC)[29]. This is an electricity generating technology that utilises hydrogen as its fuel, in comparison to electric batteries that are electricity storage technologies[30]. This allows the fuel cell to be much smaller than the batteries inside EVs as battery storage capacity is limited by the quantity of lithium ions that can be intercalated within the anode. Hence, fuel cells have begun to appear in ultra-low emission vehicles. Additionally, hydrogen's compressibility and fast refuelling makes FC

technology particularly attractive for medium and heavy duty vehicles, and for long-range applications, such as trucks[31,32]. Examples of companies in the UK establishing commercial fuel cell products include Intelligent Energy Ltd and Bramble Energy Ltd[33].

However, the source of hydrogen has to be considered, just as the source of electricity that is stored in EV batteries. The majority of hydrogen is produced via the ubiquitous steam reforming reaction of natural gas, shown in equation ( 1 ) , where methane is reacted with water to produce syngas, a combination of hydrogen and carbon monoxide[34]. The carbon monoxide can react further in the presence of water to produce hydrogen and carbon dioxide, termed the water-gas shift reaction, as shown in equation ( 2 )[35].

$$CH_4 + H_2O \rightarrow CO + 3H_2 \quad (1)$$

$$CO + H_2O \rightarrow CO_2 + H_2 \quad (2)$$

The consequence is that the carbon dioxide is what determines the sustainability of the hydrogen that is utilised in low-carbon technologies. As an example, grey hydrogen is hydrogen that has been produced via steam reforming of natural gas, with the carbon dioxide released into the environment, whereas such production with storage (sequestered) of the resultant carbon dioxide is termed blue hydrogen[36,37]. Hydrogen that is produced entirely from the splitting of water with electricity produced from renewable electricity sources is called green hydrogen and is the most sustainable form of hydrogen fuels[38]. Finally, hydrogen that is produced from the gasification of black and brown coal is termed black and brown hydrogen, respectively[36].Understandably, policies have been focused on blue and green hydrogen for low-carbon and zero-carbon technologies[39–42].

## 1.2 Fuel cell technology

A fuel cell is an alternative energy and power generation device that has received recent interest and investment in vehicles. They are a type of electrochemical cell which consists of an anode, where a reactant is oxidised (a loss of electrons), and a cathode, where a reactant is reduced (a gain of electrons). The pair of reactions described are otherwise known as a redox (reduction-oxidation) reaction. In order to prevent the two half reactions from coming into contact with each other, the two electrodes are separated by an electrolyte, a physical layer which facilitates the movement of only a specific species. In the case of the fuel cell, the reactants used are hydrogen fuel at the anode, and oxygen at the cathode. Furthermore, the oxygen can either be pure or in the form of air, and this reaction results in the overall production of water, and the generation of heat and electricity.

The concept of a fuel cell is visually displayed in Figure 1-1. The hydrogen is fed through the anode and is oxidised, producing protons that conduct through the electrolyte, and electrons that conduct through an external circuit. Consequently, the protons, electrons and oxygen then combine at the cathode, completing the reaction.

In this case, the example fuel cell described is named the polymer electrolyte fuel cell (PEFC), or polymer electrolyte fuel cells (PEFC)[43]. However, there are a vast number of different types of fuel cells, all involving similar redox reactions, but greatly differing in their use of fuels, operating temperatures, electrolyte and conductive species, to name but a few variables[44]. Examples include the direct methanol fuel cell (DMFC), the alkaline fuel cell (AFC), the molten carbonate fuel cell (MCFC) and the solid oxide fuel cell (SOFC)[45–47]. In fact, their differing operating conditions have led to their divergent applications. For example, the solid oxide fuel cell, which has an operating temperature in the range of 600 to 800°C, has use in combined heat

and power devices[48]. At the other end of the spectrum, fuel cells that operate closer to room temperature have applications geared more towards portability, such as the direct methanol fuel cell[49]. To add, several fuel cells can be further split into different temperature regions, such as the high temperature PEFCs that use phosphoric acid doped membranes[50].

Table 1-1 summarises the different types of fuel cells. The reader is referred to the referenced reviews for a more detailed explanation[51].

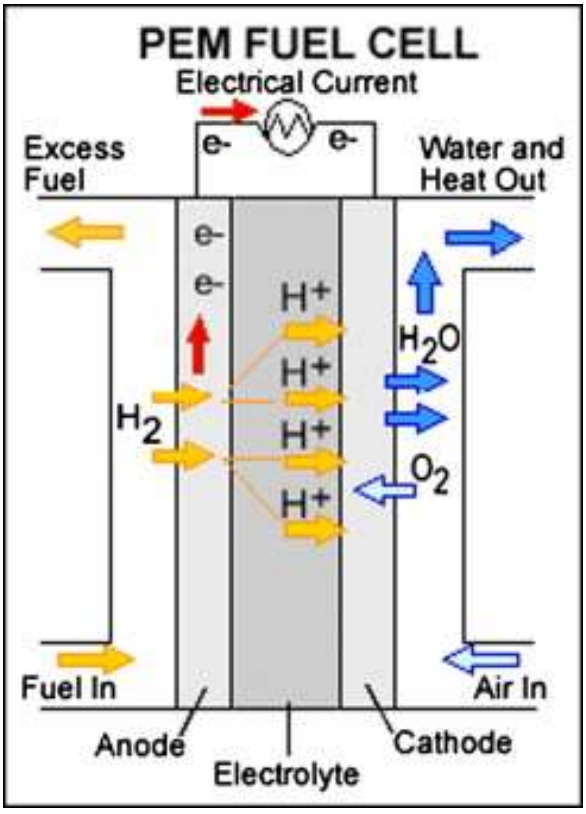



Figure 1-1: Schematic representation of a fuel cell[1]

[1] Reprinted with permission from Elsevier[52].

Table 1-1: Summary of fuel cell types.

| Fuel cell type | Temperature range | Conductive species | Application | Pros | Cons | Review |
|---|---|---|---|---|---|---|
| PEFC | 20-80°C | $H^+$ | Transport.<br><br>Portable power. | Low temperature | Expensive catalyst | Wang et al.[52] |
| SOFC | 500-1000°C | $O^{2-}$ | Combined heat and power.<br><br>Auxiliary power. | Fuel flexibility.<br><br>Efficient. | Long start up time.<br><br>Corrosion of components. | Blum et al.[53] |
| AFC | <100°C | $OH^-$ | Space<br><br>Military. | Low temperature | Sensitive to carbon dioxide poisoning. | McLean et al.[46] |
| DMFC | 30-130°C | $H^+$ | Portable, low power applications. | Easy refuelling.<br><br>Small size. | Inefficient. | Kamarudin et al.[49] |
| MOFC | 600-700°C | $CO_3^{2-}$ | Distributed generation. | Fuel flexibility.<br><br>Efficient. | Long start up time.<br><br>Corrosion of components. | Dicks et al.[54] |

As previously described, the electrochemical reaction that occurs within the fuel cell produces electricity, and this is because of the potential difference between the two individual redox reactions. In this case, the hydrogen oxidation reaction (HOR), shown in equation ( 3 ), at the anode has a potential of zero volts and the oxygen reduction reaction (ORR), shown in equation ( 4 ), at the cathode has a potential of 1.23 V. Consequently, the combined reaction produces a potential at standard conditions of 1.23 V. However, it should be noted that the kinetics of the HOR are very facile in comparison to the kinetics of the ORR, which is much slower[55].

$$H_2 \rightarrow 2H^+ + 2e^- \quad (3)$$

$$^1/_2\, O_2 + 2e^- + 2H^+ \rightarrow H_2O \quad (4)$$

$$H_2 + {}^1/_2\, O_2 \rightarrow H_2O \quad (5)$$

However, this is a theoretical value that is not replicated and hence observed in operating conditions, unless at open circuit voltage (OCV). The reason for this is the existence of losses that occur during the drawing of current during the operation of the fuel cell. These losses are named activation, ohmic and mass transport losses[56]. Firstly, activation losses are the result of needing to overcome the energetic reaction barrier and to start the reaction[57]. Secondly, ohmic losses are due to the electronic and ionic resistances throughout the fuel cell, but is dominated by the membrane resistance, where the electrolyte has an inherent resistance to the movement of ions[58]. Finally, mass transport losses are present when not enough reactants are brought to the active sites while large currents are drawn. To add, the excess water that is produced at the cathode also needs to be removed and can potentially block the active sites for the oxygen that has to be transported to the surface of the cathode active sites[59].

All three losses are experienced throughout the operation of the fuel cell, but are more prominent when current is drawn at varying levels, with activation losses dominating at low current, ohmic at medium current, and mass transport at high current levels. Therefore, it is important to stress that the operational performance of the fuel cell is very much linked with its redox reactions and performance losses.

### 1.2.1 Components of a working fuel cell

The fuel cell described so far in this thesis involves the electrodes and electrolyte, which is not representative of the full fuel cell system. Hence, an understanding of the additional components within the fuel cell is required. The individual components of the PEFC are shown in Figure 1-2, beginning from the outside[60]:

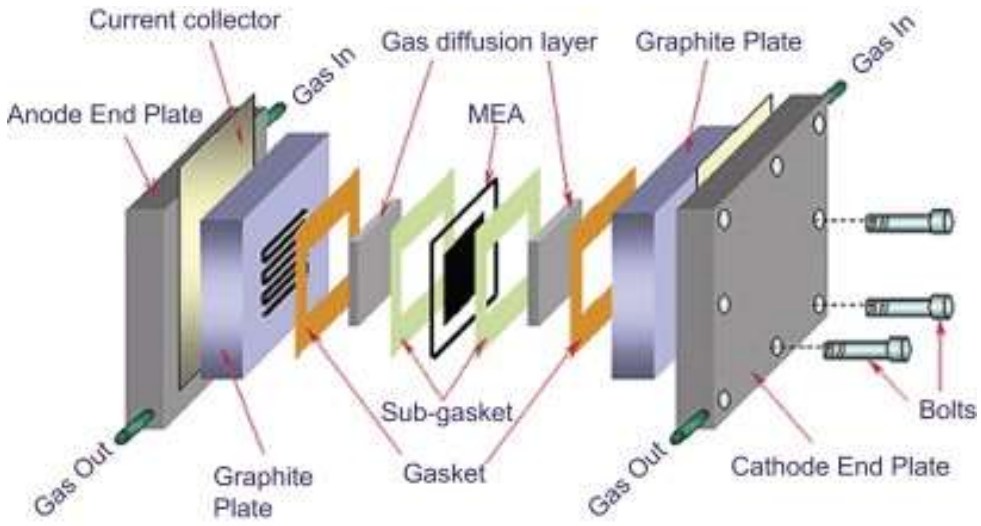



Figure 1-2: Fuel cell expanded image of components[2].

- Bipolar plates (BPP), whose role is to efficiently disperse the reactants to aid in the removal of water as a side product, collect the electrical current from the cell and provide gas tight separation to the next cell in a stack[61].
- Gas diffusion, and microporous layer (GDL and MPL, respectively), a hydrophobic porous layer which allows for effective fuel and oxidant diffusion, water removal and electrical conduction[62].

[2] Reprinted with permission from Elsevier[60].

- The catalyst layers, which consist of an anode and cathode on either side of the membrane. The catalyst layer consists of a combination of catalyst, support and an ionomer. This is where the electrochemical reactions occur[63].

- An electrolyte membrane, which facilitates ionic charge transport of a specific species[64].

Additionally, gaskets are used between the membrane electrode assembly (MEA), which consists of the membrane, catalyst, GDL, and the BPP to prevent any fuel and oxidant leakage.

To further increase the maximum power output, individual cells can be combined into a stack. However, this will require a balance of plant with system integration, power conditioning, control, fuel and oxygen delivery systems, and heat and water management to be carefully considered[65].

In recent years, PEFCs consisting of large stacks have seen use in hybrid vehicles. In comparison to other fuel cell types, the PEFC's fast start up time, combined with its relatively low operating temperature and high power-to-weight ratio makes it an ideal candidate for vehicles[66]. Benefits of hydrogen-powered fuel cell vehicles include a much longer driving range and refuelling times that are more similar to that of petrol and diesel-powered vehicles[67]. Furthermore, FCVs utilise an electric drivetrain similar to that of EVs[68,69]. One specific transport application is in the use of long range, heavy duty vehicles.

## 1.3 Challenges of integrating PEFCs technologies

Nevertheless, the promotion of decarbonisation by incorporating hydrogen as a non-fossil fuel and hydrogen fuel cells in vehicles has several challenges:

- There is a lack of infrastructure to accommodate the fuel utilisation of hydrogen, such as pipelines that require modification[70,71], and a lack of hydrogen refuelling stations in the UK[72], and therefore greater investment is required[73]. Hence, the storage, distribution and general risks of hydrogen should be carefully considered[74–76].
- PEFCs require the use of expensive platinum-group based catalysts and expensive membranes to operate[77–80]. To add, the electrolysis process to produce green hydrogen utilises costly iridium-based catalysts and an expensive membrane[81,82].
- Increasing the overall power density of PEFCs[68]. As an example, the energy system could be reduced by using lightweight materials, which is critical in aviation applications. For vehicles, the focus is more on reducing volume in order to increase the power density.

Interestingly, the power density of a PEFC can be increased by operation above the conventional temperature point of 80°C, otherwise known as intermediate temperature PEFCs (IT-PEFCs).

The benefits of this temperature increase are twofold. Firstly, the reaction kinetics of the HOR and ORR are increased. Secondly, the increase in temperature above the boiling point of liquid water results in a single phase of water (vapour), simplifying potential water management systems. To add, the greater temperature difference between the fuel cell and its surroundings will lead to simpler heat management. Therefore, it can be seen that there is great potential in the development of IT-PEFCs.

Consequently, this thesis is focused on improving the power density of the hydrogen fuel cell at elevated operating temperatures. Particular focus will be placed on the electrolyte membrane, where there is potential scope for improving FC performance[83]. The state of development of membrane technology for fuel cells will be further explored in the following chapter.

## 1.4 Aims and Objectives

The aims of this thesis include understanding the behaviour and performance of single and multilayer mixed matrix membranes composed of a polymeric phase and a 2D material phase of graphene oxide.

A physical approach has been taken where the structure of the membrane will be controlled via solution casting and the introduction of graphene oxide filler. Physical parameters such as filler loading, membrane thickness and FC operating temperature will be varied to study the influence of these parameters.

The aims of this thesis will be achieved by following the objectives set out below:

- Successfully fabricating single and multilayer mixed matrix membranes with graphene oxide (GO) filler.
- Characterising the membranes using a variety of characterisation techniques.
- Producing membrane electrode assemblies from the prepared membranes.
- Testing the membranes in a fuel cell and study their performance and studying the durability of the membranes in a fuel cell.

## 1.5 Outline of the thesis

This chapter has provided an overview of the motivation behind the work presented in this thesis and a basic introduction to fuel cells.

Chapter 2 consists of an introduction of the technology as well as a literature review of the work that has been published on membranes for fuel cells operating in an intermediate temperature range.

Chapter 3 provides information on the materials and the experimental methodology used in this thesis. This includes the synthesis of graphene oxide, the fabrication of mixed matrix membranes, the characterisation techniques used and the fuel cell testing protocol that was followed.

The characterisation of the synthesised graphene oxide and the characterisation of the single and multilayer mixed matrix membranes is presented in Chapter 4.

Chapter 5 presents the fuel cell performance of the prepared membranes. This includes single and multilayer membranes of varying graphene oxide loading, and thickness, and fuel cell testing with varying operating temperatures.

Chapter 6 demonstrates the performance of the optimised membranes in an accelerated stress test. Furthermore, samples were tested with a Nafion/cerium oxide layer painted on the gas diffusion layer to improve fuel cell durability.

Finally, chapter 7 concludes the results of this thesis and provides suggestions and thoughts about further experiments and future directions in IT-PEFC research.

# 2 Literature Review

The previous chapter gave a brief background on the challenges of decarbonisation and the potential of hydrogen as an energy vector, along with an introductory overview of fuel cell principles. This chapter will focus on providing a thorough understanding of the purpose of the membrane in the fuel cell, it's characteristics, and a current review of the strategies that allow for the development of intermediate temperature fuel cell operation. Consequently, the positioning of this thesis within the literature and the work to be performed will be explicitly explained[3].

## 2.1 Membranes for fuel cells

The central component of the fuel cell, the membrane's purpose is to regulate the transport of reactants, and it is this regulation mechanism that allows for the completion of the reaction at the cathode. Traditionally, membranes have seen strong use in many industries such as petrochemicals, food, pharmaceuticals and chemicals[84], with specific functions geared towards nanofiltration, reverse osmosis, electrodialysis and microfiltration, to name but a few[85]. Unlike porous membranes, where the goal is to filter particles via a pressure difference driving force[86], fuel cell membranes are electrically charged dense membranes and it is this electrical charge that separates certain ionic compounds[87]. Overall in the polymer membrane of the PEFC, this creates an environment that facilitates transport of positively charged ions and blocks, gases, electrons and negatively charged ions.

[3] Parts of this chapter are based on the publication: Gabriele G.Gagliardi, Ahmed Ibrahim, Domenico Borello and Ahmad El-Kharouf. Composite Polymers Development and Application for Polymer Electrolyte Membrane Technologies—A Review. Molecules 25 (7) (2020) p.1712. Doi: 10.3390/molecules25071712. Some of the data has been re-analysed since publication.

Therefore, membranes that are electrically charged are vital for fuel cell operation, and this has led to the use of perfluorosulfonic acid (PFSA) based ionomers, a group of ion-conductive polymers.

The most popular and the industry standard is Nafion, which was synthesised by Dr. Walter Grot at DuPont in the early 1960s[88], and first used in fuel cells for the NASA Apollo space programme[89]. The general structure of Nafion is shown in Figure 2-1 and consists of a hydrophobic polytetrafluoroethylene (PTFE) backbone with short side chains of sulphonic functional groups[90]. Consequently, the side chains, when acidified into $[SO3^-][H^+]$, create clusters of high ionic conductivity within a generally non-conductive polymer[91]. With the rigid PTFE backbone providing mechanical strength and chemical inertness, Nafion is well positioned for use in PEFC technologies[92].

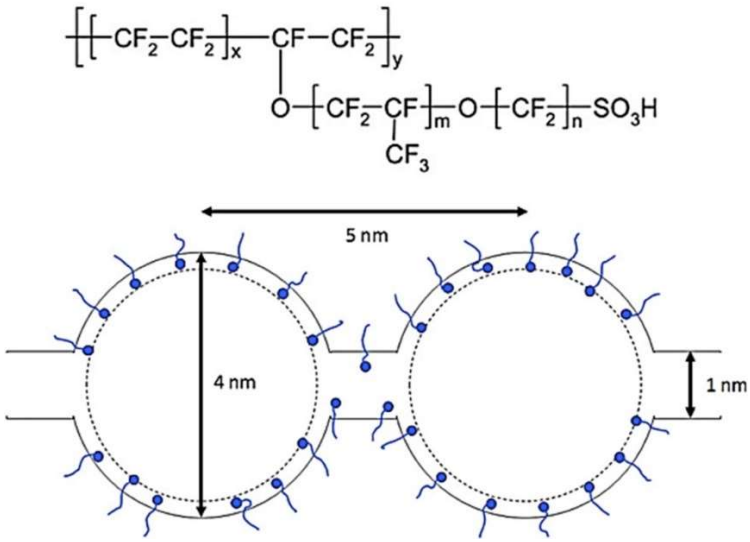



Figure 2-1: Structure of Nafion and the structure of a water channel. The blue lines are the backbone of Nafion and the blue filled circles are the sulphonic side groups[4].

[4] Reprinted with permission from Elsevier[91].

However, the ionic domains generated by the side groups are isolated from one another and would have to cross large regions of non-conductive PTFE in order for protons to pass from one side of the membrane to the other.

The secret behind Nafion's proton conductivity lies in its dependence on water, and the need to be sufficiently hydrated. When hydrated, the structure of Nafion begins to alter, as water molecules are drawn to the hydrophilic regions, creating water clusters of a diameter of approximately 4 nm. With enough water content, these hydrophilic domains begin to form 1 nm channels between them, allowing for proton and water transport[93], as shown in the bottom image in Figure 2-1.

The actual process of proton conduction along the side groups is in theory facilitated by two mechanisms, presented in Figure 2-2[94]. The first is the Grotthuss mechanism, where a proton from oxidised hydrogen fuel jumps between water molecules that have aligned themselves along the sulphonic acid groups[95]. The second is the vehicle mechanism, where a proton and water molecule form a hydronium ion through donor-acceptor bonding and it is this ion that diffuses through the membrane[96]. Generally, the activation energy for the vehicle mechanism is lower than 14 kJ $mol^{-1}$, whereas for the Grotthuss mechanism this value ranges between 14 and 40 kJ $mol^{-1}$ [97]. As a consequence of both transport mechanisms involving water molecules, the proton exchange membrane needs to be sufficiently hydrated to perform well.

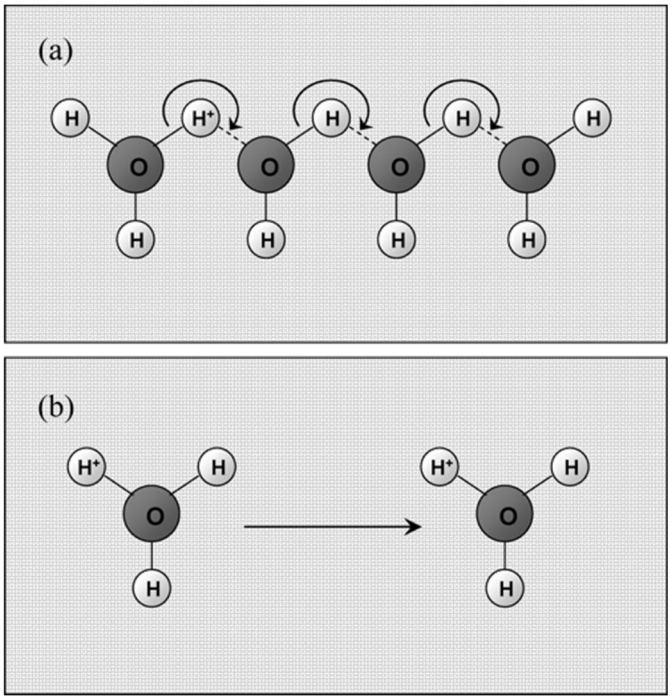



Figure 2-2: Grotthus (a) and vehicle (b) mechanisms[5].

Moreover, research in membranes for PEFCs is focused on attempting to meet industry requirements for vehicular applications. In particular, the US Department of Energy has published targets which each fuel cell component should attempt to reach[98]. For the membrane, these targets include (for 2020), a maximum hydrogen crossover of 2 mA $cm^{-2}$, a maximum operating temperature of 120°C and a cost of 20 \$ $m^{-2}$, to name but a few benchmarks[99].

Currently, the Nafion membrane is expensive[100], and this is because Nafion is still protected by patents and therefore the price is high, as there is a lack of commercial competitors[101]. Additionally, the synthesis requires the use of fluorine chemistry, which is costly as well as hazardous to the environment due to the issues of PFSAs[102]. Thus, the EU has recently launched initiatives to find non-fluorinated materials in order to avoid these issues.

[5] Reprinted (adapted) with permission from the American Chemical Society Copyright 2005[94].

## 2.2 Fuel cell operating temperatures

As briefly explained in the introduction, a way to improve fuel cell performance is to increase the operating temperature. These are the so-called intermediate temperature fuel cells that operate between 100 and 120°C[103]. The reasoning for this increased operating temperature is the higher rates of reaction, simpler water management due to only one phase of water being present (vapour) and simpler thermal management[104]. Unfortunately, at these higher temperatures water boils off and the electrolyte membrane dries out, resulting in a sharp drop in proton conductivity. To add to this, this drying also makes the membrane mechanically non robust and more susceptible to pinholes and breaks, which will lead to total failure of the fuel cell[105].

The membrane operating window is displayed in Figure 2-3. At higher temperatures, polybenzimidazole (PBI) membranes are employed due to their thermal and chemical robustness[50]. For example, Nafion has a glass transition temperature of 125°C corresponding to the movement of its backbone, and a second at 195°C which corresponds to its side groups[106]. Furthermore, the presence of water in Nafion behaves as a plasticiser, further lowering the glass transition temperature[106]. On the other hand, PBI has a glass transition temperature of 427°C and does not exhibit a melting point[107].

Moreover, at these elevated temperatures, phosphoric acid is used as the transport medium for the protons, as water would evaporate. Hence, the strong resistance of PBI towards harsh acids, high temperatures, and strong oxidising and reducing environments makes it the industry standard at the higher temperature range[108]. Consequently, there is a window between low "traditional" temperature PEFCs and the high temperature phosphoric acid-based fuel cells.

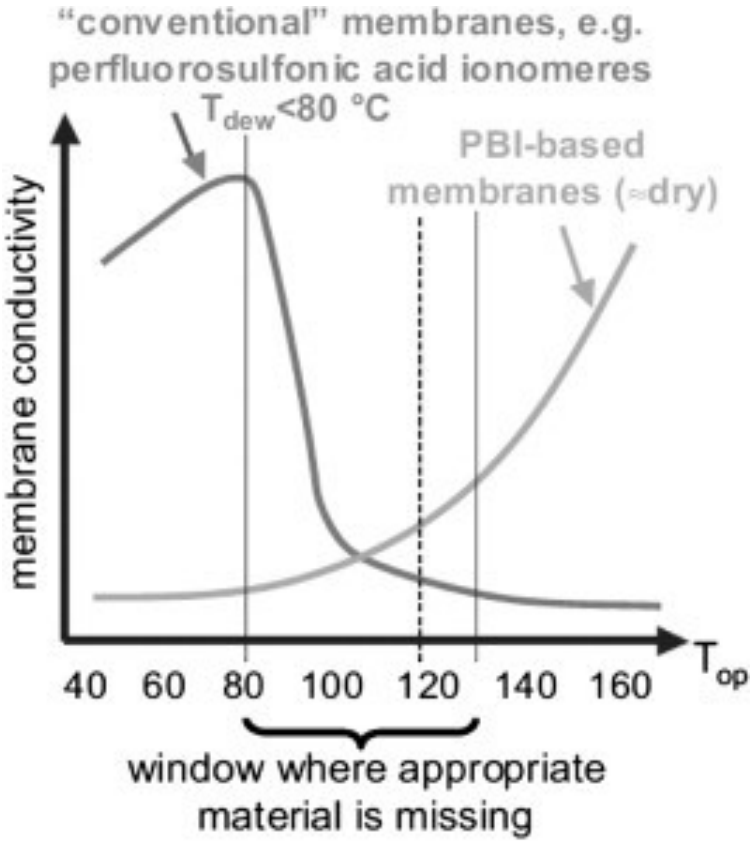



Figure 2-3: Membrane conductivity operating windows[6].

### 2.2.1 Low, intermediate and high temperature fuel cells

As explained, PEFCs are traditionally operated at 80°C due to the requirement of satisfactory membrane saturation. This saturation is provided by humidifying the inlet streams of hydrogen at the anode and oxygen or air at the cathode. Hence, the level of relative humidity (RH) of the inlet streams and hence the cell itself should be carefully controlled to prevent evaporation of liquid water within the membrane.

Interestingly, it is even possible for fuel cells to be operated at even lower temperatures, such as 70°C, 60°C and even room temperature[109]. Nevertheless, the likelihood of flooding of the

[6] Reprinted with permission from Elsevier[104].

fuel cell is exacerbated with reduced operating temperature, and the slower reaction kinetics lead to a loss in performance[110].

The action of ever so slightly increasing the operating temperature of an otherwise low temperature fuel cell still allows for the use of Nafion, but with reduced proton conductivity due to the drying of the membrane[111]. Alternatively, running a fuel cell at low temperatures under low humidity, or even anhydrous conditions can lead to similar consequences. Yet, IT-PEFCs are being considered due to their benefits of a higher tolerance towards fuel impurities, and a simpler system design[104]. Hence, current research involves attempting to retain membrane hydration by the addition of fillers, functionalisation and/or the use of substitute polymers[112].

Increasing the temperature further consequently disallows for the use of water, being replaced with phosphoric and sulphuric acids, and ionic liquids. Additionally, Nafion is no longer suitable with these acids and is substituted with alternative polymers such as polybenzimidazole (PBI) and polyether ether ketone (PEEK)[108,113–116]. The advantages of HT-PEFCs are similar to those at intermediate temperatures but further amplified[117]. For example, the cooling is quicker due to the greater temperature difference between the fuel cell and its surroundings, and the higher operating temperature allows for lower sensitivities to fuel impurities such as carbon monoxide[118,119]. To add, the use of acids allows for the control of concentration, further increasing the quantity of available conductive species.

However, a great problem is the phenomenon of “acid leaching”, which is the leaking of acid from the membrane. This can result in a reduction in the proton conductivity as well as cause significant damage to the other fuel cell components, such as the bipolar plates[120]. Hence, current research involves the fabrication of membranes with high proton conductivity and high

acid uptake, but with low acid leaching. To conclude, the individual fuel cell temperature ranges are summarised in Table 2-1.

Table 2-1: Membrane and conductive species involved at different temperatures.

| Fuel cell | Low temperature PEFC | Intermediate temperature PEFC | High temperature PEFC |
|---|---|---|---|
| Membrane | Nafion | Nafion and alternatives | PBI-based membranes |
| Conductive species | $H^+$ (from $H_2$) | $H^+$ (from $H_2$) | $H^+$ (from $H_3PO_4$) |

## 2.3 Degradation of Nafion

Temperature can have a lasting impact on the performance of PEFCs, and extended periods of elevated temperature can have a severe effect on the membrane. Hence it is vital to have a thorough understanding of the degradation mechanisms that occur in order to create solutions that will avoid them from happening and improve fuel cell performance.

Thus, the incorporation of fuel cell technology into long-range heavy-duty vehicles will require extensive durability and satisfactory performance over a long period of time. However, consistent usage can result in the degradation of the cell and its components. To add, the "start-stop" nature of vehicles results in constant hydration-dehydration cycles, further degrading the cell[121]. The membrane is particularly susceptible to these start-stop cycles, and excess degradation can lead to complete failure of cells[122]. Therefore, it is important to study and understand the mechanisms behind membrane degradation.

One performance indicator in evaluating the degradation of a fuel cell is its open circuit voltage (OCV). This is the voltage when hydrogen and air (or oxygen) are present but no current is drawn. As a consequence, fuel begins to travel through the membrane via a Fickian concentration gradient driving force, resulting in "fuel crossover"[123]. Hence, reactants can end

up at the alternate electrode (i.e. hydrogen at the cathode and oxygen at the anode), where they can react to form radicals that can attack the membrane. Therefore, the experimentally achieved OCV is a general sign of the health of the cell[124], and encompasses the losses due to fuel crossover.

Gas crossover includes both hydrogen and oxygen crossover, but in reality, hydrogen crossover is much more prominent due to the smaller size of diatomic hydrogen gas. In the case of hydrogen crossover, instead of being oxidised at the anode, some hydrogen arrives at the cathode through the membrane via a solution-diffusion mechanism[123]. As a result, the hydrogen can then react with oxygen to form radicals that travel into the membrane, leading to unzipping of the membrane backbone and thinning, a harsh reduction in membrane thickness[125]. Furthermore, the reaction between hydrogen and oxygen can generate excess heat which can create local hotspots in the membrane and potential pin holes, significantly degrading fuel cell performance[126].

At the other electrode, oxygen can crossover to the anode and consequences similar to hydrogen crossover are also observed[127,128]. Research in the area of oxygen crossover prevention involves producing barrier layers and membranes with low oxygen permeability[129,130].

Finally, there are two statements that need to be clarified. Firstly, fuel crossover can occur when current is being drawn during fuel cell operation, i.e. not at OCV. Here, some of the fuel that should undergo an electrochemical reaction does not, instead diffusing through the membrane. Secondly, the act of increasing the cell temperature increases the kinetic energy of the hydrogen and oxygen, further increasing fuel crossover. Ultimately, both the reduction in proton conduction and the increase in hydrogen crossover are significant challenges that need to be tackled in order to allow for the development of IT-PEFCs.

## 2.4 Research strategies for membrane development at intermediate temperatures

In order to allow for intermediate temperature operation, many different techniques have been explored to tackle one or more of the challenges, with particular focus on retaining membrane hydration and reducing hydrogen crossover at intermediate temperatures[104].

An additional challenge is to replace Nafion completely due to its high cost. The use of PFSAs has also come under scrutiny in recent years over their continued presence in the environment and have been dubbed "forever chemicals"[131]. Consequently, alternative polymers that are more chemically and thermally resistant than Nafion, such as polyether ether ketone (PEEK) and polyether sulfone (PES), have seen extensive use. However, like Nafion, these polymers require sulphonic acid groups to improve their proton conductivity, and hence are treated with a sulphonation process[132]. However, the presence of sulphonic groups still requires hydration of the membrane.

Alternatively, the Nafion can be replaced with a similar polymer. One example is Aquivion, which has the exact same structure as Nafion, but has a shorter side chain[133]. This shorter side chain results in reduced phase separation between the hydrophobic and hydrophilic domains, thus greater proton conductivity.

## 2.5 Use of filler materials

Another method involves incorporating filler materials into the polymer matrix to aid performance. These improvements can potentially include increased proton conductivity, increased chemical, thermal and mechanical resistance, and enhanced water retention[134]. Many different fillers have been experimented with: from metal oxides to carbon nanomaterials[135].

To add, these fillers can be functionalised to further increase their properties and/or add multifunctionality[136].

This literature review will summarise the techniques used by research groups working in this field with a particular focus on the use of filler materials and the use of alternative membrane materials, with the ultimate goal of improved fuel cell performance by either reducing hydrogen crossover, increasing proton conductivity, and/or preventing water loss.

### 2.5.1 Graphene oxide fillers

One of the most common filler materials used to prepare composite membranes is graphene oxide, the oxidative derivative of graphene. First isolated in 2004, graphene has displayed extraordinary physical properties[137]. Structured as a single atom layer of hexagonal carbon lattices[138], there has been a motivated attempt to take advantage of graphene's properties in a variety of applications, such as batteries, composite materials and electronics, to name just a few[139–145].

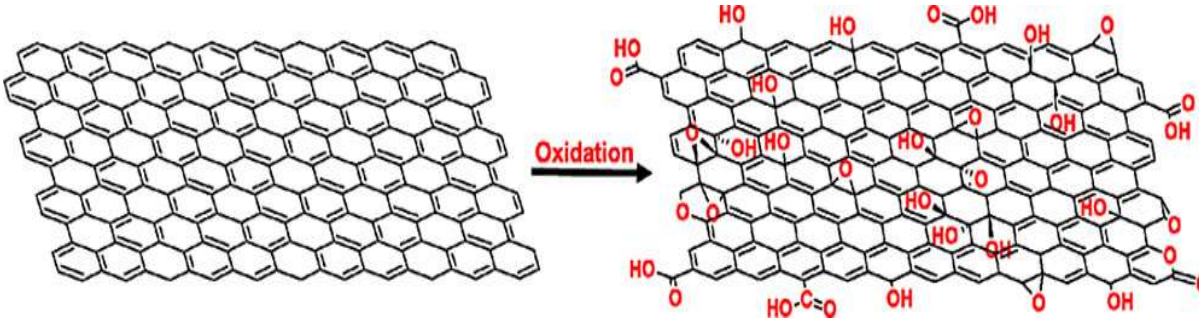



Figure 2-4: Structure of graphene and graphene oxide[7].

[7]Reprinted (adapted) with permission from the American Chemical Society Copyright 2016[138].

On the other hand, graphene oxide has seen a lot of interest in its potential as a membrane filler for PEFCs[146]. Structurally, GO is similar to graphene, as seen in Figure 2-4; however, the main difference is in the presence of oxygen-containing functional groups that are distributed on the basal planes and at the edges of the structure[147–149]. These groups include epoxides, hydroxyl, carboxylic and other carbonyl groups which stick out of the plane and consequently increase the interlayer distance between sheets[150–152]. This increase in interlayer spacing combined with GO being naturally hydrophilic due to its numerous oxygen-containing functional groups, allows for the facile dispersion in certain solvents such as water[153].

This dispersibility indicates that GO can be easily prepared to create membranes and devices in general. As an example, graphene can either be synthesised via the mechanical exfoliation of graphite (top down), or through chemical vapour deposition (bottom up)[154,155]. GO in comparison can easily be oxidised from graphite via methods such as Hummers, Staudenmaier and Hofmann to produce graphite oxide[156–158]. This can then be filtered and centrifuged to give single sheet GO dispersions[159]. Following this, membranes can be produced through methods such as vacuum filtration[160]. Incorporation of GO in membranes for the use in fuel cells began in the early 2010s[136].

A point of consideration is the different terms that are used in the literature. Terms such as “composite membranes” and “mixed-matrix membranes” are used interchangeably and will both appear in this literature review.

The simplest example is the use of non-modified GO as a filler within a Nafion membrane via solution casting, a technique where a polymer dispersed in a solvent is cast onto a plate and the subsequent evaporation of solvent leaves a film of polymer behind.

One of the earliest pieces of work on graphene oxide as a membrane filler was from the Scott group[161]. Kumar et al. fabricated GO composite membranes and their solution casting method involved dissolved precast Nafion in dimethylacetamide (DMAc) and mixing with the graphene oxide[161]. The solution was cast onto a glass plate and dried at 70°C followed by heat treatment in the oven at 140°C for two hours to remove the DMAc.

Water uptake (WU) showed that the addition of GO increased the water retention at 2 and 4% GO loadings, however, it decreased at 6%. The authors explained that this was due to the amphiphilic nature of the Nafion membrane where the concentrated hydrophilic regions are disrupted by the fillers. This was also confirmed with ion exchange capacity (IEC) and proton conductivity measurements that revealed the same characteristics.

Additionally, mechanical tensile testing discovered that the addition of GO enhanced the tensile properties, however, the extension was reduced, with a decrease in maximum stress from 4 to 6% loadings. The authors argued that this was due to the membrane becoming too brittle and stresses forming in the interfacial regions of the GO and Nafion.

Prepared membranes of varying GO loading were tested in a PEFC at 100°C and 25% relative humidity. Membranes with 4% GO loading produced a peak power density of 212 mW $cm^{-2}$, much higher than that of 56 mW $cm^{-2}$ for Nafion 212. This initial piece of work showed that there is an optimum level of loading and that increases beyond that could results in reduced performance. Hence it is important to find this optimum composition.

#### 2.5.1.1 Functionalisation

Additionally, the performance of Nafion-GO membranes can be further elevated via functionalisation, a process where various additional functional groups are added to GO via chemical treatment. Hence, functional groups that can assist in the proton conductivity and

water retention have been investigated. For example, the most common functionalisation process for GO is sulphonation, as the sulphonic acid groups can create regions of high-water content and enable the transport of protons.

One of the first examples of a composite membrane with sulphonic acid functionalised GO for intermediate temperature fuel cells was presented by Zarrin et al.[136]. Fuel cell testing at 120°C and 25% RH, as shown in Figure 2-5, revealed that the functionalised composite membrane produced a peak power output of 0.15 W $cm^{-2}$ in comparison to 0.042 W $cm^{-2}$ for recast Nafion, an almost fourfold increase in performance. Hence, it can be concluded that the use of sulphonation can bring about large improvements in proton conductivity and fuel cell performance.

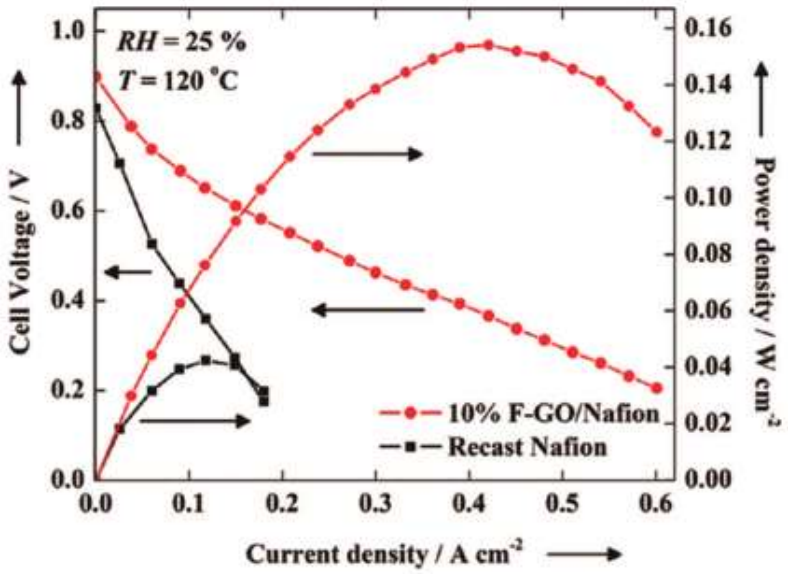



Figure 2-5: MEA polarisation and power density curves for 10 wt.% functionalised GO/Nafion and recast Nafion[8].

[8] Reprinted (adapted) with permission from the American Chemical Society Copyright 2011[136].

Moreover, sulphonation can also be applied to the polymeric phase, with the use of sulphonated hydrocarbons acting as an alternative to Nafion. Kumar et al. replaced Nafion with SPEEK and produced a composite membrane with sulphonated graphene oxide (SGO)[162]. The addition of SGO increased the IEC from 1.93 meq $g^{-1}$ for SPEEK to 2.3 meq $g^{-1}$ for SPEEK/SGO, suggesting that the sulphonic and oxygen functional groups increased the sites for potential ion exchange. This was further supported with WU values of 60% for the composite membrane versus 57.58% for SPEEK.

Finally, during fuel cell testing at 80°C and 30% relative humidity, SPEEK/SGO membranes produced a much higher peak power density of 378 mW $cm^{-2}$, whereas pure SPEEK produced a value of 250 mW $cm^{-2}$. On the other hand, the authors did not perform tensile strength analysis which would have been useful to observe whether the presence of both sulphonic groups in the polymer and filler would have weakened the membrane via excessive water retention.

Alternative chemical techniques have also seen use in composite membrane development. As an example, different functional groups can be applied to GO's large surface area to provide regions for proton conduction. These methods will be briefly discussed here.

He et al. prepared a nanocomposite membrane with graphene oxide functionalised with dopamine (DGO) within a SPEEK polymer matrix for anhydrous conditions[163]. Dopamine's structure includes two hydroxyl side groups, and hence can create hydrogen bonding with water. Furthermore, dopamine was chosen due to its ability to form a polydopamine layer that adheres strongly, improving the bonding between the GO and SPEEK. This improved bonding was confirmed via mechanical testing, with the SPEEK/DGO producing a higher maximum tensile strength, at the cost of reduced maximum elongation compared to both SPEEK/GO and SPEEK.

However, IEC values fell with introduction of filler material, due to GO's lower IEC value. The drop for DGO was explained via the SPEEK and DGO creating acid-base pairs and reducing the number of protons that can be exchanged. On the other hand, proton conductivity increases with both GO and DGO loading, with the DGO composite having much greater conductivity, which is unusual as the water uptake of DGO decreases with increasing loading (opposite to GO, whose water uptake increases with loading), which the authors explained uses acid-base pairs creating an optimum water orientation for proton hopping. Therefore, it cannot be assumed that functionalised GO will behave in a similar manner to pristine GO and extensive ex-situ characterisation is still required.

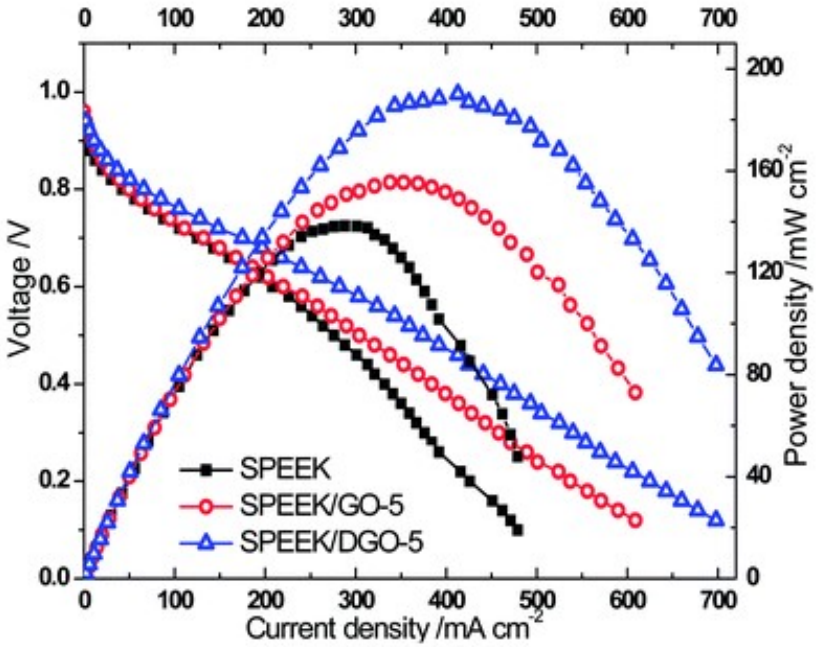



Figure 2-6: Single cell performances of the membranes with anhydrous $H_2/O_2$ operated at 120°C, under anhydrous conditions[9].

[9] Reprinted with permission from the Royal Society of Chemistry Copyright 2014[163].

Liu et al. developed a composite membrane from chitosan, a linear polysaccharide prepared from the skeleton of shellfish, which was then combined with firstly SGO and secondly phosphorylated graphene oxide (PGO)[164,165]. Phosphoric acid was chosen instead of sulphuric acid due to its higher binding energy with water and lower energy in transferring protons.

Addition of GO, SGO and PGO reduced both the water uptake and swelling, due to the reduction in chain motion of the chitosan and inhibiting the free volume of the membrane, hence being able to store less water. The IEC measurements displayed the opposite trend, with addition of GO and SGO increasing the IEC. This increase in IEC was more pronounced the greater the filler loading and degree of sulphonation, with the filler material providing proton conducting groups. Sulphonic and phosphoric groups are very similar, thus it is expected that they would behave similarly.

Other techniques include the use of crosslinking agents to improve mechanical strength and reduce excessive swelling[166], and radiation grafting[167].

Chemical grafting for example can make it possible to attach Nafion and Nafion-like groups onto the surface of GO, to improve the interaction between the polymer phase and the filler phase. As such, Peng et al. chemically reacted Nafion onto GO via an atom transfer radical addition reaction[168]. Subsequently, the proton conductivity was shown to be better than recast Nafion and amazingly even close to Nafion 212.

However, the authors stated that the low proton conductivity for some of the composite membranes (different loadings were tested) could be due to the unmodified GO interfering with the ionic clusters. Conclusively, the authors suggested an optimum study on the processing conditions to improve the conductivity.

Lim et al. fabricated a composite membrane consisting of a Sulfonated Poly (Arylene Ether Sulfone) matrix with GO that has perfluoropolyether chemically grafted onto it[169,170]. The water uptake decreased with the introduction of grafted GO, with the authors explaining this drop due to the decrease of free volume of the polymer for water storage due to the restrictive behaviour of the PFPE-GO. This reduced water uptake led to slightly lower proton conductivity values compared to pristine SPAES. In this case the authors argued that their graphene oxide was slightly reduced and therefore had more of a blocking behaviour with regard to the hydrophilic channels.

#### 2.5.1.2 More than one filler

As a matter of fact, the number of fillers does not have to be limited to just one. As an example, Lee et al.[171] prepared Nafion membranes with either graphene oxide or platinum nanoparticles deposited onto graphene oxide for low-humidifying fuel cells. Nafion ionomer was mixed with graphene oxide or graphene oxide-platinum, which was prepared via microwave treatment, ultrasonicated and spread onto a glass substrate, followed by heat treatment. Platinum was chosen due to its properties of catalysing the oxidation of crossed hydrogen with oxygen to form water[172]. In-situ fuel cell testing showed Nafion-GO membranes improves the cell performance at different RHs with varying GO loadings, relative to Nafion. However, this was not the case for Nafion embedded with GO and platinum. This is because the microwave treatment to reduce the platinum also reduced the GO to graphene, making it hydrophobic. Furthermore, the presence of platinum nanoparticles produced a network of electrical conduction throughout the membrane which caused electron loss. Essentially, electrons that were meant to flow through the external circuit were instead passing through the membrane and potentially causing an internal short circuit.

The authors continued with this line of research by presenting a membrane with platinum particles on graphene as well as silicon dioxide to improve the "self-humidifying" properties of the membrane by the use of hygroscopic silica to hold the water produced by the platinum-graphene[173]. The water uptake and proton conductivity of these novel composite membranes increased with increasing silica content, with a peak water uptake of 30% achieved with 3% Pt-Gr and 3% silica content. Fuel cell experiments disclosed that the addition of silica enhanced the polarisation curve. Unfortunately, performance fell with high amounts of silica at low relative humidity, which the authors explained was due to the filler blocking the ionic pathways.

Yang et al. designed composite membranes with titania and platinum particles deposited on the titania. This was then incorporated with graphene oxide into a Nafion matrix[174]. The composite membranes had a better IEC and proton conductivity than recast Nafion, with an inflection point at 20% GO loading, where further loading decreased IEC. Fuel cell testing at varying levels of RH showed that the Pt-$TiO_2$ increased fuel cell performance. However, the authors observed that this was still not sufficient at zero RH. Including GO resulted in an even greater enhancement in cell polarisation. Additionally, the introduction of GO not only improved the current density, but also prevented significant OCV loss when the humidity was reduced, suggesting that the GO filler reduced hydrogen crossover.

Alternative fillers with different characteristics can also be incorporated with GO. To illustrate, Beydaghi et al. fabricated polyvinyl acetate (PVA) composite membranes with iron oxide (IO) nanoparticles deposited onto sulphonated graphene oxide for direct methanol fuel cell applications[175].

Here, the concept involved using magnetic nanoparticles to induce through-plane alignment of graphene oxide during casting with the application of a magnetic field. This was motivated by

the need to improve the uniformity of filler throughout the membrane and to improve the proton conductivity by orientating the GO sheets perpendicular to the membrane.

The proton conductivity of the membrane increased with addition of the filler due to the SGO, until 5%, where it begins to decrease. The authors explained that this was because of the aligned SGO sheets blocking the polymer chain movement in the ionic domains. The presence of PVA, SGO and IO created numerous amounts of hydrogen bonds between their functional group. This led to increased tensile strength but at the cost of reduced elongation. The addition of the SGO-IO also led to reduced methanol permeability. However, orientating the SGO-IO increased methanol crossover due to larger methanol transport channels and less tortuosity. Therefore, the orientation of the filler material within the polymer matrix has to be considered.

On a similar note, Ma et al. fabricated a composite film of quaternised polyvinyl alcohol (QPVA) with graphene oxide and iron oxide nanoparticles for alkaline fuel cell applications[176]. However, this time the magnetic field was applied along the in-plane direction. Expectedly, the addition of filler once again decreased elongation compared to the pristine QPVA reference sample. Interestingly however, the aligned membrane produced an elongation limit of 52.4% compared to 28.3% for the unaligned membrane. This was because the GO-IO was aligned to the membrane and hence aligned to the tensile force applied during the experiment. To add, the authors claimed that the filler material stops the polymer chains from moving and unfolding during alkaline uptake tests, resulting in a reduced uptake in comparison to QPVA[177]. Either way, composite membranes with and without magnetisation achieved greater conductivities than QPVA at all temperatures.

Finally, in-situ testing within a direct methanol alkaline fuel cell test (at 30°C) revealed that the aligned composite membrane (0.1% GO) had a higher peak power density than both the

unaligned and QPVA (83 vs 68 vs 50 mW $cm^{-2}$). Furthermore, elevating the operating temperature to 60°C resulted in the aligned composite membrane's peak power density increasing drastically to 172 mW $cm^{-2}$, in comparison to 127 mW $cm^{-2}$ for the unaligned composite. It can be observed in the two cases described above that the alignment of the filler has an influence on the composite membrane's characteristics and performance.

Iron oxide nanoparticles do not only have use for magnetic alignment of GO sheets. As many fillers are multifunctional and have more than one characteristic this can make them attractive for use in composite membranes.

For example, iron oxide nanoparticles are also hygroscopic and can be blended with Nafion and SGO to generate regions of high water content[178]. In addition, the nanoparticles draw the Nafion and SGO closer together via hydrogen bonding and electrostatic interaction, compacting the ionic domains. Hence, due to the high density of $–SO_3H$ groups, Nafion/SGO-IO achieved the greatest IEC value of 1.36 meq $g^{-1}$, followed by Nafion/GO (1.03 meq $g^{-1}$) and then recast Nafion (0.89 meq $g^{-1}$).

Furthermore, the combination of the sulphonic acid groups from Nafion and the high surface area SGO, and the hygroscopic IO led to the formation of hydrogen bonds between the free water molecules, resulting in greater water uptakes. In the case of multiple fillers, it would have been useful to perform long term fuel cell durability tests, to observe whether the SGO and iron oxide have the propensity to migrate within the membrane.

Interestingly, the additional filler that is incorporated with GO does not have to be a simple particle. Yang et al.[179] developed a composite membrane with graphene oxide modified with a metal organic framework (MOF) for low humidity applications. The MOF used was ZIF-8 ($Zn(MeIM)_2$, MeIM = 2-methylimidazole) and was grown onto the graphene oxide. At 80°C,

the composite membrane had a proton conductivity 15 times greater than recast Nafion. Fascinatingly, the conductivity did not decrease with temperature, with the authors hypothesising that this was due to water being trapped in the cages of the MOF, thus less likely to be affected by the increase in temperature.

#### 2.5.1.3 Localisation of filler

The previous pieces of work cited prepared membranes with fillers dispersed throughout the entirety of the polymer matrix. However, it is also possible to control the region where the filler is located within the membrane. This spatial control allows the filler to be located at the exact area that it is required.

A simple example is to cast multiple layers on top of the initial layer to create "multilayer membranes". One of the few pieces of research that investigated the fabrication of multilayer membranes via solution casting is the work of Branco et al.[180]. Multilayer membranes with two Nafion outer layers and an inner layer consisting of graphene oxide and another with sulphonated polyindene were designed with either solution casting and/or hot-pressing techniques. The solution casting involved heating the first Nafion layer to 100°C for two hours to evaporate the solvents in the Nafion dispersion, followed by the addition of the graphene oxide and water dispersion and another two hours at the same temperature. The final Nafion layer was applied and the multilayer membrane was heated for one hour at 120°C. The higher temperature was required to anneal the polymer. The cross-sectional SEM image of a multilayer membrane consisting of two outer Nafion layers with an internal GO layer is presented in Figure 2-7.

Multilayer membranes that were cast showed better performance and proton conductivity than the hot-pressed multilayer membranes. This was because the cast membranes had better

interfacial interaction between the individual layers compared to the hot-pressed membranes, which suffered from delamination. This is an important aspect to be considered, as delamination can compromise the proton conductivity, increase resistances, and allow large amounts of hydrogen to crossover.

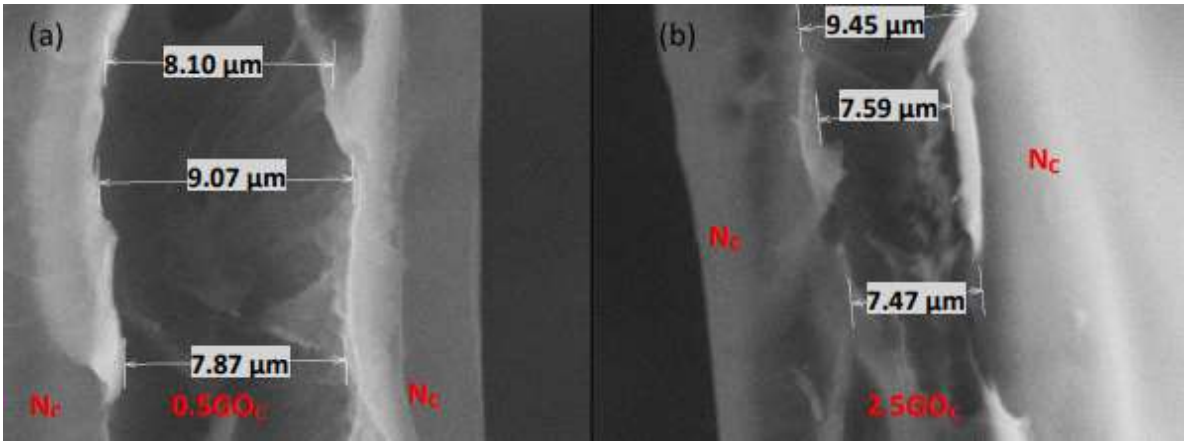



Figure 2-7: SEM images of a) GO (0.5 wt.%) multilayer b) GO (2.5 wt.%) multilayer[180].

The idea of producing membranes consisting of defined layers can be taken even further via the label-by-layer (LbL) technique. Here the layers are very thin with each layer being of the thickness of the width of the molecules used. This involves immersing a polymer into oppositely charged solutions to build up numerous amounts of layers. Furthermore, multiple different functionalities can be incorporated with this technique[181].

For instance, Wang et al. fabricated a graphene oxide Nafion composite membrane via LbL for direct methanol fuel cells[182]. Recast Nafion was used as the immersed support polymer and layers of GO were built up, with the use of 1, 4-phenyldiamine hydrochloride (PDHC) as a crosslinking agent to prevent GO dissolution in water. The assembly process involved immersing the Nafion membrane into PDHC solution followed by rinsing with DI water. The membrane was then placed into a GO solution to attach the GO to the PDHC. The steps were

then repeated to build up the number of required GO layers and FT-IR was used to confirm the successful LbL assembly.

Increasing the number of GO layers led to higher IEC values, improved oxidative stability, lower methanol crossover, and a higher OCV. However, proton conductivity decreased, with the authors claiming that this reduction was linked with the lower water uptake results and that the addition of GO hindered the effective proton diffusion channels. To add, the GO sheets were covered in polar oxygen containing groups and as methanol is less polar than water, hence less likely to cause swelling[183].

One consideration is that the process of producing the layers can take a very long time due to the constant washing and immersion of the support layer. On a large scale, this process can be sped up with the use of automated machinery but in the laboratory scale methods such as casting are more effective. It would be interesting to see the durability of these layers, and whether there is any removal of the layers during fuel cell operation.

Interestingly, the concept of completely replacing the polymer in the membrane has also been proposed, with Bayer et al. preparing a pure GO membrane with no polymer matrix via vacuum filtration[184]. The GO membrane displayed higher water uptake in comparison to Nafion, making it promising for fuel cell applications at elevated temperatures and/or reduced humidity. However, the membrane swelled much more than Nafion, which could compromise performance. Additionally, at increased temperatures proton conductivity and fuel cell performance decreased, likely due to the loss of oxygen groups. However, this is a promising example of completely replacing the polymer membrane within a fuel cell.

This work was followed up exchanging cations before filtration in order to produce a GO membrane suitable for use in an alkaline fuel cell[185]. The concept of ion exchange before

membrane fabrication is an interesting idea and in this case the potassium hydroxide treated GO membrane displayed a permeability of around 5 times lower than in GO.

On a similar note, it is also possible to create a membrane with a distinct polymeric region and a distinct GO region. In this case, Lin et al.[186] designed a Nafion 115 membrane laminated with a layer of graphene oxide "paper", which was compared to pristine Nafion 115.

The laminated membrane had a much lower WU of 10.3% in comparison to 28.8% for Nafion 115, but a higher IEC value of 0.99 meq $g^{-1}$ versus 0.89 meq $g^{-1}$ for Nafion 115. The authors explain the higher IEC due to the –COOH on the basal plane releasing protons when humidified, as well as the compatibility of GO and hydrophilic Nafion. However, this is not represented in proton conductivity measurements, with the laminated membrane experiencing a slight decrease compared to Nafion 115. Furthermore, the defined GO layer led to more than a 40% higher selectivity than that of Nafion 115, due to the laminated membrane being less susceptible to methanol crossover due to the reduced swelling.

However, the process to fabricate the membrane involves hot-pressing, and work from Branco[180] has shown that the membrane will delaminate during PEFC operation. There is also a chance that the GO paper will be reduced during fuel cell operation and become more graphene-like, hence more conductive and lead to reduced performance.

Instead of laminating the GO layer and to prevent potential layer separation, a smaller layer and a smaller region of GO can be applied onto Nafion through simple methods such as spin coating and drop casting. A comprehensive study on the effects of drop casting and spin coating GO onto wet Nafion 212 was performed by Lue et al[187].

The addition of the GO layer caused a reduction in the water uptake, IEC, and ionic conductivity, compared to Nafion 212, with decreases growing with GO loading. The authors

explained that this was due to the hydrophobic behaviour of the $sp^2$ domain as well as the GO sheets interfering with the ionic domains and creating steric hindrance which prevented the uptake of water. It is interesting to note that some research groups have reported increased water uptake and IEC levels, and others the opposite[136,163,184]. It would therefore be important to try to resolve this issue.

The permeabilities of the membranes were tested in formic acid and the addition of GO reduced the permeability of formic acid of the composite membrane, with increasing GO loading resulting in decreased permeability. In addition, spin coated composite membrane had a lower methanol and ethanol permeability than drop-cast and this was because of the spin coating producing an even, very uniform GO layer, compared to drop casting.

The proposal of creating thin layers can be taken even further by simply replacing the membrane and instead applying ionomer directly onto the GDE, a technique named direct membrane deposition (DMD) developed by Freiburg University[188]. Applying ionomer directly onto the cathode and anode gas diffusion electrodes, which are then placed facing each other, can produce "membranes" of only 12 μm. However, the very thin layer creates large hydrogen crossover and potential electrical shorts.

As a solution, Breitwieser et al. adapted the technique of using an interlayer region consisting of GO and cerium oxide, in addition to replacing Nafion with Aquivion[189]. GO was utilised to facilitate proton conduction, and to block crossover, with cerium oxide behaving as a radical scavenger to remove any radicals formed from the result of crossover. Furthermore, the insulating nature of GO could prevent any electrical shorts which become more common with thinner membranes, hence a very thin interlayer of 200 nm of cerium oxide and graphene oxide separated the ionomer sprayed GDEs, as shown in Figure 2-8.

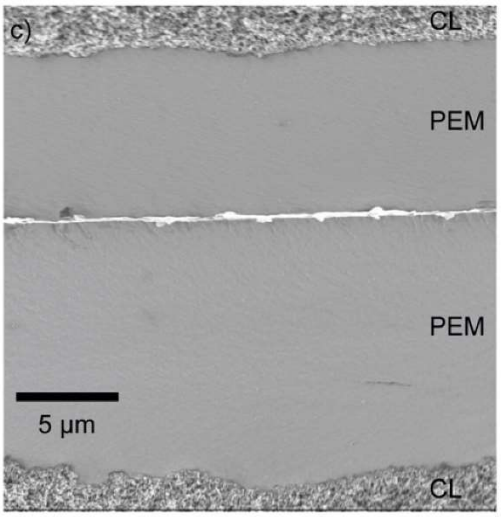



Figure 2-8: Cross-sectional SEM image of the multilayer DMD MEA showing the catalyst layer (CL), the sprayed ionomer layers (PEM), and the GO/cerium oxide interlayer in the middle[10].

Fuel cell testing of the aforementioned 12 µm sample produced a lower peak power output compared to Aquivion membranes of 10 and 20 µm. The authors hypothesised that the inclusion of the graphene oxide/cerium oxide interlayer increased the contact resistances due to the multiple interfaces. This was confirmed with in-situ impedance spectroscopy with the pristine 20 µm Aquivion having a contact resistance of 32 mΩ $cm^2$ and the MEA with the graphene oxide/cerium oxide interlayer having a contact resistance of 48 mΩ $cm^2$.

As expected, the interlayer sample produced a very low hydrogen crossover rate of 1 mA $cm^{-2}$. Thus, the addition of an interlayer of graphene oxide has the potential to decrease hydrogen crossover, which would be more important for higher temperature fuel cells, due to increased hydrogen crossover at elevated temperatures. However, what should be considered is that the

[10] Reprinted with permission from Elsevier[189].

use of applying ionomer onto the gas diffusion layer could block fuel transport to the catalyst layer. In addition, excess hydrophilic ionomer can make it difficult to remove excess water produced at the cathode, resulting in mass transport losses, and potentially flooding.

### 2.5.2 Inorganic materials

Graphene oxide is not the only type of material that has been studied and incorporated into polymer membranes for fuel cells. In fact, inorganic fillers preceded GO, having been explored much earlier, with work consistently published from the early 2000s.

These fillers tend to be oxides, such as silica and titania. The concept behind using inorganic fillers aims at their capability of reducing crossover, their high thermal and mechanical strength, and their hygroscopic behaviour. The concept of reducing crossover comes from the solution-diffusion model, where the gas first dissolves into the membrane before diffusing through the membrane[87]. Thus, the incorporation of filler materials increases the tortuosity as well as preventing polymer thermal rearrangement into the free space of the membrane and this leads to a reduction in crossover. This hydrogen crossover is also more prominent at higher temperatures, where the water channels are not fully saturated with water due to evaporation. This dehydration results in a reduction in the size of the channels within the membrane and hence less water for protons to travel via the Grotthus mechanism or via diffusion. Overall, this leads to an increase in activation energy for these proton conducting mechanisms and a reduction in proton conductivity and subsequent fuel cell performance.

As an example, one of the first pieces of work on the use of inorganic fillers were by Nunes et al. who proposed the use of several different types of inorganic fillers: such as silicon, titanium and zirconium dioxide for methanol fuel cells, in order to block methanol crossover[190].

Methanol crossover was successfully repressed, however, the fillers led to a reduction in proton conductivity.

Di Noto et al. studied mixed organic-inorganic membranes consisting of Nafion and various metal oxides, such as titanium, zirconium, hafnium, tantalum and tungsten oxides[191]. The idea behind this project was to study the behaviour of the different composite membranes.

All membranes were gravimetrically stable below 170°C implying suitable use in intermediate temperature PEFCs. Additionally, four different water regions were detected in the composite membrane, which had to do with the many interactions such as bulk water and water soluble ions interacting with the sulphonic side group. This is interesting as generally water domains in membranes for fuel cells are seen as either bound or non-bound (free) water. The authors suggested that the conduction mechanism within the studied membranes involved hopping of protons through different fluctuating water domains[192].

As a result of the large quantity of available inorganic oxides, there has been plenty of work in using different fillers for composite membranes[193]. Metal oxide fillers such as titania, silica, alumina, and zirconia were studied by Adjemian et al. for fuel cell testing between 80 to 130°C[194]. Compared to recast Nafion, the titanium oxide and silica composite membranes performed better at higher temperatures and lower humidity.

Interestingly, the carbon monoxide tolerance of the catalyst layer at 130°C was improved to tolerating 500 ppm of carbon monoxide without failing compared to 50 ppm at conventional operating conditions, by using the composite membrane in comparison to recast Nafion. This shows that some fillers could have potential benefits outside of just the membrane in the fuel cell system.

Furthermore, just like GO, inorganic fillers can also be functionalised, for example, hydrophilic fillers can attract high quantities of water, thus improving proton conductivity and reducing the unfavourable effects of increased temperatures.

Giffin et al., for instance, prepared and characterised a composite membrane comprised of sulphonated zirconia dispersed in a Nafion matrix to improve the proton conductivity at higher temperatures[195]. The sulphonic groups were able to create hydrogen bonds with the water molecules and hence were less affected by elevated temperatures. Proton conductivity measurements at 120°C and under dry conditions revealed that the membrane had a conductivity of $3 \times 10^{-3}$ S $cm^{-1}$.

A comprehensive study on the influence of sulphonation on zirconium oxide was published by D'Epifanio et al.[196]. Water uptake experiments performed at 25°C and a RH ranging from 30 to 100% revealed that the sulphonated zirconium oxide composite membrane outperformed recast Nafion. This is quite important as most water uptake experiments are performed by immersion of liquid water, which is not exactly representative of fuel cell operation. However, the WU experiment was operated at 25°C, which is not realistic. Thus, it would have been very interesting to have observed the results at temperatures corresponding to fuel cell operation.

Fuel cell polarisation experiments at 70°C, 83% RH and 0.6 V revealed that the sulphonated composite membrane achieved a current density of 1015 mA $cm^{-2}$, vastly outperforming recast Nafion at 680 mA $cm^{-2}$. This difference in performance was especially prominent in the ohmic and mass transport regions, revealing that the filler reduced ohmic resistance, with the authors hypothesising that the improvement in the mass transport region is due to the extra $SO_4^{2-}$ groups creating additional acid sites for water diffusion. Finally, a test at 30% RH showed even larger

differences with current densities of 930 mA $cm^{-2}$ versus only 200 mA $cm^{-2}$. Hence, the use of functional groups to add extra characteristics has become quite a common technique.

Equally essential is the actual quantity of filler used, as with GO composite membranes, there is also an optimum loading for inorganic composite membranes. Zirconium oxide of various loadings of 5, 10 and 20% were examined by Saccà et al[197].

Water uptake values increased from 20% for recast Nafion to 24, 24, and 30% for loadings of 5, 10 and 20%, respectively. Surprisingly, water uptake did not decrease with a zirconia loading of 20%. Unfortunately, this increase in water uptake can be detrimental at standard fuel cell operating conditions, as at 80°C, the membrane with 20% filler had a lower potential, possibly due to excessive uptake of water. However, composite MEAs with 10% zirconia produced higher cell polarisation compared to Nafion at both temperatures with a peak power density of 400 mW $cm^{-2}$, which was achieved at 130°C, 85% RH, and between 0.5 and 0.6 V.

Other optimum loadings were studied for composite membranes by Saccà et al., testing titanium oxide at 5, 10, and 15 wt.% in Nafion for reduced humidity fuel cell applications[198].Cross-sectional SEM images showed that the lower weight loadings were better dispersed whereas, higher weight loading membranes revealed the presence of agglomerates. One point of reflection is that excessive filler loading can result in the formation of stiffer and thus more fragile membranes. The composite membranes had lower swelling than recast Nafion, however, fuel cell start-up operation could result in the membrane's dehydration, which could damage it.

The authors continued their work by testing these composite membranes for fuel cells at medium temperatures[199], with the composites outperforming the recast control membrane. Additionally, the cell resistance of the recast control membrane increased after 100°C, whereas

the composite increased after 110°C. Thus, it can be concluded that there is an optimum quantity of fillers, and that this can vary depending on characterisation technique.

Furthermore, inorganic composite membranes can vary significantly, and while oxides are the most common types of inorganic filler employed, other analogues of inorganic fillers have also been studied, such as zirconium phosphate, to improve the proton conductivity and stability of membranes[200]. Furthermore, fillers can also be incorporated into the polymer matrix using a variety of methods, instead of simple mixing, but the amount of loading has to be well controlled[201].

To demonstrate, Costamagna et al. fabricated zirconium phosphate Nafion composite membranes via the impregnation technique with Nafion 115 and recast Nafion[202]. This technique involves swelling the as-prepared Nafion membrane, followed by dipping the swollen membrane in different reactants to form the zirconium phosphate salt in-situ. SEM cross-sectional images displayed a high level of uniformity of filler throughout the membrane. This was most likely because any excess salt can be rinsed away during the fabrication.

Single cell tests at 130°C and 0.45 V showed that recast Nafion achieved a current density of 250 mA $cm^{-2}$, whereas the composite membrane produced with Nafion 115 achieved a current density of 1000 mA $cm^{-2}$, 4 times as much. Even more interesting, the composite membrane produced with the recast Nafion as the base membrane reached 1500 mA $cm^{-2}$. This was most likely because the recast Nafion was much thinner than the Nafion 115, and hence the addition of in-situ zirconium phosphate additionally reduced crossover.

Xu et al. utilised this method by swelling a Nafion membrane with silica to fabricate a composite membrane, in comparison to the standard solution casting technique[203,204]. They

explained that this method maintained the ordered nanophase-separation structure of Nafion, which differs to the solution-cast composite membrane.

This was revealed in water uptake tests, where the swollen composite achieved a higher water uptake but lower swelling, in contrast to the recast membrane. Fuel cell testing at 110°C and 20% RH disclosed that the swollen composite achieved a maximum power density of 113 mA $cm^{-2}$, in comparison to 80 mW $cm^{-2}$ for recast Nafion without any filler. The higher result was explained by the lower internal resistance of the composite membrane, which would be due to the swelling method maintaining the inherent structure of Nafion.

Hence, the effect of filler materials on the morphology of the subsequent composite membrane is very important. This is because the dispersion of the filler should be as uniform as possible. If this is not the case, this would result in non-uniform behaviour within the membrane, e.g. proton conductivity would differ between regions within the membrane. Ultimately, this fabrication technique is rather simple and could be attempted for other polymer membranes such as sulphonated hydrocarbons.

Oh et al. utilised a simple single-step sol-gel calcination process to produce sulphonated silica Nafion composites[205]. Optimisation of the filler was performed and an optimum loading was observed at 1% filler loading, beating 0.5, 1.5%, and recast Nafion.

Fuel cell testing at reduced humidity also confirmed the initial ex-situ results, with the authors attributing the improved performance to effective proton transport due to the well-defined phases in the membrane structure which were observed with transmission electron microscopy. Thus, the actual quality of the membrane morphology is very important and the sol-gel method allowed for better dispersion and therefore an improved interface between the polymer and filler.

Similarly, Amjadi et al.[206] presented two membranes fabricated via two methods, solution casting and in-situ sol-gel synthesis. EDX mapping of the composite membrane elucidated that the sol-gel composite had improved dispersion of particles, which eventually led to more uniform properties. One example was water uptake, where both composites had greater uptake compared to recast Nafion. However, because of the agglomeration and hence nonuniformity in the cast composite, the water uptake increase was not as high as that of the sol-gel composite. In both cases, there was a fall in proton conductivity, which was concluded to be because of the disruption of proton pathways in the membrane. Fuel cell testing at 110°C revealed that the composite membrane achieved a peak current density of nearly 600 mA $cm^{-2}$, in contrast to over 200 mA $cm^{-2}$ for Nafion 117.

#### 2.5.2.1 Filler morphology

Beyond preparation methods, the shape of the filler material can also be adapted. Many inorganic oxides can be synthesised into a variety of different structures. Work by Matos et al., involved studying three types of titania: spherical nanoparticles, high surface area mesoporous particles, and nanotubes which were explored for the application of PEFCs operating at temperatures up to 130°C[207].

Water uptake tests discovered that any addition of spherical or high surface area titania led to a fall in water uptake in comparison to the recast Nafion, with larger decreases at higher filler weight loadings. However, the water uptake for the titania nanotube composite membrane increased, reaching a peak of nearly 60% at 15% weight loading, in contrast to 42% for recast Nafion. The authors stated that this was due to the morphology of the nanotube in which water molecules are able to position themselves inside the nanotube.

Single cell tests performed at 80°C revealed that Nafion outperformed the composite membranes. However, at 130°C, the pristine membrane's performance degraded significantly. This is in comparison to the three composite membranes, which exhibited a smaller decrease in polarisation. On the other hand, increasing filler loading in all three composite membranes led to a decrease in polarisation, as shown in Figure 2-9, particularly in the ohmic region, which the authors explained was due to the reduction in proton conductivity with greater filler loading.

Another structure of titanium oxide which was explored as a filler material are titanium oxide nanowires[208]. The concept behind this is that the nanowires would provide unique mechanical reinforcement to the membrane, in comparison to nanoparticles.

Similar to the results from other research groups, the addition of the filler led to a fall in water uptake and swelling, with the drop being greater with increasing quantity of filler. The reduction in swelling would assist in maintaining mechanical integrity during fuel cell operation. Fuel cell testing at 90°C revealed that the composite membrane experienced a smaller reduction in polarisation when humidity was reduced, in contrast to Nafion. Furthermore, humidity cycling stress tests showed that the composite membrane exhibited stress than the recast Nafion, and that the stress introduced decreases with increasing loading.

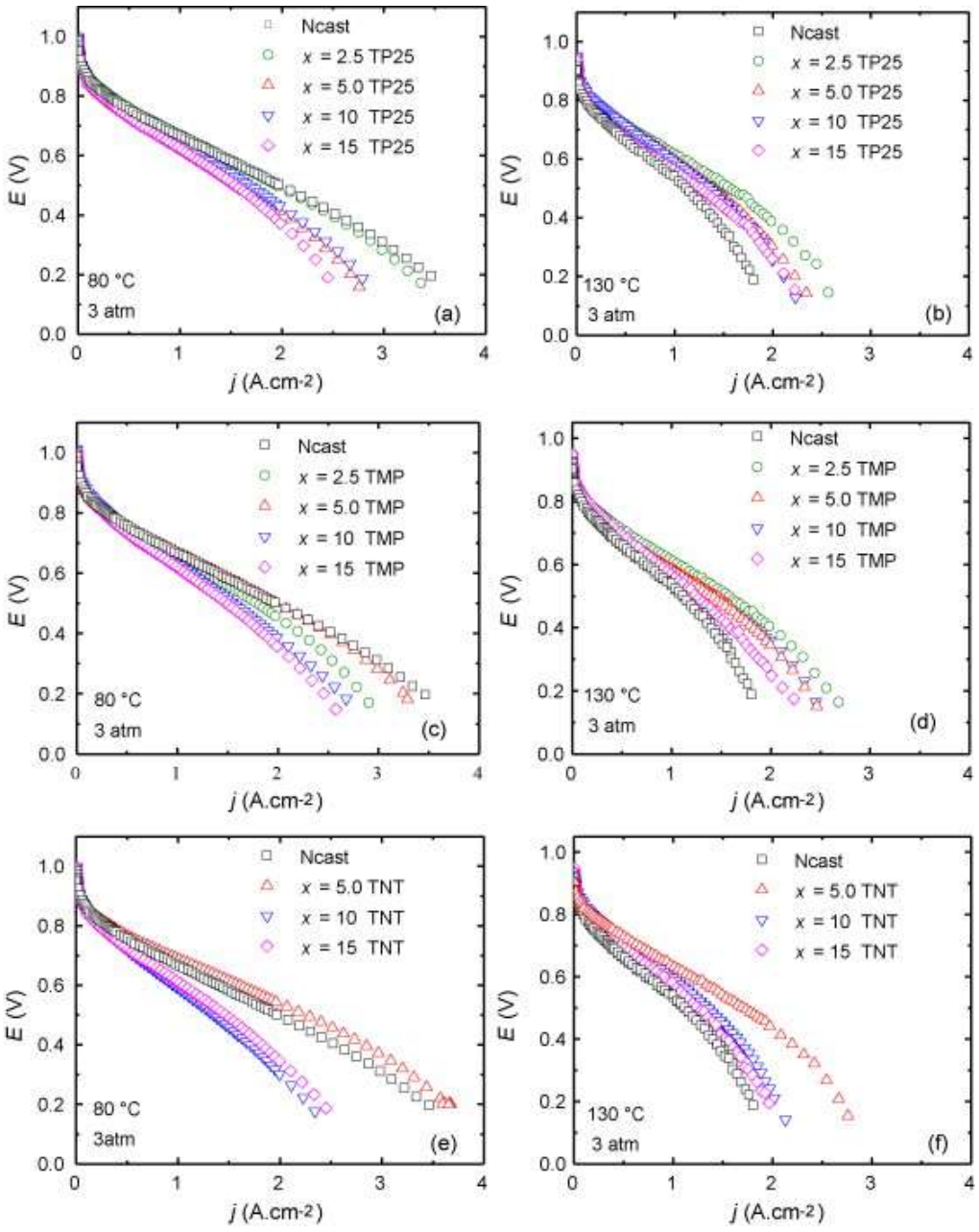



Figure 2-9: Polarisation curves for the: (a,b) titania nanoparticles TP25, (c,d) mesoporous particles TMP, and (e,f) titanium oxide nanotube (TNT) composites measured at 80 and 130°C[11].

[11] Reprinted with permission from Elsevier[207].

Further development in titanium oxide fillers included titanium oxide nanotubes[209], where composite membranes with 10, 20, and 50% filler were fabricated. The membranes with 10% nanotube filler achieved a greater water self-diffusion coefficient of $3.527\times10^{-9}$ $m^2$ $s^{-1}$, compared to $2.003\times10^{-9}$ $m^2$ $s^{-1}$ for Nafion 212. Hence, it can be observed that the structure of the filler allows for water to travel though the nanotube.

This improved movement of water was also observed in fuel cell experiments at 80°C and 100% RH with the composite membranes performing a lot better than the recast membrane, with achieved current densities at 0.6 V of 1777, 1609, 1498, and 1357 mA $cm^{-2}$ for the composite membranes with filler loadings of 10, 20, and 50% titanium oxide nanotube, and recast Nafion, respectively. Thus, the likelihood of flooding was reduced via the nanotube configuration.

Furthermore, the OCVs of the composites ranged from 0.97 to 1.03 V, signifying low hydrogen crossover levels. Finally, a 100-hour stability test at an applied voltage of 0.5 V at 80°C and 18% relative humidity, established that the composite membrane's maximum power density decreased from 470 to 442 mW $cm^{-2}$, whereas Nafion 212 only managed to achieve a maximum power density of 55 mW $cm^{-2}$, which even fell to 22 mW $cm^{-2}$ after 100 hours, a remarkable difference in performance.

Nanotubes can also be functionalised and Jun et al. prepared titanium oxide nanotubes by using 3-mercaptopropyl-tri-methoxysilane (MPTMS) as a sulphonic acid functionalisation agent[210].

These nanotubes displayed greater water uptake, with 27.2 compare to 23.7%, for functionalised nanotubes versus functionalised nanoparticles. Proton conductivity measurements at 120°C and with varying relative humidities showed that the functionalised titania nanotubes displayed higher conductivities than recast Nafion, at all humidities, with the difference being larger at lower RH. Consequently, the effective water transport properties of

nanotubes can be combined with the grafting of sulphonic functional groups to further enhance water uptake and proton conductivity.

Fillers can have their structure altered and an example of this is the use of mesoporous zirconium oxide nanotubes[211]. In this example, the inorganic filler has the structure of a nanotube and also has pores. The tubular structure and the pores should in theory improve water transport, hence leading to better proton conductivity.

The introduction of the filler led to improved power densities at 0.6 V, and this implied a reduction in ohmic resistance. At higher current densities where mass transport losses dominate (at an applied voltage of 0.3 V in this work), the composite membrane displayed higher current densities.

This observation lends credence to the concept of improved water transport and the authors stated that this was because of to the more efficient back diffusion from the cathode to the anode, preventing flooding. Finally, the composite membranes also showed improved durability. In this case, a membrane with 1.5 wt.% filler underwent a 200-hour durability hold test (at 80°C and 18% relative humidity), only resulting in an OCV drop from 0.99 to 0.92 V.

Instead of changing the filler, the polymer matrix can easily be replaced, especially as Nafion's high costs have led to work in alternative polymers[212]. Here the filler materials in this case can be used to improve the performance of these alternative polymers in areas where they are not competitive with Nafion.

Devrim et al. for instance designed a membrane with titanium oxide and sulphonated polysulfone as the polymer matrix[213]. Unlike prepared Nafion, the degree of sulphonation of the polymer can be controlled during synthesis and hence greater degrees of sulphonation can

lead to higher water uptake, with a 15% degree of sulphonation corresponding to water uptake of 7%, in contrast to 33% for a sulphonation degree of 40%.

However, adding titanium oxide to the sulphonated polymer led to a decline in water uptake to 29%. The authors declared that this was because the filler reduced the membrane's free volume and ability to swell sufficiently, though, unlike with Nafion composites, the degree of sulphonation can be controlled, or in this case increased, so that the effect of the filler can be mitigated.

Nevertheless, single cell tests at operating temperatures from 60 to 85°C disclosed that the reference sulphonated polysulfone experienced excessive swelling above 70°C, resulting in a lower power output. In this case, the reference sulphonated polysulfone membrane produced a maximum power density of 0.16 W $cm^{-2}$ at 85°C, in contrast to 0.24 W $cm^{-2}$ for the composite membrane. Therefore, we can see that the composite membrane outperformed the reference membrane as the filler offered mechanical support to the membrane, avoiding disproportionate swelling and deformation.

Another sulphonation study was performed by Carbone et al. who prepared two types of SPEEK composite membranes with amino-functionalised silica filler, one with a degree of sulphonation of 35%, and the other with a sulphonation degree of 52%[214].

Interestingly, the filler did not affect the water uptake of the 35% SPEEK, but the uptake in the 52% SPEEK composite fell from 400 to 120% and the degree of swelling ratio from 4 to 1.5. This was explained by the strong interaction between the sulphonic and amino groups, which reduced the intensity of swelling. Additionally, the composite membrane consisting of 20 wt.% of filler within SPEEK of a 52% degree of sulphonation produced a peak power density of 246 mW $cm^{-2}$ compared to 179 mW $cm^{-2}$ for 52% SPEEK without filler.

This work was followed by a similar study on SPEEK-based composites with a zeolite filler, in order to improve the mechanical resistance of SPEEK due to its excessive swelling at higher temperatures[215].

Zeolite addition of 5, 10, and 15% resulted in a drop in IEC from 1.55 (pristine SPEEK), to 1.47, 1.4, and 1.31 meq $g^{-1}$, respectively. This was a surprise as the large cavities of the framework were hypothesised to carry water molecules and ions more efficiently. At 80°C, the pristine SPEEK outperformed the three composite membranes; however, at 120°C all three composite membranes outperformed the SPEEK reference membrane.

On top of mixing inorganic fillers with alternative polymers, the fillers themselves can also be functionalised, creating membranes with multiple incorporated functionalities. An example of this is the work of Sambandan et al., who compared the performances of two types of membranes: SPEEK/silica, and SPEEK/sulphonated silica[216]. Interestingly, water uptake results showed that the composite membrane took up less water compared to pristine SPEEK.

However, fuel cell testing at 80°C and 75% relative humidity, in addition to 50% relative humidity, demonstrated that the composite membranes, and principally those with functionalised filler, displayed polarisation behaviour similar to that of recast Nafion. For a working principle, this is a good performance for an alternative electrolyte, i.e. having a performance similar to that of Nafion. There still needs to be further testing, especially for durability, though this is a promising approach.

Furthermore, mixed-matrix membranes do not have to be limited to only one filler and one polymer. The idea of adding more than one polymer has been studied by Therese at al.[217] who fabricated a SPEEK/PAI (poly amide imide) membrane with sulphonated silica.

The PAI was included in the SPEEK to provide mechanical strength and chemical resistance at elevated operating temperatures. The aforementioned composite membrane achieved a proton conductivity of 8.12 x $10^{-2}$ S $cm^{-1}$ at 90°C. The idea of blending more than one polymer for composite membranes is thought-provoking. However, the uniformity and dispersion need to be carefully controlled with the addition of different polymers.

A creative method to improve fuel cell performance is to coat the filler with a polymer before fabricating the composite membrane. Elakkiya et al. presented sulphonated $TiO_2$ coated in polyaniline within a SPES polymer matrix[218]. This could potentially improve interfacial contact between the filler and polymer and improve the membrane morphology and dispersion. However, this assumes that the coating polymer is the same as the matrix. If not, it depends on the polymer's properties. In this case water uptake and proton conductivity increased with the introduction of the coated filler. Unfortunately, no in-situ testing was performed.

#### 2.5.2.2 Inorganic fillers for high temperature fuel cells

An area where inorganic filler materials are also utilised is for high temperature PEFCs (HT-PEFCs), with an operating temperature of around 160 to 180°C. Here, the use of fillers is meant to prevent the acid leaching phenomenon, where the PBI membrane, doped with phosphoric acid, leaks acid into the fuel cell system, resulting in severe damage, though depending on the molarity of the acid.

A project was performed to assess the viability of several different fillers: silicon dioxide, titanium dioxide, and zirconium phosphate (ZrP) for PBI based composite membranes for HT-PEFCs[219], with a specific emphasis on improved uptake and retention of acid.

Acid leaching tests revealed that pristine PBI lost 85.2% of its doped acid, PBI/$SiO_2$ 81.5%, PBI/$TiO_2$ 77.4%, and PBI/ZrP 75.9%. In addition, PBI/$SiO_2$ and PBI/ZrP exhibited enhanced

proton conductivity in contrast to pristine PBI, with both membranes producing their maximum conductivity at 180°C, with values of 0.113 and 0.200 S $cm^{-1}$, respectively. However, PBI/$TiO_2$ showed proton conductivities lower than the pristine PBI. This was due to the agglomeration of titanium oxide within the PBI, which was detected by SEM.

Lee et al. designed a PBI composite with sulfophenylated titanium oxide nanoparticles for high temperature fuel cells[220]. The addition of the filler material enhanced acid retention and proton conductivity. The composite membrane achieved a maximum power output of 621 mW $cm^{-2}$, whereas pristine PBI achieved 471 mW $cm^{-2}$, both at 150°C.

Similar to membranes such as SPEEK for intermediate temperatures, PBI can also be functionalised. In this case, Ooi et al. synthesised partially fluorinated PBI for the purpose of improved acid retention and oxidative stability[221]. The polymer was combined with caesium hydrogen sulfate-silicotungstic acid ($CsHSO_4$–$H_4SiW_{12}O_{40}$, CHS-WSiA). This composite membrane showed greater acid retention rates, which was credited to the fluorinated PBI and the filler. This retention was further scrutinised in an in-situ stability test of 24 hours, where a voltage of 0.614 V at a constant current of 0.2 A $cm^{-2}$ was achieved.

Devrim et al.[222] found that their composite membrane comprising of PBI and silica displayed decreased acid leaching because of the improved covalent bonding between the filler and acid. Proton conductivity results measured at 140, 165, and 180°C showed that the composite membrane had higher conductivity than pristine PBI: 0.0675 to 0.0600, 0.0866 to 0.0765, and 0.1027 to 0.0944 S $cm^{-1}$, respectively. Fuel cell testing was also completed and at 140°C, the pristine PBI surpassed the composite. Nevertheless, at the following two higher temperatures the composite membrane achieved a greater maximum power density. The best performance

was achieved by the composite membrane at 165°C, creating a maximum power density of 0.24 to 0.2 W $cm^{-2}$ for the pristine PBI, at an applied potential of 0.6 V.

One type of filler material that has become quite popular in recent years is clay. In comparison to other fillers, certain clays can be ubiquitous in availability and can be naturally found in the environment. The utilisation of clay fillers has potential due to their unique structures and ion exchange capacity[223]. As an example, Plackett et al. fabricated a composite membrane consisting of a laponite clay filler dispersed within PBI as a potential electrolyte for HT-PEFCs[224]. Two types of fillers were designed, the first functionalised with an imidazole group and the second with a quaternary ammonium group.

The composite membranes experienced minimal acid swelling, due to the interaction between the clay and the doped acid. Impressively, the composite membranes had an OCV of 1.02 V at room temperature, 0.96 V at 125°C, and 0.91 V at 200°C. This small drop in OCV over a large temperature range showed that there was a minimal increase in reactant crossover.

Furthermore, fillers that reduce swelling allow for a higher molarity of phosphoric acid to be used. Aili et al. achieved this by doping silica with phosphotungstic acid for use as a filler in phosphoric acid doped PBI[225]. Durability testing at 200°C discovered that the composite membrane achieved a decay rate of 27 μV $h^{-1}$, whereas PBI decayed at a rate of 129 μV $h^{-1}$.

#### 2.5.2.3 Cerium oxide

Direct methods to improve durability encompass employing an inorganic filler that explicitly scavenge radicals formed during fuel cell operation, with cerium oxide being the most studied of these fillers.

Influential work by Pearman et al.[226] showed that cerium oxide can act as a radical scavenger in PEFCs. Two types of oxides were studied to observe whether the size of the oxide had an

effect on durability, 2 to 5 nm and 20 to 150 nm. The addition of the oxides led to a reduced OCV decay rate, from 0.9 mV $hr^{-1}$ for pristine Nafion, to 0.4 mV $hr^{-1}$ for the composites. This was further reinforced with electron microscopy, which showed fewer platinum particles in the composite membrane in contrast to the reference sample, implying less degradation.

Figure 2-10 shows a 500-hour OCV holding test with pre and post-test polarisation curves, confirming that the Nafion-cerium membranes experienced a smaller change compared to the reference Nafion membrane. This is quite important as durability testing is rarely performed for this long.

The authors followed this publication up by studying the proton conductivity of the composite membranes[227]. Unfortunately, the composite membranes performed worse than the reference Nafion, with a four-day conductivity testing leading to a decrease in conductivity.

The authors explained that this was because of the excess acidity of the PFSA during operation. Combined with the humidity and gas flow, the cerium oxide was reduced into its (III) form, which then binds to the sulphonic groups, hindering proton conduction. This hypothesis was confirmed by reprotonating the samples with sulphuric acid, upon which the proton conductivity returned to its initial value.

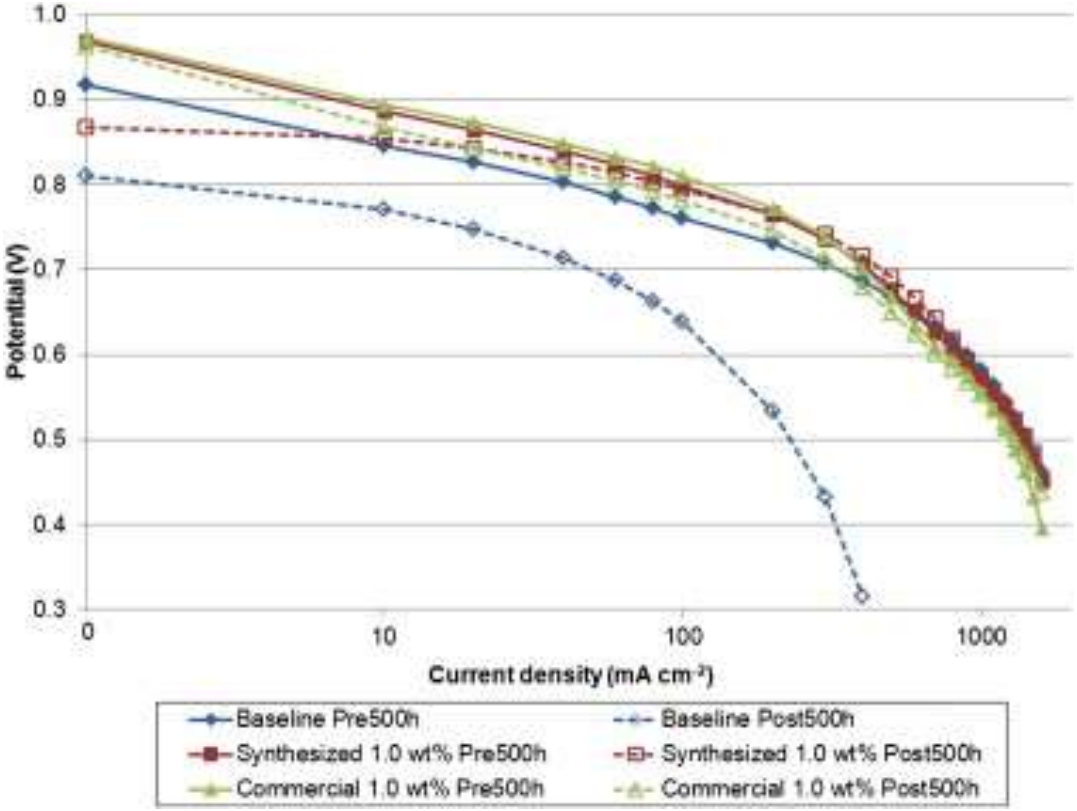



Figure 2-10: Pre- and post-500 h test performance curves[12].

Cerium reducing proton conductivity was also a finding observed by Lee et al.[228]. The cerium oxide impregnated SPES (50% degree of sulphonation) additionally reduced water uptake and IEC. However, ex-situ Fenton testing, where membranes are immersed in "Fenton's solution", which consists of a solution of hydrogen peroxide containing ferrous ions to imitate a fuel cell environment of the aforementioned membrane, led to a reduction in oxidative degradation in comparison to the reference sample. An OCV hold test at 90°C and 30% relative humidity showed that the composite membrane was stable for up to a very impressive 2200 hours, in comparison to 670 hours for the pristine SPES.

[12] Reprinted with permission from Elsevier[226].

Sahin et al. prepared a SPEEK and cerium phosphate composite membrane to improve fuel cell performance[229]. Fenton tests of the samples determined that the composite membrane lost 10% in weight over 80 hours, whereas the SPEEK membrane was entirely destroyed. Thus, this highlights the potential of cerium-based fillers for oxidative stability, which is important in being able to produce a composite membrane with similar durability to that of Nafion.

Interestingly, platinum nanoparticles have also been incorporated as a radical scavenger. However, a dispute is ongoing whether the existence of platinum inside the membrane would be another possible reason for the formation of further radicals. However, some researchers have observed that platinum within the membrane can scavenge hydrogen peroxide and radicals. As a case study, Rodgers et al. successfully utilised platinum nanoparticles to remove radicals formed during fuel cell operation and hence mitigate degradation[230].

Fluoride emission was used to characterise the degradation within the membrane. This is a technique where the water in the anode and cathode effluent is analysed through ion chromatography for fluoride ions. These fluoride ions steam from the membrane, or in this case, Nafion.

A concern is that the presence of excessive amounts of platinum nanoparticles could result in the formation of an electrical pathway through the membrane and cause an electrical short. However, the authors did not observe this phenomenon, using cell resistance measurements. Furthermore, Nafion membranes impregnated with 30 and 50% platinum developed platinum bands. However, these two membranes also displayed reduced degradation after 100 hours, due to less fluoride ion emission.

### 2.5.3 Acids and ionic liquids

Another strategy to allow for the operation of intermediate temperature fuel cells involves using the technology of HT-PEFCs, and reducing the temperature down to those of intermediate temperatures, instead of using low temperature fuel cell technology and increasing the operating temperature.

Similar to HT-PEFCs, phosphoric acid and not water is utilised as the conductive proton pathway. To add, the difference between acids and water include their boiling points and that the concentration can be controlled for acids. Hence it is possible to provide a greater amount of conductive species. Here, the use of fillers is aimed at mostly preventing the excessive swelling of the PBI membrane and stop the leaching of acid into the rest of the fuel cell system.

As an example of how fillers can be used, Xu et al. fabricated a polybenzimidazole (PBI) and sulphonated graphite oxide membrane for HT-PEFCs[231]. Proton conductivity tests under anhydrous conditions and with a temperature range between 105°C and 180°C revealed that both the GO and SGO composite membranes performed better than the pristine PBI, with the SGO being the best performing membrane. Thus, the presence of GO and SGO provided bonding sites for the phosphoric acid, reducing potential leaching.

At these reduced temperatures, it is possible to use Nafion and other PFSAs instead of PBI, as well as alternative acids. Choi et al. prepared two types of Nafion membranes doped with phosphotungstic acid, one with an equivalent weight of 1100 and the second of 750[232]. These acid-doped membranes,750 and 1100 EW, produced a voltage of 0.55 and 0.51 V at 120°C, in comparison to 0.47 V for Nafion. To add, the doped membranes experienced a lower ohmic resistance, implying that the electrical resistance was low, and that proton conduction was facilitated.

A systematic study of several heteroplyacids-doped Nafion membranes were performed by Ramani et al., with four acids considered: Phosphotungstic (PTA), silicotungstic (STA), phosphomolybdic acid (PMA) and silicomolybdic acid (SMA)[233]. Fuel cell tests at 120°C and 35% RH of Nafion/PTA, Nafion/STA and Nafion/SMA exhibited comparative performance, with Nafion/PTA and Nafion/STA achieving a peak current density of around 800 mA $cm^{-2}$.

The same authors undertook a more detailed study on the heteropolyacid, phosphotungstic acid-doped Nafion[234]. The MEA was firstly "stabilised" through high temperature heat treatment, completed at 200°C and 30 atmospheres. However, to avert membrane degradation and to prevent acid leaching, the MEA was ion exchanged in caesium carbonate, replacing the protons for much larger caesium ions. Thermogravimetric experiments revealed that this stabilised membrane degraded at higher temperatures in contrast to its proton exchanged counterpart.

In-situ testing at 120°C and at 35% relative humidity revealed that both the stabilised and reference membrane had similar polarisation performance. However, the stabilised membranes differed in their specific area resistance which was lower for the stabilised membrane. The authors described that this was due to the lower contact resistance from the high temperature heat treatment. Hence, if filler materials were to be incorporated, they would have to be thermally resistant up to 200°C for the stabilisation treatment.

Another alternative filler used are ionic liquids. These are salts that have lower melting points, hence they tend to be liquid at either room temperature or at the fuel cell operating temperatures[235]. Therefore, Ionic liquids have been expansively utilised in fuel cells operating at higher temperatures due to their high thermal and electrochemical stability under anhydrous fuel cell conditions[236].

Lee et al. fabricated a membrane composed of a sulphonated polymer matrix doped with a fluorohydrogenate ionic liquid, for anhydrous IT-PEFC operation[237]. Intriguingly, the ionic conductivity of the doped membrane grew with temperature, from 11.3 mS $cm^{-2}$ at 25°C to 34.7 mS $cm^{-2}$ at 130°C. Supplementary conductivity measurements beyond these temperatures would have been useful to discover the optimum temperature. Furthermore, the sample had stability issues, as it was only able to achieve an OCV of 1 V for 5 hours at 130 °C.

Another example involves that of a sulphonated polyimide doped with protic ionic liquid diethylmethylammonium trifluoromethanesulfonate ([dema] [TfO])[238]. The thermal decomposition temperature of this compound was 300°C, which would make it more suitable for anhydrous fuel cell operation. The composite membrane was tested at two different temperature ranges, 80 and 30°C, as shown in Figure 2-11. At 80°C and anhydrous conditions, the fuel cell produced a maximum power density output of 100 mW $cm^{-2}$ at a current density of 240 mA $cm^{-2}$. Intriguingly, the membrane at 30°C produced a peak power density of 68 mW $cm^{-2}$ at 300 mA $cm^{-2}$, showing some potential of room temperature, dry PEFC operation. However, it would have been useful to observe the performance at higher operating temperatures.

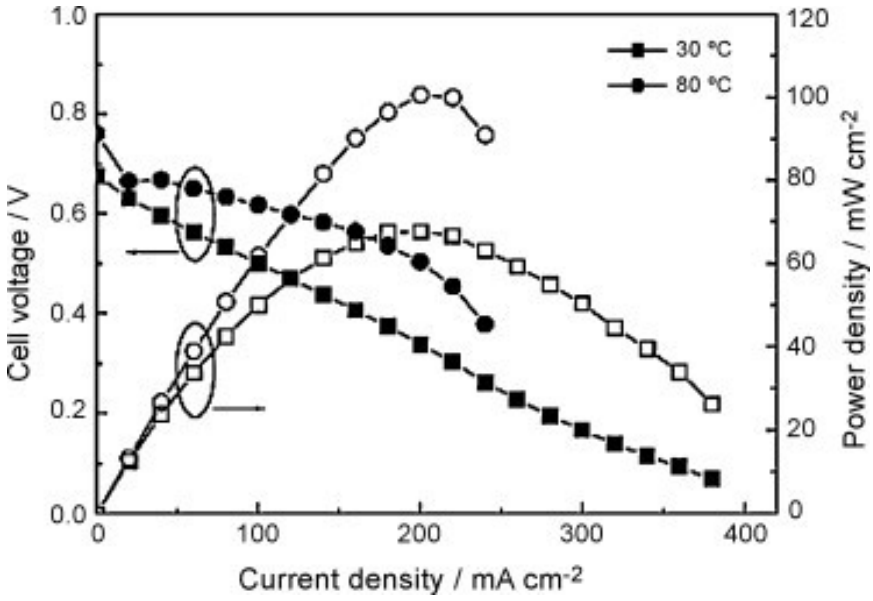



Figure 2-11: Polarisation curves of a $H_2/O_2$ fuel cell using a SPI-1.51(50) composite membrane without humidification at gas utilisation ratios of 30% for $H_2$ and 15% for $O_2$ operation at 30°C, and operation at 80°C[13].

Yi et al. prepared two composite membranes within a SPEEK matrix of 67% degree of sulphonation, one with 1-butyl-3-methylimidazolium tetrafluoroborate (BuMeImBF4), and the second with 1-decyl-3-methylimidazolium tetrafluoroborate (DeMeImBF4)[239].

Proton conductivity measurements of SPEEK/BuMeImBF4 revealed that the conductivity improved with increasing temperature, attaining a maximum of $8.4 \times 10^{-3}$ S cm$^{-1}$ at 170°C. The authors proposed that the rise was due to the drop in viscosity of the ionic liquid enhances its mobility and movement, improving proton transport in the membrane. This is an interesting explanation as it would be possible to synthesise ionic liquids with reduced viscosity to take advantage of this result.

[13] Reprinted with permission from Elsevier[238].

Furthermore, a proton conductivity test was performed on the membranes prior and post immersion in water to see how much ionic liquid was retained in the membrane. Unfortunately, SPEEK/BuMeImBF4 was undetectable after 1 hour of immersion in water. SPEEK/DeMeImBF4 managed better, being detectable after 2 hours of immersion, but eventually the conductivity also became unnoticeable. Immersion in water is not the most realistic scenario in a fuel cell at these operating temperatures, but water is still produced at the cathode, which will interact with the membrane materials to some degree before being removed.

A method to prevent this leaching is through the use of crosslinkers. Malik et al. used ethylene glycol as a crosslinker within a composite of SPEEK and ionic liquid[240]. The composite membranes experienced lower leaching weight loss in contrast to the non-crosslinked membranes, though, the proton conductivity of the crosslinked membranes was lower. This was because some of the sulphonic groups present were used in the crosslinking process, resulting in lower conductivity. Hence, there is a trade-off between proton conductivity and reducing leaching.

Yasuda et al attempted to alter the position of sulphonic groups in order to improve proton conduction[241]. This was done by synthesising sulphonated polyimide/ionic liquid (SPI) composite membranes with different polymer structures, one with a random arrangement, and the other with a more block-copolymer arrangement. Anhydrous in-situ testing at 120°C revealed that the random chain SPI and homopolymer SPI achieved maximum power densities of 100 and 70 mW $cm^{-2}$, respectively.

This shows that the random arrangement is potentially more suited than a controlled structure for fuel cells. It would be interesting to observe the proton conduction and mechanical tensile

strength as there should be a difference due to membrane morphology and how the polymer chains assemble.

## 2.6 Trends and perspectives

As observed, there have been many different research strategies utilised to allow for the performance of fuel cells operating at intermediate temperatures. However, the most common is through the use of filler materials. Research based on membranes with fillers such as GO has grown significantly and there is a lot of active research in this area.

Several trends and observations that are apparent include the wide variety of GO sources and synthesis techniques used. For example, Hummers, modified Hummers, Brodie, Hofmann, Staudenmaier, and Tour's methods encompass most of the GO synthesis methods[156–158,242–244]. This will result in slightly different structures of GO, mostly by having different oxygen contents[245], which will then influence the behaviour of the subsequent composite membranes.

There has also been some work producing membranes with multiple layers either through hot pressing or solution casting, and they have the potential of combining many different materials as well as isolating the filler within certain regions of the membrane. At the moment, issues such as delamination have been observed, but generally not much work has been done in solution casted multilayer membranes. Pure membranes of GO have also been proposed as an interesting alternative for fuel cell testing, due to being impermeable to all gases and liquids but for water[246]. However, reduction of GO and dissolution in water is something that should be carefully avoided.

Other methods of isolating GO within the membrane include spin coating, laminating, and layer by layer assembly. Furthermore, the actual orientation of GO fillers can be controlled through the use of additional magnetic fillers and the application of a magnetic field. This can result in

reduced fuel crossover and more efficient proton conduction. Therefore, combining multiple filler materials with GO can provide new functionalities and properties of the subsequent membrane, but care should be taken to prevent agglomeration.

Additionally, many research groups have functionalised their GO, with the most common being sulphonation by the addition of sulphonic acid groups. This can improve the retention of water and improve proton conduction. Another chemical technique is to graft GO onto Nafion to improve membrane dispersion as well as the interface between polymer and filler.

However, from the work reviewed, there are conflicting observations regarding the influence of GO filler on water uptake and ion exchange capacities. Some have observed WU and IEC to increase with increasing GO, due to the oxygen functional groups of GO allowing for increasing sites for water bonding and ion exchange. Others have observed the opposite, a decrease due to the filler preventing polymer movement and disturbing the free volume of the membrane. Sulphonated GO almost always led to increasing WU and IEC in the literature.

Either way, work that has shown that GO fillers increase WU and IEC has also shown an optimum level of loading, where any more loading will result in subsequent reduction. Additionally, GO impeded mechanical elongation, and composite membranes become more brittle, though they can sustain a higher stress.

The use of inorganic fillers has been broad and extensive in fuel cell membranes, with metal oxides receiving immense research interest.

Firstly, the shape of the filler can be varied, such as utilising nanoparticles, nanotubes or nanowires. Nanotubes, in particular, can provide pathways for water molecules to travel through and nanowires can provide lateral mechanical reinforcement from the negative effects of excessive swelling. Secondly, the surface can be tuned with functional groups just like GO,

with sulphonic acid groups once again being the most popular. Thirdly, the surface can also be physically altered, such as introducing pores to produce mesoporous hygroscopic nanoparticles.

The thermal and chemical resistance of these fillers allows for the use of alternative polymers, especially highly sulphonated polymers that experience excessive swelling. These resistances also make inorganic fillers suitable for HT-PEFCs applications, where the higher operating temperatures and phosphoric acid doped electrolyte require materials that are highly robust.

Interestingly, inorganic oxides are not only useful for their hygroscopic characteristics, with cerium oxide in particular having a unique niche as a radical scavenger. Its suitability has also been studied in long-term durability tests. However, the addition of non-functionalised inorganic fillers leads to a reduction in water uptake, IEC, and proton conductivity, if not sulphonated.

Possible pitfalls include the potential of agglomeration, phase separation and non-uniformity of the membrane and, hence, properties. The likelihood of this happening is even higher if further fillers are added.

Thus, it can be observed that membrane fillers are very versatile in chemical structure, size, dimensions, etc. with many different features to adapt to specific application, whether that is operating at intermediate temperatures and/or, low relative humidity, or increasing mechanical strength, preventing acid leaching, or increasing proton conductivity, to name just a few. In addition, they can also be functionalised to either improve these characteristics or provide a secondary functionality.

There is a downside, as this variety makes it very difficult to compare results, and once membrane fabrication and fuel cell operating conditions are included it becomes even more challenging. In addition, the oxidation level of GO and the degree of sulphonation of

sulphonated polymers are further variables to consider. Very little reference has been made to the thickness of the prepared composite membranes. This is important, as fuel cell performance results as well as hydrogen crossover are strongly influenced by the membrane thickness.

Accordingly, the reviewed studies indicate promising performance for composite membranes; however, they also highlight the need for further research to improve the lifetime and durability of these membranes. Most functionalised fillers were grafted with sulphonic acid groups and these membranes displayed a better performance in terms of proton conductivity and cell polarisation at elevated temperatures, being credited to the water retaining abilities of these functional groups.

Different filler types demonstrated different performances, and this is because of chemical as well as physical structure, such as nanoparticles, nanotubes, and nanowires. Therefore, when selecting a filler material not only should the material itself and possible functionalisation be considered, but also the shape of the filler itself. An additional factor is the polymer matrix that the filler is embedded in, in this case, composite membranes were prepared using different polymers such as Nafion, SPEEK, and SPAES. The different polymers and filler combinations result in a different membrane morphology due to the interactions between the polymer and fillers.

However, as it stands, only Nafion achieves industry standards regarding lifetime and durability. This implies that composite membranes should use a Nafion matrix in addition to Nafion ionomer in the gas diffusion electrode (GDE). Using a non-Nafion membrane but a Nafion ionomer for the catalyst layer formulation can result in additional proton conduction interfaces as well as inconsistencies in the hot-pressing assembly of the MEA, leading to low efficiencies in fuel cell performance. Hence, membrane performance has to be assessed through

a variety of experiments such as cell polarisation and power, long-term durability, and ex-situ tests.

A membrane that initially performs well in a fuel cell might not perform as well at different operating conditions such as higher temperatures, lower relative humidities and lower backpressures.

A point of reflection is the interface between the composite membrane and the catalyst layer. The addition of a filler material could potentially affect this interaction. For example, the filler may have been added to only improve the membrane performance, but if some of the filler is positioned closer to the surfaces of the membrane, then this could interfere with the anode and cathode functions. For instance, certain fillers could interfere with the catalyst reactions, such as electrically insulating graphene oxide, or block reactants and products. Hydrophilic fillers situated close to the cathode could result in greater mass transport losses through potential flooding[247].

Composite membranes are tested for their performance in-situ and ex-situ; however, their durability in-situ is an area of research that has not been fully explored. In order to be competitive with conventional Nafion membranes, the composite membrane must be able to perform better at higher temperatures and lower relative humidities, but also perform adequately over extended periods.

In terms of manufacturing process, solution casting is the most widely used due to its simplicity, as other techniques might be more difficult to implement in mass manufacture. Metal oxides were initially used as fillers, but in recent years carbon nanomaterials such as GO have become very popular. However, there a still some conflicting conclusions regarding the effect of fillers

on water uptake, IEC and proton conductivity, with some groups reporting increases with loading and others the opposite. In addition, the optimum loading is often not identified.

A final point of consideration is that not all groups presented in-operando fuel cell results. Some only provided ex-situ proton conductivity tests which are not completely representative of in-situ fuel cell testing. Furthermore, the fuel cell tests performed tend to be at one fixed temperature and relative humidity hence there is scope for further fuel cell testing at differing operating parameters.

A summary of the results of the literature review is presented in Table 2-2, separated into a systematic listing consisting of polymer/graphene oxide membranes, polymer/metal oxide membranes, and finally acid doped composite membranes. Additionally, Table 2-3 provides an overview of the advantages and disadvantages of some of the membranes that were discussed in this chapter.

Table 2-2: Summary of membrane performance. X is data that was not presented in referenced journal article.

| Membrane | Voltage (V) | Current density (mA $cm^{-2}$) | Power density (mW $cm^{-2}$) | Temperature (°C) | Relative humidity (%) | Membrane thickness (µm) |
|---|---|---|---|---|---|---|
| **Polymer/Graphene Oxide membranes** | | | | | | |
| Nafion-GO(4%)[161] | 0.47 | 440 | 212 | 100 | 25 | 50 |
| Nafion-SGO(10%)[136] | 0.4 | 400 | 150 | 120 | 25 | X |
| SPEEK-SGO(5%)[162] | 0.375 | 1100 | 378 | 80 | 30 | X |
| SPEEK-DGO(5%)[163] | 0.45 | 400 | 170 | 120 | 0 | 60-70 |
| Chitosan-S(4)GO(2%)[164] | 0.45 | 320 | 147 | 120 | 0 | 60-68 |
| Chitosan-PGO(1.5%)[165] | 0.5 | 200 | 100 | 120 | 0 | 65-73 |
| Nafion-GO(3%)[171] | 0.6 | 1000 | 600 | 80 | 40 | X |
| Nafion-GO/Pt(3%)[171] | 0.6 | 360 | 200 | 80 | 0 | X |
| Nafion-GO/Pt-$SiO_2$(1.5%)[173] | 0.6 | 110 | 100 | 80 | 0 | X |
| Nafion-GO(0.8)/Pt(0.2)-$TiO_2$[174] | 0.5 | 1100 | 450 | 80 | 0 | X |
| Pure GO[184] | 0.15 | 0.6 | 0.2 | 80 | 100 | 36 |
| Aquivion-GO/$CeO_2$-Aquivion[189] | 0.5 | 1500 | 750 | 80 | 95 | 20 |
| **Polymer/Metal Oxide membranes** | | | | | | |
| Nafion-$SiO_2$(3%)[194] | 0.6 | 587 | X | 130 | 75 | 125 |
| Nafion-$TiO_2$(3%)[194] | 0.6 | 582 | X | 130 | 75 | 125 |
| Nafion-$AlO_3$(3%)[194] | 0.6 | 406 | X | 130 | 75 | 125 |
| Nafion-$ZrO_2$(3%)[194] | 0.6 | 458 | X | 130 | 75 | 125 |
| Nafion-S$ZrO_2$(5%)[196] | 0.6 | 930 | X | 70 | 30 | 70-80 |
| Nafion-$ZrO_2$(10%)[197] | 0.6 | X | 387 | 130 | 85 | 100 |
| Nafion-$TiO_2$(3%)[199] | 0.5 | 580 | 254 | 130 | 100 | 100 |
| Nafion-ZrP(23%)[202] | 0.45 | 1500 | X | 130 | 100 | 90 |
| Nafion 115-ZrP(23%)[202] | 0.45 | 1000 | X | 130 | 100 | 165 |
| Nafion-$SiO_2$(3%)[203,204] | 0.35 | 350 | 113 | 110 | 20 | X |
| Nafion 212-$SiO_2$[203,204] | 0.3 | 450 | 140 | 110 | 20 | X |
| Nafion-S$SiO_2$(1%)[205] | 0.2 | 2062 | 454 | 80 | 25 | X |

| Membrane | Voltage (V) | Current density (mA $cm^{-2}$) | Power density (mW $cm^{-2}$) | Temperature (°C) | Relative humidity (%) | Membrane thickness (µm) |
|---|---|---|---|---|---|---|
| Nafion-$TiO_2$(3%)[206] | 0.4 | 200 | X | 110 | X | X |
| Nafion-$TiO_2$(2.5%) Spherical[207] | 0.6 | 1100 | X | 130 | 100 | 105 |
| Nafion-$TiO_2$(2.5%) Mesoporous[207] | 0.6 | 1250 | X | 130 | 100 | 105 |
| Nafion-$TiO_2$(5%) Nanotube[207] | 0.6 | 1300 | X | 130 | 100 | 105 |
| Nafion-$TiO_2$(5%) Nanowire[208] | 0.59 | 600 | X | 90 | 50 | 30 |
| Nafion-$TiO_2$(10%) Nanotube[209] | 0.6 | 390 | 641 | 80 | 18 | 50 |
| Nafion-$ZrO_{1.95}$(1.5%) Porous nanotube[211] | 0.4 | 1500 | 572 | 80 | 18 | 50 |
| SPS-$TiO_2$(5%)[213] | 0.6 | 300 | 240 | 85 | X | X |
| SPEEK(52% d.o.s)-$SiO_2/NH_2$(20%)[214] | 0.6 | 250 | 246 | 120 | 100 | 100-150 |
| SPEEK(50% d.o.s)-HBeta Zeolite (15%)[215] | 0.6 | 350 | 285 | 120 | 100 | 131 |
| **Acid doped polymer composite membranes** | | | | | | |
| PBI-$STiO_2$(2%)[220] | 0.6 | 900 | 621 | 150 | X | 23 |
| PBI-$SiO_2$(5%)[222] | 0.6 | 120 | 140 | 140 | X | 55 |
| PBI-GO(2%)[231] | 0.6 | 200 | 300 | 175 | 0 | 70 |
| PBI-SGO(2%)[231] | 0.6 | 350 | 400 | 175 | 0 | 70 |
| Nafion(1100 EW)-PTA(15%)[232] | 0.55 | 400 | X | 120 | 35 | 25 |
| Nafion(750 EW)-PTA(15%)[232] | 0.51 | 400 | X | 120 | 35 | 25 |
| Nafion-PTA(25%)[233] | 0.6 | 300 | X | 120 | 35 | 38-64 |
| Nafion-STA(25%)[233] | 0.6 | 300 | X | 120 | 35 | 38-64 |
| Nafion-SMA(25%)[233] | 0.6 | 80 | X | 120 | 35 | 38-64 |
| Nafion-PTA(15%)[234] | 0.6 | 220 | X | 120 | 35 | 25-30 |

Table 2-3: Summary of membrane characteristics.

| Membrane | Preparation method | Pros | Cons |
|---|---|---|---|
| Nafion | Solution casting | High proton conductivity | Cost<br>Water loss and reduced proton conduction at intermediate temperatures<br>“Forever chemical” |
| Alternatives to Nafion (e.g. SPEEK) | Solution casting | Degree of sulphonation can be controlled<br>Lower cost | Increased swelling<br>Lower proton conductivity |
| Pure graphene oxide | Vacuum filtration | Single medium<br>Reduced crossover | Risk of disintegration when in contact with water<br>Risk of reduction due to operating temperature |
| Nafion-graphene oxide | Solution casting | Improved proton conduction<br>Reduced acid leaching | Increased swelling |
| Nafion-graphene oxide | Lamination, spin coating, drop casting | Isolate filler in specific region<br>Reduced crossover | Risk of disintegration when in contact with water<br>Risk of reduction due to operating temperature<br>Risk of delamination |
| Nafion-graphene oxide | Layer by layer assembly | Consistent with a repetitive structure<br>No agglomeration<br>Reduced crossover | Time consuming<br>Requires use of crosslinkers to prevent disintegration when in contact with water |
| Multilayer: Nafion, graphene oxide, Nafion | Solution casting | Isolate filler in specific region | Risk of delamination |
| Nafion-sulphonated graphene oxide | Solution casting | Degree of sulphonation can be controlled<br>Reduced acid leaching<br>Improved water retention | Increased swelling |

| Membrane | Preparation method | Pros | Cons |
|---|---|---|---|
| Nafion-grafted graphene oxide | Solution casting | Improved interface between Nafion and graphene oxide<br>Improved uniformity | Additional preparation steps and additional material required for chemical grafting |
| Nafion-graphene oxide-platinum | Solution casting | Operation at low humidity | Risk of agglomeration |
| PVA-sulphonated graphene oxide-iron oxide | Solution casting | Can align graphene oxide to improve proton conductivity and/or reduce crossover | Risk of agglomeration |
| Nafion-titanium/silicon/zirconium/hafnium oxide | Solution casting | Enhanced water retention | Risk of agglomeration at high loadings |
| Nafion-inorganic oxide (nanotube) | Solution casting | Improved water retention and diffusion | Risk of agglomeration |
| Nafion-inorganic oxide (nanowire) | Solution casting | Mechanical reinforcement | Risk of agglomeration |
| Nafion-inorganic oxide | Swelling/impregnation | Non-destructive incorporation of filler | Reduction in proton conduction |
| Nafion-cerium oxide | Solution casting | Radical scavenging | Reduction in proton conduction<br>Risk of agglomeration |
| Nafion-graphene oxide-cerium oxide | Direct membrane assembly (DMD) | Very thin membrane<br>Radical scavenging | Risk of electrical shorting |

## 2.7 Purpose of thesis and next steps

On the back of the reviewed literature this thesis will present work that will answer questions and provide additional information on the capabilities of composite membranes at intermediate temperature PEFC operation.

Firstly, composite membranes composed of Nafion and GO will be fabricated and presented in this thesis. Solution casting will be utilised as it is a straightforward technique to prepare lab scale membranes, and GO has been selected as the filler due to its simple dispersion in several solvents and potential for functionalisation.

The quantity of GO filler will be varied to understand its influence on fuel cell performance. Furthermore, water uptake and ion exchange capacity experiments will be performed to resolve the conflicting findings in the literature. To add to this, thickness is a parameter that has not been studied extensively in the literature and thus the influence of thickness on fuel cell performance will be investigated.

Secondly, the proposition of multilayer membranes composed of three layers via solution casting will be explored. There has been minimal work in this area and hence there is potential scope in this membrane design for fuel cell applications. The middle layer of the membrane will consist of a combination of Nafion and GO for two reasons: 1) to isolate the GO in a region within the membrane in order to create an interlayer for effective hydrogen crossover reduction, and 2) the combination of Nafion and GO would prevent delamination that could occur with a pure GO layer.

A gap identified in the literature review involves the lack of single cell tests at intermediate temperatures (100°C to 120°C). Furthermore, fuel cell testing generally is reported at one set temperature. Therefore, it is undertaken to perform fuel cell testing at three different

temperatures 80, 100 and 120°C at reduced relative humidity to provide a better understanding of the fuel cell performance of the fabricated membranes.

Finally, durability testing of the composite membranes will be performed. Single layer and multilayer membranes with the optimum GO loading and thickness will be fabricated but with in-house synthesised GO instead of commercial GO. Furthermore, the use of cerium oxide as a radical scavenger will be studied.

# 3 Materials and Methods

This chapter will detail the materials used in this thesis as well as the methods of fabrication and analysis used. These methods include the synthesis of graphene oxide, the preparation of novel membranes, the characterisation of said graphene oxide and membranes, in-situ fuel cell testing, and durability testing.

## 3.1 Materials

The materials employed are detailed in Table 3-1, and were used without further purification.

Table 3-1: Materials used in thesis.

| Material | Detail | Supplier |
|---|---|---|
| Graphite | N/A | Alfa Aesar |
| Potassium permanganate | ACS grade, 99% | Alfa Aesar |
| Sulphuric acid | ACS grade, 95 to 98% w/w | Alfa Aesar |
| Ethanol | Absolute > 99.8% | Alfa Aesar |
| Isopropanol | N/A | Alfa Aesar |
| GO powder | N/A | Nanoinnova |
| GO sheets | Number of layers assessed as 15 via atomic force microscopy | Sigma Aldrich |
| Hydrogen peroxide | 30% w/w in water | Sigma Aldrich |
| Cerium oxide nanopowder | < 25nm nanoparticle size | Sigma Aldrich |
| Sodium nitrate | ACS grade, 99.5% | Merck |
| Nafion dispersion | D1021, EW 1100, 10% w/w in water | Ionpower and Fuel Cell Store |
| Nafion 211 | 25 μm | Fuel cell store |
| Sodium chloride | N/A | Fischer Scientific |
| Sodium hydroxide | 10M | Fluka |
| Hydrochloric acid | 37% w/w | Fluka |
| Phenolphthalein indicator | N/A | Fluka |
| Gas diffusion electrodes | 0.2 mg $cm^{-2}$ Pt/C 20% | Fuel Cell Store |
| Milli-Q Ultrapure water | > 18.2 MΩ cm and room temperature | In lab |

## 3.2 Methods

### 3.2.1 Graphene oxide synthesis

Along with commercial GO, in-house GO synthesised via Hummers' method was provided by a colleague[152]. To summarise, graphite (4.0 g) in concentrated sulphuric acid (92 mL) was treated with sodium nitrate (2.0 g) and potassium permanganate (12.0 g). The resultant brownish-grey paste was diluted with deionised water and treated with hydrogen peroxide. Finally, the synthesised GO was vacuum-filtered, washed, centrifuged and freeze-dried.

### 3.2.2 Sulphonated graphene oxide synthesis

Sulphonated graphene oxide was synthesised through a treatment of exfoliated GO in 2 M sulphuric acid solution at 80°C overnight. The synthesised sGO dispersion was centrifuged and washed several times until a PH of 7 was achieved. Then, the dispersion was freeze-dried to produce SGO powder.

### 3.2.3 Graphene oxide usage in this thesis

Three sources of graphene oxide were used, two commercial: Nanoinnova and Sigma Aldrich, and one in-house synthesised graphene oxide. Initially, commercial GO from Nanoinnova was used but this was changed to GO from Sigma Aldrich in order to ensure a consistent supply of GO, as Sigma Aldrich was integrated into the internal procurement system of the university.

Commercial GO was firstly used during optimisation of membrane parameters such as GO loading and membrane thickness. Then, synthesised GO and synthesised sulphonated GO was utilised during durability tests with the optimised parameters.

## 3.3 Membrane preparation and characterisation

Solution casting is the technique that was selected to prepare membranes as it is facile and efficient in producing lab-scale membranes. It has wide usage in producing membranes and polymer films for a wide variety of applications such as fuel cells, batteries [248–250] and sensors [251–253].

The process involves dispersing a polymer in a solvent and then casting it onto a petri dish or a glass plate. The excess solvent is then evaporated off, leaving a polymer skin layer on the surface of the support. The temperature of the evaporation is set by the choice of solvent. Solvents such as ethanol and isopropanol can be evaporated at lower temperatures, whereas other solvents such as water or dimethyl acetamide require the use of higher temperatures above their boiling point. The choice of solvent is usually dependant on several factors, including solubility, boiling temperature, polymer-solvent interactions[254] and others.

The thickness of the membrane can be controlled by either controlling the solid weight percentage of cast solution (higher polymer content leads to a thicker membrane), or by the use of a doctor blade on a cast solution on an open-ended glass plate. The polymer chains in the membrane are randomly arranged through thermodynamics, polymer-polymer and polymer-solvent interactions[90].

To prepare composite membranes, a filler material is incorporated into the polymer solution. A wide variety of fillers can be incorporated, from organic and inorganic to nanoparticles. What has to be understood are the interactions between the filler, the solvent and the polymer. These interactions could result in a non-homogenous dispersion of filler material within the polymer matrix. Solution casting is usually used to produce single layer films, however, there has been work on producing double and multi-layer polymer membranes[255,256].

### 3.3.1 Single layer Nafion membrane fabrication

To prepare a single layer of Nafion membrane the following process was completed[180]:

1. A specific quantity of Nafion dispersion was mixed with ethanol. The ethanol ensured that the total volume of dispersion was sufficient for completely covering the petri dish, especially when casting thinner membranes.
2. The combined dispersion was placed in a vacuum desiccator to remove any dissolved gasses that could interfere in the casting procedure and compromise the uniformity and dispersion of the membrane.
3. The desiccated dispersion was cast onto a borosilicate petri dish with a 9 cm diameter.
4. The petri dish was placed into an oven with a heating profile of two hours at 100°C followed by one hour at 120°C.

The Nafion fabrication parameters are displayed in Table 3-2.

Table 3-2: Nafion membrane fabrication parameters, values correspond to Nafion D1021 EW 1100 (10% in water) with a 9 cm diameter petri dish.

| Membrane | Thickness (μm) | Nafion content (mL) | Ethanol content (mL) |
|---|---|---|---|
| Nafion | 50 | 4.9 | 5 |
| Nafion | 40 | 3.6 | 5 |
| Nafion | 30 | 3 | 5 |

### 3.3.2 Single layer mixed matrix membrane fabrication

To prepare a single layer composite membrane with graphene oxide filler the procedure was as follow[180]:

1. A Nafion dispersion was diluted with ethanol and placed in a vacuum desiccator overnight.

2. A separate graphene oxide suspension was prepared by wetting the graphene oxide with 4 mL of deionised water.
3. The GO suspension was sonicated in an ultrasonic bath (U-series, Ultrawave) to exfoliate the GO, followed by probe sonication (Sonics Vibra cell) to further break up the GO suspension. The probe sonication was used in two steps: 5 minutes at 60% with an on-off duration of 5 seconds each, followed by 4 minutes at 40% with an on duration of 5 seconds and an off duration of 1 second.
4. The Nafion dispersion and GO suspension were combined in a vial, followed by casting onto a petri dish, and placed into an oven with a heating profile of two hours at 100°C followed by one hour at 120°C.

Nafion-GO fabrication parameters are presented in Table 3-3. Furthermore, composite membranes with differing GO weight loadings were prepared by varying the mass of GO. The GO loadings investigated in this thesis were 1.5, 3, 4.5 and 6 wt.%.

Table 3-3: Nafion-GO membrane fabrication parameters, values correspond to Nafion D1021 EW 1100 (10% in water) with a 9 cm diameter petri dish and 4.5 wt.% of GO.

| Membrane | Thickness (μm) | Nafion content (mL) | Ethanol content (mL) |
|---|---|---|---|
| Nafion-GO(4.5) | 50 | 4.2 | 5 |
| Nafion-GO(4.5) | 40 | 3.2 | 5 |
| Nafion-GO(4.5) | 30 | 2.4 | 5 |

### 3.3.3 Multilayer mixed matrix membrane fabrication

The prepared multilayer membranes had three distinct layers. The first layer (bottom layer) comprised of Nafion, the second layer (middle layer) was a Nafion-GO composite layer, and the third layer (top layer) was completed with another Nafion layer. To prepare a multilayer membrane with a mixed matrix middle layer[180]:

1. A single layer Nafion membrane was cast as described in section 3.3.1.

2. A single layer Nafion-GO membrane, as described in section 3.3.2 was cast, on top of the first layer. However, it was important to ensure that the Nafion dispersion was diluted with deionised water instead of ethanol.
3. A single layer Nafion membrane was cast as described in section 3.3.1, on top of the previous two layers. However, again, it was key to ensure that the Nafion dispersion is diluted with deionised water instead of ethanol.

Multilayer membrane fabrication parameters are displayed in Table 3-4. Furthermore, multilayer membranes with varying GO weight loadings were prepared by varying the mass of GO. Additionally, the naming convention as well as the corresponding GO loadings are presented in Table 3-5 for further clarification. To conclude, Figure 3-1 presents the cross-sections of the different types of prepared membranes and Table 3-6 provides a summary of membrane samples fabricated.

Table 3-4: Multilayer-GO membrane fabrication parameters; values correspond to Nafion D1021 EW 1100 (10% in water) with a 9 cm diameter petri dish and 0.79 wt.% of GO.

| Membrane | Thickness (μm) | 1st layer Nafion content (mL) | 1st layer ethanol content (mL) | 2nd layer Nafion content (mL) | 2nd layer water content (mL) | 3rd layer Nafion content (mL) | 3rd layer water content (mL) |
|---|---|---|---|---|---|---|---|
| ML-GO(0.79) | 50 | 2 | 5 | 0.85 | 5 | 2 | 5 |
| ML-GO(0.79) | 40 | 1.5 | 5 | 0.85 | 5 | 1.5 | 5 |
| ML-GO(0.79) | 30 | 1 | 5 | 0.85 | 5 | 1 | 5 |

Table 3-5: Multilayer membrane naming convention with GO weight loadings.

| Membrane | GO loading with respect to total Nafion content (wt.%) | GO loading with respect to middle layer Nafion content (wt.%) |
|---|---|---|
| ML-GO(0.26) | 0.26 | 1.5 |
| ML-GO(0.53) | 0.53 | 3 |
| ML-GO(0.79) | 0.79 | 4.5 |
| ML-GO(1.05) | 1.05 | 6 |
| ML-GO(4.5) | 4.5 | 26 |




Figure 3-1: Diagrams of: A) single layer Nafion, B) single layer mixed matrix membrane with graphene oxide filler, and C) multilayer mixed matrix membrane with an inner composite layer with graphene oxide filler.

Table 3-6: Summary of membranes prepared.

| Samples prepared | Single or multilayer | Thickness (μm) | GO source |
|---|---|---|---|
| Nafion | Single layer | 50, 40 and 30 | N/A |
| Nafion-GO(1.5) | Single layer | 50 | Commercial (Sigma Aldrich) |
| Nafion-GO(3.0) | Single layer | 50 | Commercial (Sigma Aldrich) |
| Nafion-GO(4.5) | Single layer | 50, 40 and 30 | Commercial (Sigma Aldrich and Nanoinnova) |
| Nafion-GO(6.0) | Single layer | 50 | Commercial (Sigma Aldrich) |
| ML-GO(0.26) | Multilayer (3 layers) | 50 | Commercial (Sigma Aldrich) |
| ML-GO(0.53) | Multilayer (3 layers) | 50 | Commercial (Sigma Aldrich) |
| ML-GO(0.79) | Multilayer (3 layers) | 50, 40 and 30 | Commercial (Sigma Aldrich) |
| ML-GO(1.05) | Multilayer (3 layers) | 50 | Commercial (Sigma Aldrich) |
| ML-GO(4.5) | Multilayer (3 layers) | 50 | Commercial (Sigma Aldrich) |

### 3.3.4 Membrane activation

Membrane activation is a process that is performed prior to fuel cell testing. The general process involves fully immersing the membrane in warm water to promote full hydration. Then, hydrogen peroxide and sulphuric acid are added to remove organic impurities and to activate the membrane, respectively.

The crucial step in this sequence is the activation of the membrane in sulphuric acid. This is because the proton conductivity of the activated membrane is higher than that of its non-activated counterpart. Research groups have different ways to activate the membrane: some use water, hydrogen peroxide and sulphuric acid, whereas others simply boil the membrane in sulphuric acid. However, it is essential to not skip the sulphuric acid step. The activation protocol performed is as follows:

1. Immerse the membrane in deionised water for one hour at 80°C.
2. Remove the membrane and immerse in a solution of 3% hydrogen peroxide for one hour at 80°C.
3. Remove the membrane and immerse in deionised water for one hour at 80°C.
4. Remove the membrane and place in a solution of 0.5 M sulphuric acid for one hour at 80°C.
5. Remove the membrane and immerse in deionised water for one hour for 80°C.
6. Turn off the heat and store the membrane in deionised water overnight.
7. Remove the membrane and store between two pieces of filter paper (Whatman) until needed.

### 3.3.5 Ex-situ characterisation

Characterisation techniques are employed to understand the properties and behaviour of both the graphene oxide and membrane samples. These techniques can assist in elucidating thermal and mechanical behaviour for example, or to confirm the successful incorporation of certain functional groups. A brief explanation of the following characterisation techniques utilised in this thesis, the procedures and parameters are presented.

#### 3.3.5.1 Water uptake

Water uptake (WU) is a common technique used to assess the ability of membranes to take up and retain water, which is a useful characteristic for intermediate temperature fuel cell operation. Membrane samples were dried and measured to confirm their original weight, followed by immersion in water for 24 hours. The samples were then taken out, and excess water was quickly removed with filter paper. The membranes were then weighed again. The difference between the dry and wet weight as a percentage is the water uptake.

$$\text{Water uptake (\%)} = \left(\frac{W_{Wet} - W_{Dry}}{W_{Wet}}\right) \times 100 \quad (6)$$

Where $W_{Wet}$ is the wet weight and $W_{Dry}$ is the dry weight of the membrane.

#### 3.3.5.2 Ion exchange capacity

The ion exchange capacity (IEC) defines the ability of a material to contain and readily exchange ions. In the scenario of a fuel cell electrolyte membrane, higher IECs suggest a higher exchange of ions are possible and thus for PFSAs, greater proton conduction. Membranes samples were first dried and measured to confirm their original dry weight. The membrane was then immersed in a solution of 0.1 M hydrochloric acid for 24 hours. Afterwards, the membrane was rinsed with water to remove excess acid and stored in a salt solution of saturated sodium

chloride for 72 hours. The sample was then titrated with a solution of 0.01 M sodium hydroxide with a phenolphthalein indicator. The IEC is calculated using the following equation:

$$\mathrm{IEC} = \frac{\mathrm{V_{NaOH}} \times \mathrm{C_{NaOH}}}{\mathrm{W_{Dry}}} \quad (7)$$

Where $\mathrm{V_{NaOH}}$ is the volume of sodium hydroxide titrated and where $\mathrm{C_{NaOH}}$ is the concentration of sodium hydroxide.

3.3.5.3 Environmental scanning electron microscopy

Environmental scanning electron microscopy (ESEM) is employed to study the surface and morphology of samples through the use of electron beams instead of a light source, allowing for greater levels of magnification. ESEM is usually performed on membranes to study the surface and cross section. In addition, Energy Dispersive X-ray Analysis (EDX) is a complementary technique that can be implemented to study the elemental composition across the sample.

The membrane sample was immersed in liquid nitrogen and was then snapped in half, revealing the cross section. The sample was then placed cross section side up, supported with super glue on the base of a sample holder. A schematic of the prepared sample is shown in Figure 3-2.

A Philips XL-30 ESEM was used in this work. A variety of magnifications were used with a spot size of 7, a working distance between 10 and 12 mm, and an electron beam strength between 5 and 10 kV. In the results chapters, electron micrographs will have their parameters displayed on the images.

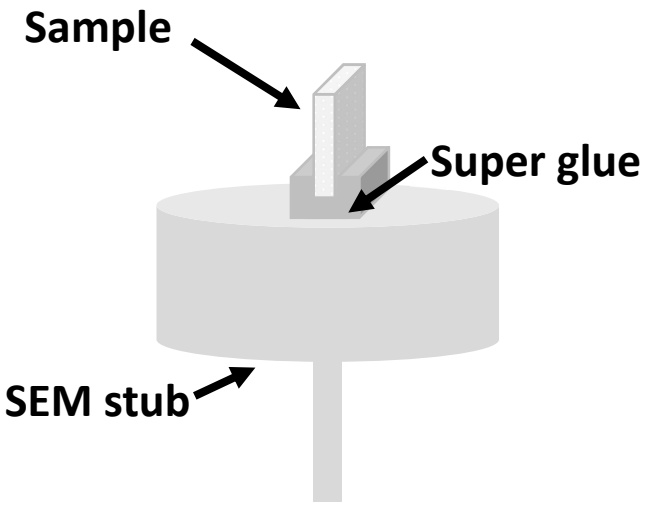



Figure 3-2: ESEM sample preparation.

3.3.5.4 Thermogravimetric analysis

Thermogravimetric analysis (TGA) studies the thermal behaviour and thermal stability of materials. For fuel cell electrolyte membranes, it is essential that the membrane is thermally stable at the required operating temperature.

The device consists of a sample holder on top of a mass measurement system with a heater which heats up the sample at a heating profile decided by the device software programme. The change in mass is recorded over time, thus determining the evaporation and oxidation of components as a function of temperature.

Prior to actual sample measurement, a reference "blank" test was performed, which involved running the experiment with the empty aluminium oxide crucible. One blank test was completed, and following this, the procedure was repeated with the membrane sample placed inside the crucible, with the same heating profile. As the temperature increases, the sample begins to disintegrate and the results can be presented as a graph of percentage mass loss over temperature[257].

A Netzsch TG 209 F1 TGA was used, with nitrogen flow of 50 ml $min^{-1}$, and a heating profile of a constant heating rate of 5 K $min^{-1}$ from room temperature to 800°C (1073.15 K).

The degree of conversion was calculated with equation ( 8 ), where $m_0$ is the initial sample mass, $m_T$ is the sample mass at a given temperature T and $m_\infty$ is the residual mass of the sample.

$$Degree\ of\ conversion, \alpha\ = \frac{m_0 - m_T}{m_0 - m_\infty} \quad (8)$$

The differential thermogravimetry, or DTG is the derivative of the TGA results and is the rate of mass change as a function of temperature. The DTG is calculated through the use of a differentiation function in Origin 2018 software.

3.3.5.5 Tensile strength analysis

Tensile strength experiments are employed to understand the mechanical properties of materials, and in this case, the fabricated membranes. The sample was placed in a sample holder and a constant extension was applied over a certain time, with the force recorded, until the membrane experienced mechanical failure. The stress and strain were then plotted, and compared between different samples and materials.

An Instron 5848 MicroTester was used for the tensile testing, with an extension rate of 2 mm $min^{-1}$. Prior to testing, the sample was cut into a dog bone-like shape via the use of a dog bone die (50% ASTM D638 TYPE V).

#### 3.3.5.6 Fourier transform infrared spectroscopy

Fourier transform infrared spectroscopy (FT-IR) is a useful tool that provides a spectrum of absorption and transmission of sample materials in the infrared region[258]. Infrared radiation from the device passes through the sample, with some of the resultant radiation being absorbed and the rest passing through. As different chemical structures display inherently different behaviour from being exposed to infrared radiation, this results in a unique FT-IR spectrum.

FT-IR was employed to confirm successful incorporation of GO into Nafion. The sample was scanned from a wavenumber of 4000 $cm^{-1}$ to 400 $cm^{-1}$ with a resolution of 1 $cm^{-1}$, with 64 scans taken to produce the spectrum. Two FT-IR spectrometers were used, a Cary 660 FTIR spectrometer (Agilent Technologies) and a Bruker Tensor 27 FTIR spectrometer.

#### 3.3.5.7 Raman spectroscopy

Raman spectroscopy is a technique used to provide detail on carbon-based materials, for example their degree of disorder. This has been utilised to understand the characteristics of GO and to confirm incorporation of GO into Nafion. The device aims a laser of specified wavelength at a sample which leads to inelastic scattering and results in a scattered light signal with a different wavelength. The subsequent scattered light passes through grating and a spectrum is presented.

GO and membrane samples were placed in a Renishaw inVia Qontor Raman microscope, and a green laser of 532 nm wavelength, with a 10% of maximum laser power and grating of 1800 $mm^{-1}$ was applied. Prior to laser application, an optical image was taken of the sample with a lens providing five times magnification. The background was not subtracted during data analysis.

#### 3.3.5.8 X-ray diffraction

A material's crystal structure can be studied with X-ray diffraction (XRD). This is a technique that exposes a sample to X-rays, analysing the resultant X-ray signal that leaves the sample, either via scattering or as a pass-through signal. XRD was employed to study the interlayer spacing of GO as well as confirming integration of GO into the Nafion.

Samples were prepared by sticking the membranes onto the plastic sample holders with a small amount of blue tack. GO was prepared in a similar manner but without the use of blue tack, and instead packed onto the sample holder with scotch tape.

A Bruker D8 Advance with a copper source (X ray generator voltage of 40 kV and current of 40 mA) was used to analyse the samples, with the scanning completed within a 2-theta range of 10 and 50°.

The spacing between the graphene oxide sheets was calculated with Bragg's law:

$$\lambda = 2d \sin\theta \qquad (9)$$

Where λ is the x-ray beam wavelength, d is the layer distance, and θ is the diffraction angle.

#### 3.3.5.9 X-ray photoelectron spectroscopy

X-ray photoelectron spectroscopy (XPS) is a tool that is used to study a sample's surface. The sample is irradiated with X-rays and the kinetic energy of the electrons that are emitted from the surface are quantified and presented as a photoelectron spectrum. The spectrum will have peaks corresponding to particular levels of binding energy. XPS was used to confirm the presence of oxygen functional groups in the GO material.

Samples were prepared depending on whether they were in powder or membrane form. For powders, the sample was dispersed and sonicated in deionised water and then drop-cast onto

silicon wafer substrates under a heat lamp. No modification was required for membrane samples.

The samples were sent to Harwell XPS which is operated by Cardiff University and UCL. The spectrometer used was a Thermo Fisher Scientific NEXSA spectrometer fitted with a monochromated Al Kα X-ray source (1486.7 eV), a spherical sector analyser and 3 multichannel resistive plate, as well as 128 channel delay line detectors. All data was recorded at 19.2 W and an X-ray beam size of 400 × 200 μm. Survey scans were recorded at a pass energy of 200 eV, and high-resolution scans recorded at a pass energy of 40 eV. Electronic charge neutralisation was achieved using a dual-beam low-energy electron/ion source (Thermo Scientific FG-03, ion gun current = 150 μA, ion gun voltage = 45 V). All sample data was recorded at a pressure below $10^{-8}$ Torr and a temperature of 294 K (room temperature). CasaXPS software was used for data analysis[259].

## 3.4 In-situ performance testing

In contrast to ex-situ characterisation, which only considers the properties of the membrane materials, in-situ characterisation involves incorporating the membrane into a single cell system and assessing the cell's electrochemical behaviour. Here the characterisation assists in revealing significantly useful information regarding fuel cell capabilities. Additionally, a variety of electrochemical characterisation techniques can be performed in order to further illuminate the influence of GO on fuel cell performance. However, prior to single cell tests, membranes had to be converted into MEAs in order to allow for testing inside a fuel cell.

### 3.4.1 MEA fabrication

To manufacture the MEA, the membrane was cut into a 5 cm × 5 cm square and sandwiched between two pieces of gas diffusion electrodes with dimensions of 2 cm × 2 cm with the

electrode side facing the membrane. This assembly was then placed between two PTFE masks and wrapped in foil, to prevent the membrane from coming into contact with the foil and thus reducing the risk of tearing.

The complete assembly was placed between the two plates of the hot press and exposed to a temperature of 140°C, with the first two minutes performed at zero applied pressure (but with the plates very close to each other to warm the assembly). The second two minutes were performed at 0.1 ton of applied pressure. The method and subsequent hot-pressed membranes are shown in Figure 3-3 and Figure 3-4, respectively.

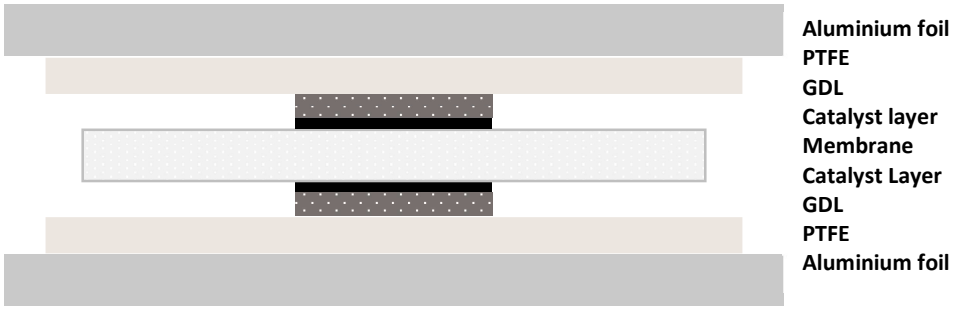



Figure 3-3: Hot-pressing method assembly and method.



Figure 3-4: Nafion (left) and Nafion-GO(4.5) (right) MEAs.

### 3.4.2 Assembly of fuel cell and activation

Once the MEA was fabricated, it had to be incorporated into the fuel cell. The MEA was placed between two gaskets that prevented any fuel leaks and provided sufficient pinch to the membrane. The MEA and gaskets were then positioned between two bipolar flow plates with a serpentine configuration. The system was then secured with bolts with a torque of 3.5 N applied before the inlet and outlet fuel pipes, electrodes, heater bars, and thermocouple were attached to the fuel cell. The fuel cell testing system used was a Scribner 850e fuel cell station with the "fuel cell" software. The fuel cell system and set up is shown in Figure 3-5.

To summarise, the steps taken before operating the cell was as follows:

1) The MEA was placed in the fuel cell and assembly was completed.
2) Inlet and outlet pipes, heater bars, electrodes, and a thermocouple were attached to the cell.
3) Fuel was passed through the cell and the set temperature applied.
4) Once the temperature in the cell, the anode, and cathode had reached the required temperature, backpressure was gradually applied. This was applied for both the anode and cathode at the same time, to prevent any large pressure difference which could damage thinner membranes.
5) The experiment was performed once the back pressure was stable and constant.

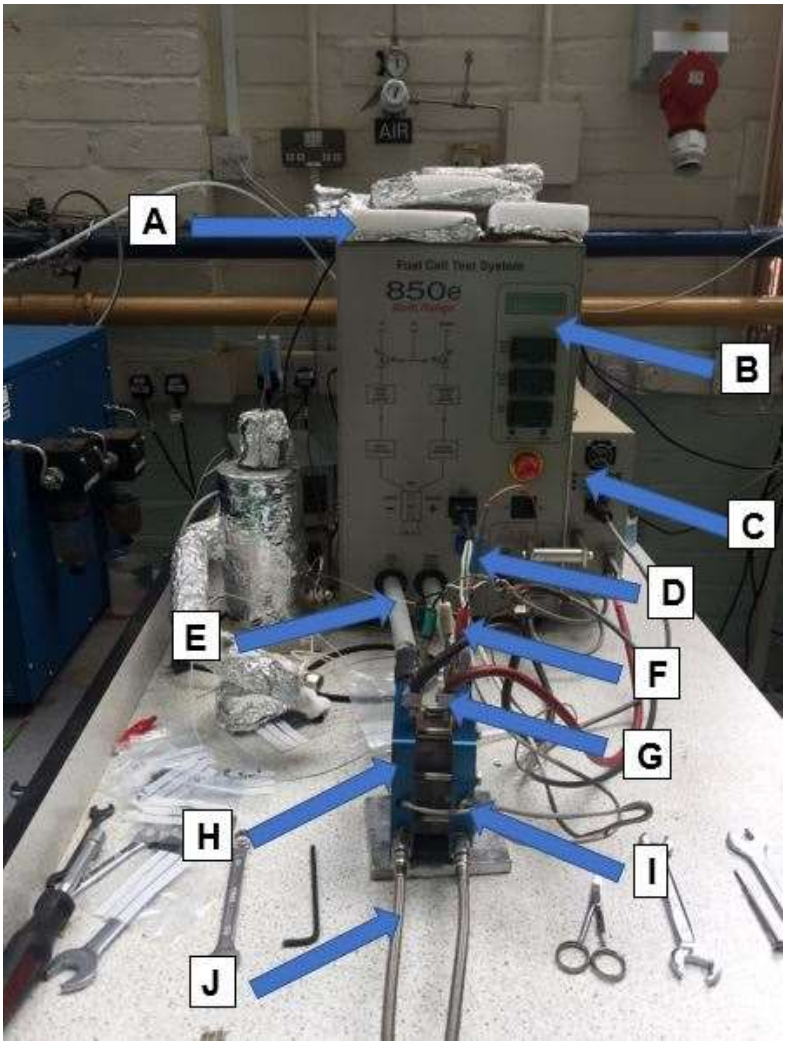



Figure 3-5: Set up of fuel cell station, from top to bottom: A) Insulation to keep fuel cell at elevated temperatures, B) fuel cell station, C) external potentiostat, D) thermocouple, E) fuel inlet, F) four probe electrode system, G) current collector cables, H) fuel cell, I) heating bars, and J) outlet leading to back pressure system.

The MEA required sufficient "conditioning" in-situ before fuel cell testing. This was necessary to acclimatise the MEA to the operating conditions within the fuel cell, as its performance would greatly change while it is being hydrated. Hydrogen and air were passed at 80°C, 100% RH, and with a voltage of 0.6 V. During the activation process the current density would greatly increase until a plateau was reached, indicating that the MEA was ready to be tested. Furthermore, to ensure full hydration, the membrane was also conditioned during the time it took for the fuel cell to increase in temperature once testing at a certain temperature was completed (e.g. from 80 to 100°C, and 100 to 120°C). The testing parameters for the activation procedure are presented in Table 3-7. The back pressure is relative to atmospheric pressure (gauge).

Table 3-7: Fuel cell activation parameters

| Parameter | Value |
|---|---|
| Fuel | Hydrogen at anode and air at cathode |
| Temperature | 80°C at anode, cathode, and internal cell temperature |
| Fuel stoichiometry | 1.3 at anode and 1.5 at cathode |
| Relative humidity | 100% at both anode and cathode |
| Back pressure | 150 kPa at anode and 130 kPa at cathode |
| Voltage | 0.6 V |

### 3.4.3 Polarisation curves

A common tool for in-situ characterisation of MEAs are polarisation curves. This technique involves varying the load to control the current density upon which the respective voltage is recorded. The voltage at zero current is produced is called the open circuit voltage (OCV) and is normally between 0.9 and 1 V. This value regularly deviates from the theoretical voltage of 1.23 V. A polarisation curve is produced when the voltage is scanned from OCV down to a low enough voltage such as 0.2 or 0.25 V and polarisation curves can be scanned down or up, and the scan rate can be controlled, with slower scans being more accurate, as the operating conditions in the cell have time to adjust to the new set point.

The polarisation curve reveals specific behaviour within three distinct regions, as presented in Figure 3-6[260]. In the context of this work, the OCV will provide an idea of the level of hydrogen crossover. The ohmic region reveals the potential electrical conductivity of the membrane, and the mass transport region presents the extent of reactant depletion and product accumulation at high current densities. The potential was scanned from OCV to 0.25 V in steps of 0.05 V, with each point held for 5 minutes. The scan was then reversed from 0.25 V back to OCV and the upward scan was used for the polarisation curve due to potential formation of surface platinum oxides during the downward scan, and a higher temperature following the higher currents. Additionally, a power curve can be produced to identify the maximum power density produced by the fuel cell. This is achieved by multiplying the corresponding current density with the corresponding voltage and plotting the power density over the respective current.

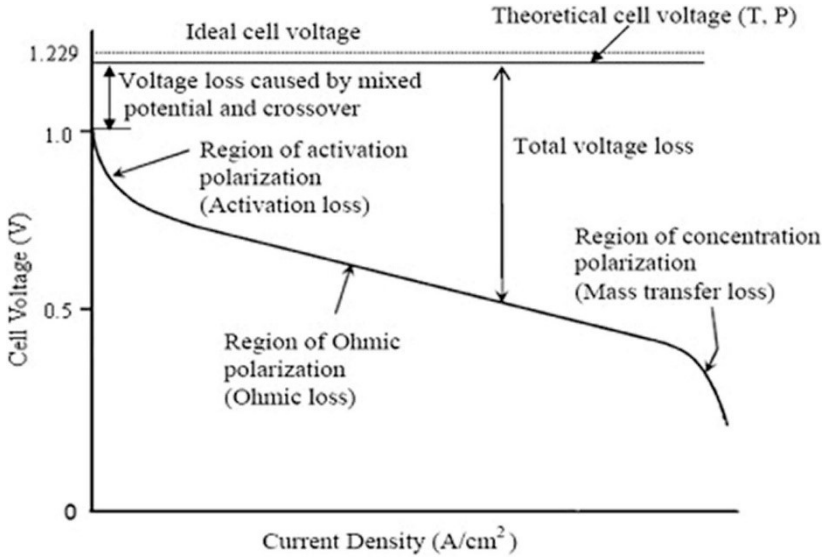


Figure 3-6: Polarisation curve with identified losses[14].

### 3.4.4 Electrochemical impedance spectroscopy

Electrochemical impedance spectroscopy (EIS) is a technique used to understand the individual contribution of each fuel cell component to the total resistance experienced. A small alternating current or voltage is applied, and a corresponding voltage and current signal is received. This can then be plotted as a Nyquist plot as semicircles and analysed.

For example, the cathode overpotential is almost always the largest contributor to total resistance as the cathode kinetics are the slowest in the MEA. The impedance of the membrane can be identified which can then be used to calculate the resistance and the conductivity. The high frequency resistance (HFR) technique was used, which isolates the ohmic resistance of the fuel cell by the use of high frequencies[261].

EIS was performed at 0.6 V corresponding to the ohmic region of the polarisation curve. An AC signal with a frequency sweep from 0.1 Hz to 10 kHz and an amplitude of 10% of the DC

[14] Reprinted with permission from Elsevier[260]

voltage was used. The HFR was identified as the point where the Nyquist plot crossed the x-axis .

### 3.4.5 Hydrogen crossover

Hydrogen crossover is a technique that can be employed to estimate the amount of hydrogen, in units of current density, that directly crosses from the anode to the cathode through the membrane. This crossover is detrimental and leads to a damaged membrane, catalyst layer, and ultimately reduced performance due to a reduced electrochemical potential between the electrodes. However, the crossover can be estimated by simulating this phenomenon. The anode and cathode inlets are fed with hydrogen and nitrogen respectively, with a voltage of 0.5 V at the cathode. Any hydrogen that passes through the membrane is oxidised when it encounters the cathode, and a current is produced. Thicker membranes will have lower crossover rates and a lower crossover rate will result in a higher OCV value. Generally, the hydrogen current crossover density was recorded for 15 to 30 minutes, until the quantity observed reached a plateau. The test parameters are shown in Table 3-8.

Table 3-8: Hydrogen crossover parameters.

| Parameter | Value |
|---|---|
| Fuel | Hydrogen at anode and nitrogen at cathode |
| Temperature | 80, 100, and 120°C |
| Relative humidity | 100% at both anode and cathode |
| Back pressure | 150 kPa at anode and 130 kPa at cathode |
| Voltage | 0.5 V |

Hydrogen permeability was calculated from equation ( 10 ):

$$H_2 Permeability = \frac{J.L}{n.F} \qquad (10)$$

Where $J$ is the hydrogen crossover current density, $L$ is the membrane thickness, $n$ is the number of electrons involved in the reaction, which is two, and $F$ is Faraday's constant. The permeability was normalised with respect to pressure with equation ( 11 ):

$$Pressure\ normalised\ H_2Permeability = \frac{H_2Permeability}{Pressure} \quad (11)$$

Where the pressure, in bar, is the total of the backpressure applied at the anode outlet and the pressure at the inlet.

## 3.5 Lifetime testing

Durability tests are a useful technique to understand long-time fuel cell performance by either operating at real life operating conditions or harsher environments such as higher temperature and lower humidity. A preliminary 24-hour OCV holding test was performed to understand the influence of GO addition to the membrane. Following from in-situ fuel cell testing, membranes with the optimum GO loading and membrane thickness were to be prepared and tested for accelerated stress tests (AST).

### 3.5.1 24-hour OCV holding test

Holding the fuel cell at OCV results in no current density being drawn and thus no reaction between the anode and cathode feed streams. Hence the consequence is hydrogen diffusing to the cathode which leads to the formation of free radicals and the degradation of the membrane and catalyst layer. To add, the higher temperatures will also lead to deterioration of the fuel cell components.

Tests for OCV, hydrogen crossover, and polarisation curves were performed at 80 and 120°C, and recorded before and after a 24 hour hold at OCV conditions. Post-mortem SEM analysis

was performed with the MEAs immersed in liquid nitrogen and snapped in half. The fuel cell test parameters are displayed in Table 3-9.

Table 3-9: 24-hour OCV hold test parameters

| Parameter | Value |
|---|---|
| Fuel | Hydrogen at anode and air at cathode |
| Temperature | 80 and 120°C |
| Fuel stoichiometry | 1.3 at anode and 1.5 at cathode |
| Relative humidity | 50 and 30% at anode and cathode respectively |
| Back pressure | 150 kPa at anode and 130 kPa at cathode |
| Voltage | Open circuit voltage |

### 3.5.2 Accelerated stress tests (AST)

The mechanical integrity of the membrane can be evaluated with an accelerated stress test (AST). This involves cycling through humidity from dry to 100% , leading to expansion and contraction of the membrane. Once the membrane is mechanically compromised, the performance will drop and this can be observed in the polarisation curve, EIS, and crossover measurements, which were performed at regular intervals.

The membrane was cycled between 0 and 100% RH. Each cycle took 4 minutes to complete, with 2 minutes at 0, and 2 minutes spent at 100% RH. After 24 hours (360 cycles), OCV, hydrogen crossover, and polarisation curves were recorded. The test parameters are shown in Table 3-10.

Table 3-10: AST test parameters

| Parameter | Value |
|---|---|
| Fuel | Air at anode and air at cathode |
| Temperature | 100°C |
| Relative humidity | 0 % at anode and cathode under dry conditions and 100% under wet conditions |
| Back pressure | 150 kPa at anode and 130 kPa at cathode |
| Voltage | Open circuit voltage |

A proof of concept experiment was performed with a cerium oxide interlayer applied to the GDEs to improve the durability by preventing the formation of radicals from hydrogen crossover. For MEA samples with a Nafion and cerium oxide interlayer, Nafion dispersion (50.4 µL), cerium oxide nanoparticles (1.6 mg), and isopropanol (50.4 µL) were sonicated before being painted onto the electrode side of the GDE with a paint brush to create a total Nafion loading of 0.3 mg $cm^{-2}$ and a total cerium oxide loading of 0.1 mg $cm^{-2}$. This was followed by hot-pressing at the same parameters as discussed in 3.4.1. Table 3-11 summarises the samples that were tested.

Table 3-11: Optimised samples tested.

| Membrane | Single or multilayer | Membrane thickness (µm) | GO source | Cerium oxide interlayer | AST |
|---|---|---|---|---|---|
| Nafion-synGO(1.5) | Single layer | 30 | In-house | No | No |
| ML-SynGO(0.26) | Multilayer (3 layers) | 30 | In-house | No | No |
| Nafion-synSGO(1.5) | Single layer | 30 | In-house | No | Yes |
| ML-SynSGO(0.26) | Multilayer (3 layers) | 30 | In-house | No | Yes |
| Nafion-synSGO(1.5) | Single layer | 30 | In-house | Yes | Yes |
| ML-SynSGO(0.26) | Multilayer (3 layers) | 30 | In-house | Yes | Yes |
| Nafion 211 | Single | 25 | N/A | No | Yes |

# 4 Characterisation and fabrication

This chapter will present the successful synthesis of graphene oxide, proven via a variety of characterisation techniques. In addition, the membrane fabrication process and subsequent characterisation will be discussed.

## 4.1 Graphene oxide characterisation

GO samples were characterised to quantify the oxygen content on both the surface and within its layers. In the case of synthesised GO, characterisation was also used to confirm successful synthesis. Commercial GO in this section refers to GO sourced from Sigma Aldrich. GO characterisation data from Nanoinnova is provided in the summary (4.1.6).

### 4.1.1 X-ray photoelectron spectroscopy

XPS was utilised to confirm the successful oxidation of the synthesised GO. The survey spectra for the SynGO, SynSGO and commercial GO was shown in Figure 4-1 a). It can be observed that all three samples display two sharp peaks at 285 eV and 532 eV, corresponding to C1s and O1s, respectively. The oxygen atomic concentration was calculated to be 31.51%, 27.27% and 25.68% for the three samples, respectively, and the carbon-oxygen ratio was found to be 3.85 carbon for each oxygen and 2.90 carbon for each oxygen for commercial GO and synthesised GO, respectively. Hence, the synthesised GO had the greatest level of oxidation. This implies that the synthesised GO had a greater quantity of oxygen functional groups on its surface, and this should allow for easier dispersion in solvents and provide facile access for the formation of water channels once incorporated with Nafion.

Figure 4-1 b) displays the C1s spectra for synthesised GO. Four peaks were identified during the peak fitting procedure. The first, at 284.85 eV refers to $Sp^2$ carbon within the graphitic

regions. The second, at 284.99 eV, corresponds to $Sp^3$ carbons, and produced the lowest counts. Another peak was recognised at 286.85 eV, which is related to epoxy and phenolic groups. The last peak at 288.32 eV is the presence of carboxylic acids. The latter two peaks correspond to functional groups that contain oxygen, therefore confirming the successful oxidation of GO[262].

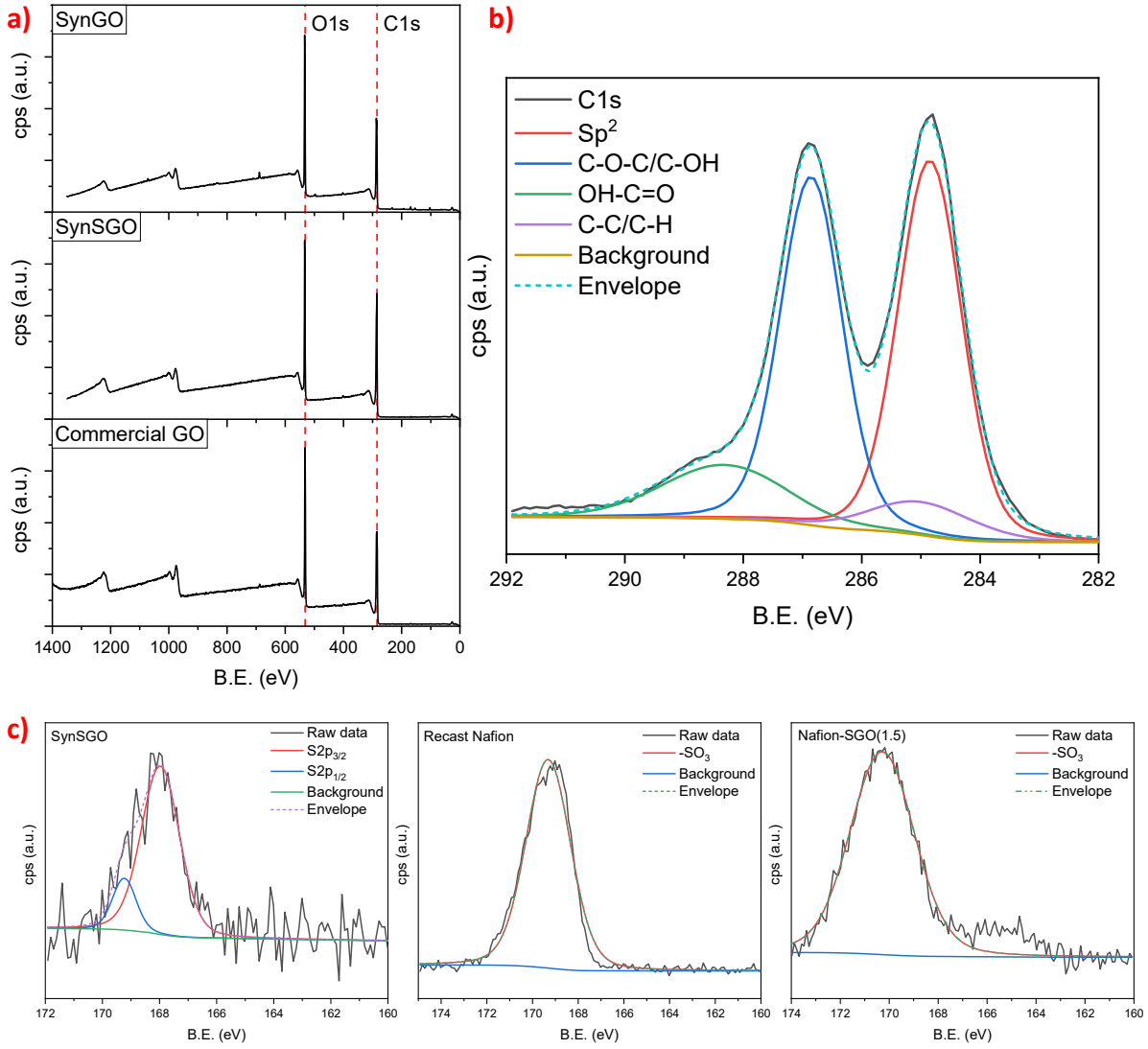



Figure 4-1: a) Survey spectra, b) C1s spectrum of synthesised GO, and c) S2p spectra.

Figure 4-1 c) shows the S2p spectra. A distinct peak is observed in SynSGO, confirming successful sulphonation. This peak is at 168.1 eV, which is distinctive of the sulphonic groups in GO[263,264]. The S2p spectra for recast Nafion and a composite of Nafion and SynSGO are also shown. Here, the peaks are at 169.3 eV and 170.2 eV, respectively, which refer to the sulphur in the side groups of Nafion[265,266]. Furthermore, the counts per second of the three samples were found to be 837, 1321 and 2869 for SynSGO, recast Nafion and the composite membrane, implying that the extra counts were from the addition of the sulphonated GO.

### 4.1.2 Raman spectroscopy

Raman spectroscopy was performed, as shown in Figure 4-2,with microscopy images of GO prior to laser application. The spectra all show clear D and G bands, with the G bands referring to carbon-carbon stretching and the D band corresponding to the restricted vibrations caused by the addition of functional groups[267,268]. The ratio of the intensity of the D band and the intensity of the G band was 0.82, 0.84 and 0.92 for SynGO, SynSGO and commercial GO, respectively, which is common for graphene oxide[184]. Furthermore, the intensity ratios for all 3 GO samples correspond to multiple layers of graphene oxide. To add, the sulphonation process resulted in the slight increase in the ratio, due to the addition of sulphur groups.

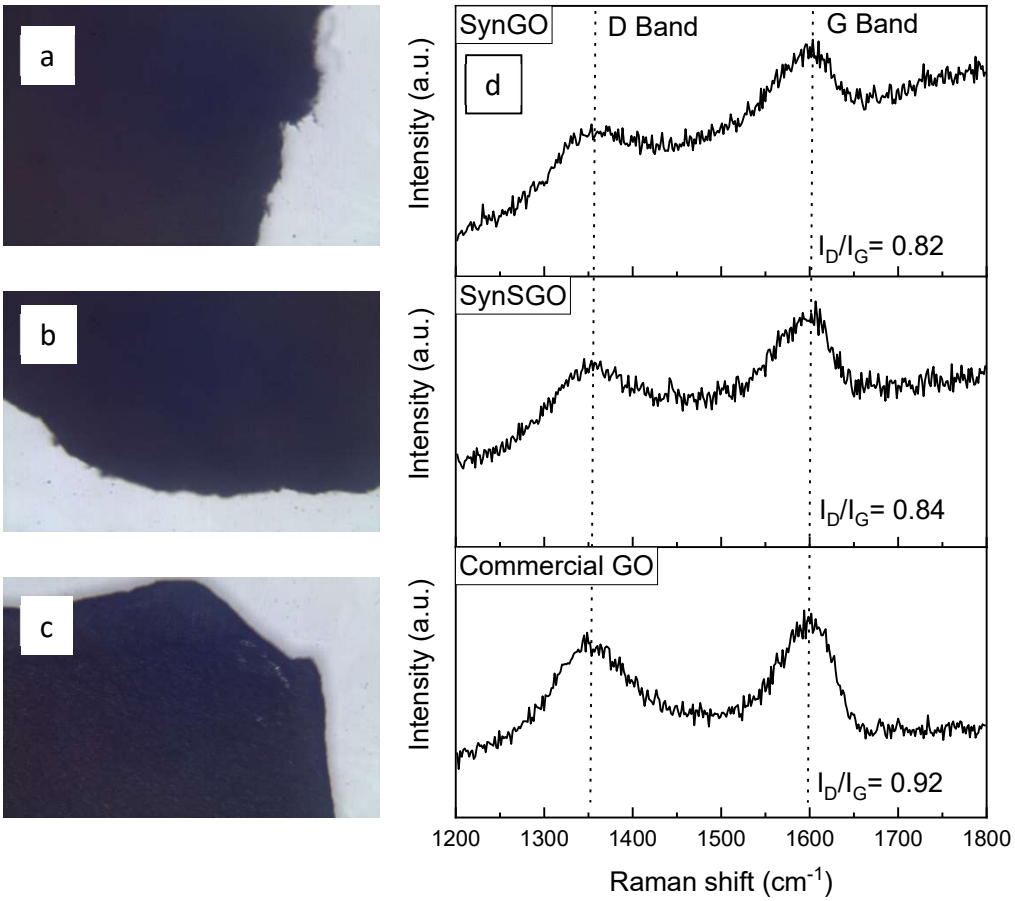



Figure 4-2: Raman microscopy images of a) synthesised GO, b) synthesised sulphonated GO, c) commercial GO, and d) Raman spectra of the GO samples.

### 4.1.3 Fourier transform infrared spectroscopy

Figure 4-3 presents the FT-IR spectra for the three GO samples. All samples display a broad stretch around 3380 $cm^{-1}$ which refers to the O-H bond. A small dip at around 2885 $cm^{-1}$ is due to C-H bonds. A sharp peak at 1724 $cm^{-1}$ for SynGO and SynSGO and 1713 $cm^{-1}$ for the commercial GO is due to C=O bonds from the carboxylic acid functional group. C=C domains were observed at 1620 $cm^{-1}$ for the synthesised samples and at 1577 $cm^{-1}$ for the commercial sample. Finally, two peaks corresponding to C-O bonds, from carboxylic acid and from epoxy groups, were identified[269]. Interestingly, functional groups corresponding to sulphonation were not found. This is because the region where the S=O sulphonate stretch occurs overlapped with

the C-O aromatic ester stretch, implying that the level of sulphonation was low. Overall, FT-IR analysis confirmed the presence of numerous oxygen functional groups in the different sources of GO.

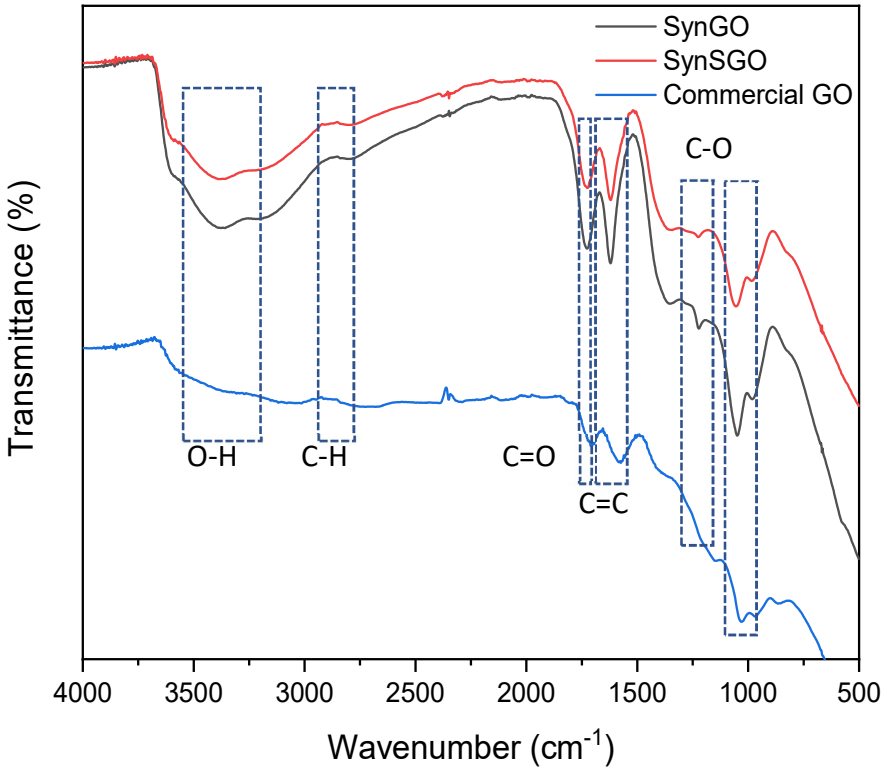



Figure 4-3: FT-IR spectra of the GO samples.

### 4.1.4 X-ray diffraction

XRD was performed to better understand the structure of the commercial GO. The XRD spectra in Figure 4-4 reveal a sharp peak at 11.25°, which is consistent of that found in GO[184]. This two-theta value corresponds to a d-spacing of 0.79 nm, which is more than twice the spacing than that of graphite at 0.34 nm. This increase is due to the introduction of oxygen functional groups between the individual atomic layers of carbon[270]. Synthesised GO prepared by Aliyev et al.[152] displayed a two-theta value of 10.7 °, corresponding to a d-spacing of 0.83 nm. This is slightly greater than for commercial GO, likely due to the higher oxygen content. Finally, there

were no other sharp peaks observed in the XRD, such as those due to graphite, confirming complete oxidation.

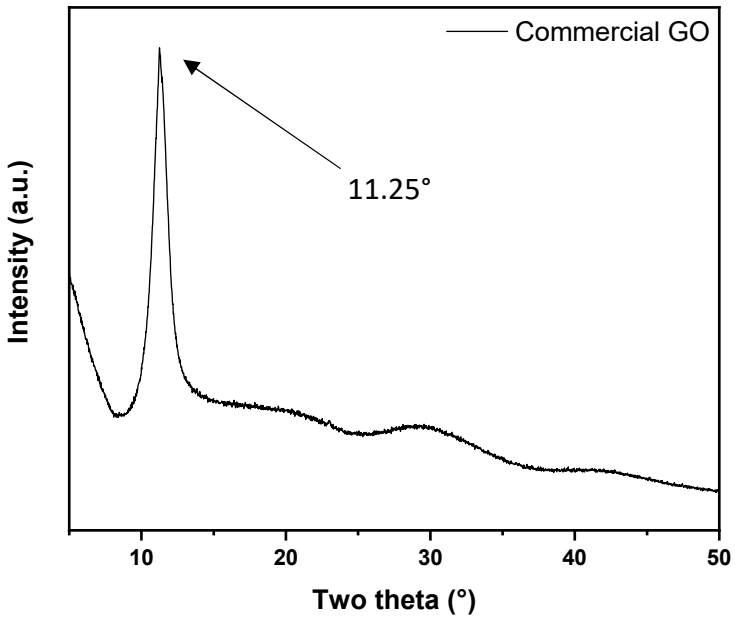



Figure 4-4: XRD spectrum of commercial GO.

### 4.1.5 Thermogravimetric analysis

TGA results shown in Figure 4-5 display three distinct temperature regions where mass loss occurs. The first, from room temperature to around 130°C is due to the evaporation of absorbed water. The second region, from 130 to 220°C, is because of a loss of functional groups such as hydroxyl and carbonyl groups. The final region, occurring from 220 to 400°C refers to the decomposition of functional groups such as ketones[271]. The samples did not completely decompose as the experiment was performed with nitrogen gas and hence only the graphitic regions remained as residual mass. From the residual mass, it was observed that the synthesised GO samples had a lower residual mass, hence greater levels of oxidation. In contrast, the commercial GO had a greater residual mass of 53%, and hence lower levels of oxygen. This suggests that the commercial GO had a greater propensity for agglomeration as the lower oxygen quantity will allow for less facile dispersion. Furthermore, the commercial GO

experiences a smaller decrease in mass between room temperature and 200°C, suggesting less absorbed water and functional groups such as hydroxyl, but a large mass decrease at 200°C.

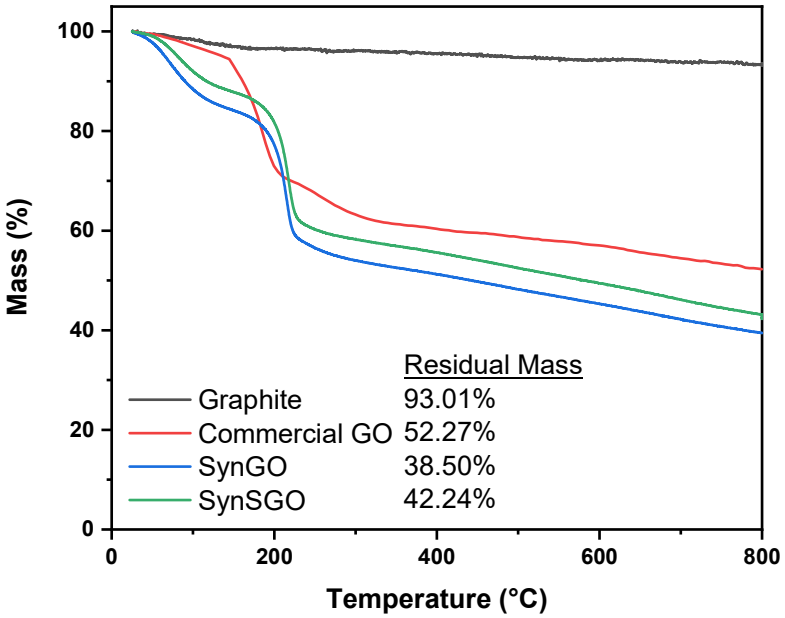



Figure 4-5: TGA of graphite and GO samples.

### 4.1.6 Summary

All GO samples revealed characteristic O1s and C1s peaks in their XPS spectra, with similar intensity ratios from Raman Spectroscopy, as well as the expected oxygen functional groups in the FT-IR spectrum. Commercial GO from Sigma Aldrich had the lowest carbon to oxygen ratio, suggesting fewer oxygen functional groups on its surface. Additionally, commercial GO also had the greatest residual mass out of the GO samples during TGA, implying less oxygen between its layers. For completion, XPS and TGA data from Nanoinnova's GO is included in the summary Table 4-1, which had a much higher C/O ratio and a similar residual mass to the synthesised GO. This suggests that the majority of oxygen functional groups were situated on the surface.

Table 4-1: Summary characterisation results for the GO samples.

| GO source | XPS C/O ratio | TGA residual mass (%) |
|---|---|---|
| Commercial GO (Sigma Aldrich) | 3.80 | 52.27 |
| Commercial GO (Nanoinnova)[15] | 1.53 | 37.66 |
| Synthesised GO | 2.95 | 38.50 |

## 4.2 Fabrication of mixed matrix composite membranes

The fabrication process for preparing single layer composite membranes will be presented in the following section, and factors such as sonication, desiccation and oven level will be discussed.

The GO characterised in the previous section was used to produce composite membranes with Nafion as the polymer phase. Initially, the project was to replicate the methodology of Branco et al[180]. Initially, mixed matrix membranes were fabricated, and then the multilayer mixed matrix membranes, both using commercial GO. Once the optimum GO content and membrane thickness was found via fuel cell tests, membranes using the synthesised GO and synthesised SGO were prepared.

### 4.2.1 Influence of probe sonication

The initial process involved a simple mixing procedure of Nafion dispersion and GO powder that was wetted with water and bath sonicated, following from Branco's protocol[180]. Essentially, a certain quantity of Nafion dispersion was pipetted into a vial and combined with a dispersion consisting of GO powder wetted with 4 mL of DI water that was bath sonicated for 10 minutes. The combined vial was then shaken by hand and cast onto a petri dish.

[15] Obtained from Nanoinnova GO characterisation sheet.

Subsequent casting of this dispersion and heat treatment led to the formation of a membrane where the polymeric Nafion regions and nanomaterial GO regions were distinct and separate. The phase separation was spontaneous after a few minutes in the oven, and required constant shaking of the petri dish to mix the solution. This was because of the very different nature of both materials and hence the preference to agglomerate. For example, Nafion is polymeric, with a hydrophobic Teflon backbone and sulphonic acid side groups, hence this results in hydrophobic and hydrophilic domains. Graphene oxide is almost fully carbon with some oxygen functional groups. Even though the presence of oxygen groups above and below the carbon honeycomb results in a slightly weaker π-π interaction because of the larger interlayer spacing, GO can still agglomerate. This can be seen in Figure 4-6 a) where translucent regions correspond to Nafion and the black regions to GO. Hence, bath sonication does not provide the necessary mechanical exfoliation to fully disperse GO, even in the presence of water.

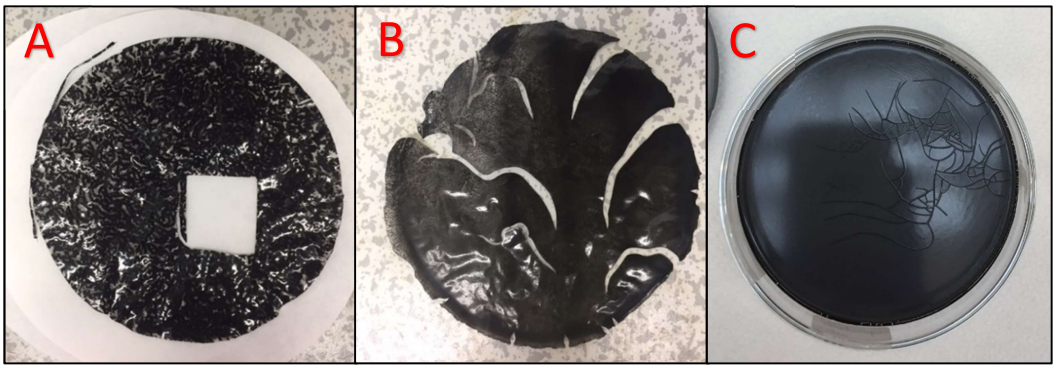



Figure 4-6: Fabrication challenges: a) Phase separation, b) cracks, and c) cracks prior to removal.

In order to improve the dispersion, probe sonication was incorporated along with the initial bath sonication. The GO-DI water dispersion was bath sonicated for 10 minutes and then underwent probe sonication to successfully disperse the GO in water. The probe sonication procedure firstly involved sonication at 60% power for 5 minutes with an on-and-off sequence of 5

seconds each. The initial high power was chosen to help exfoliate and disperse GO and the 5 seconds off timer would allow the dispersion that was coated on the side of the vial due to sonication to have enough time to fall back into the dispersion before the probe was turned on again. The off timer would also allow the dispersion to cool down (the vial was placed in a beaker of ice), and prevent the overheating of the dispersion.

This was followed by sonication at 40% with a timer of 5 seconds on and 1 second off for 4 minutes. This was to break up any GO that was not fully exfoliated, and the lower power would prevent the dispersion from coating the sides of the vial.

Afterwards, the Nafion dispersion was added and the solution was sonicated again at a power of 20% for 2 minutes with a sequence of 5 seconds on and 1 second off. The use of probe sonication led to the formation of membranes with improved dispersion, but it unfortunately resulted in clear and visible cracks, as seen in Figure 4-6 b). Essentially, probe sonication damaged the polymer chains preventing the formation of crack free membranes. Figure 4-6 c) clearly shows a Nafion-GO(4.5) membrane that has just been removed from the oven with clear cracks in the membrane. To alleviate this issue, probe sonication was not used after the addition of Nafion. Hence, Nafion solution was added to the sonicated GO solution and casted onto a petri dish.

### 4.2.2 Influence of desiccation

An issue observed during the casting procedure was the presence of bubbles and dissolved gasses that were located on top of the casted solution. These are the result of bubbles formed when pouring the vial contents onto the petri dish as well as the sonication process introducing dissolved gasses into the dispersion. This is detrimental as these bubbles could produce empty voids either on top or inside the membrane, potentially disrupting the properties of the

membrane. To counter this, Nafion dispersion prior to combining with GO was vacuum desiccated overnight to remove any dissolved gasses.

Prepared composite membranes are shown in Figure 4-7. It was noted that these membranes show good dispersion of GO and that they do not have any cracks or artefacts. Observed is that there is a somewhat prominent circumference of GO around the edge of the petri dish. This was also observed in membranes prepared by Branco[180]. This is likely the result of the "coffee-ring" effect, where particles migrate to the outer edge of a droplet during evaporation[272,273].



Figure 4-7: Nafion-GO(4.5) membranes.

### 4.2.3 Influence of oven level

For producing membranes of different thicknesses, a varying quantity of Nafion dispersion was used, as described in Table 3-2. Additional ethanol solvent was added to Nafion dispersions during the desiccating process as the quantity of Nafion for thinner membranes was not sufficient to completely cover the 9 cm diameter petri dish.

The prepared membranes experienced a gradient in thickness from the centre of the membrane to the circumference, with the circumference region experiencing a reduction in thickness, as shown in Figure 4-8. However, the 5 by 5 cm region which was used to produce the MEAs are ± 5 μm within the target thickness. A variety of parameters such as the oven level and tray

position are responsible for this feature. In order to prevent extensive deviations in thickness, a spirit level was utilised in the oven to identify flat regions prior to heat treatment. Overall, the method was optimised to produce membranes of a suitable quality that would allow for ex-situ characterisation and fuel cell testing.

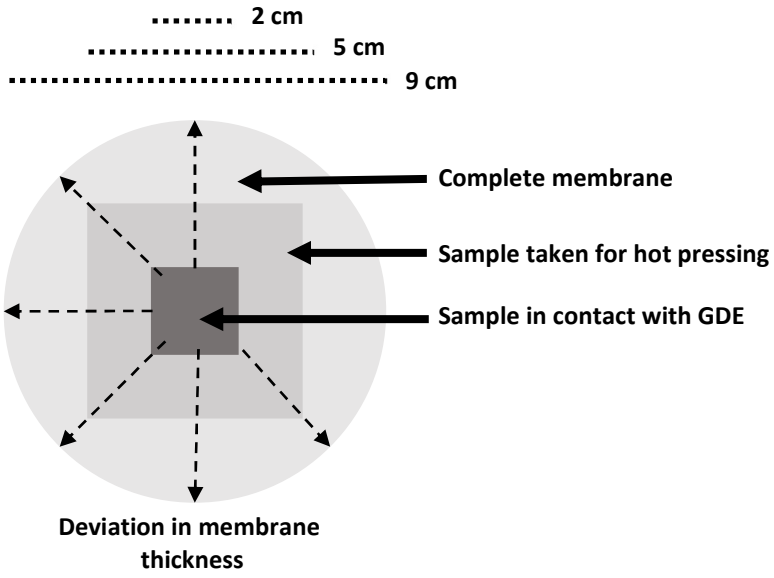



Figure 4-8: Membrane thickness deviation (not to scale).

### 4.2.4 Summary

Single layer composite membranes were successfully prepared and factors such as sonication, desiccation and oven level were discussed. Probe sonication produced an improved dispersion of GO but caused damage to the membrane, whereas desiccation was utilised to prevent the formation of bubbles during the casting process. The final and optimised fabrication method resulting from this process has already been presented in Chapter 3.

## 4.3 Single layer membrane characterisation

The characterisation of composite membranes was performed to confirm the successful introduction of GO into Nafion. Furthermore, the influence of GO loading was studied, with techniques utilised to study the physical structure, thermal behaviour, and water uptake properties.

### 4.3.1 Environmental scanning electron microscopy

In order to understand the membranes' physical structure, such as their cross section and surface, ESEM analysis was performed. Electron micrographs are presented in Figure 4-9 to Figure 4-13, showing cross sections of recast Nafion and composite membranes of varying GO loading of 1.5, 3, 4.5 and 6%. It can be observed in Figure 4-9 that the Nafion sample has a clear, smooth cut with a uniform cross section implying purity. In comparison, the composite membranes differ significantly, with a layered structure, due to the presence of GO, which is dispersed parallel to the membrane surface. This is proven with the layering being more prominent with increasing loading, which is not present in Nafion at all. In addition, higher magnification micrographs focused on areas with this layering shows what strongly resembles GO, such as images d), e), and f) in Figure 4-11.

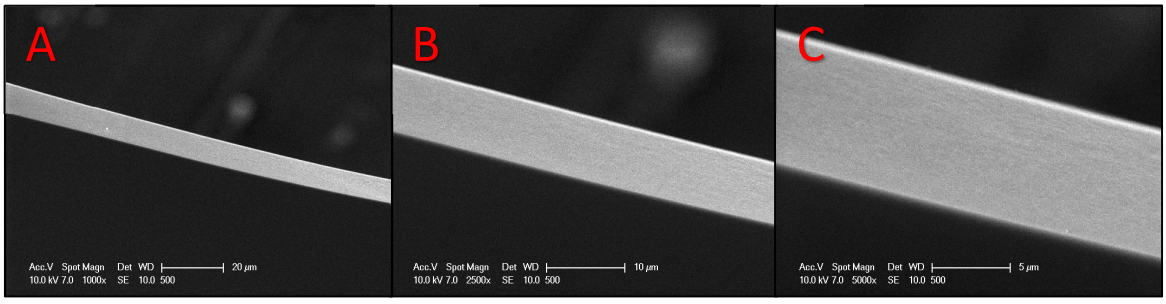



Figure 4-9: ESEM images of recast Nafion at a magnification of A) 1000, B) 2500, and C) 5000.

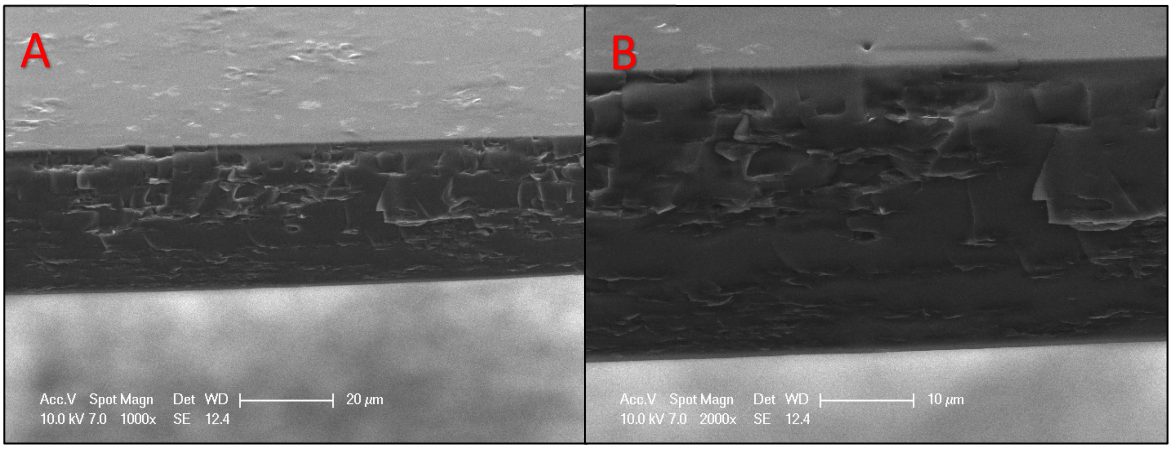



Figure 4-10: ESEM images of Nafion-GO(1.5) at a magnification of A) 1000, and B) 2000.

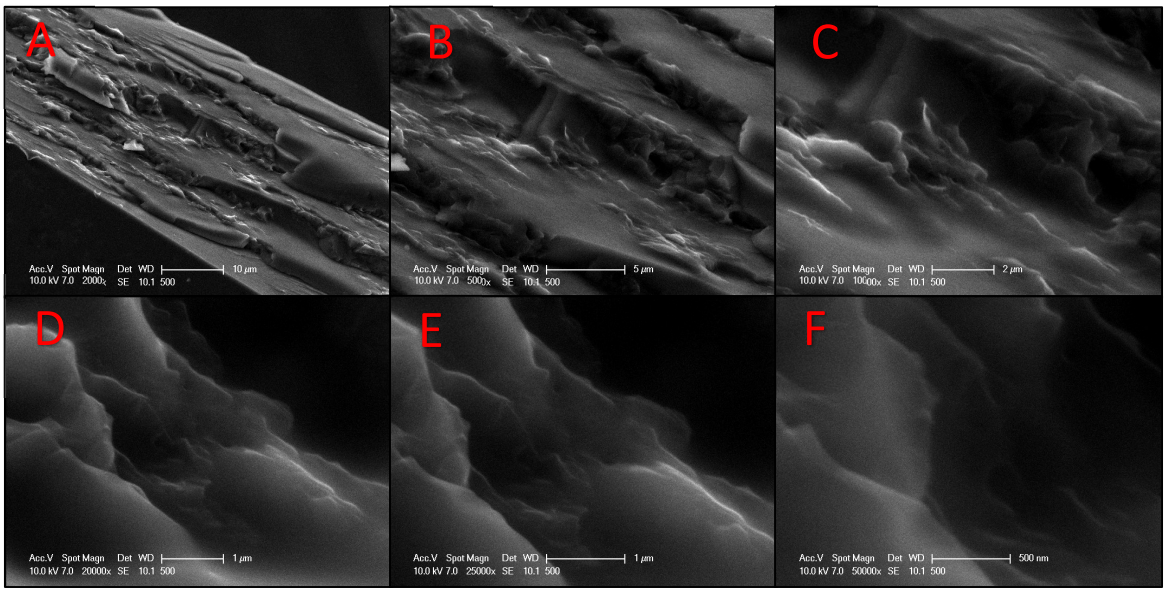



Figure 4-11: ESEM images of Nafion-GO(3) at a magnification of A) 2000, B) 5000, C) 10,000, D) 20,000, E) 25,000, and F) 50,000.

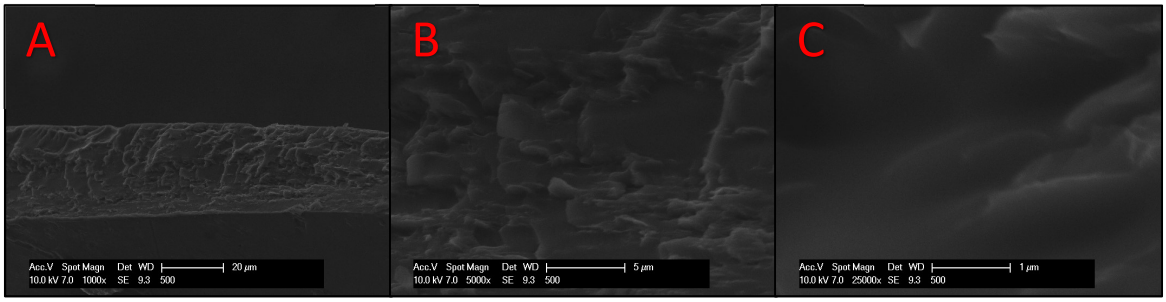



Figure 4-12: ESEM images of Nafion-GO(4.5) at a magnification of A) 1000, B) 5000, and C) 25,000.

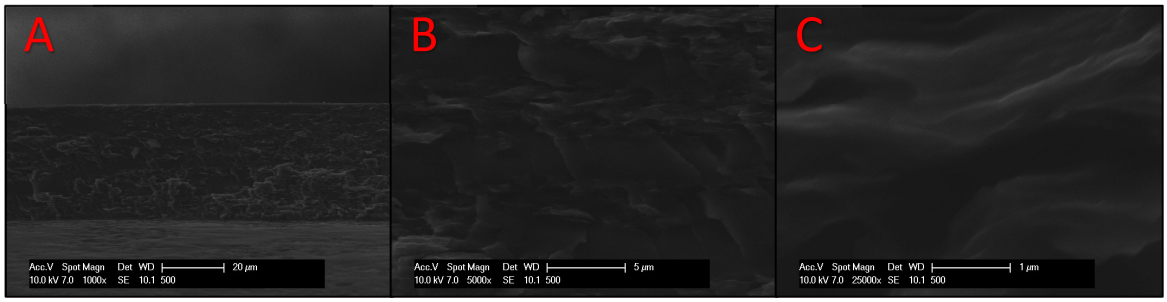



Figure 4-13: ESEM images of Nafion-GO(6) at magnification of A) 1000, B) 5000, and C) 25,000.

Additionally, with the higher weight loading, sedimentation of GO occurs, with this being most obvious with Nafion-GO(6) in Figure 4-13. Under gravitational forces the GO layers sediment onto the petri dish when the composite skin layer forms through the evaporation of the solvent. This results in the agglomeration GO layers on one side of the membranes. For a comparison, Figure 4-14 presents the electron micrographs of Nafion-GO(1.5) on the left and Nafion-GO(6) on the right. The layered structure is much more prominent in Nafion-GO(6) with the presence of layers extending deeper into the membrane. This was because the Nafion-GO(6) membrane has 4 times the quantity of GO .

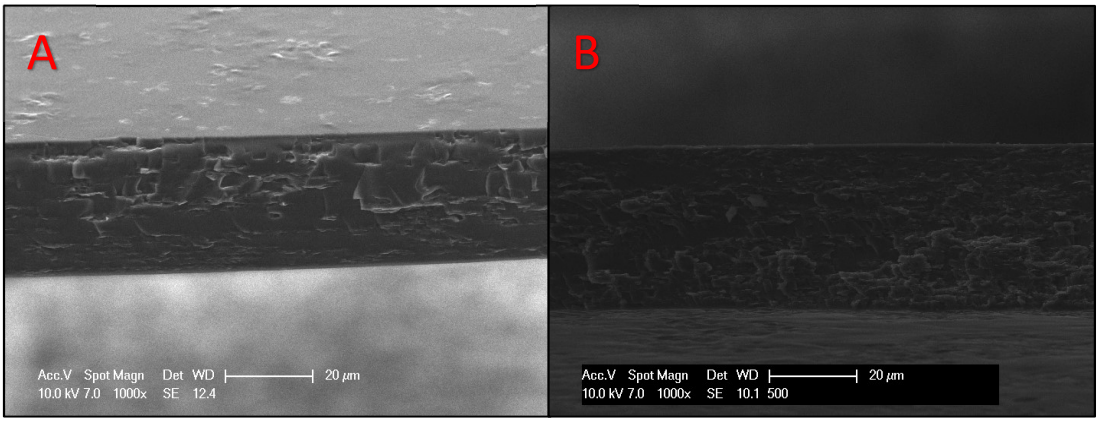



Figure 4-14: ESEM images of a) Nafion-GO(1.5), and b) Nafion-GO(6).

### 4.3.2 Thermogravimetric analysis

Thermal degradation studies were performed to understand the thermal behaviour of the multilayer samples, with Figure 4-15 presenting both the TGA and DTG. Recast Nafion experienced three significant losses in mass[274]. The first, corresponding with the removal of water, occurred between room temperature and 200°C[275]. The thermal decomposition of the sulphonic side groups occurred between 200 and 375°C. The final step, from 375 to 550°C referred to the total degradation of the Nafion backbone. These three steps can be clearly observed in the DTG. The mass loss percentages of each sample have been summarised in Table 4-2.

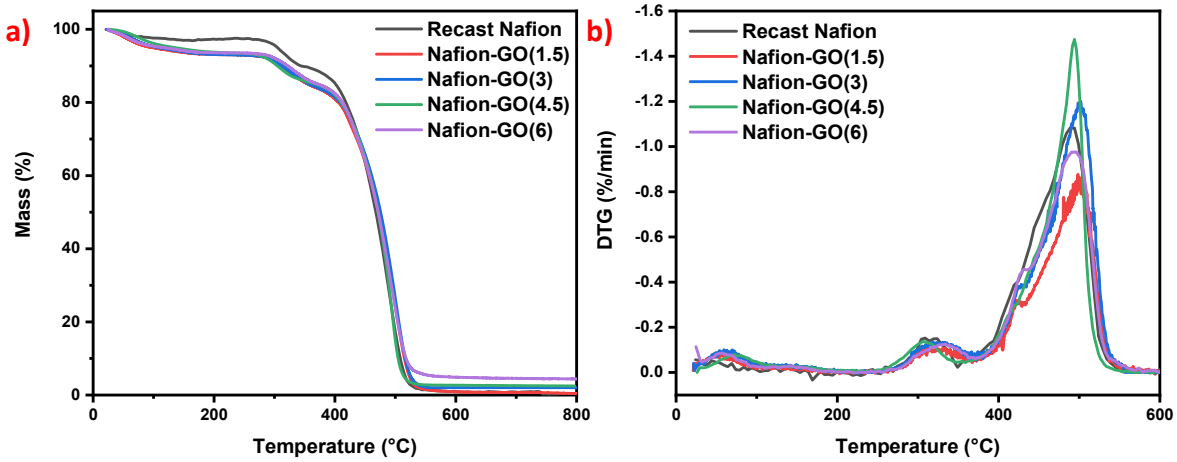



Figure 4-15: a) TGA and b) DTG of mixed matrix membrane samples.

Table 4-2: Mass loss percentages during different temperature regions for mixed matrix membrane samples.

| | Mass loss (%) | | |
|---|---|---|---|
| Sample | 0 to 200°C | 200 to 375°C | 375 to 550°C |
| Recast Nafion | 2.7 | 8.8 | 87.0 |
| Nafion-GO(1.5) | 6.9 | 9.4 | 82.1 |
| Nafion-GO(3) | 6.9 | 9.3 | 81.6 |
| Nafion-GO(4.5) | 6.2 | 9.1 | 81.9 |
| Nafion-GO(6) | 6.4 | 8.8 | 79.3 |

The addition of GO resulted in an increase in mass loss below 200°C. This mass consisted of a combination of evolved water from both the Nafion and GO, and some of the oxygen functional groups. There was a general decrease in mass loss with increasing loading in the following temperature regions, referring to the greater quantity of GO. This can also be observed with the residual mass at the end of the TGA, where Nafion-GO(6) had the highest mass, representing the graphitic regions of GO.

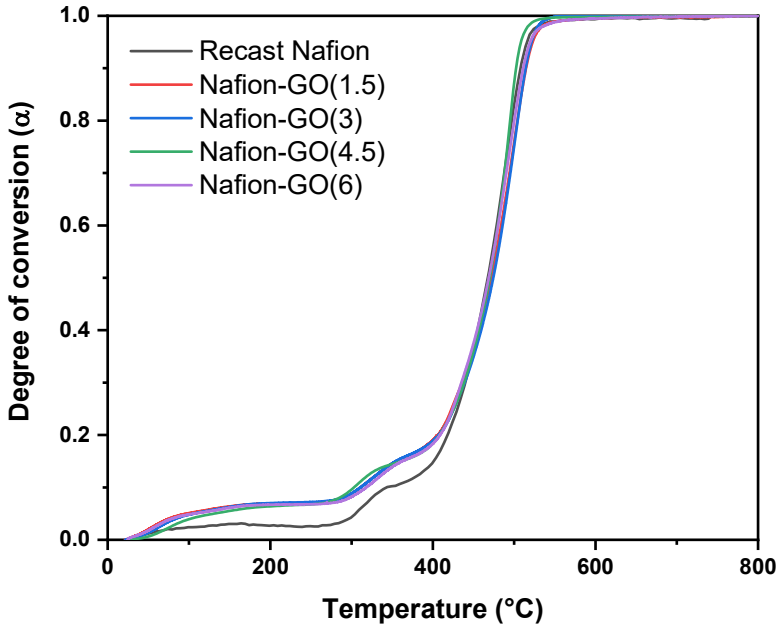



Figure 4-16: Degree of conversion of mixed matrix membranes.

### 4.3.3 X-ray diffraction and Fourier transform infrared spectroscopy

The crystalline structure of the prepared membranes was studied with XRD, displayed in Figure 4-17. The cast Nafion displayed a very broad mark around 17°, which corresponded to the Teflon-like regions on Nafion[276]. This was also observed in the composite membranes. The sharp peak around 28° refers to the intrachain distance between Nafion chains[277]. However, the GO peak was not visible in the composite membranes. This was most likely due to two reasons: firstly, the loading of the nanoparticles was quite low and hence not picked up[278]. Secondly,

GO is amorphous and not crystalline. The FT-IR is shown in Figure 4-18. The spectra are similar for all samples due to the low levels of GO loading.

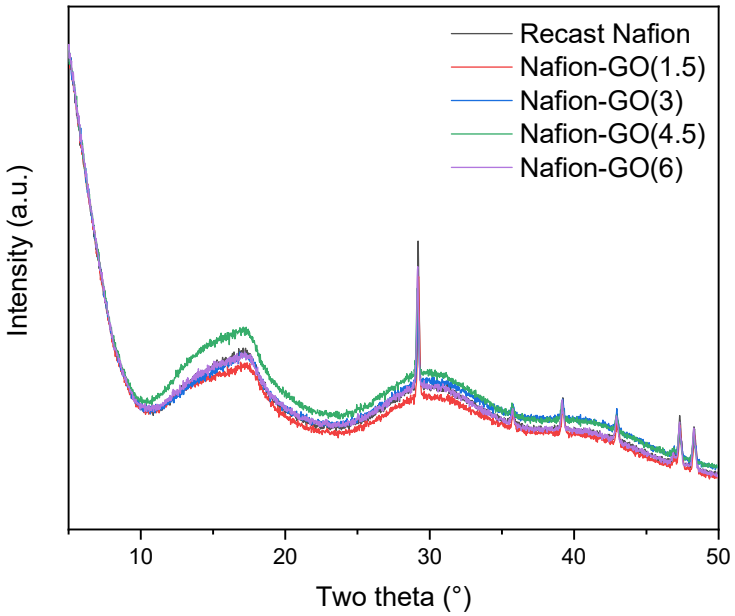



Figure 4-17: XRD patterns of mixed matrix membranes.

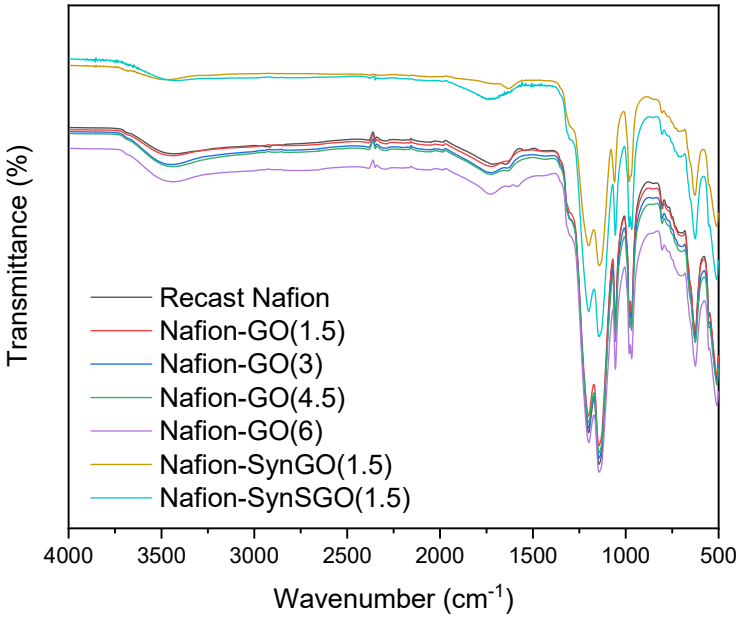



Figure 4-18: FT-IR spectra of mixed matrix membranes.

### 4.3.4 Water uptake and Ion exchange capacity

Water uptake and IEC values are presented in Figure 4-19. Composite membrane samples with increasing quantities of GO were tested to study their influence on the amount of retained water. There was a significant increase in water uptake with the addition of any amount of GO. This suggests that the oxygen functional groups aid in the retention of water. Potential variations can be due to the dispersion of GO throughout the membrane and where the sample was taken from the membrane. Furthermore, potential systematic error in the removal of the surface water process could have resulted in the large standard deviation.

The IEC also increased with the introduction of GO and this is in agreement with Kumar et al.[279]. Gagliardi et al. [280] in particular found the same relationship while using an identical method with an identical GO source to produce membranes, with IEC values of 0.83, 0.92, 0.99, 1.07, 1.18, and 1.29 meq $g^{-1}$ for recast Nafion, 0.5 wt.% GO, 1 wt.% GO, 1.5 wt.% GO, 3 wt.% GO, and 6 wt.% GO respectively. The addition of GO creates extra sites for potential ion exchange. Variations within IEC can be explained by several causes. Firstly, the calculation of filler loading is not always specified. For example, is the total composite weight fixed (i.e. increased GO mass means reduced polymer mass) or is the polymer mass fixed? Secondly, the uniformity of filler within the polymer matrix could be inhomogeneous, which can produce slightly different results if samples are taken from that region[281]. Finally, the titration is based on a visual change in colour, introducing human error[280].

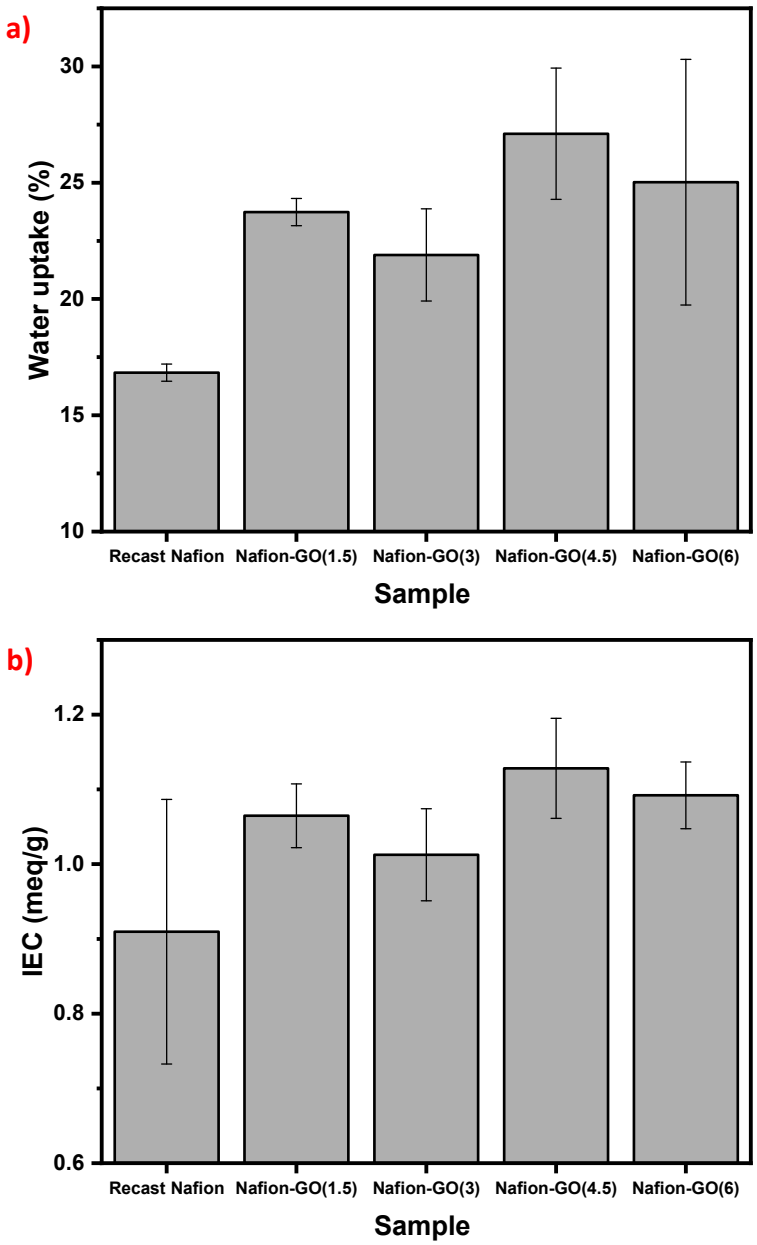



Figure 4-19: a) Water uptake, and b) IEC of mixed matrix membranes.

### 4.3.5 Summary

Composite membranes were successfully characterised and ESEM revealed that the cross section of composite membranes had a distinctive layered topography that increased in intensity with higher weight loadings of GO.

WU and IEC values increased with GO loading, and this agrees with some of the literature. On the other hand, other publications discussed in the literature review experienced a drop in WU

and IEC with GO loading. This was explained by the GO preventing the full polymer movement and disrupting the ionic domains. However, this was not found in the samples characterised in this section.

## 4.4 Fabrication of multilayer membranes

The fabrication process of multilayer membranes will be discussed in the following, with emphasis on the changes made to optimise and improve the membrane quality. The procedure of preparing multilayer membrane was adapted from Branco et al[180], and involved the fabrication of a 3-layer membrane. Essentially, the first and third layers of pure Nafion were fabricated similarly to those of single layer membranes described previously, with the use of a combined solution of Nafion dispersion and ethanol. The middle layer was prepared to be equivalent to that of a "composite membrane" with Nafion and GO to improve interfacial contact with the outer layers.

This was because the use of pure GO in the middle layer leads to delamination due to the chemical differences between GO and Nafion, such as similar functional groups[180]. Generally, there would be hydrogen bonding between the sulphonic groups of Nafion and the oxygen functional groups of GO, but a middle layer of pure GO would disintegrate in contact with water and compromise the entire membrane. This would be because of the expansion of GO with the introduction of water molecules between the individual layers of GO. Additionally, during casting, there were traces of observed GO left on the petri dish after the membrane was removed, implying some GO travelled from the middle layer to the circumference of the membrane and drying on the side of the petri dishes. Thus, this could alter the weight loading quantity.

### 4.4.1 Influence of casting solvent

In order to cast the middle layer, a variety of solvents were tested. Nafion membrane can swell when in contact with particular solvents, which is a consequence of Nafion being very difficult to dissolve, due to parts of its chemical structure being very hydrophobic and others very hydrophilic, resulting in excessive swelling.

The implication of this swelling is that the surface is not smooth, which would be detrimental for casting the final layer. For example, large variations in membrane height can influence the contact with the GDE and hence fuel cell performance.

Solvents including ethanol, IPA, and water were chosen. Firstly, due to their lower boiling points of 78, 82 and 100°C, which would prevent thermal reduction of GO during heat treatment. This is in contrast to solvents such as DMSO (189°C), DMF (153°C), DMAc (165°C) and NMF (183°C). Secondly, it was found that water-alcohol Nafion dispersions produced higher proton conductivities in comparison to Nafion dispersions in DMAc and DMF, due to the formation of larger ionic clusters[254].

Figure 4-20 presents several prepared multilayer membranes. It can be observed: a) that there were large regions of GO separated by polymeric regions. The first Nafion layer had swollen in areas concentrated with Nafion polymer, causing non-uniform swelling, and the second layer consisting of GO settled in between these “wells”. This formation of swelling made it easier for the GO to accumulate. Figure 4-20 b), c) and d) show multilayer membranes prepared with ethanol and IPA, producing membranes with a very bumpy appearance, with ridges and the impression of severe swelling.

Additionally, an observation that occurred during casting is the formation of GO lines across the membrane. This occasionally arose during casting and the lines of GO formed seemed to

correspond with metal trays inside the oven used for thermal treatment, shown in Figure 4-20 e). The metal tray heats up first resulting in parts of the petri dish in contact with the metal tray also heating. The consequence is that the GO in the areas in contact with the metal tray dry first. A preventative measure involved the placement of the petri dish containing the membrane on top of a glass slide which itself was positioned on top of the metal tray. The glass slide in contact with the metal tray warms up evenly, which allowed the petri dish to heat uniformly.

Subsequently, water was used as the solvent for the middle layer and the membrane swelling dissipated, and resulted in multilayer membranes without any swelling. Furthermore, the third layer casting process was also important as the incorrect solvent could cause swelling within previous layers. To conclude, ethanol was utilised for the first Nafion layer, but the solvent was switched to water for the middle composite layer and the final Nafion layer. For the complete multilayer methodology please refer to Chapter 3.

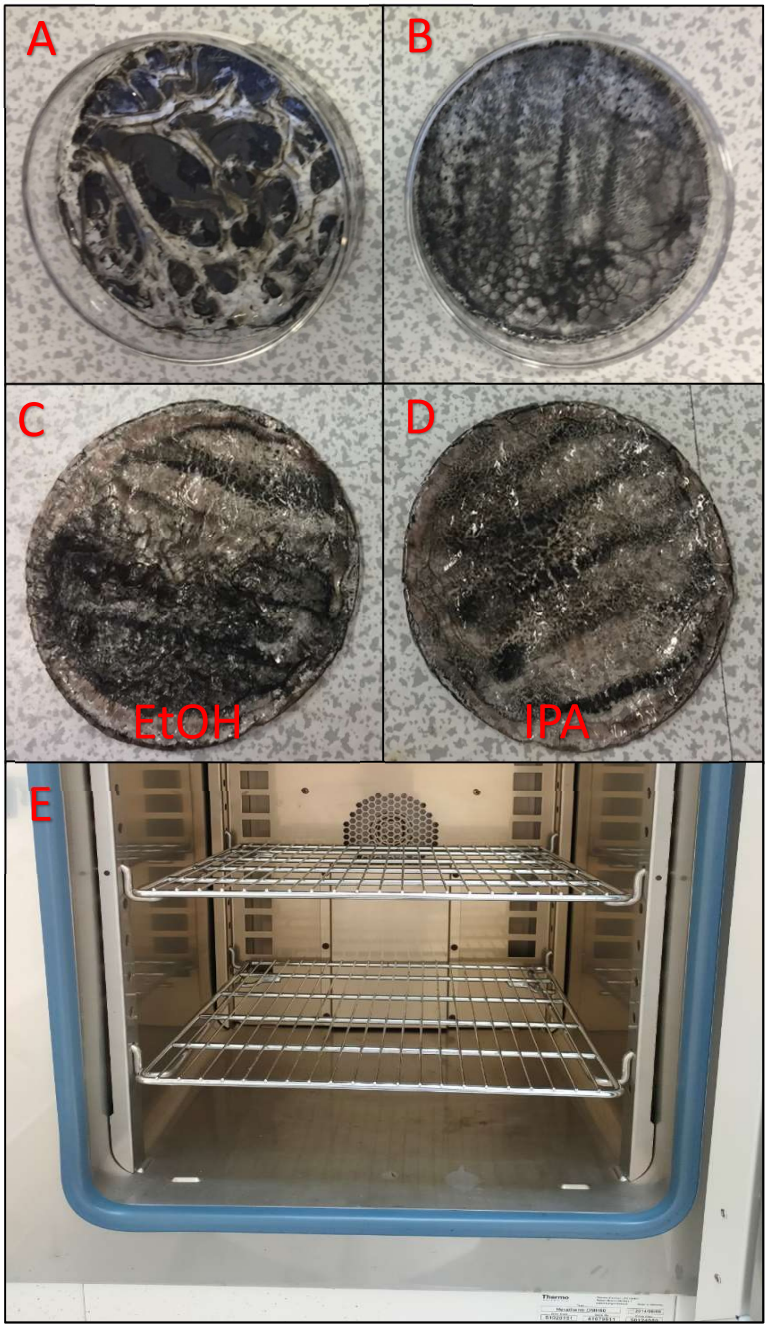



Figure 4-20: Multilayer membrane with a) wells of GO, b) lines of GO, c) multilayer membranes prepared with ethanol and d) isopropyl alcohol, e) inside of oven with metal trays.

### 4.4.2 Influence of activation

Prior to fuel cell testing, multilayer membranes were activated. During activation, occasionally water would get in between the membrane layers and result in bubbles inside the multilayer membrane, as shown in Figure 4-21. This would inevitably compromise the performance and hence these membranes were not used. Figure 4-22 presents some of the membranes prepared, with the cuts on the circumference used to identify the membranes after activation. A ring of GO is observed around the circumference which is due to movement of GO to the outer edge during casting.




Figure 4-21: A Multilayer membrane after activation.

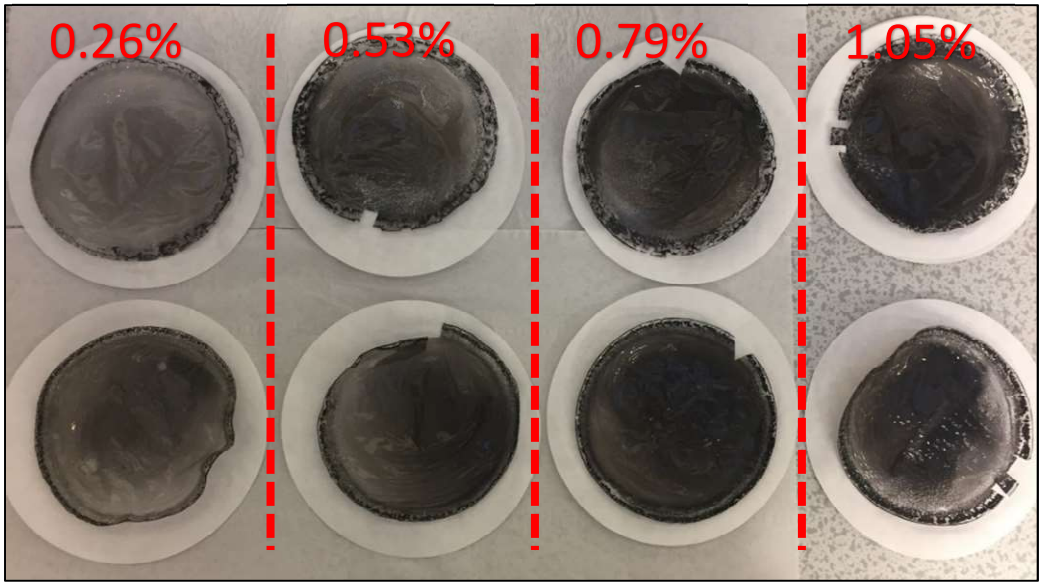



Figure 4-22: Multilayer membranes with varying GO loading.

### 4.4.3 Summary

Multilayer membranes comprising of a layer of Nafion, a composite of Nafion and GO, and a final layer of Nafion were successfully prepared. The choice of solvent was carefully investigated and it was found that water was the most appropriate solvent for the second and third layer as it led to minimal swelling in comparison to ethanol and IPA. Furthermore, activating the multilayer membrane could result in trapped water within the membrane, which would compromise the properties of the MEA produced using this membrane.

## 4.5 Multilayer membrane characterisation

Characterisation of multilayer membranes was performed to confirm the successful introduction of a Nafion-GO middle layer. To add, the influence of GO loading was investigated, with techniques utilised to study the physical structure, thermal behaviour and water uptake properties.

### 4.5.1 Environmental scanning electron microscopy

The environmental electron micrographs of multilayer membranes of varying GO weight percentages are presented in Figure 4-23 to Figure 4-26. All of the membranes have the expected structure of a top and bottom Nafion layer with a middle layer of Nafion and GO. There is a thin layer in the middle of the membrane with a similar appearance as the composite membranes described previously. This implies successful incorporation, with both the top and bottom layer of pure Nafion having similar thickness as well as the same uniform cross section seen in Nafion. However, occasionally some stress can be seen, such as in Figure 4-24, which is an artefact of the freeze cracking process.

With increasing loading of GO, the middle layer displays a more pronounced layering of GO. A line and spot EDX scan were attempted, as seen in Figure 4-27. However, this led to damage of the membrane and hence the scanning was aborted. Overall, the middle layer displayed a structure that was very similar to the composite membrane, with higher magnification micrographs revealing a distinctive layered structure.

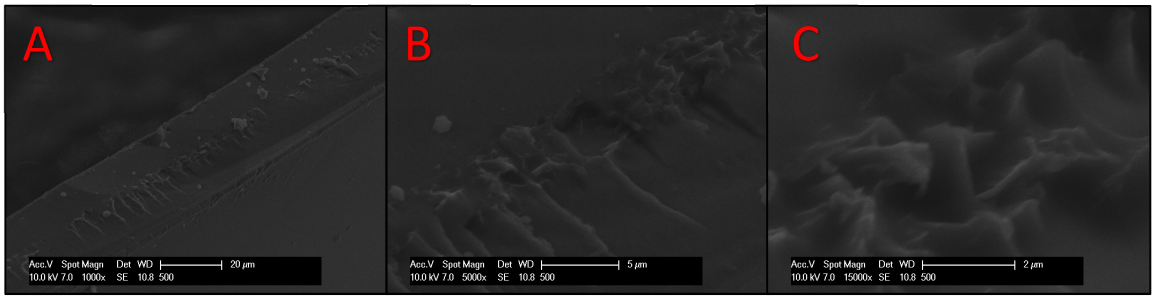



Figure 4-23: ESEM images of ML-GO(0.26) at a magnification of A) 1000, B) 5000, and C) 15,000.

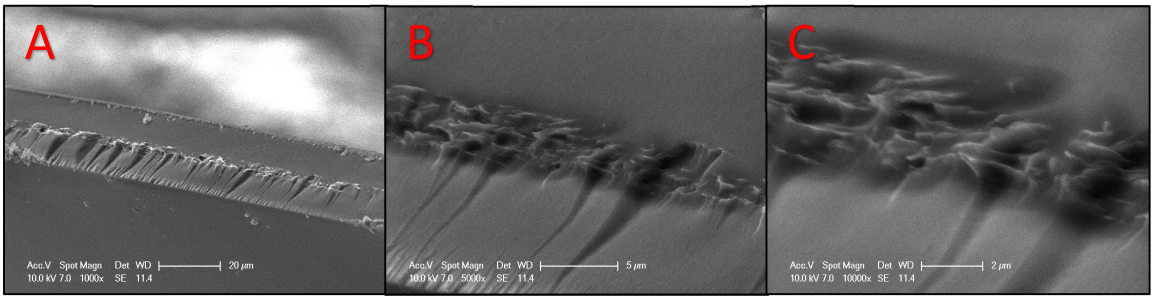



Figure 4-24: ESEM images of ML-GO(0.53) at a magnification of A) 1000, B) 5000, and C) 10,000.

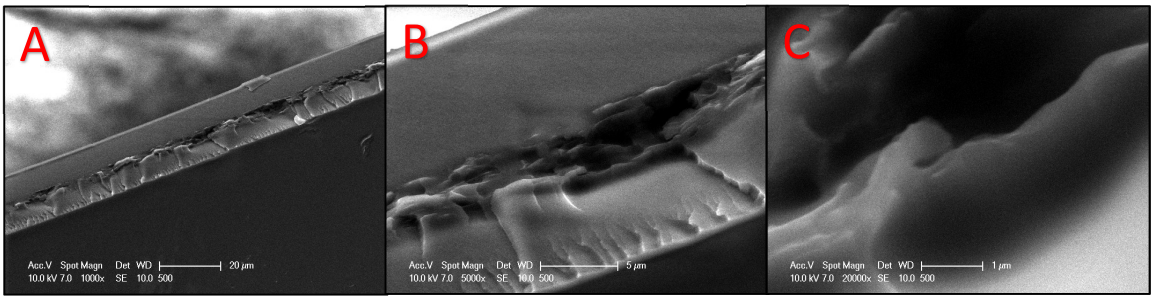



Figure 4-25: ESEM images of ML-GO(0.79) at a magnification of A) 1000, B) 5000, and C) 20,000.

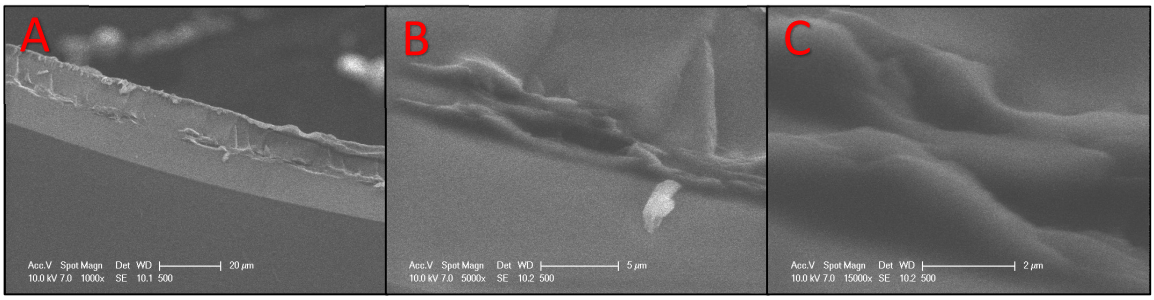



Figure 4-26: ESEM images of ML-GO(1.05) at a magnification of A) 1000, B) 5000, and C) 15,000.

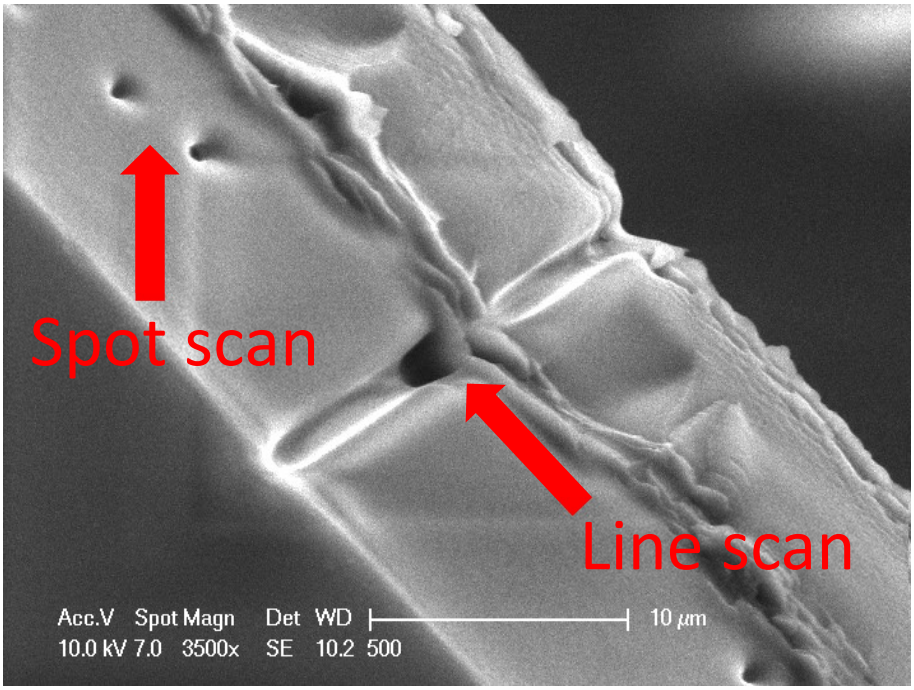



Figure 4-27: Attempted spot and line scan on ML-GO(1.05).

An additional membrane was prepared with a much greater quantity of GO in the middle layer, corresponding to 4.5 wt.%, as shown in Figure 4-28. What can be observed is that the middle layer settled close to the top of the membrane.

This was because the large quantity of GO settled deep into the middle layer during the casting process instead of being suspended in the middle layer. As this was observed close to the top

of the membrane it can be assumed that the sample was characterised upside down. Furthermore, this middle layer displayed a very consistent layered structure similar to that of GO. Thus, there is a maximum amount of GO that can be used without the layer moving away from the middle of the membrane.

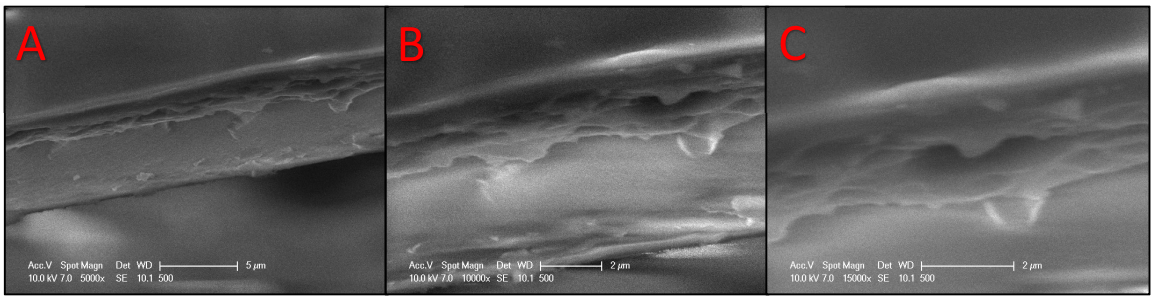



Figure 4-28: ESEM images of ML-GO(4.5) at a magnification of A) 5000, B) 10,000, and C) 15,000.

The asymmetric design of this membrane is highlighted in Figure 4-29. The multilayer membrane ML-GO(4.5) strongly bends, in comparison to the multilayer layer membrane ML-GO(0.79). This is due to the GO layer being closer positioned to one side of the Nafion layer. In this case, the samples were cut after activation and placed between filter paper. This implies that it's the water that is responsible for the difference in behaviour, with the higher GO content responding favourably.

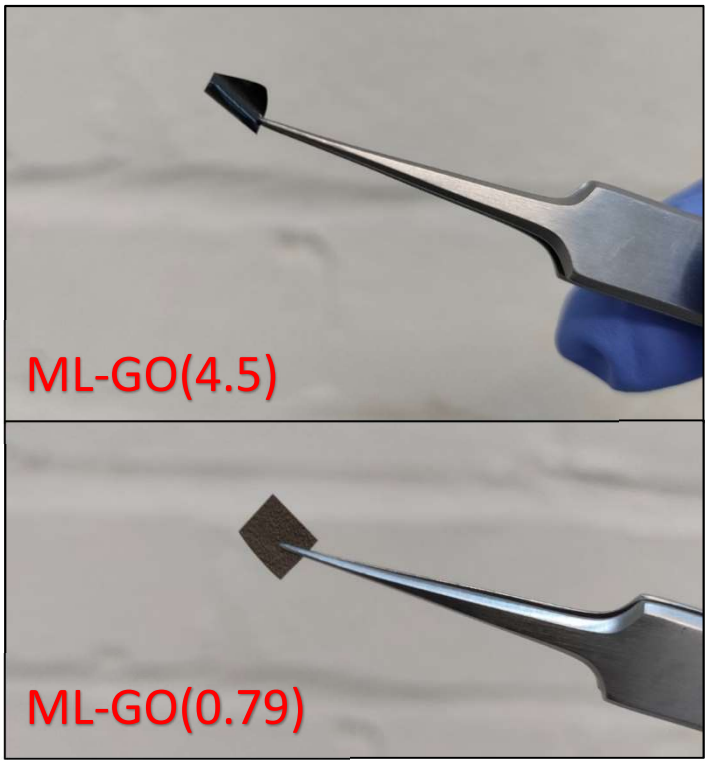


Figure 4-29: Bending in ML-GO(4.5), and no bending in ML-GO(0.79).

### 4.5.2 Thermogravimetric analysis

Thermogravimetric data for the multilayer membranes is shown in Figure 4-30. Fundamentally their thermal behaviour was the same as the composite membranes described previously. This was to be expected as the difference in membrane architecture did not change as the membranes were made from the same materials and therefore still experienced the same thermal decomposition behaviour. However, there were large rates of mass loss from room temperature to 100°C, implying a greater presence of adsorbed water in the membranes, and potentially small amounts of water between the individual layers.

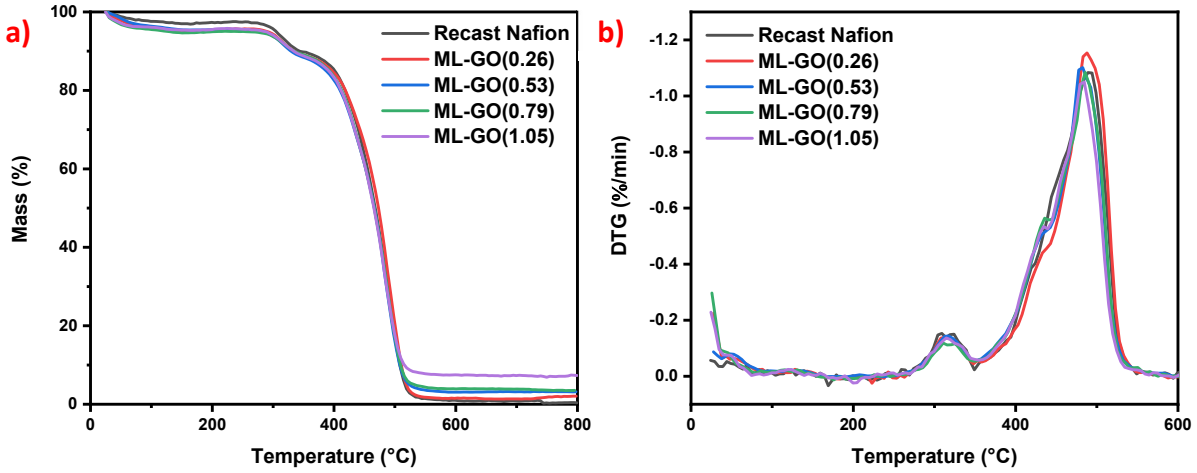



Figure 4-30: a) TGA and b) DTG of multilayer mixed matrix membrane samples.

Table 4-3: Mass loss percentages during different temperature regions for mixed matrix multilayer membrane samples.

| | Mass loss (%) | | |
|---|---|---|---|
| Sample | 0 to 200°C | 200 to 375°C | 375 to 550°C |
| ML-GO(0.26) | 4.6 | 8.1 | 85.5 |
| ML-GO(0.53) | 4.6 | 9.1 | 82.8 |
| ML-GO(0.79) | 5.1 | 7.6 | 83 |
| ML-GO(1.05) | 4.5 | 8.4 | 79.3 |

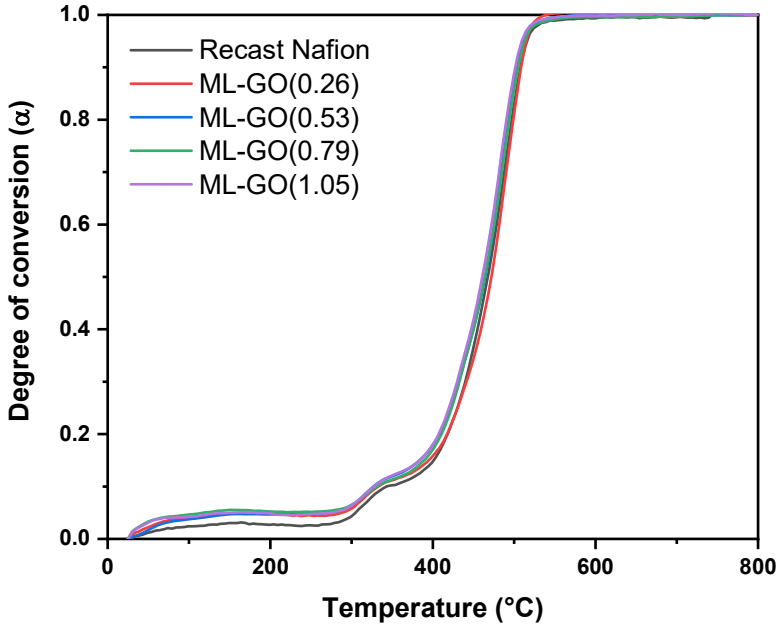


Figure 4-31: Degree of conversion of multilayer mixed matrix membranes.

### 4.5.3 X-ray diffraction and Fourier transform infrared spectroscopy

Figure 4-32 presents the X-ray powder diffractograms of the multilayer membranes. The difference in membrane structure did not change the main findings from the diffractograms, with the multilayer membranes displaying very similar characteristics to the single layer composite membranes. The same broad peak can be identified between 15 and 20°, which is a combination of the amorphous and crystalline scattering from the polyfluorocarbon chains of Nafion, at 2θ values of 16° and 17.5°, respectively[282]. Figure 4-33 presents the FT-IR of the multilayer membranes. The spectra are similar due to the low GO weight loading, which is even lower in the multilayer membranes.

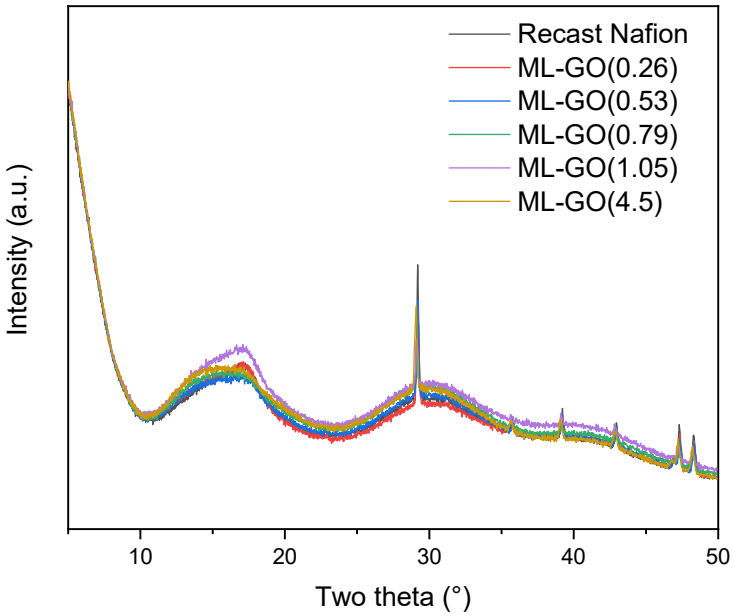



Figure 4-32: XRD patterns of multilayer mixed matrix membranes.

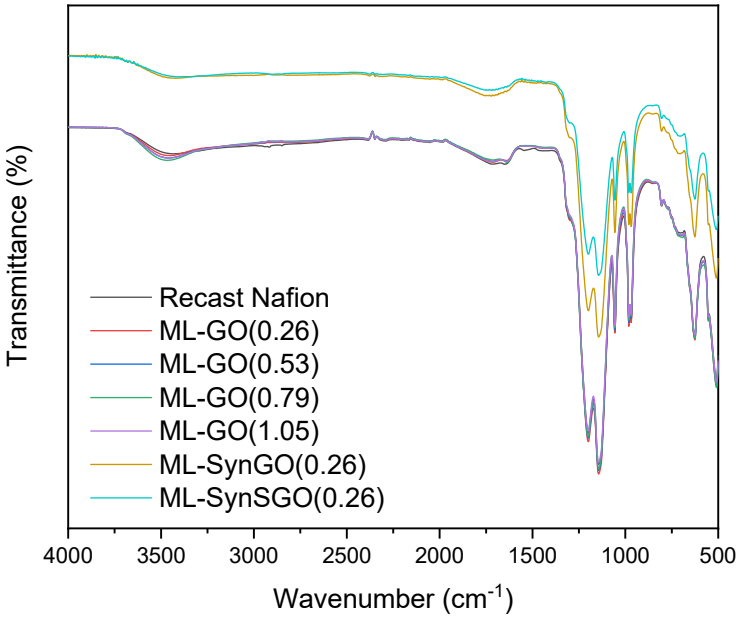



Figure 4-33: FT-IR spectra of multilayer mixed matrix membranes.

### 4.5.4 Water uptake and ion exchange capacity

The water uptake for fabricated multilayer membranes with different quantities of GO in the middle layer is displayed in Figure 4-34. The multilayer samples display a very small increase in water uptake with increasing GO loading. The increase is very small due to the incremental increases in GO loading. The IEC (Figure 4-34) reveals a small increase with GO loading. This

is a combination of the extra GO allowing additional sites for ion exchange as well as potentially some of the solutions during the experiment potentially remaining trapped in the layers.

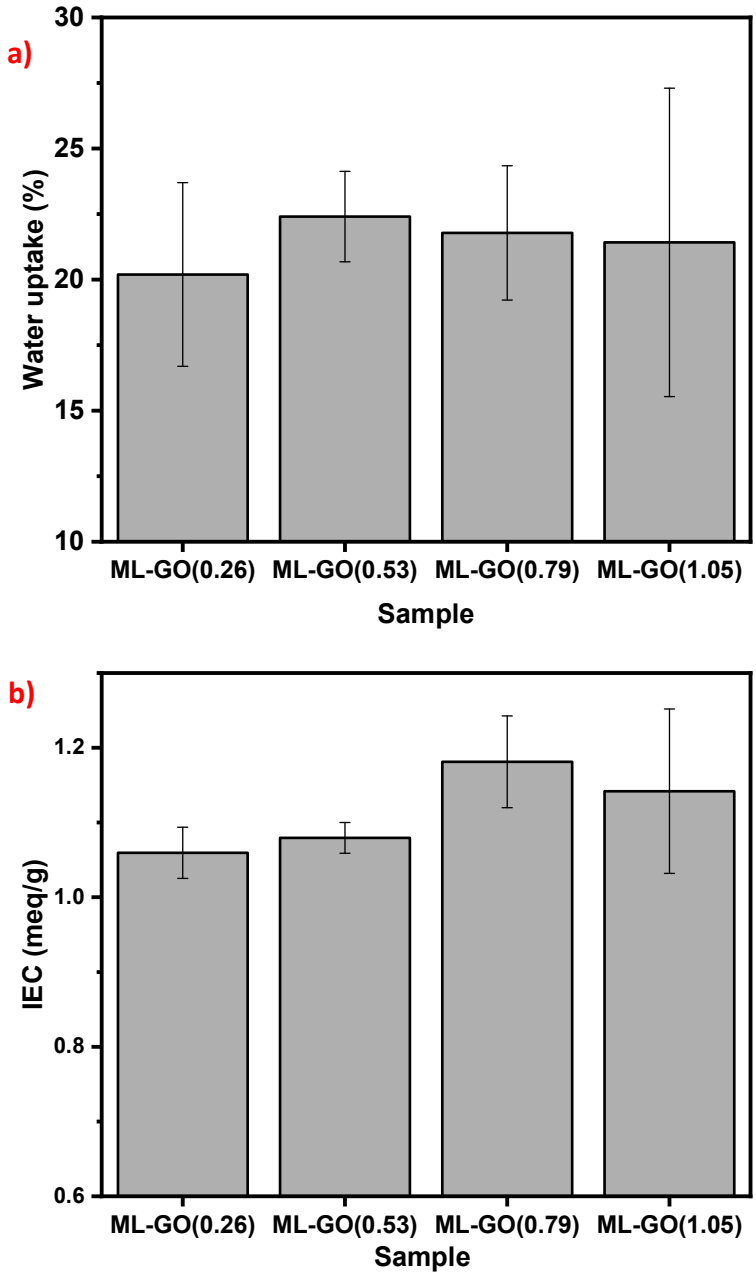



Figure 4-34: a) Water uptake and b) IEC of multilayer membranes.

### 4.5.5 Summary

Characterisation such as ESEM of the multilayer membranes revealed a defined structure consisting of two Nafion outer layers and a GO containing layer in the middle, confirming successful fabrication. However, multilayer membranes with the greatest GO weight percent presented an uneven middle layer due to the high loading. The thermal behaviour of the multilayer membranes showed a similar trend to those of single layer membranes but with a greater water loss at lower temperatures. Finally, water uptake and IEC values slightly increased with GO loading.

## 4.6 Optimised membrane fabrication

Membranes with optimised levels of GO loading of 1.5 wt.% for single layers and 0.26 wt.% for multilayer membranes with a thickness of 30 μm were prepared with the synthesised graphene oxide, as shown in Figure 4-35. The synthesised GO displayed a sponge-like appearance due to it being freeze dried and showed improved dispersibility, with no agglomeration or sedimentation observed. This is likely due to the centrifugation process removing any GO flakes that were too small or large. The prepared membranes showed improved uniformity in GO homogeneity, with no observable agglomeration or presence of regions with uneven Nafion content. However, removing the membranes from the petri dishes proved difficult as the addition of DI water resulted in the membrane beginning to crack and disintegrate, as presented in Figure 4-36. As the Nafion content and fabrication methodology remained unchanged, it was determined that this was due to the higher level of oxidation in the synthesised GO, as proven earlier in XPS and TGA analysis.

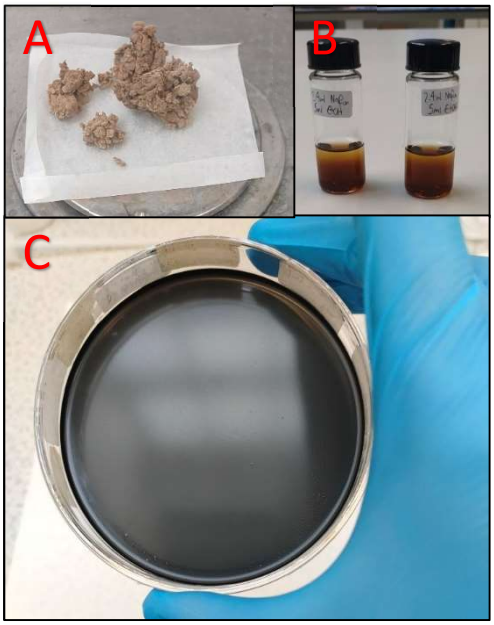



Figure 4-35: Membrane fabrication process: a) SynGO, b) SynGO, Nafion and ethanol dispersions and c) Nafion-SynGO(1.5) membrane.

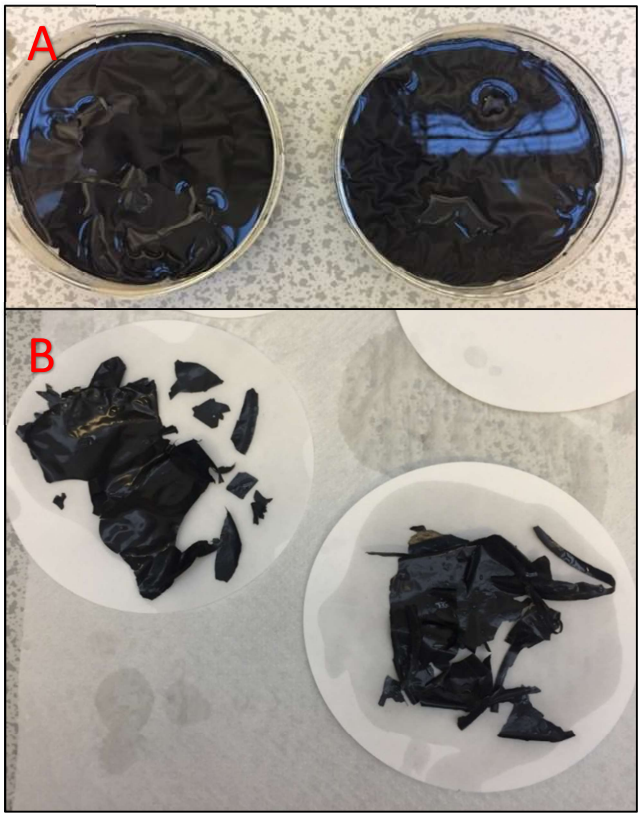



Figure 4-36: a) Cracked membranes and b) Subsequent membranes removed from petri dishes.

Furthermore, previous membranes displayed small regions of higher Nafion content, which could provide more integrity when in contact with water. This is in comparison to the membranes prepared with synthesised GO, which displayed better homogeneity and hence these Nafion rich regions did not appear. Therefore, the thermal treatment process was altered with the annealing temperature increased to 140°C for one hour, instead of 120°C. This alteration was successful and membranes had mechanical integrity and could be easily removed from the petri dish. These membranes are shown in Figure 4-37.

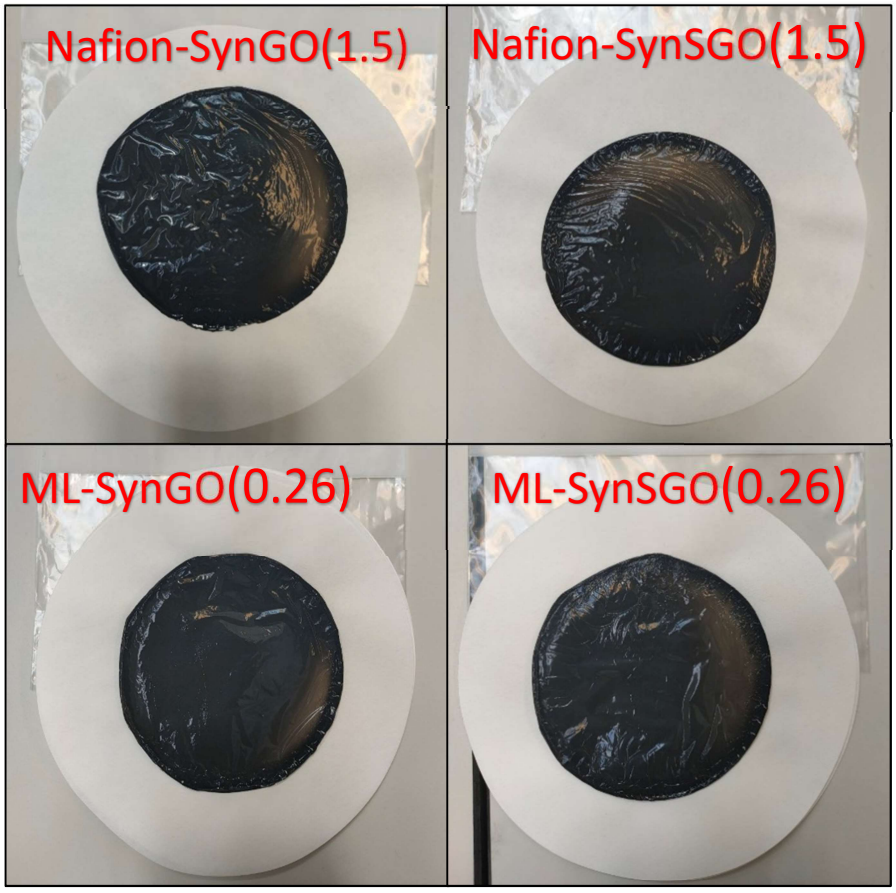



Figure 4-37: Membranes prepared with synthesised GO.

## 4.7 Optimised membranes characterisation

The optimised membranes were characterised to understand if there were any differences between the use of synthesised GO and commercial GO. In particularly, ESEM and Raman spectroscopy were utilised to accurately characterise the influence of GO in the membrane.

### 4.7.1 Environmental scanning electron microscopy

Environmental scanning electron microscopy of the cross sections was performed, shown in Figure 4-38 and Figure 4-39. The Nafion-SynGO(1.5) cross section revealed evenly dispersed GO, with no agglomeration or settling. There was a presence of a Nafion skin layer due to solvent evaporation and the GO was strongly layered with a wrinkled appearance. The ML-SynGO(1.5) cross section displayed similar characteristics for its middle layer, with the outer layers being pure Nafion. Thus, the membranes prepared with synthesised GO achieved improved uniformity. This could be due to the higher oxygen content and the centrifuge process removing GO flakes that are either too small or too big. This produced a homogenous dispersion of similarly sized GO flakes with high oxygen content, which after solvent evaporation became highly uniform.

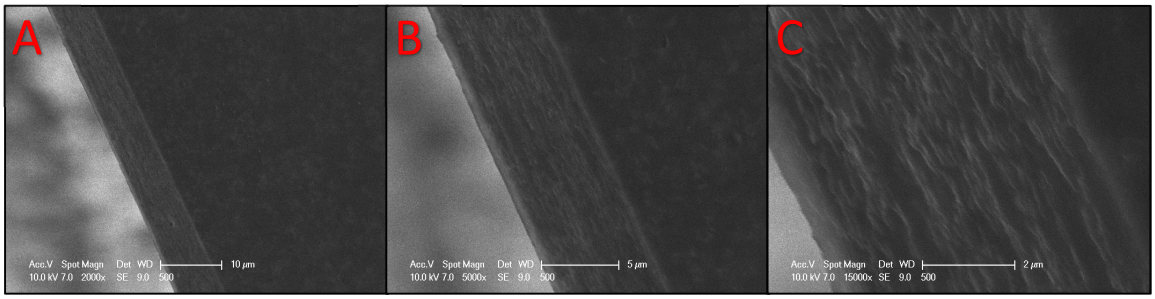



Figure 4-38: ESEM images of Nafion-SynGO(1.5) at a magnification of A) 2000, B) 5000, and C) 15,000.

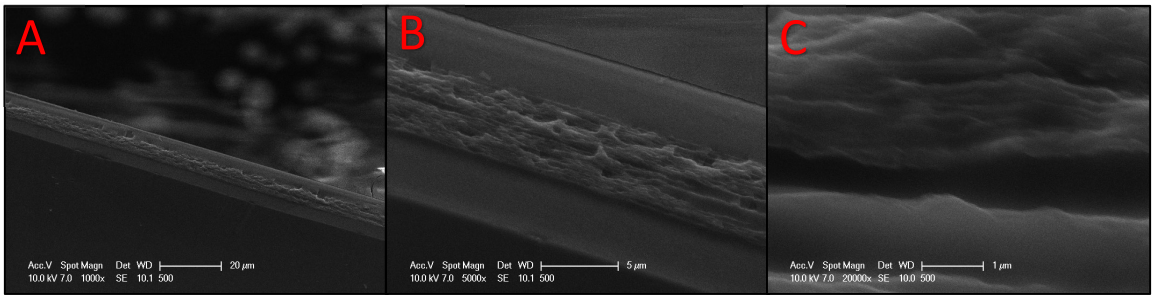



Figure 4-39: ESEM images of ML-SynGO(0.26) at a magnification of A) 1000, B) 5000, and C) 20,000.

### 4.7.2 Raman spectroscopy

To understand more about the differences in GO uniformity, Raman microscopy was performed on all composite and multilayer membranes. Figure 4-40 presents the Raman spectra as well as the microscopy images of the regions that were analysed. The membranes with lower GO loading showed regions of higher Nafion content, such as Nafion-GO(1.5). With increased GO loading, this observation began to disappear to the naked eye. However, Raman spectra for membranes prepared with commercial GO showed weak D and G bands, with only Nafion-GO(1.5) producing distinguishable peaks, and this was not because of low signals. In contrast, the two single layer membranes with synthesised GO and synthesised sulphonated GO both produced defined D and G peaks, even with the lower loading, with intensity ratios of 0.90 and 0.92 for Nafion-SynGO(1.5) and Nafion-SynSGO(1.5) respectively. This was because of the better dispersion throughout the membrane, preventing the formation of Nafion dense regions, which do not give a signal. On the other hand, all multilayer membranes failed to produce any D or G peaks, as seen in Figure 4-41. This was because the GO content was far too low. In addition, the use of commercial GO clearly showed non-uniformity in ML-GO(1.5) and ML-GO(3), for example. FT-IR analysis of both single layer and multilayer membranes could not identify any peaks consistent to those found in GO (Figure 4-18 and Figure 4-33).

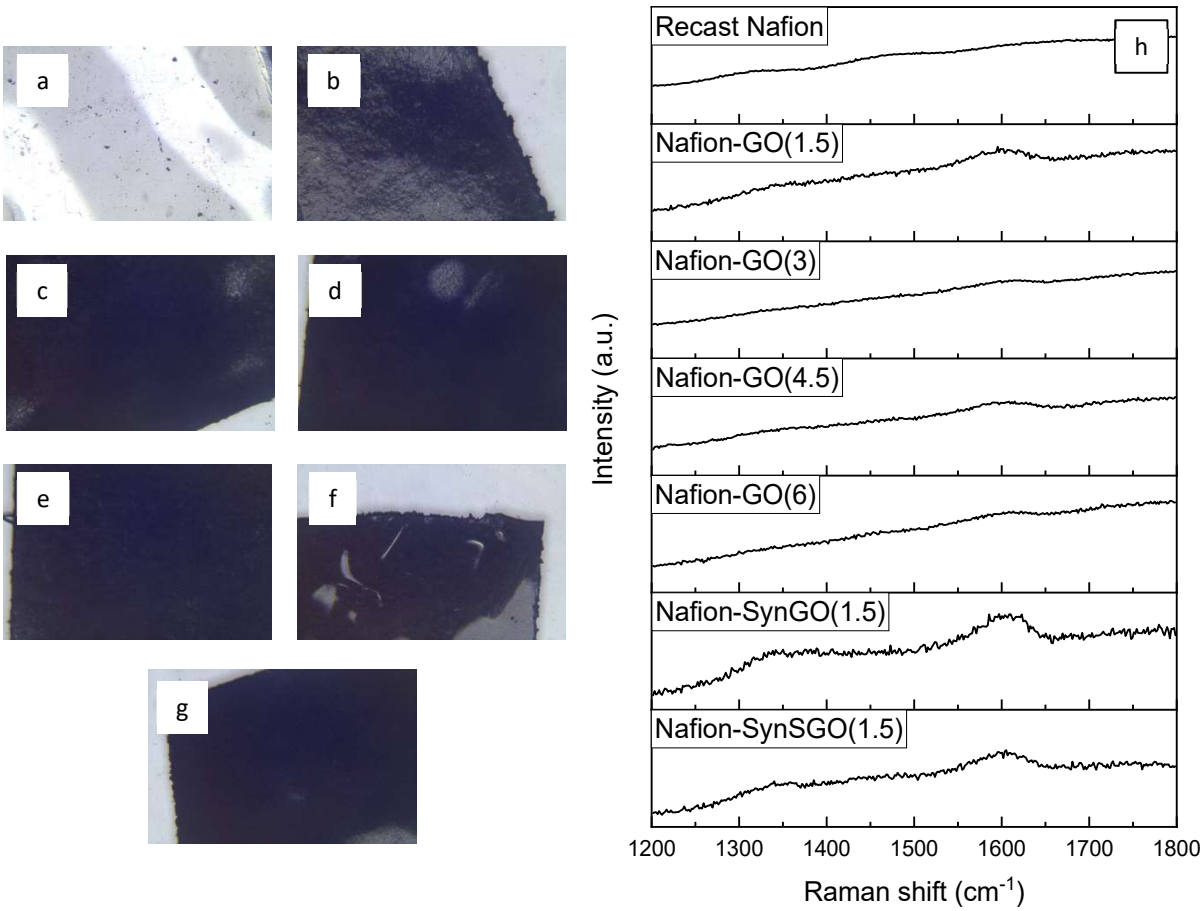



Figure 4-40: a-g) Raman microscopy images of Recast Nafion, Nafion-GO(1.5), Nafion-GO(3), Nafion-GO(4.5), Nafion-GO(6), Nafion-SynGO(1.5) and Nafion-SynSGO(1.5), and h) Raman spectra.

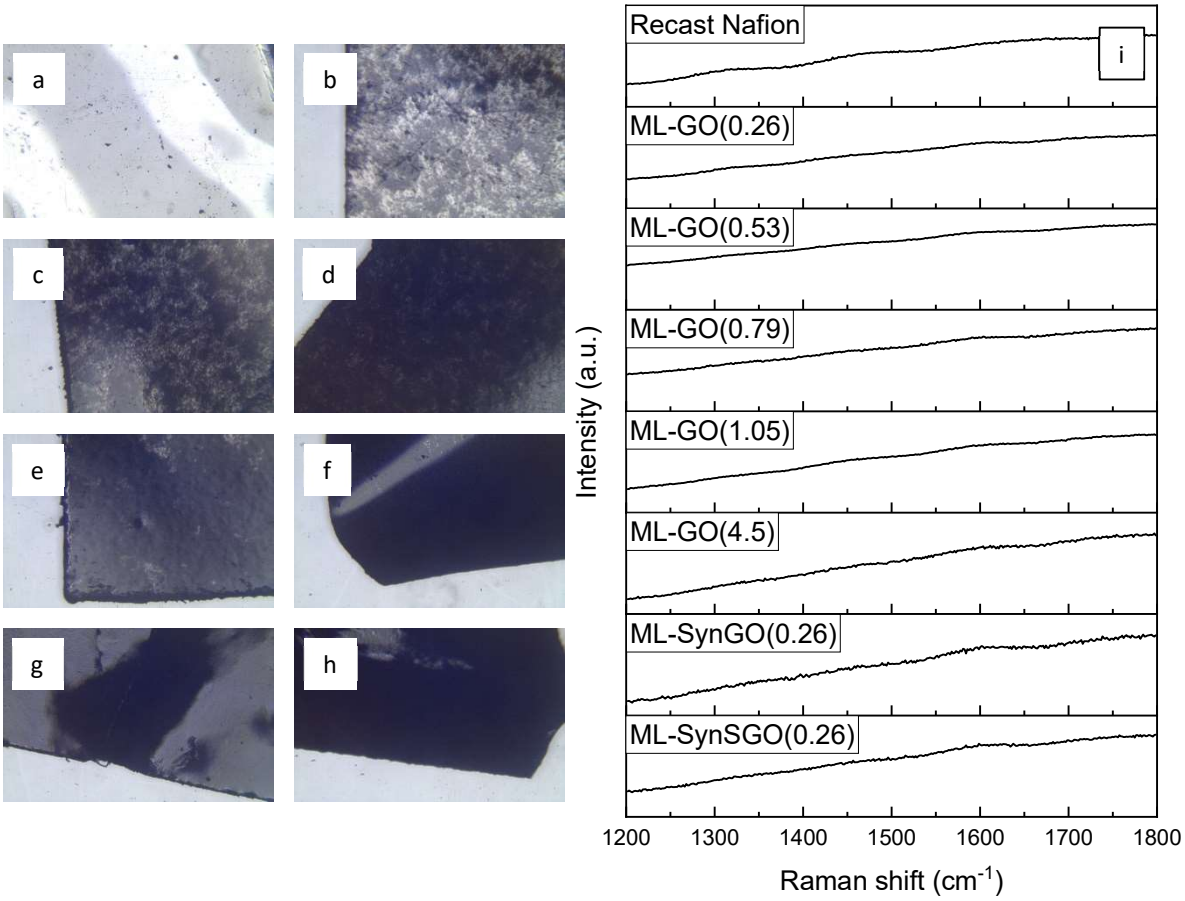



Figure 4-41: a-h) Raman microscopy images of Recast Nafion, ML-GO(0.26), ML-GO(0.53), ML-GO(0.79), ML-GO(1.05), ML-GO(4.5), ML-SynGO(0.26) and ML-SynSGO(0.26), and i) Raman spectra.

### 4.7.3 Mechanical testing

The mechanical behaviour was investigated by applying a tensile force on recast Nafion and Nafion-SynGO membranes, as shown in Figure 4-42. A single membrane type was tested as the tensile force applied in this experiment was not translatable to the mechanical forces experienced inside the fuel cell. This is because the membrane inside the MEA of a fuel cell swells when saturated with water and contracts when dry due to the expansion and contraction of water channels that are formed. On the other hand, this experiment produces tensile strain in one direction only. However, this is still a somewhat useful measure of a membrane's mechanical strength and more realistic tests can be performed, such as in-situ mechanical cycling. The recast Nafion membrane expectedly produced a large strain due to its polymeric nature. With addition of graphene oxide, the maximum produced stress increased, from 12.73 MPa for recast Nafion to 18.20 MPa for Nafion-GO(4.5). This was because the GO filler provided mechanical reinforcement to the membrane. At the same time, the reinforcement restricted the elongation of the Nafion chains while under tensile strain, with the maximum strain reducing from 2.35% for recast Nafion to 0.31% for Nafion-GO(4.5).

Interestingly, Nafion-GO(1.5) did not follow this trend, producing a higher strain than Nafion (3.01%). This is explained with the low GO loading (1.5 wt.%) and full exfoliation and dispersion of GO within the polymer membrane. This combination resulted in later sample failure as there were not large areas of GO to act as a potential breaking point, until greater loadings. Nafion-GO(6) was attempted to produce but proved to be too brittle.

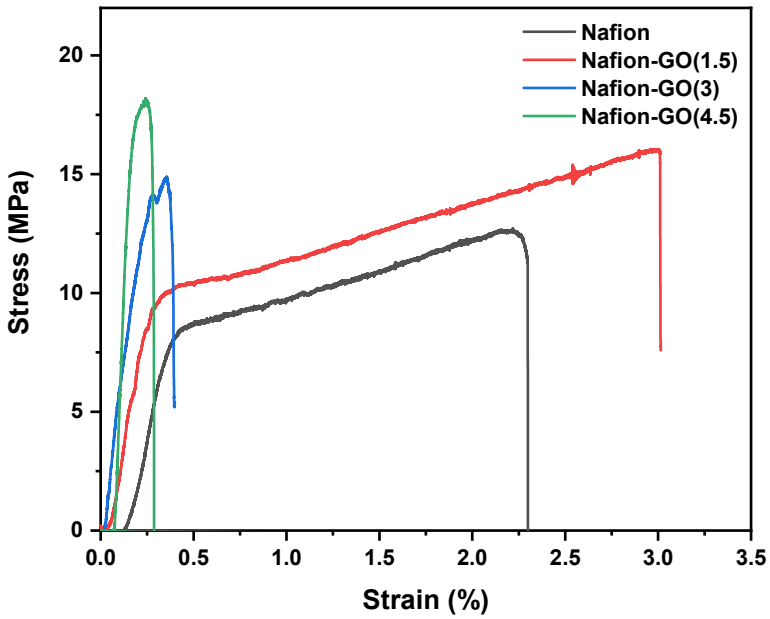


Figure 4-42: Stress-strain curves of single layer mixed-matrix membranes.

### 4.7.4 Summary

Single and multilayer membranes prepared with synthesised GO showed greater uniformity and dispersion, as confirmed via ESEM and Raman spectroscopy. However, the membrane required annealing at 140°C due to disintegrating when in contact with water. Mechanical testing with single layer membranes revealed that there was a general trend of increasing tensile strength at the expense of maximum elongation with increasing GO content.

### 4.7.5 Progress assessment and best practices

It is recommended that in order to produce robust single layer composite membranes, water (from the Nafion dispersion) and ethanol (5 ml) are used as the casting solvent for two reasons. Firstly, water-alcohol produced Nafion membranes with higher proton conductivities[254]. Secondly, the lower boiling point will create a slower evaporation of solvent and less vigorous boiling, which could interfere with the uniformity of GO. Furthermore, the boiling point should not be too high that the GO filler begins to lose oxygen functional groups. To add, the use of a

glass slide between the oven trays is suggested to prevent any uneven heating of the petri dish that can produce nonuniform GO.

For the fabrication of multilayer membranes, it is recommended that the second and third casting solvent is wholly water to prevent swelling of the previous layers. Furthermore, multilayer membranes after activation should be carefully inspected for trapped liquid between the individual layers. Finally, it is suggested that the sample for fuel cell testing is taken from the centre of the membrane to prevent deviations in thickness.

## 4.8 Conclusions

- Synthesised GO and SGO were successfully prepared, with the synthesised GO (C/O ratio of 2.95) having a higher oxygen content than that of commercial GO (C/O ratio of 3.8).
- Single layer and multilayer composite membranes were produced with varying GO content. Incorporation was confirmed with a variety of characterisation techniques such as ESEM and TGA. Increasing GO weight content led to increased water uptake and IEC.
- Finally, membranes prepared with synthesised GO had improved GO uniformity throughout the membrane structure.

# 5 In-situ performance testing

Single layer and multilayer membranes that were fabricated and characterised ex-situ were tested in-situ in a single cell system and their performance assessed. Electrochemical characterisation techniques such as polarisation curves, electrochemical impedance spectroscopy, and hydrogen crossover were utilised to assist in understanding the influence of GO loading, operating temperature and membrane thickness. Finally, fuel cell performance was compared to results reported in literature[16].

## 5.1 Single layer Nafion-GO membrane

Single layer Nafion and GO composite membranes with varying GO weight loadings of 1.5, 3, 4.5 and 6 wt.% were prepared for fuel cell testing. Additionally, composite membranes consisting of 4.5 weight percent of GO were fabricated with varying thicknesses of 50, 40 and 30 μm. A summary of the samples tested in this section is presented in Table 5-1.

Table 5-1: Summary of single layer composite membranes tested.

| Membrane sample | Thickness (μm) | GO source |
|---|---|---|
| Recast Nafion | 50, 40 and 30 | N/A |
| Nafion-GO(1.5) | 50 | Commercial (Sigma Aldrich) |
| Nafion-GO(3) | 50 | Commercial (Sigma Aldrich) |
| Nafion-GO(4.5) | 50, 40 and 30 | Commercial(Sigma Aldrich and Nanoinnova) |
| Nafion-GO(6) | 50 | Commercial (Sigma Aldrich) |

[16] Parts of this chapter are based on the publication: Ahmed Ibrahim, Oheen Hossain, Jagjit Chaggar, Robert Steinberger-Wilckens and Ahmad El-Kharouf. GO-Nafion composite membrane development for enabling intermediate temperature operation of polymer electrolyte fuel cell. International Journal of Hydrogen Energy 45 (8) (2020) 5526-5534. Doi: 10.1016/j.ijhydene.2019.05.210. Some of the data has been re-analysed and re-formatted since publication.

### 5.1.1 Influence of GO loading and temperature

Nafion and Nafion composite membranes were tested in a fuel cell setting to understand the influence of GO, its weight loading and the operating temperature. It was hypothesised that the use of GO would improve proton conduction, retain more water and thus improve fuel cell performance at elevated temperatures. Prior to assembly, the membranes were measured and had an average thickness of ± 5 μm of the required membrane thickness (50, 40 and 30 μm).

#### 5.1.1.1 Polarisation curves

Polarisation and power curves of Nafion and composite membranes are displayed in Figure 5-1. Additionally, achieved current densities and power densities at 400 mV are shown in Figure 5-2 for simplicity. It can be observed that the addition of GO reduced the maximum current density and maximum power produced. The order in performance was as follows: Nafion, Nafion-GO(1.5), Nafion-GO(4.5), Nafion-GO(3), Nafion-GO(6). The Nafion-GO(4.5) produced a slightly greater maximum current density and peak power than Nafion-GO(3). This was assumed to be due to the agglomeration of the GO in the composite membranes. However, comparing the smallest amount of GO loading (1.5%) with the largest (6%), a trend can be observed, as any amount of GO had a detrimental effect on performance. The incorporation of GO, especially more agglomerated GO, created regions of pure GO that suppressed proton conduction. Bayer et al.[184] tested a pure GO membrane that only produced a maximum power density of 35 mW $cm^{-2}$, and thus it can be explained that the addition of GO reduced the current and power density.

Compared to the recast Nafion, the introduction of GO had a clear effect on the ohmic region in the polarisation curve, with estimated ohmic losses smallest for the recast Nafion and largest for the Nafion-GO(6). This was not because the GO had thermally reduced, as prior TGA

experiments revealed that GO only lost absorbed water prior to 130°C. Hence, the GO filler increased the resistance of the conduction of ions through the membrane.

At 100°C and 120°C, the current and power density was reduced as the membranes experienced drying, thus removing water that was essential for proton transport. The order of performance of the membranes remained consistent to that at an operating temperature of 80 °C. Hence increases in GO loading combined with the higher temperature resulted in greater ohmic losses.

However, the composite membranes experienced very little change in current density and power density from 100 to 120°C, whereas the recast Nafion experienced a noticeable reduction. It was shown in water uptake measurements earlier in Chapter 4 that the composite membranes took up more liquid water than recast Nafion and this could be responsible for the minor change in performance at these temperatures, as the GO retained a larger proportion of water.

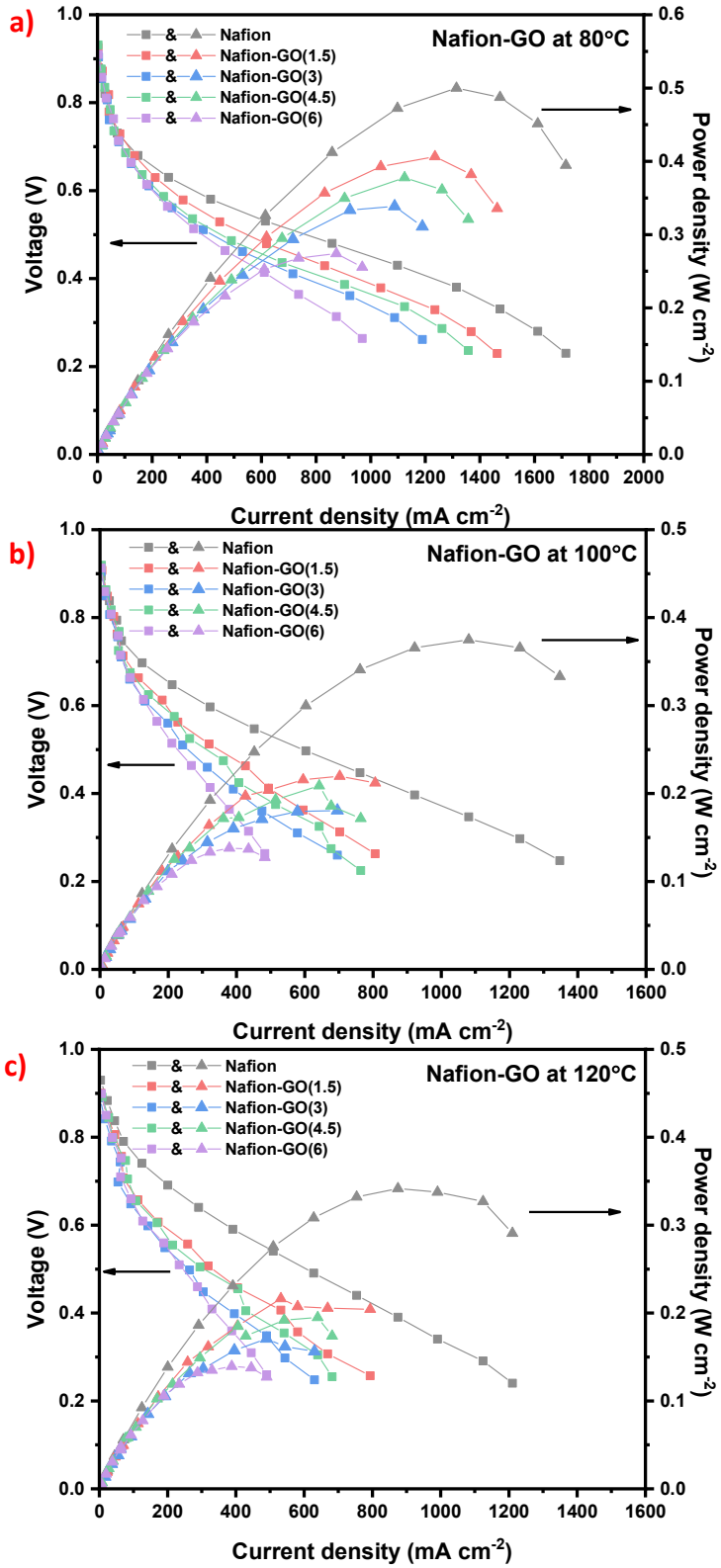



Figure 5-1: Polarisation and power curves of single layer membranes at 80, 100, and 120°C.

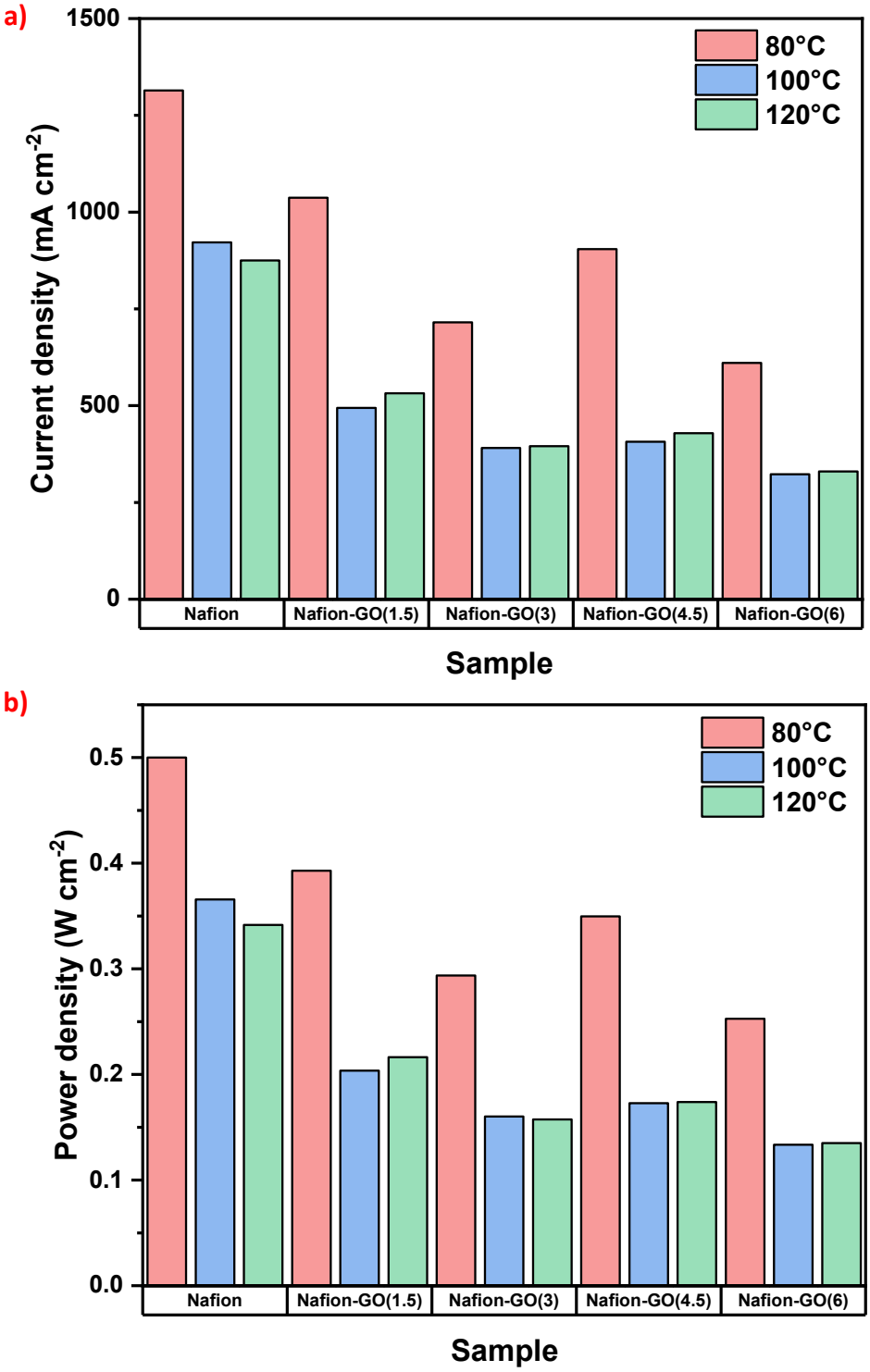



Figure 5-2: a) Current density, and b) power density at 400 mV achieved by single layer membranes at 80, 100 and 120°C.

#### 5.1.1.2 HFR

An example Nyquist plot and the subsequent HFR values achieved from EIS are presented in Figure 5-3. The x-intercept at the beginning of the semi-circle correspond to the HFR resistance value used. With increasing GO loading, the individual Nyquist plots shift to the right, resulting in an increased HFR value, indicating that the sample had a higher resistance. This agrees with the prior polarisation curves that reveal large deviations in the ohmic region of the composite samples, as the GO caused a decrease in proton conduction. Increasing the fuel cell temperature also increased the HFR, as the presence of water is required for effective proton conduction. As a consequence, higher HFR values result in large drops in fuel cell performance.

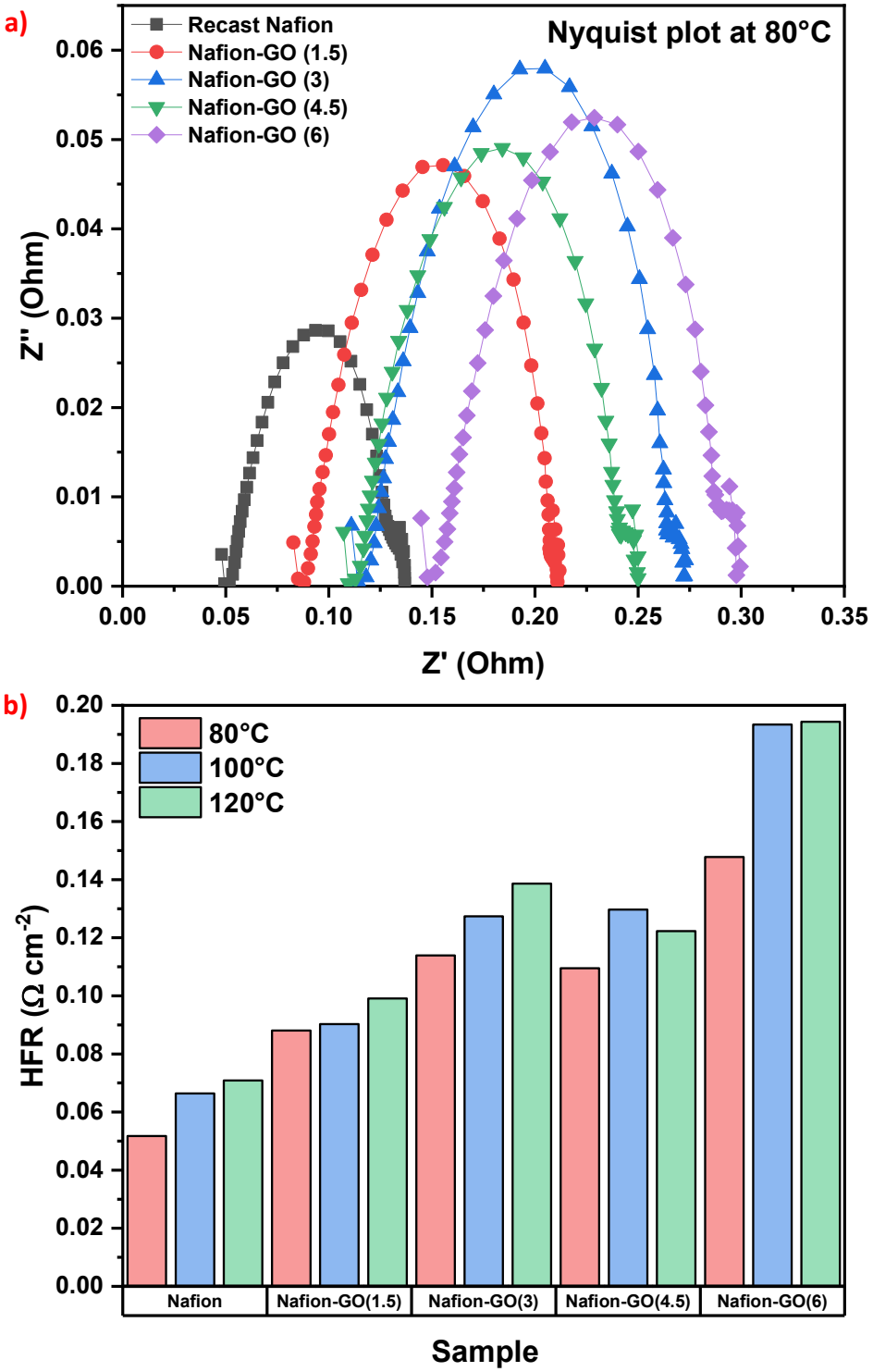



Figure 5-3: a) Nyquist plot, and b) high frequency resistance of single layer membranes at 80, 100 and 120°C.

#### 5.1.1.3 Hydrogen crossover

The hydrogen crossover values of the composite membranes are recorded in Figure 5-4. At 80°C, hydrogen crossover was not prominent as the water pathway channels through the membrane were still saturated and the membrane was not at risk of drying. Nafion-GO(4.5) and Nafion-GO(6) membranes exhibited crossover values less than half of that of recast Nafion, but the Nafion-GO(1.5) and Nafion-GO(3) membranes experienced slightly higher crossover values.

However, at 100°C, the membrane within the MEA dried, and the non-bound water evaporated. Subsequently, the hydrogen crossover increased in all membranes. Here, the increase in GO loading and the subsequent decrease in hydrogen crossover was strongly correlated. Increasing the operating temperature to 120°C ensured that the membrane was close to dry and the Nafion sample experienced a drastic increase in crossover, experiencing an increase from just under 5 mA $cm^{-2}$ to 11 mA $cm^{-2}$. In comparison, the composite membranes showed a much smaller increase in hydrogen crossover. Hence, GO loading and hydrogen crossover were highly correlated.

The incorporation of GO in the polymer matrix introduced a more tortuous path, which should increase the diffusion length, hence decrease hydrogen crossover and this crossover should decrease with increasing filler loading. Furthermore, increases in temperature resulted in an increase in the thermal kinetic energy of hydrogen as well as relaxation in the Nafion polymer chain, increasing the free volume, which is countered with the presence of GO.

Hydrogen crossover through dense membranes involves dissolution into the matrix, diffusing through the electrolyte membrane, and the eventual desorption onto the cathode, as shown in Figure 5-5. However, Nafion has regions of free volume as a result of the packing of the

polymer chains and side chain groups. Hence, within the Nafion, the hydrogen will have to diffuse through open space before dissolving into the solid phase.

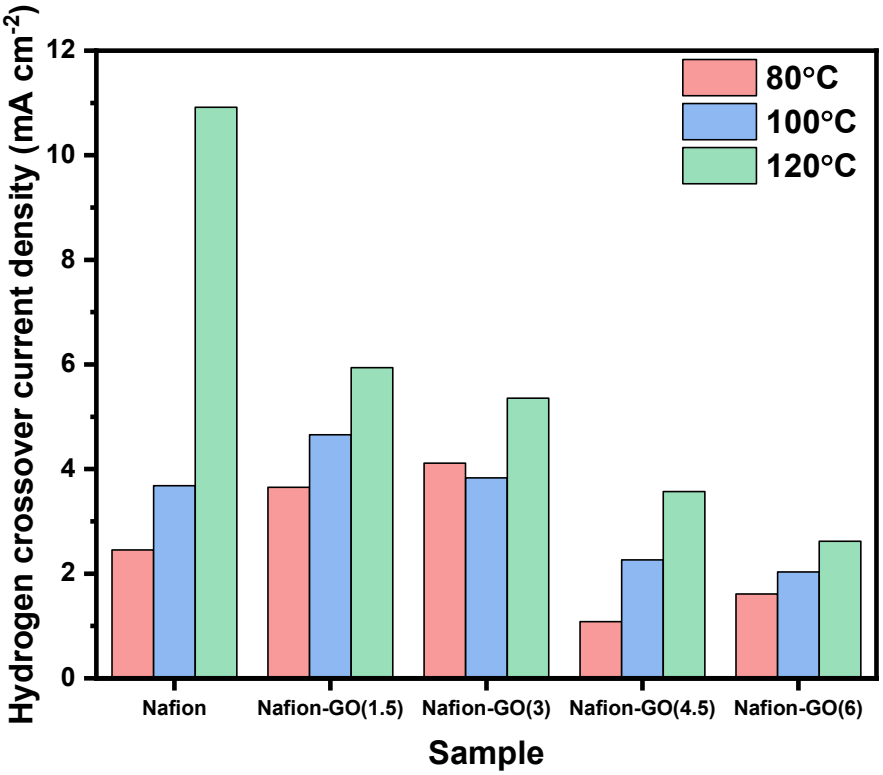



Figure 5-4: Hydrogen crossover current densities produced by single layer membranes at 80, 100 and 120°C.

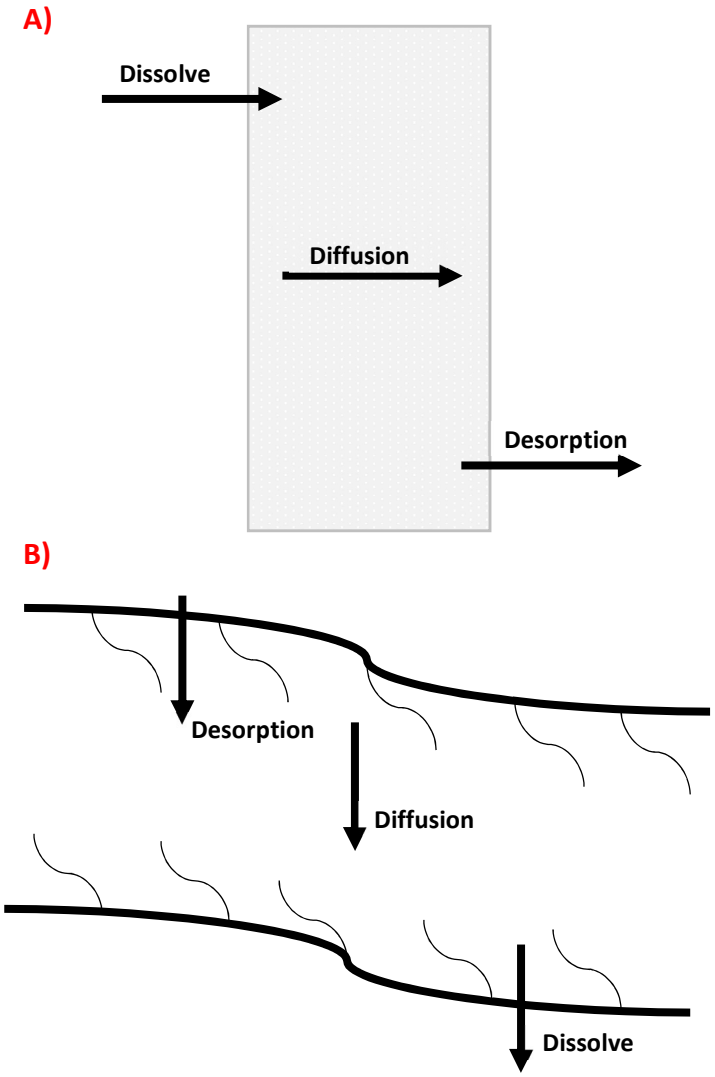



Figure 5-5: A) Hydrogen transport through a dense Nafion membrane, and B) Hydrogen transport between Nafion chains.

The addition of GO into Nafion and the subsequent hydrogen transport mechanism is presented in Figure 5-6. The presence of GO increases the tortuosity and the diffusion distance. Hydrogen can also adsorb onto the surface of GO and travel along the surface before desorption. Furthermore, the use of probe sonication can produce pores in the GO, through which hydrogen can travel, if not absorbed[283]. Thus, all these possible scenarios help to decrease hydrogen crossover.

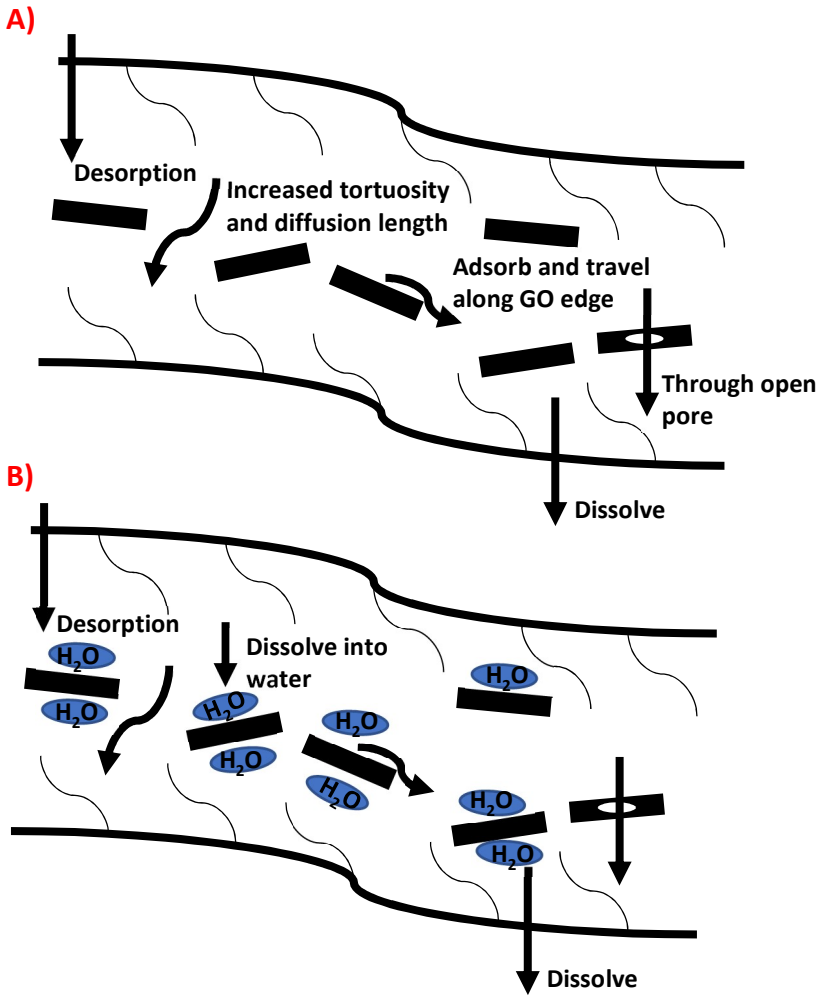



Figure 5-6: A) Hydrogen transport through Nafion-GO and B) Hydrogen transport between hydrated Nafion-GO chains.

Furthermore, the presence of humidity in the membrane produces the water chains along the Nafion's sulphonic side chains. Hence, hydrogen can dissolve into these regions and the transport becomes a "mixed pathway", with transport through free volume and water, as initially presented by Schalenbach et al.[284]. Additionally, humidity-induced swelling increases the thickness of the membrane, and therefore a further increase to the diffusion length. However, this can also reduce the size-sieving effect due to larger chain mobility, the presence of GO restricting the mobiliy.[285,286]. Consequently, GO is a very effective hydrogen blocking filler.

#### 5.1.1.4 Summary

Membranes consisting of recast Nafion and composite membranes were successfully tested in-situ. Introduction of GO led to a reduction in current and power density due to regions of GO limiting proton conduction, strongly observed in the ohmic region and with increased HFR. GO considerably reduced hydrogen crossover at 100 and 120°C, due to increases in the diffusion pathway for hydrogen, countering the hydrogen's increased thermal kinetic energy. Finally, increasing the operating temperature also reduced polarisation performance as a consequence of water removal, however the presence of GO reduced the decrease in current density in comparison to recast Nafion because of greater water uptake.

### 5.1.2 Influence of membrane thickness

Nafion and Nafion-GO membranes with thicknesses of 50, 40 and 30 µm were prepared and tested in-situ. The GO weight loading was fixed to 4.5 wt.%. The aims were to observe the effect of reducing membrane thickness on fuel cell performance, and whether the use of GO could alleviate the negative consequences of reducing membrane thickness.

#### 5.1.2.1 Current and power density

Current and power densities achieved at 400 mV are recorded in Figure 5-7. The maximum power density was achieved at 100°C. This was due to the reduction in mass transport losses stemming from the presence of single-phase water, and not two phases of water. This was also observed in maximum current density measurements[287]. Furthermore, the GO utilised was from Nanoinnova, and had a greater oxygen content. This difference resulted in an increase in performance from 80 to 100°C, instead of a drop which was seen in membranes with varied GO loading from Sigma Aldrich. This led to less agglomeration and regions of high GO which could compromise the performance.

Reducing the thickness of the membrane in the MEA led to in an increase in performance, due to the decrease in membrane thickness allowing for faster water back diffusion and removal from the cathode, preventing mass transport losses. Additionally, less thickness lowers the ohmic resistance.

Recast Nafion of a thickness of 50 µm displayed higher performance than its composite counterpart. However, composite membranes achieved a greater maximum power output for the 40 and 30 µm membranes, in comparison to the recast Nafion MEAs of the corresponding thickness, implying that the use of GO was more effective at lower membrane thickness due to preventing higher hydrogen crossover.

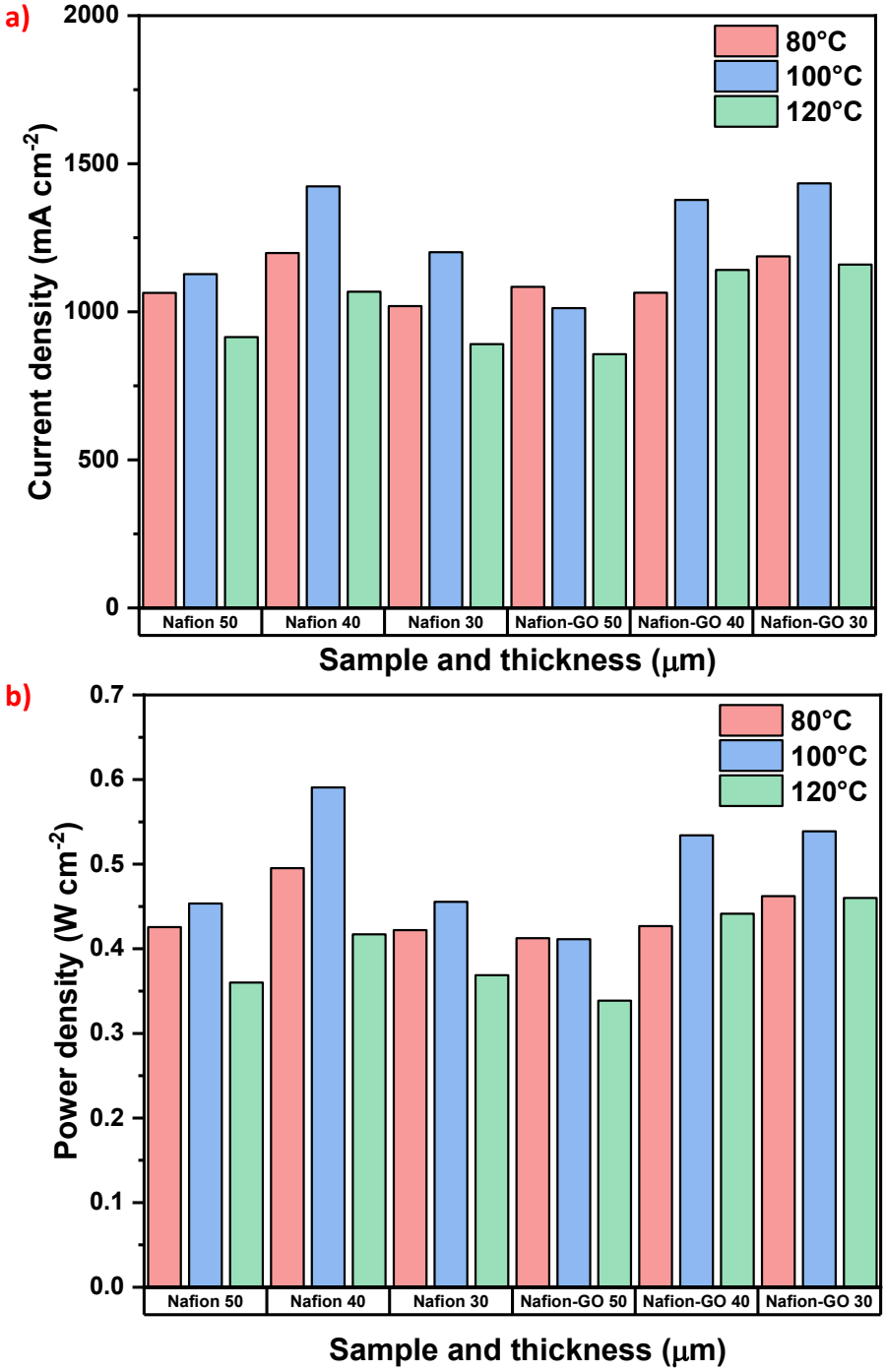



Figure 5-7: a) Current density, and b) power density achieved at 400 mV by recast Nafion and Nafion-GO(4.5) membranes of 50, 40 and 30 μm thickness

#### 5.1.2.2 HFR

HFR values were calculated and are presented in Figure 5-8. Increased membrane thickness led to an increase in the HFR value and thus thicker membranes experienced greater ohmic loss. This can be observed in the resistivity equation ( 12 ) , where increasing the value of $L$, increases the resistance.

$$R = \rho \frac{L}{A} \quad (12)$$

Where $R$ is the resistance, $\rho$ the resistivity, $L$ the length and $A$ the active area.

Increasing the operating temperature increased the HFR values, which was also previously observed. However, the use of GO led to small increases in HFR compared to their Recast Nafion counterpart, at the same temperature. These increases were smaller than observed for the composite membranes with varying loading presented previously. This was due to the GO being less agglomerated and better dispersed throughout the membrane, in comparison to prior membranes prepared with GO from Sigma Aldrich, preventing the formation of heavy GO regions that are detrimental to performance.

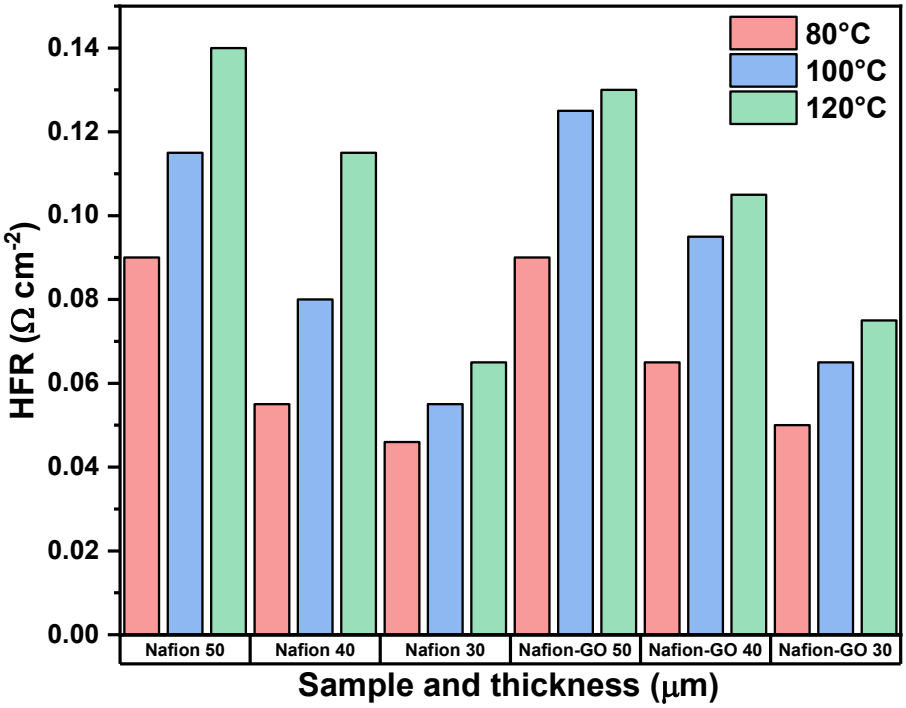



Figure 5-8: HFR values achieved by recast Nafion and Nafion-GO(4.5) membranes of 50, 40 and 30 μm thickness.

5.1.2.3 OCV

OCV values of Nafion and Nafion-GO(4.5) membranes are presented in Figure 5-9. Recast Nafion experienced larger drops in OCV with temperature, and this was further emphasised with the thinner membranes, with the recast Nafion achieving an OCV just above 0.8 V at 120°C. This was due to a combination of increased hydrogen crossover and shrinkage of the membrane. In contrast, the OCV for the 40 μm and 50 μm composite Nafion-GO(4.5) membranes was almost the same with temperature, and there was a small drop in OCV for the 30 μm membrane. As previously shown, GO can reduce potential hydrogen crossover at elevated temperatures, and this was still possible with thinner membranes. In comparison to previous results of membranes with varying thicknesses, it was observed that reducing the thickness of the membrane had a positive effect on performance and that the subsequent increase in hydrogen crossover was mitigated with the use of GO, as reflected in the OCV.

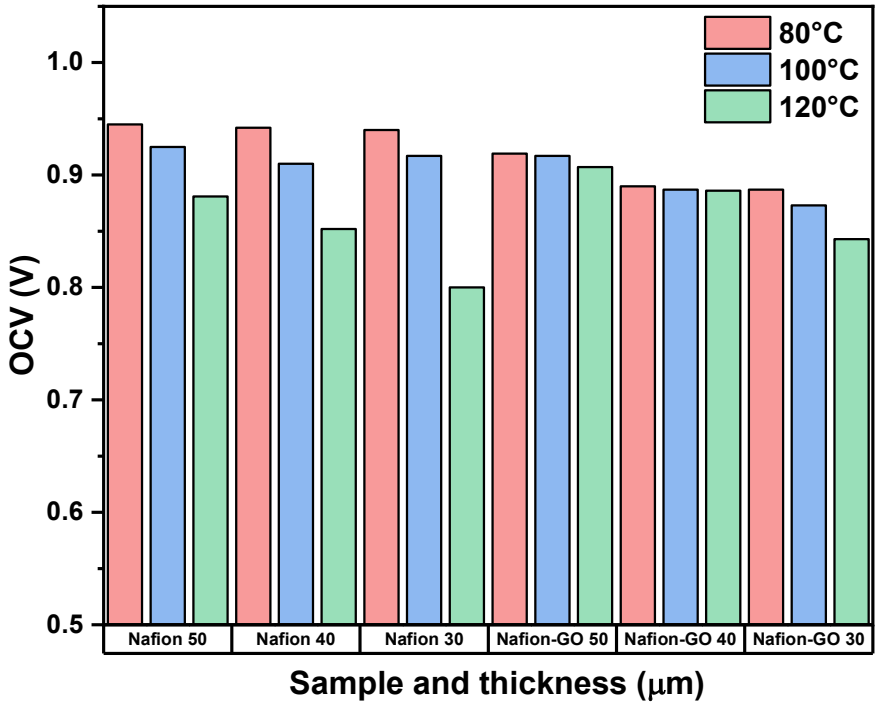



Figure 5-9: OCV of recast Nafion and Nafion-GO(4.5) membranes of 50, 40 and 30 μm thickness.

#### 5.1.2.4 Summary

Single layer Nafion and Nafion-GO membranes with 1.5, 3, 4.5 and 6 wt.% and thickness of 50, 40 and 30 μm were successfully tested in-situ and electrochemically characterised. Increasing GO loading led to a drop in maximum current and power density due to the formation of GO agglomerates. However, there was minimal reduction in performance from 100 to 120°C, compared to recast Nafion. GO was very effective at suppressing hydrogen crossover, due to the formation of a larger diffusion pathway.

The use of GO with a higher oxygen content led to membranes with improved dispersion and hence the use of GO led to smaller decreases in current and power density in comparison to membranes with GO with lower oxygen content. Furthermore, the HFR increased less with the incorporation of this GO. Overall, reducing membrane thickness, in combination with GO proved a useful technique to improve fuel cell performance.

## 5.2 Multilayer membranes

Multilayer membranes with three layers were assembled into MEAs and tested at 80, 100 and 120°C. The aim was to understand whether the change in membrane architecture influenced the performance and if the composite middle layer could behave as a hydrogen crossover blocking layer. It was hypothesised that membrane layers that were produced via a solution casting process would experience less interfacial issues. Furthermore, the influence of GO loading, temperature, and membrane thickness on fuel cell performance was assessed. Prior to assembly, the membranes were measured and had an average thickness of ± 5 μm of the required membrane thickness, as given in Table 5-2.

Table 5-2: Summary of multilayer membranes tested.

| Membrane sample | Thickness (μm) | GO source |
|---|---|---|
| Recast Nafion | 50 | N/A |
| ML-GO(0.26) | 50 | Commercial (Sigma Aldrich) |
| ML-GO(0.53) | 50 | Commercial (Sigma Aldrich) |
| ML-GO(0.79) | 50, 40 and 30 | Commercial(Sigma Aldrich) |
| ML-GO(1.05) | 50 | Commercial (Sigma Aldrich) |
| ML-GO(4.5) | 50 | Commercial (Sigma Aldrich) |

### 5.2.1 Influence of GO loading and temperature

In comparison to single layer composite membranes that were previously discussed, the multilayer membranes consisted of a specific region that contained GO. Thus, it was investigated whether the use of GO in a confined region such as a middle layer was more effective than GO dispersed throughout the membrane matrix, e.g. in the way of reduced HFR or improved suppression of hydrogen crossover.

#### 5.2.1.1 Polarisation curves

The polarisation and power curves of multilayer membranes with varying levels of GO loading and under different temperature regimes are presented in Figure 5-10. Additionally, current and power densities achieved at 400 mV are displayed in Figure 5-11 for simpler reading. Incorporation of GO led to a reduction in current and power density in comparison to Nafion, even in samples with low GO loadings such as ML-GO(0.23) and ML-GO(0.53). Expectedly, increasing the operating temperature from 80 to 100 and 120°C resulted in a fall as the proton conducting water channels along the Nafion sulphonic groups dehydrated and shrunk. Thus, the presence of GO in this case did not prevent the reduction in performance. The multilayer membrane with the greatest quantity of GO loading, ML-GO(4.5), experienced the greatest performance loss, especially significant within the ohmic region. Hence, the large amount of GO in the middle layer of the membrane behaved as a suppressor of proton conduction.

Furthermore, the multilayer membranes did not follow an exact order in performance in GO loading. This was the consequence of a combination of very low weight loading of GO in the middle layer combined with the potential of having differences in GO dispersion and homogeneity. However, ML-GO(0.79) suffered a significant decline in performance when the operating temperature increased from 80 to 100 and 120°C. The membrane underwent significant interfacial resistance build up between the different layers, which only occurred at elevated operating temperature. Otherwise, the performance was similar to the other membranes at 80°C. This implies that even with the solution casting method, major issues with the membrane layer interface are still prevalent.

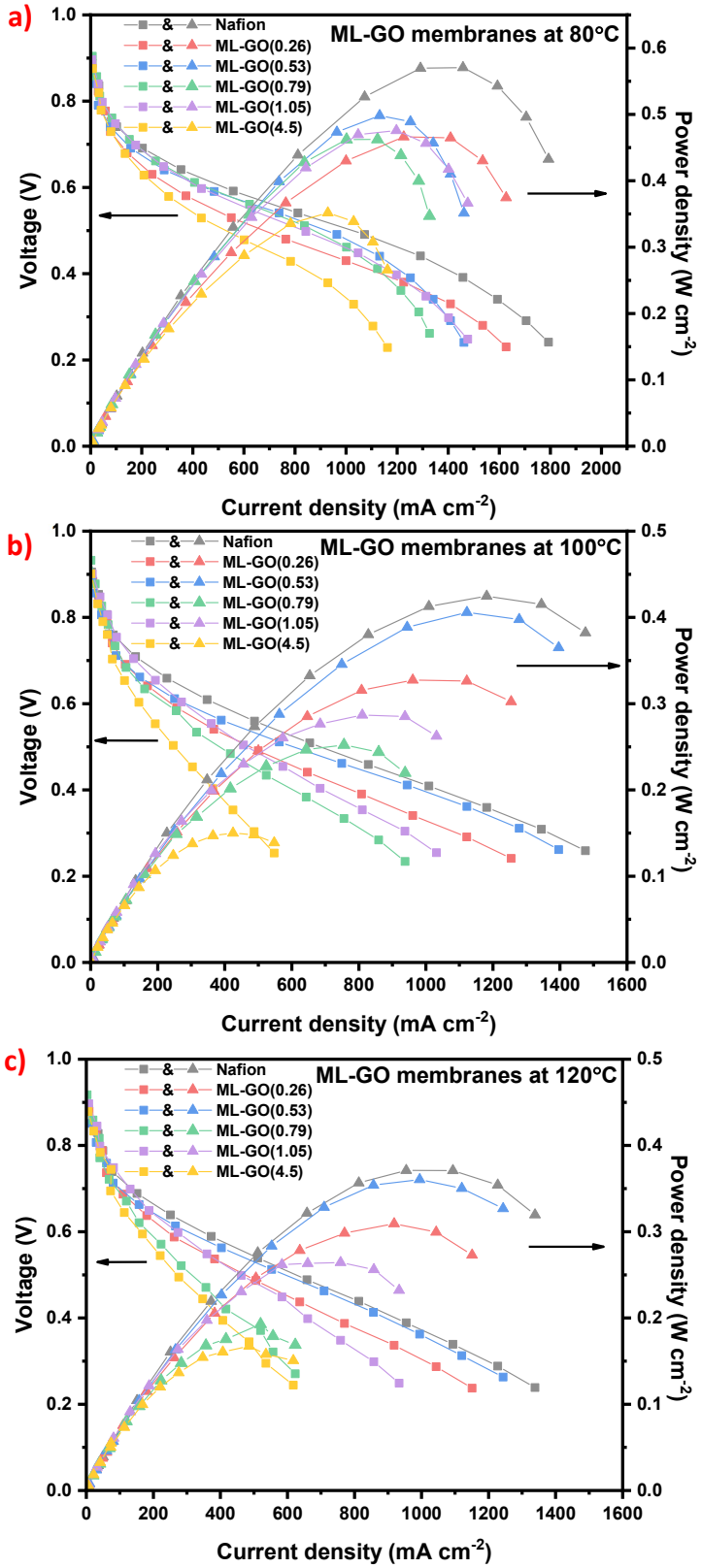



Figure 5-10: Polarisation and power curves of multilayer membranes at 80, 100, and 120°C.

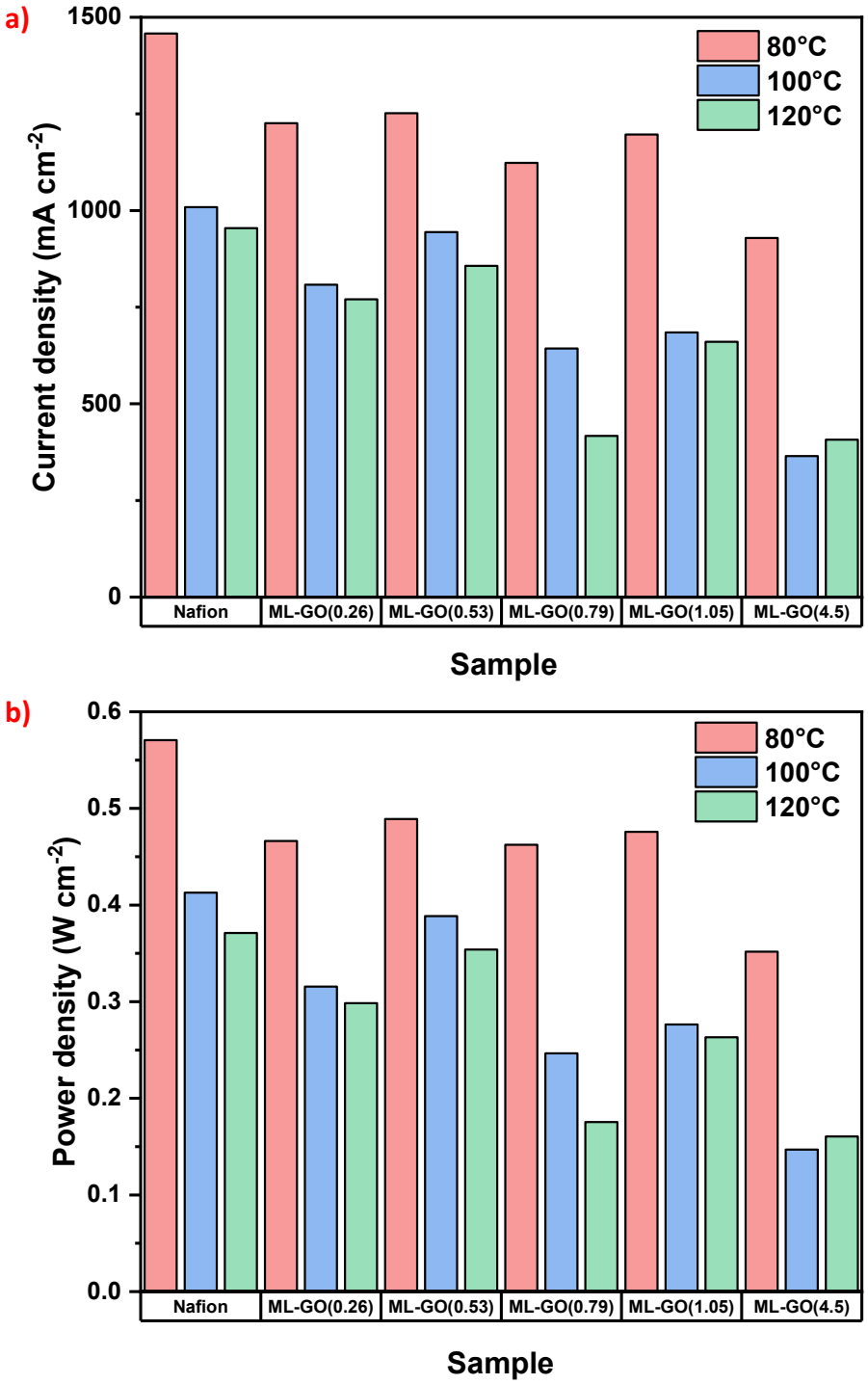



Figure 5-11: a) Current density, and b) power density at 400 mV achieved by recast Nafion and multilayer membranes at 80, 100 and 120°C.

#### 5.2.1.2 HFR

Figure 5-12 displays the HFR values of tested multilayer membranes. It was observed that the introduction of GO and multiple layers resulted in an increase in HFR. However, both the ML-GO(0.53) and ML-GO(0.79) revealed large HFR at 100 and 120°C. The large reduction in polarisation performance in ML-GO(4.5) at 100 and 120°C (Figure 5-10) directly corresponded to the sudden increase in HFR. There is a small decrease in HFR from 100 to 120°C for most samples, which suggests that the membranes are already completely dry[288].

Secondly, it can be observed that ML-GO(0.79) produced a large HFR at 120°C. The implication was that there were interfacial resistances that occurred at the highest temperature when the membrane dried and experienced shrinkage. This increase in HFR would be expected if the multilayer membrane was produced in a method such as hot pressing, whereby the individual layers are placed in contact by applying heat and pressure. However, the solution casting process heats the previously casted layer to close to its glass transition temperature, improving the contact with each layer, and is hence less likely to delaminate. Furthermore, the middle layer was essentially a composite consisting of predominately Nafion, which should further improve the contact resistance between the outer Nafion layers via the sulphonic groups. It could be possible that the activation process introduced water within the membrane and disrupted the contact between layers. Overall, this showed that solution cast multilayer membranes can still experience high levels of interfacial resistance due to potential sub-optimal contact between the layers that are compromised during activation or potentially during fuel cell hydration via conditioning or by cathode water formation.

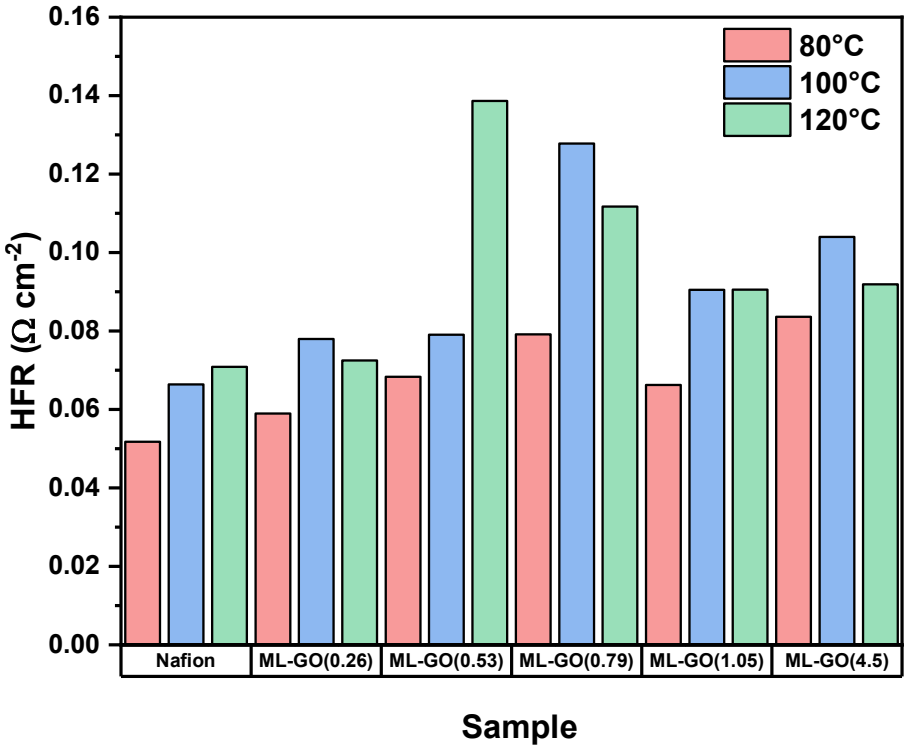



Figure 5-12: High frequency resistance values of recast Nafion and multilayer membranes at 80, 100 and 120°C.

#### 5.2.1.3 Hydrogen crossover

The impact of the multilayer structure and the use of GO was assessed with hydrogen crossover tests which are presented in Figure 5-13. At 80 and to an extent at 100°C, there were slight differences between all membranes, with the hydrogen crossover current density increasing with temperature. However, at 120°C, there was a significant increase in hydrogen crossover current density for the single layer Nafion membrane, reaching 11 mA $cm^{-2}$. In comparison, the multilayer membranes produced a crossover current of around 5 mA $cm^{-2}$ at 120°C. Hydrogen crossover is exacerbated at elevated temperatures due to the increase in kinetic energy of hydrogen gas. The interface between the layers meant that there was a barrier for the hydrogen to cross and based on the solution-diffusion mass transport model, the hydrogen would have to essentially pass through three barriers: the outer Nafion layers and the middle composite layer,

this combined with the graphene oxide inside the middle layer increasing the tortuosity results in the decrease in hydrogen crossover.

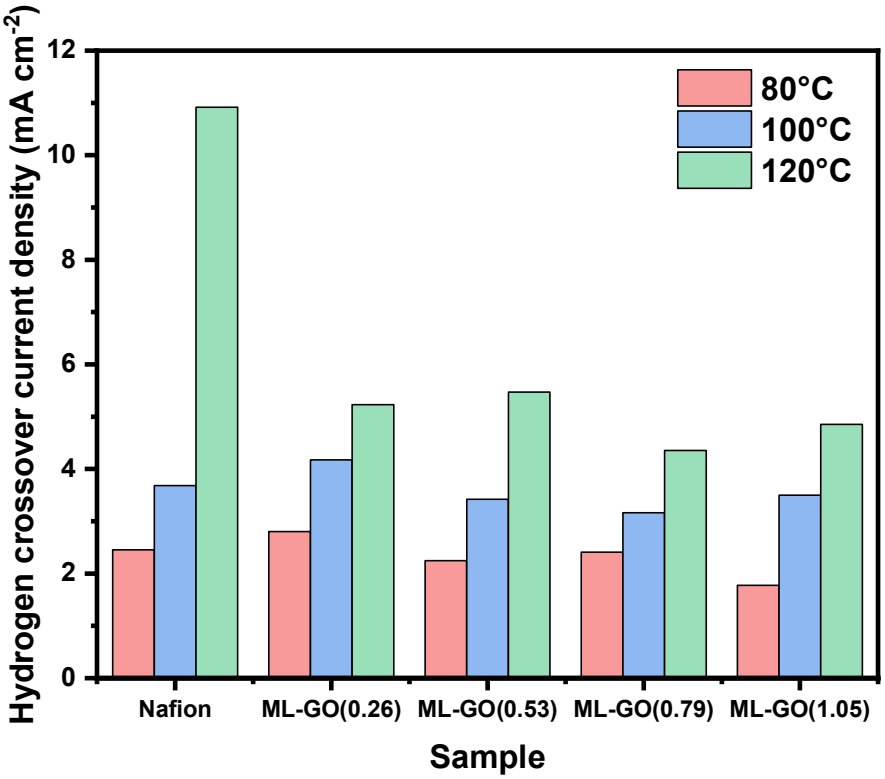



Figure 5-13: Hydrogen crossover current densities of recast Nafion and multilayer membranes at 80, 100 and 120°C.

#### 5.2.1.4 Summary

Multilayer membranes with middle layer GO loadings of 0.26, 0.53, 0.79, 1.05 and 4.5 wt.% were tested as a fuel cell electrolyte membrane. Any addition of GO led to a drop in current and power density as the GO prevented sufficient proton conduction. Furthermore, the use of three layers potentially resulted in interfacial issues shown by HFR values which become significant at 100 and 120°C, resulting in a drop in fuel cell performance. However, the multilayer membranes were very effective hydrogen crossover blocking layers, maintaining low hydrogen crossover current densities at 100 and 120°C.

### 5.2.2 Influence of membrane thickness

Multilayer membranes with total thicknesses of 50, 40 and 30 μm were tested as a fuel cell membrane, with a variety of electrochemical characterisation techniques to understand how the performance varied with thickness. The middle composite layer was fixed in thickness and fixed with a GO loading of 0.79 wt.%. Hence, the two Nafion outer layers were reduced to lower the total thickness of the multilayer membrane. The specific fabrication details were explored in Chapter 3.

#### 5.2.2.1 Current and power density

Current and power densities achieved at a voltage of 400 mV are shown in Figure 5-14. Decreasing the total membrane thickness from 50 μm led to increases in the current and power density. This was because thinner membranes experienced lower resistance. Additionally, thinner membranes allowed for faster water diffusion through the membrane from the cathode to the anode, permitting for a higher current density to be achieved. However, the decrease in thickness from 40 to 30 μm did not provide any considerable increase in performance and it can be observed that the achieved performance values were similar. Thus, either decreasing the outer Nafion layers reaches a plateau in performance before the middle layer should also be reduced in thickness, or the solution casting process utilised would have to be adapted to fabricate thinner membranes (e.g. spraying).

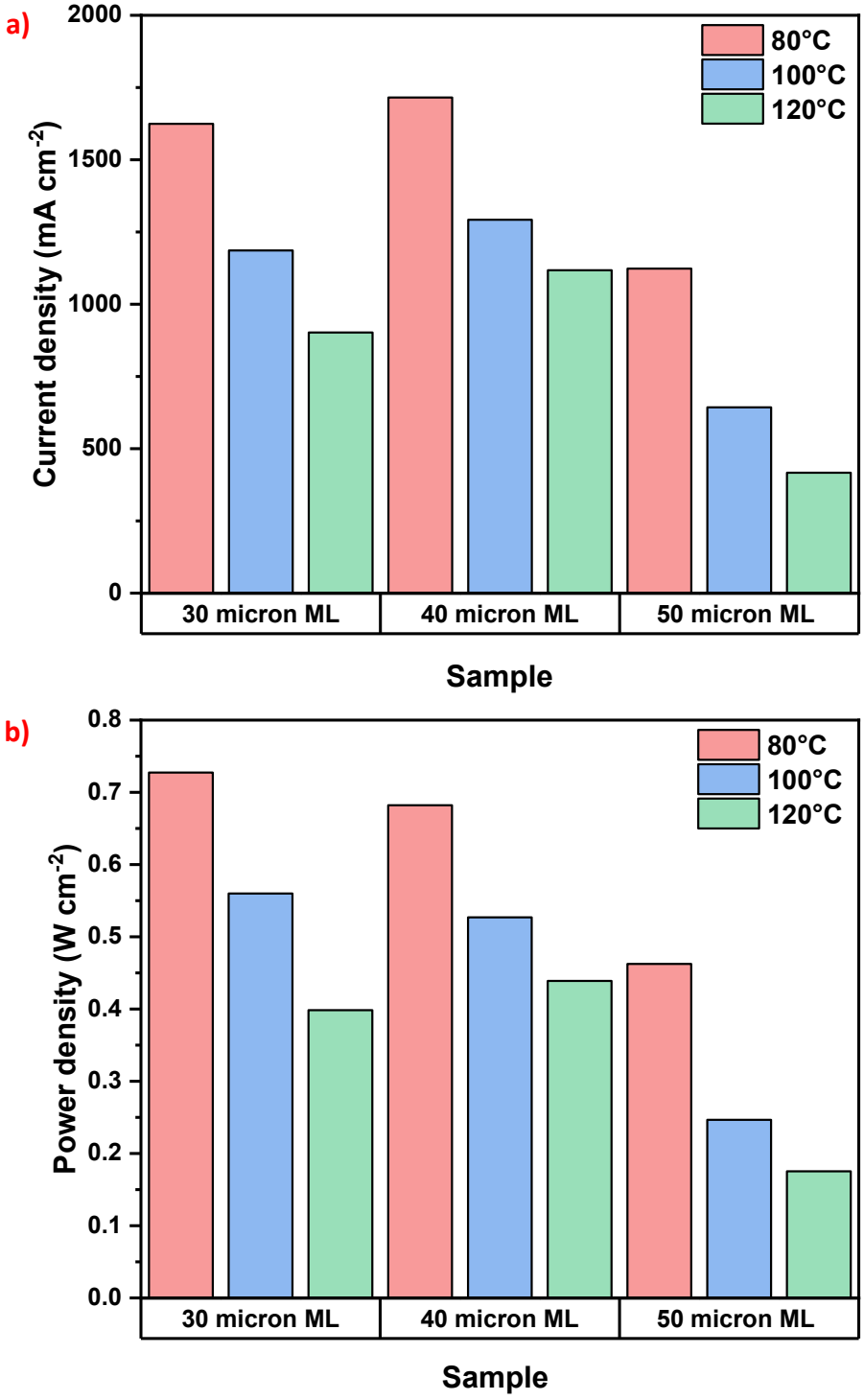



Figure 5-14: a) Current density, and b) power density achieved at 400 mV by multilayer membranes of varying thickness at 80, 100 and 120°C.

.

5.2.2.2 HFR

Decreasing membrane thickness significantly reduced the HFR, as shown in Figure 5-15. The HFR values of the 40 and 30 µm membranes are very similar, suggesting that to achieve further decreases in HFR would require the use of a thinner middle layer. The HFR values were less than those obtained by the single composite layers. This suggested that the addition of GO increased the resistance of the membrane. As the GO loading in the multilayer membrane was low, the increase in HFR with temperature could be attributed to the removal of water and interfacial resistances between the individual layers.

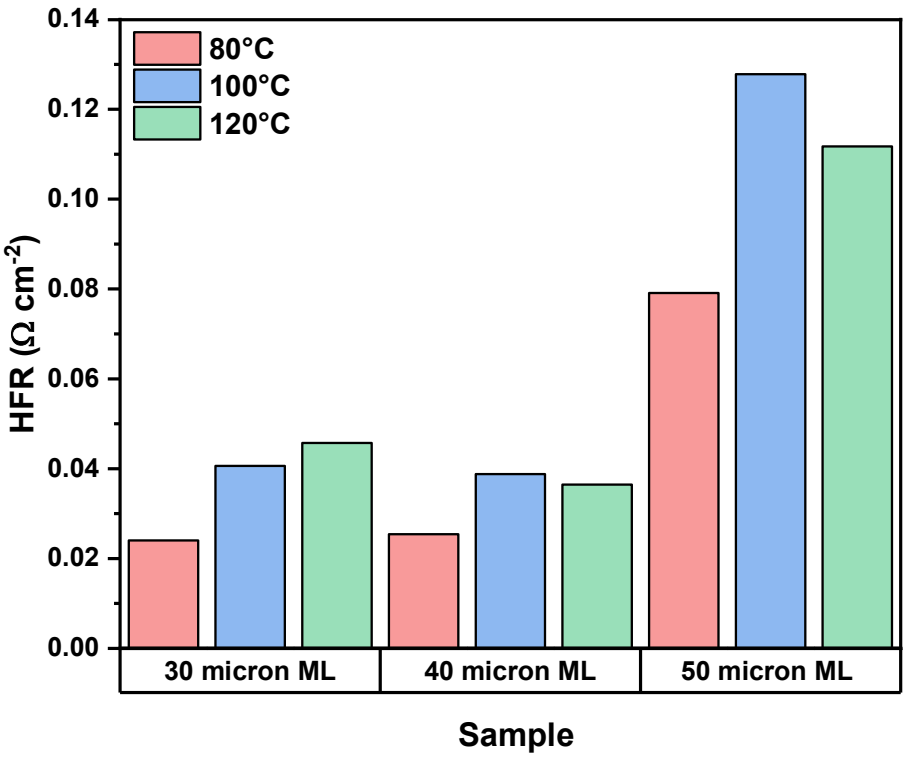



Figure 5-15: High frequency resistance values of ML-GO(0.79) membranes of varying thickness at 80, 100 and 120°C.

#### 5.2.2.3 Hydrogen crossover

Measured OCV and hydrogen crossover values are shown in Figure 5-16. Hydrogen crossover increased with increasing operating temperature and the lower OCV is a direct consequence of hydrogen crossover. As previously explained, hydrogen gas has to cross multiple layers or barriers in the multilayer structure instead of a single membrane, resulting in less hydrogen being able to crossover. 40 and 50 μm thick membranes exhibited similar OCV values, at around 0.9 V, whereas the 30 μm had a lower OCV at around 0.8 V with operation at 120°C bringing the OCV down to 0.7 V, indicating significant hydrogen crossover. Furthermore, the thinner multilayer membranes were mechanically fragile and would be susceptible to crossover at higher temperatures when water had been removed. This was because the removal of water reduced the thickness of the membrane, increasing the concentration gradient of hydrogen. Furthermore, hydrogen no longer dissolved in the water in the membrane, and instead passed through the free volume of the Nafion polymer.

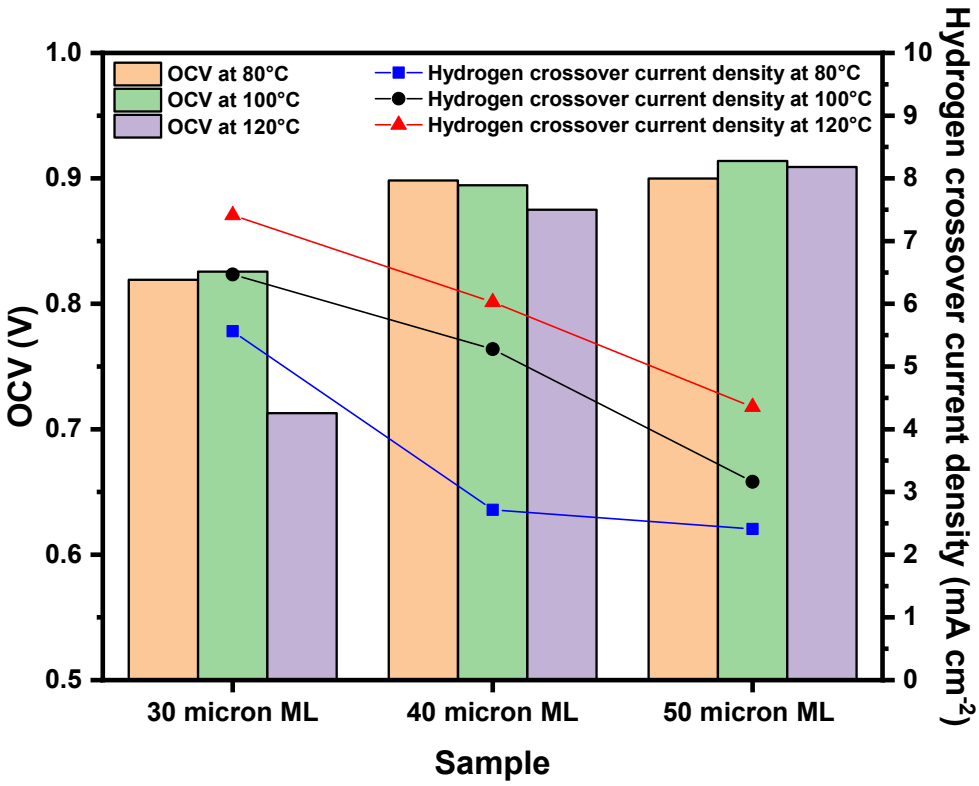



Figure 5-16: OCV and hydrogen crossover current densities of ML-GO(0.79) membranes of varying thickness at 80, 100 and 120°C.

#### 5.2.2.4 Summary

Reduction of multilayer membrane thickness to 40 and 30 μm led to increased current and power density, with a subsequent decrease in HFR and hydrogen crossover. However, diminishing returns were observed, with further improvements requiring either the reduction of the middle composite layer, or an adaptation of the membrane fabrication process.

### 5.2.3 Progress assessment and best practices

It is recommended that thinner membranes are utilised to produce greater current densities. However, the decrease in membrane thickness will result in a higher hydrogen crossover current density. Thus, the use of GO can prevent excessive hydrogen crossover rates that would result in a reduced OCV and a polarisation curve shifted downwards. However, it should be stressed that any amount of GO can result in a drop in performance and hence a small amount of GO should be used. It is further recommended that GO with a higher oxygen content as well as less agglomerated GO is used, to reduce the change of GO impeding proton conduction. Finally, alternative fabrication techniques, such as spraying should be explored if fabricating membranes thinner than 30 μm.

## 5.3 Comparison with literature

The results of the best performing membranes were compared to values obtained from literature, as presented in Table 5-3. The literature values were obtained from articles that specifically utilise only GO as a filler and Nafion as the polymer. Generally, the best performing membranes in this thesis have a comparable or better peak power density at intermediate temperatures to those found in the literature. Samples 12 and 13 corresponded to Nafion-GO(4.5) with a thickness of 30 µm at 100 and 120°C respectively. Samples 14 and 15, and samples 16 and 17 refer to ML-GO(0.79) at 30 and 40 µm. However, many literature sources did not reveal the thickness of the prepared membranes.

Table 5-3: Comparison of fuel cell results with literature.

| Sample # | Temperature (°C) | Peak power density (W $cm^{-2}$) | RH at cathode (%) | Reference |
|---|---|---|---|---|
| 1 | 80 | 0.612 | 100 | [289] |
| 2 | 120 | 0.15 | 25 | [210] |
| 3 | 80 | 0.6 | 40 | [171] |
| 4 | 120 | 0.25882 | 25 | [178] |
| 5 | 100 | 0.212 | 25 | [161] |
| 6 | 80 | 0.488 | 20 | [290] |
| 7 | 80 | 0.841 | 20 | [290] |
| 8 | 120 | 0.11 | 20 | [180] |
| 9 | 120 | 0.31 | 40 | [180] |
| 10 | 100 | 0.15 | 20 | [180] |
| 11 | 100 | 0.315 | 40 | [180] |
| 12 | 100 | 0.55 | 30 | Thesis and [287] |
| 13 | 120 | 0.47 | 30 | Thesis and [287] |
| 14 | 100 | 0.57 | 30 | Thesis |
| 15 | 120 | 0.4 | 30 | Thesis |
| 16 | 100 | 0.53 | 30 | Thesis |
| 17 | 120 | 0.44 | 30 | Thesis |

## 5.4 Conclusion

Single layer and multilayer composite membranes were successfully tested as fuel cell electrolyte membranes at various operating temperatures, GO weight loading, and membrane thicknesses.

- The addition of GO reduced the maximum current and power density achieved. This was due to the agglomeration of GO within the polymer matrix creating regions of high GO density which were detrimental to proton conduction. This was confirmed by composite membranes with GO with higher oxygen contents not experiencing the same large reductions.
- Increasing the operating temperature resulted in a drop in the maximum current and power density achieved due to the removal of water. However, the reduction in performance from 100 to 120°C was smaller for the composite membranes than for recast Nafion.
- Reducing membrane thickness increased the maximum current and power density, to the detriment of greater hydrogen crossover and lower OCV.
- The incorporation of GO reduced hydrogen crossover, with increasing GO loading further reducing hydrogen crossover.
- The fabrication process of the multilayer membrane could still result in insufficient contact between the layers, and as a consequence lead to performance drops.

Fuel cell tests results are summarised in Table 5-4 and Table 5-5. Hydrogen permeability was calculated from hydrogen crossover current densities to provide a numerical value of the actual quantity of hydrogen in contact with the cathode and not the current produced.

Table 5-4: Summary of fuel cell testing: current and power density at 400 mV, hydrogen crossover current density and hydrogen permeability.

| | Current density at 400 mV (mA $cm^{-2}$) | | | Power density at 400 mV (W $cm^{-2}$) | | | Hydrogen crossover current density (mA $cm^{-2}$) | | | Hydrogen permeability (mol $m/m^2$ s Pa) × $10^{-14}$ | | |
|---|---|---|---|---|---|---|---|---|---|---|---|---|
| Sample | 80°C | 100°C | 120°C | 80°C | 100°C | 120°C | 80°C | 100°C | 120°C | 80°C | 100°C | 120°C |
| Nafion (Ref) | 1314 | 922 | 875 | 0.50 | 0.37 | 0.34 | 2.45 | 3.68 | 10.92 | 2.53 | 3.79 | 11.3 |
| Nafion-GO(1.5) | 1037 | 494 | 532 | 0.39 | 0.20 | 0.22 | 3.65 | 4.65 | 5.94 | 3.76 | 4.79 | 6.12 |
| Nafion-GO(3) | 715 | 391 | 395 | 0.29 | 0.16 | 0.16 | 4.11 | 3.83 | 5.36 | 4.24 | 3.95 | 5.53 |
| Nafion-GO(4.5) | 904 | 407 | 429 | 0.35 | 0.17 | 0.17 | 1.08 | 2.26 | 3.57 | 1.11 | 2.33 | 3.68 |
| Nafion-GO(6) | 611 | 323 | 330 | 0.25 | 0.13 | 0.13 | 1.61 | 2.03 | 2.62 | 1.66 | 2.09 | 2.70 |
| Nafion (Ref) | 1458 | 1009 | 954 | 0.57 | 0.41 | 0.37 | X | X | X | X | X | X |
| ML-GO(0.26) | 1226 | 808 | 770 | 0.47 | 0.32 | 0.30 | 2.80 | 4.17 | 5.22 | 2.89 | 4.30 | 5.38 |
| ML-GO(0.53) | 1252 | 944 | 857 | 0.49 | 0.39 | 0.35 | 2.25 | 3.42 | 5.47 | 2.32 | 3.53 | 5.64 |
| ML-GO(0.79) | 1124 | 643 | 417 | 0.46 | 0.25 | 0.18 | 2.41 | 3.16 | 4.35 | 2.48 | 3.26 | 4.48 |
| ML-GO(1.05) | 1197 | 685 | 661 | 0.48 | 0.28 | 0.26 | 1.78 | 3.50 | 4.85 | 1.84 | 3.61 | 5.00 |
| ML-GO(4.5) | 929 | 365 | 407 | 0.35 | 0.15 | 0.16 | X | X | X | X | X | X |
| Nafion-GO(4.5) 30µm | 1186 | 1434 | 1160 | 0.46 | 0.54 | 0.46 | X | X | X | X | X | X |
| Nafion-GO(4.5) 40µm | 1064 | 1378 | 1141 | 0.43 | 0.53 | 0.44 | X | X | X | X | X | X |
| Nafion-GO(4.5) 50µm | 1084 | 1013 | 857 | 0.41 | 0.41 | 0.34 | X | X | X | X | X | X |
| ML-GO(0.79) 30µm | 1624 | 1186 | 902 | 0.73 | 0.56 | 0.40 | 5.56 | 6.47 | 7.41 | 3.44 | 4.00 | 4.58 |
| ML-GO(0.79) 40µm | 1715 | 1293 | 1117 | 0.68 | 0.53 | 0.44 | 2.71 | 5.28 | 6.03 | 2.24 | 4.35 | 4.97 |
| Nafion 30µm | 1020 | 1202 | 891 | 0.42 | 0.46 | 0.37 | X | X | X | X | X | X |
| Nafion 40µm | 1198 | 1424 | 1068 | 0.50 | 0.59 | 0.42 | X | X | X | X | X | X |
| Nafion 50µm | 1064 | 1127 | 914 | 0.43 | 0.45 | 0.36 | X | X | X | X | X | X |

Table 5-5: Summary of fuel cell testing: Peak current and peak power density, high frequency resistance and OCV.

| | Peak current density ($mA.cm^{-2}$) | | | Peak power density ($W.cm^{-2}$) | | | HFR ($\Omega\ cm^{-2}$) | | | OCV (V) | | |
|---|---|---|---|---|---|---|---|---|---|---|---|---|
| Sample | 80°C | 100°C | 120°C | 80°C | 100°C | 120°C | 80°C | 100°C | 120°C | 80°C | 100°C | 120°C |
| Nafion (Ref) | 1715 | 1347 | 1210 | 0.5 | 0.37 | 0.34 | 0.052 | 0.066 | 0.071 | X | X | X |
| Nafion-GO(1.5) | 1463 | 806 | 794 | 0.41 | 0.22 | 0.22 | 0.088 | 0.090 | 0.099 | 0.930 | 0.919 | 0.908 |
| Nafion-GO(3) | 1189 | 696 | 630 | 0.34 | 0.18 | 0.17 | 0.114 | 0.127 | 0.139 | 0.914 | 0.921 | 0.918 |
| Nafion-GO(4.5) | 1261 | 677 | 640 | 0.38 | 0.21 | 0.20 | 0.109 | 0.130 | 0.122 | 0.939 | 0.924 | 0.912 |
| Nafion-GO(6) | 969 | 483 | 490 | 0.27 | 0.14 | 0.14 | 0.148 | 0.193 | 0.194 | 0.914 | 0.922 | 0.919 |
| Nafion (Ref) | 1793 | 1476 | 1339 | 0.57 | 0.42 | 0.37 | X | X | X | X | X | X |
| ML-GO(0.26) | 1627 | 1254 | 1151 | 0.47 | 0.33 | 0.31 | 0.059 | 0.078 | 0.073 | 0.887 | 0.892 | 0.890 |
| ML-GO(0.53) | 1462 | 1396 | 1243 | 0.50 | 0.41 | 0.36 | 0.068 | 0.079 | 0.134 | 0.899 | 0.916 | 0.905 |
| ML-GO(0.79) | 1327 | 938 | 624 | 0.46 | 0.25 | 0.19 | 0.079 | 0.128 | 0.112 | 0.900 | 0.914 | 0.909 |
| ML-GO(1.05) | 1476 | 1032 | 933 | 0.48 | 0.29 | 0.26 | 0.066 | 0.091 | 0.091 | 0.902 | 0.906 | 0.911 |
| ML-GO(4.5) | 1106 | 488 | 536 | 0.35 | 0.15 | 0.17 | 0.084 | 0.104 | 0.092 | 0.888 | 0.898 | 0.900 |
| Nafion-GO(4.5) 30µm | 1330 | 1633 | 1398 | 0.48 | 0.55 | 0.47 | 0.050 | 0.065 | 0.075 | 0.887 | 0.873 | 0.843 |
| Nafion-GO(4.5) 40µm | 1225 | 1606 | 1346 | 0.43 | 0.54 | 0.46 | 0.065 | 0.095 | 0.105 | 0.890 | 0.887 | 0.886 |
| Nafion-GO(4.5) 50µm | 1092 | 1084 | 1032 | 0.33 | 0.36 | 0.31 | 0.090 | 0.125 | 0.130 | 0.919 | 0.917 | 0.907 |
| ML-GO(0.79) 30µm | 1963 | 1813 | 1311 | 0.74 | 0.57 | 0.40 | 0.024 | 0.041 | 0.046 | 0.819 | 0.826 | 0.713 |
| ML-GO(0.79) 40µm | 2062 | 1759 | 1550 | 0.70 | 0.53 | 0.44 | 0.025 | 0.039 | 0.037 | 0.898 | 0.895 | 0.875 |
| Nafion 30µm | 1271 | 1465 | 1314 | 0.38 | 0.46 | 0.39 | 0.046 | 0.055 | 0.065 | 0.940 | 0.899 | 0.800 |
| Nafion 40µm | 1259 | 1443 | 1235 | 0.46 | 0.50 | 0.39 | 0.055 | 0.080 | 0.115 | 0.942 | 0.910 | 0.852 |
| Nafion 50µm | 1189 | 1387 | 1131 | 0.46 | 0.45 | 0.36 | 0.090 | 0.115 | 0.140 | 0.945 | 0.925 | 0.881 |

# 6 Durability studies

This chapter summarises the performance of fabricated membranes through two types of durability tests, a 24-hour open circuit voltage (OCV) hold and an accelerated stress test (AST). Membranes with optimised graphene oxide (GO) loading and membrane thickness were prepared and tested via an AST. These included single layer and multilayer membranes with synthesised sulphonated GO (SGO), and membranes with a Nafion-cerium oxide interlayer applied onto the gas diffusion electrodes (GDEs). The aims involve understanding the influence of GO, SGO, and the Nafion-cerium oxide interlayer on fuel cell (FC) durability. It was hypothesised that sulphonated GO can increase water retention and that cerium oxide can scavenge radicals that are harmful for long term fuel cell operation. To assist, a variety of electrochemical characterisation techniques such as polarisation curves, hydrogen crossover and high frequency resistance (HFR) were utilised.

## 6.1 24-hour OCV hold test

In order to understand the stability of the membranes under fuel cell operation, single layer membranes were prepared for 24-hour testing under OCV operating conditions. Recast Nafion and a composite membrane consisting of Nafion with GO (4.5 wt.%) were fabricated, with OCV tests performed at 80 and 120°C. The aim was to understand the influence of GO on fuel cell performance after a set amount of time at OCV. It was hypothesised that the use of GO would reduce degradation by suppressing hydrogen crossover and thus limiting the formation of harmful radicals. Table 6-1 presents the samples that underwent the 24-hour OCV hold test.

Table 6-1: Table of OCV hold test samples.

| Sample | Initial thickness (μm) | GO Source |
|---|---|---|
| Nafion | 50 | N/A |
| Nafion-GO(4.5) | 50 | Sigma Aldrich |

### 6.1.1 Polarisation curves

Figure 6-1 displays the polarisation and power curves of Nafion and Nafion-GO(4.5) at 80 and 120°C. Operating at 80°C revealed that the recast Nafion membrane electrode assembly (MEA) experienced a larger difference in polarisation after being held at OCV for 24 hours in comparison to the composite membrane. The Nafion membrane showed a significant decrease in performance and power density after the 24 hrs OCV test. The OCV hold conditions created an environment where hydrogen and oxygen were not electrochemically reacting. This resulted in large concentration gradients, and thus a strong driving force to increase hydrogen crossover and respective losses in performance which the Nafion membrane experienced greatly than the Nafion-GO.

Greater decreases in polarisation and power density occurred at an operating temperature of 120°C for both membranes due to the challenging operating conditions at a higher temperature, especially for recast Nafion. This was confirmed by the low OCV of 0.81 V. The composite's performance also fell, but the decrease was less than with Nafion, implying a suitable application for higher temperatures. The drop in OCV was due to the increased thermal activation of hydrogen crossover, as thermal polymer movement resulted in larger free spaces of volume. This was due to the operating temperature being close to the glass transition temperature of the Nafion backbone, and thus resulted in movement of the polymer. Furthermore, the membrane underwent shrinking due to the evaporation of water, which led to a reduction in membrane thickness and therefore increased hydrogen flux. The use of GO increased the diffusion length required for the hydrogen to pass through the membrane and also restricted polymer flexibility, reducing the number of void spaces hydrogen could to travel through.

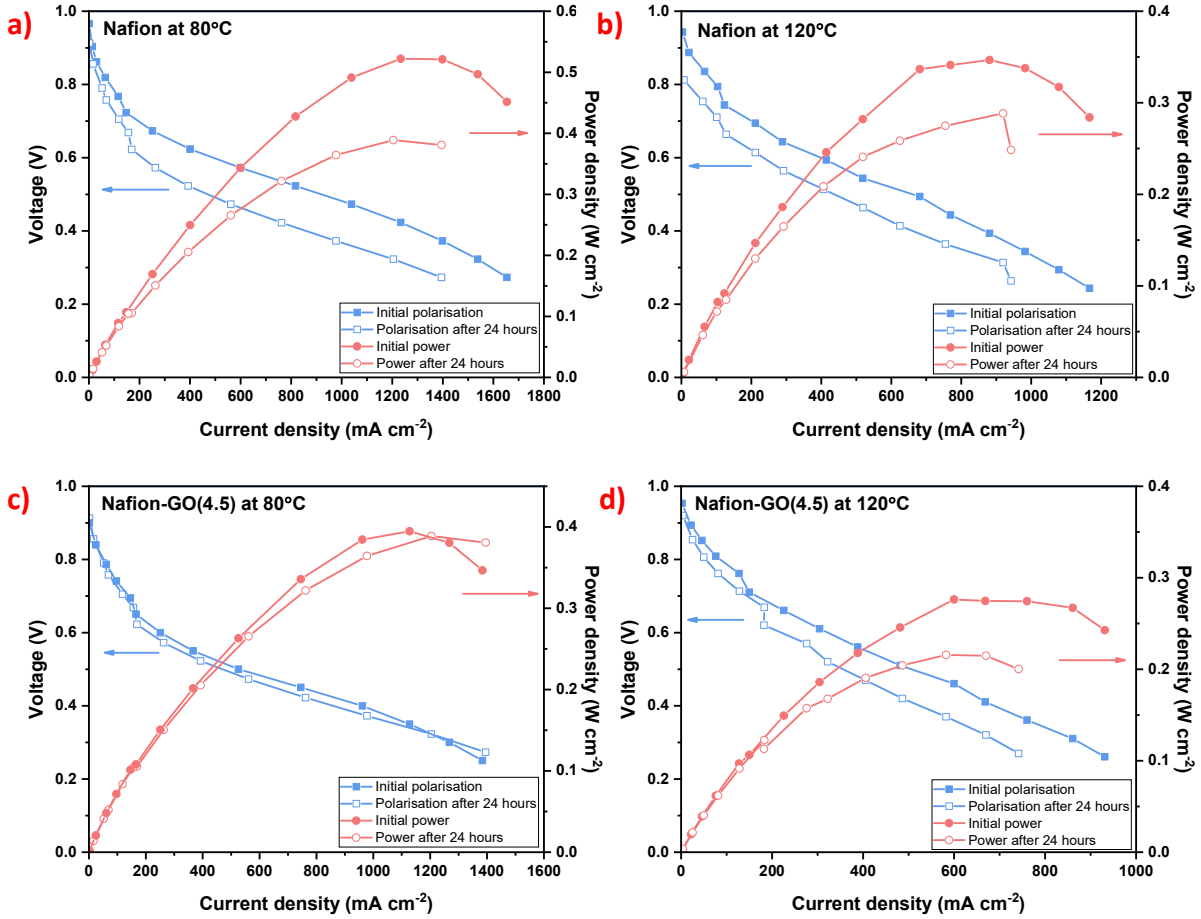



Figure 6-1: Polarisation and power curves of a) Nafion at 80°C, b) Nafion at 120°C, c) Nafion-GO(4.5) at 80°C and d) Nafion-GO(4.5) at 120°C.

### 6.1.2 OCV and Hydrogen crossover

OCV and hydrogen crossover current densities were recorded before and after the tests, shown in Figure 6-2. Following the degradation test, the OCV of the recast Nafion membrane decreased from 0.97 V to 0.92 V (5 %) and from 0.94 V to 0.81 V (14 %) at 80°C and 120°C, respectively, whereas the OCV of the Nafion-GO(4.5) showed a much lower change, with the OCV dropping from 0.92 V to 0.9 V (2 %) and from 0.96 V to 0.94 V (2 %) at 80°C and 120°C, respectively.

This was further confirmed with the hydrogen crossover values recorded. The Nafion-GO experienced minor changes in hydrogen crossover at both temperatures. This was assumed to be due to the increased tortuosity of the membrane with the addition of graphene oxide[291]. As expected, there was a large increase in crossover in the Nafion membrane when tested at 120°C, in fact from 3 to 15 mA $cm^{-2}$, a 400% increase. This crossover value was also implicitly reflected in the reduced OCV.

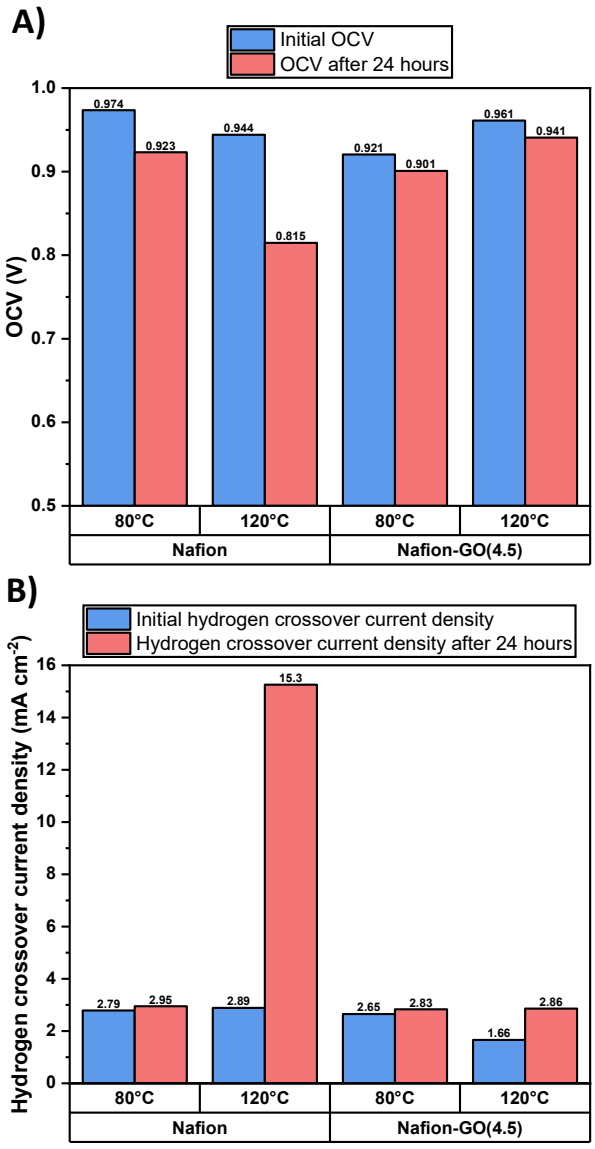



Figure 6-2: A) OCV, and B) hydrogen crossover current densities of Nafion and Nafion-GO(4.5) at 80°C and 120°C.

### 6.1.3 Post-mortem SEM

The MEA cross sections were studied after the OCV hold at both temperatures, with a Nafion membrane cross section for comparison. Figure 6-3 and Figure 6-4 present SEM cross sectional images of Nafion, Nafion MEA, Nafion-GO(4.5) and Nafion-GO(4.5) MEA. The cross section of the Nafion MEA tested at 80°C displayed a smooth and uniform membrane, similar to that of recast Nafion, suggesting that the membrane did experienced minimal degradation. This was supported by the thickness of the Nafion MEA reduced from 50 to 46.4 μm. The Nafion MEA tested at 120°C experienced a much greater difference in initial and final membrane thickness and hence greater thinning. To add, the cross section of the Nafion MEA tested at 120°C was no longer smooth and revealed a jagged, uneven cross section.

On the other hand, the Nafion-GO(4.5) MEA experienced close to no thinning after testing at 120°C, and the cross section of Nafion-GO(4.5) MEA at both 80 and 120 °C show a similarly in surface roughness due to the presence of GO. The results of the OCV hold tests are presented in Table 6-2. Furthermore, the OCV decay was much greater for Nafion at 120 °C, as expected, but interestingly remained constant for Nafion-GO(4.5). This implied that the use of GO was able to prevent extensive OCV decay even at 120°C, where crossover should be more prevalent, due to the GO loading (4.5 wt.%).

It should be stated that the images all show different samples since it is not possible to freeze crack a membrane prior to producing a MEA with the same cracked membrane. All membranes are prepared to be 50 μm ± 5μm. MEAs experience a compression and a decrease in membrane thickness due to the applied torque during the fuel cell assembly process, however this was consistent for all samples.

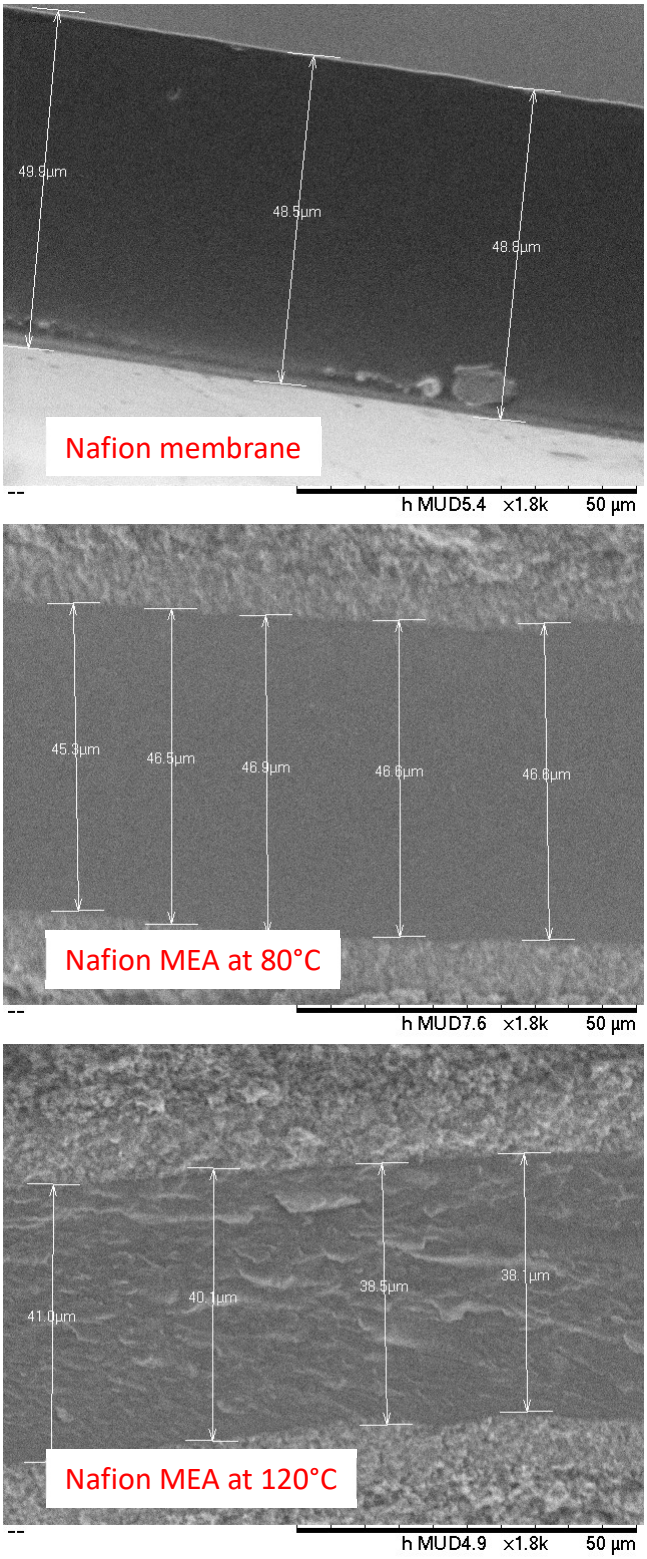



Figure 6-3: SEM cross sections of Nafion, and post OCV hold test Nafion MEAs after testing at 80°C and 120°C.

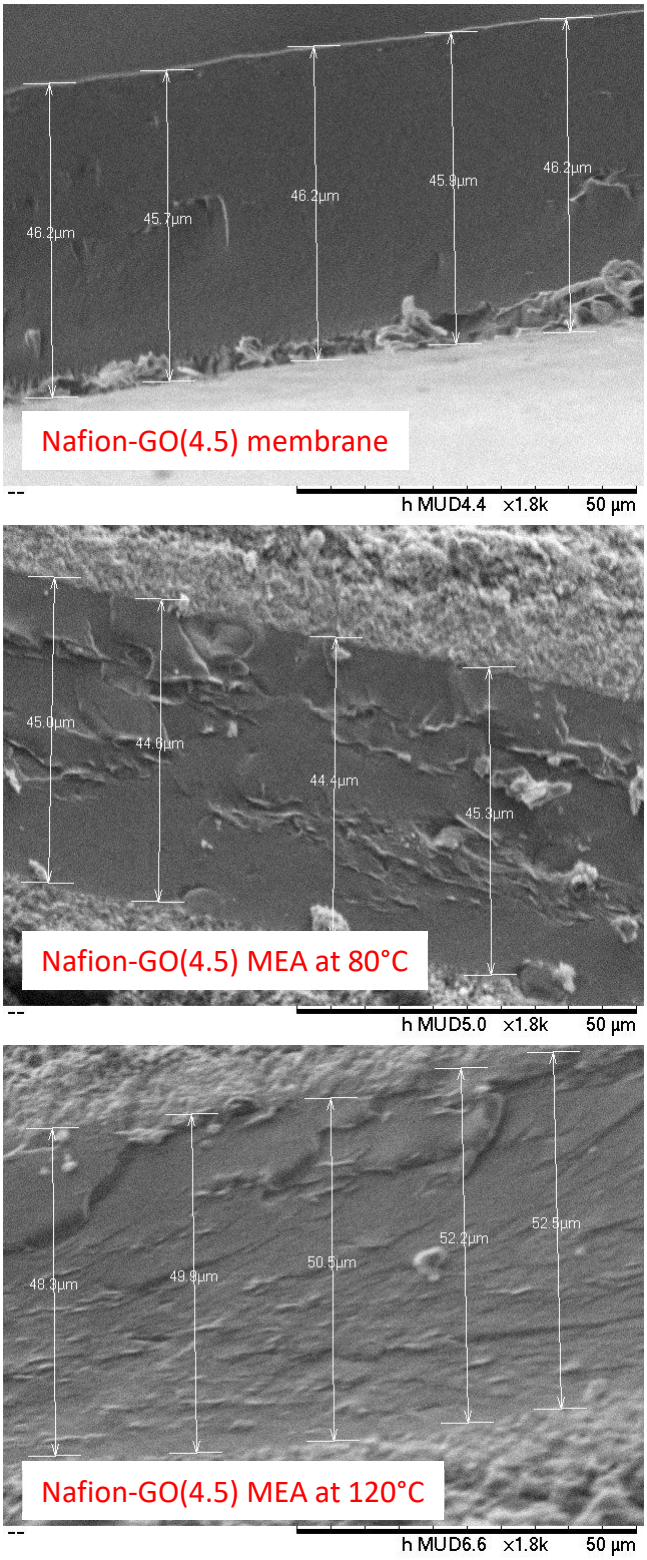



Figure 6-4: SEM cross sections of Nafion-GO(4.5), and post OCV hold test Nafion-GO(4.5) MEAs after testing at 80°C and 120°C.

Table 6-2: Summary of 24-hour OCV hold test, membranes have an initial thickness of 50µm

| Sample | Temperature (°C) | Final thickness (µm) | Initial OCV (V) | Final OCV (V) | OCV decay rate (mV $h^{-1}$) |
|---|---|---|---|---|---|
| Nafion #1 | 80 | 46.4 | 0.974 | 0.923 | 2.125 |
| Nafion #2 | 120 | 39.4 | 0.944 | 0.815 | 5.375 |
| Nafion-GO(4.5) #1 | 80 | 44.8 | 0.921 | 0.901 | 0.833 |
| Nafion-GO(4.5) #2 | 120 | 50.1 | 0.961 | 0.941 | 0.833 |

### 6.1.4 Summary

Nafion and Nafion-GO(4.5) membranes were held at OCV conditions for 24 hours to investigate the influence of GO on longer term fuel cell performance. Composite membranes with GO experienced a smaller loss in OCV and membrane thickness, as well as a negligible increase in hydrogen crossover at 120°C. Interestingly, the OCV decay was the same for the composite at both 80 and 120°C, suggesting that the use of GO was very effective at reducing hydrogen crossover and preventing excessive OCV decay.

## 6.2 Optimised membrane tests

Fuel cell testing of membranes in Chapter 5 revealed that the addition of GO with lower oxygen content reduced performance, and thus any addition of GO led to a decrease in current and power density. However, the use of GO with higher oxygen content did not show the same behaviour. Therefore, a compromise of the lowest GO weight loading was chosen for the optimised membrane, 1.5 wt.% for the single layer and 0.26 wt.% for the multilayer. The optimum thickness was chosen to be 30 µm. Subsequently, membranes with the optimum characteristics were prepared with the use of in-house GO. The fabrication process was described in detail in Chapter 4. Initially, membranes with 1.5 wt.% GO with a thickness of 30 µm were tested in a protocol equivalent to that performed in Chapter 5. Following, similar

membranes, but with sulphonated GO underwent an accelerated stress test. Both single layer composite and multilayer membranes were investigated, even though the multilayer membrane experienced some delamination.

The use of sulphonated GO was decided for three reasons: 1) to improve water retention at elevated and low humidity conditions, 2) to improve the dispersion between Nafion and GO by creating similarity between the sulphonated GO and sulphonic groups in the Nafion and 3) to reduce the chance of delamination between the individual layers in the multilayer membrane. It was hypothesised that the use of synthesised GO which showed improved dispersion, and SGO, which should improve the middle layer interface, could prevent delamination from occurring.

Finally, a new set of membranes were prepared but this time with a Nafion/cerium oxide interlayer coating, as a method to reduce hydrogen crossover.

### 6.2.1 Single and multilayer membranes with synthesised GO

Figure 6-5 presents the polarisation and power curves of Nafion-GO(1.5), whereas Figure 6-6 shows the current and power density achieved at 400 mV, HFR and hydrogen crossover. The single layer membrane produced the greatest current and power density at 80°C, which was consistent with the results in the previous chapter. This performance then began to decrease with increasing operating temperature. Additionally, the increase in temperature led to an increase in high frequency resistance, which can also be observed in the polarisation curve's ohmic region. Furthermore, the hydrogen crossover also rose with temperature. Overall, the results presented were similar to what was observed in Chapter 5.

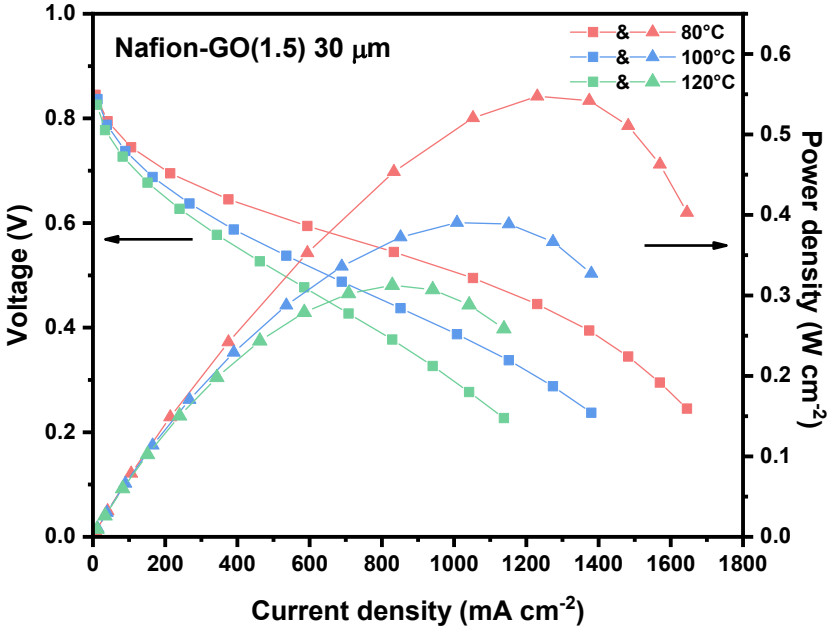



Figure 6-5: Polarisation and power curves of Nafion-GO(1.5) at 80, 100, and 120°C.

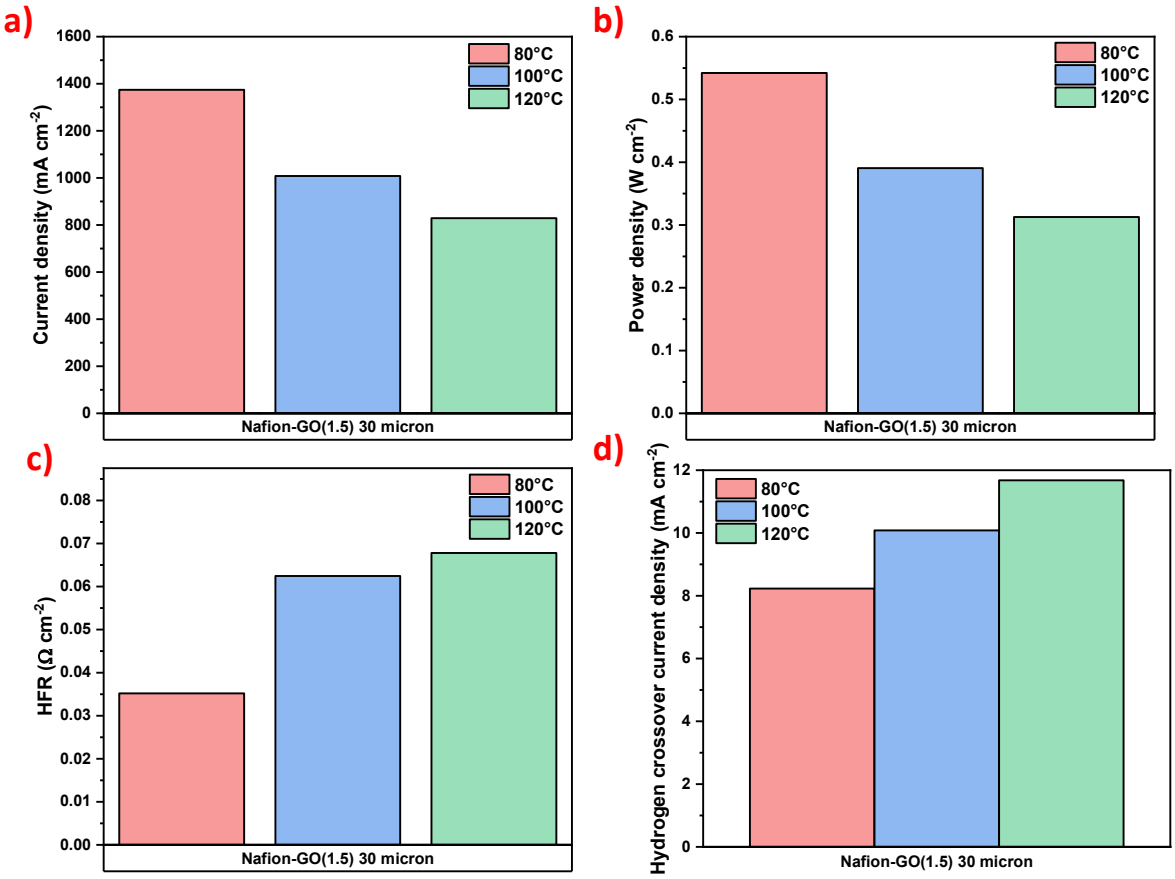



Figure 6-6: Results of Nafion-GO(1.5): a) current density at 400 mV, b) power density at 400 mV, c) HFR and, d) hydrogen crossover current density at 80°C, 100°C and 120°C.

Figure 6-7 and Figure 6-8 displays the fuel cell results for the multilayer membrane. The sample performed similarly to previously tested multilayer membranes. However, the hydrogen crossover current density increased significantly at 120°C. It would be expected that the crossover would be higher at 120°C, but overall, less than with the single layer membrane. It is unlikely that the crossover was the result of a pinhole, as that would result in a complete deterioration in fuel cell performance. Hence, this increase could be due to interlayer delamination. The individual layers of the multilayer membrane were composed of three separate layers cast one after another. Therefore, at elevated operating temperatures, each layer could undergo a slightly different shrinkage, which could exacerbate the potential of delamination.

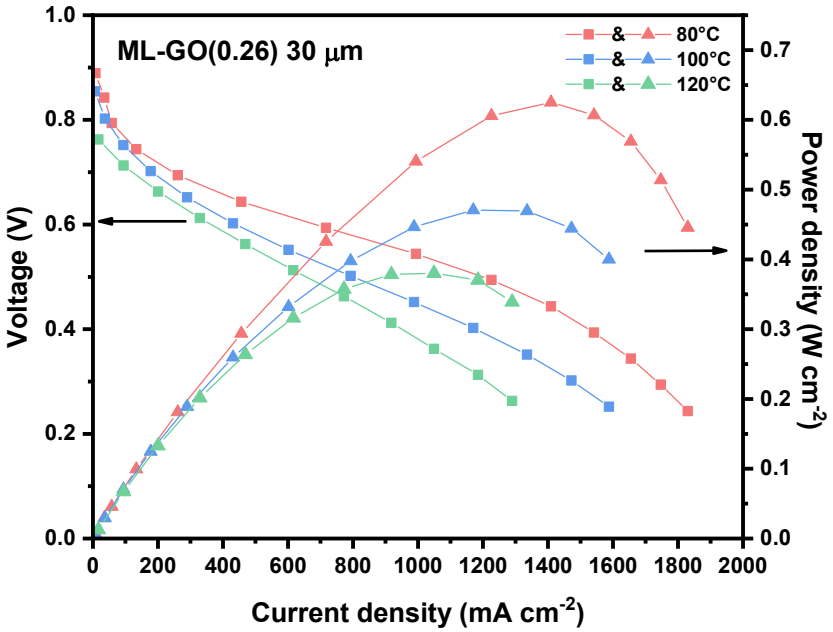


Figure 6-7: Polarisation and power curves of ML-GO(0.26) at 80, 100, and 120°C.

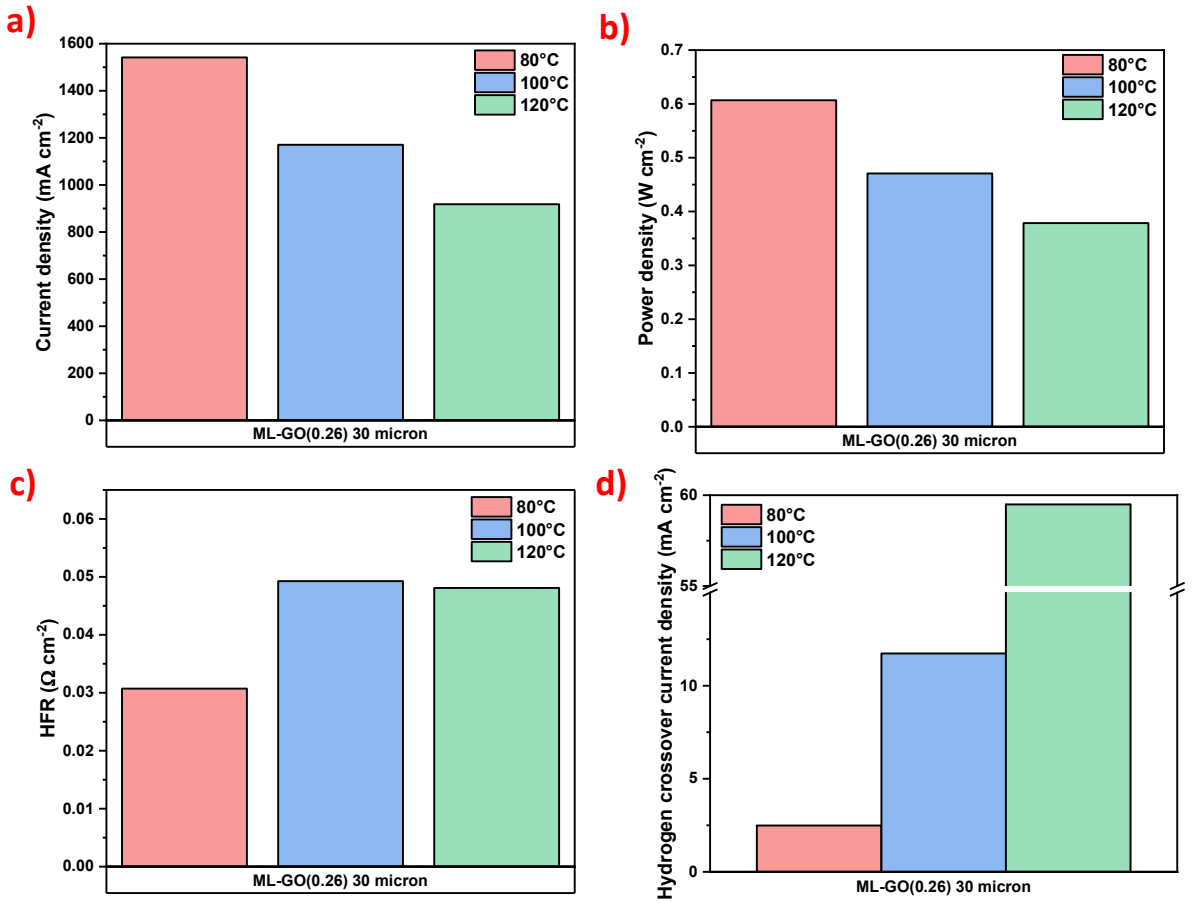



Figure 6-8: Results of ML-GO(0.26): a) current density at 400 mV, b) power density at 400 mV, c) HFR and, d) hydrogen crossover current density at 80°C, 100°C and 120°C.

The results of the use of in-house GO compared to recast Nafion is presented in Table 6-3. In contrast to commercial GO, the introduction of synGO caused a large improvement in maximum power density at 80°C, from 0.38 to 0.55 W $cm^{-2}$. This deviation minimised when the temperature increased from to 100 and 120°C, implying that the quantity of GO used was not enough to prevent the dehydration of the proton-conductive water channels.

Table 6-3: Comparison between Nafion and Nafion-SynGO(1.5) membranes.

| | Peak current density (mA $cm^{-2}$) | | | Peak power density (W $cm^{-2}$) | | |
|---|---|---|---|---|---|---|
| Sample (30µm) | 80 °C | 100 °C | 120 °C | 80 °C | 100 °C | 120 °C |
| Nafion | 1271 | 1465 | 1314 | 0.38 | 0.46 | 0.39 |
| Nafion-SynGO(1.5) | 1645 | 1380 | 1138 | 0.55 | 0.39 | 0.31 |

The structure of Nafion with the commercial and synthesised GO is presented in Figure 6-9. It is proposed that the use of commercial GO resulted in a composite membrane with agglomerations. This has been shown in Chapter 4 through optical images where the membranes with synthesised GO displayed a more uniform distribution even with a lower weight loading of GO. Furthermore, TGA results revealed that commercial GO has the lowest levels of oxidation due to a higher residual mass (Figure 4-4). This led to stronger Van der Waals forces between the layers as there were less oxygen functional groups between the graphene layers, making it harder to fully exfoliate and making sufficient dispersion more challenging.

This was also shown with the steeper mass decrease at a slightly higher temperature compared to the synthesised GO, as the oxygen was harder to remove. The electron micrographs further support this with the cross section of Nafion-SynGO(1.5) revealing a very layered structure (Figure 4-38), in contrast to the more jagged cross section of Nafion-GO(1.5) (Figure 4-10). Hence the use of fully exfoliated synthesised GO allows for effective proton conduction as the oxygen functional groups are fully accessible.

Overall, this would explain why the use of the specific commercial GO led to a reduction in power density in comparison to the synthesised GO. However, introduction of GO significantly reduced hydrogen crossover, and this was consistent with all types of GO used. To conclude, the use of commercial GO (from Sigma Aldrich) would have required additional treatment steps such as centrifugation and long-term exfoliation instead of the use of ultrasonic and probe sonication.

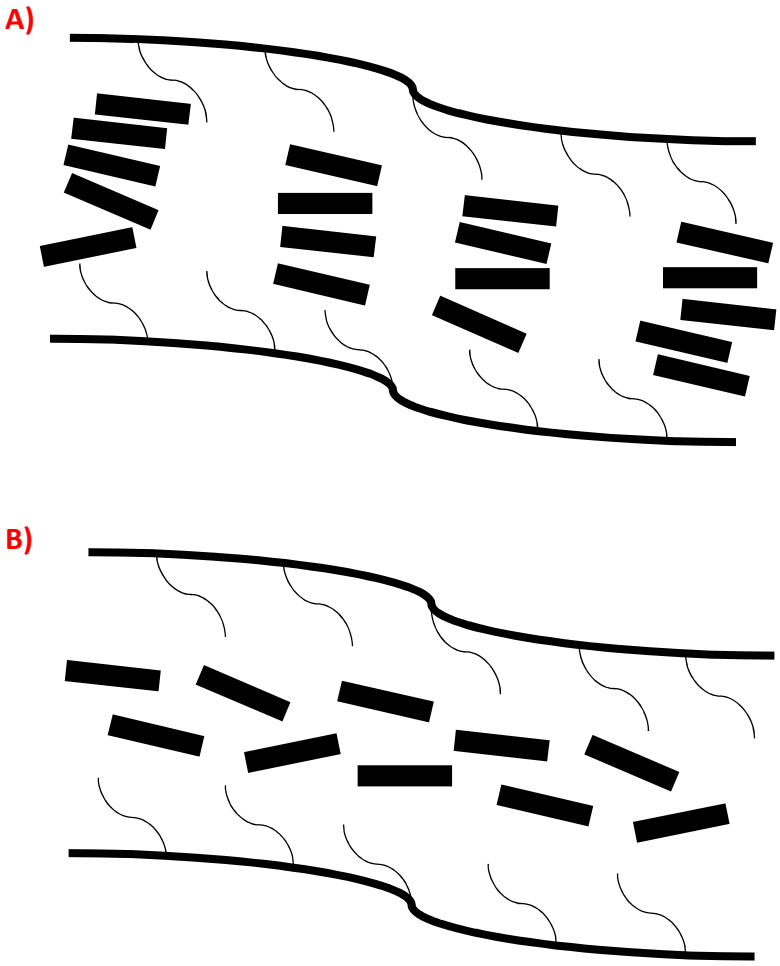


Figure 6-9: Structure of: A) Nafion-GO and B) Nafion-SynGO.

### 6.2.2 Single and multilayer membrane with synthesised sulphonated GO

Single layer and multilayer membranes with sulphonated graphene oxide as the filler were also fabricated and their durability assessed through accelerated stress tests. Figure 6-10 presents the polarisation and power curves during AST, and Figure 6-11 shows the achieved current and power density at 400 mV. It can be seen in these graphs that the performance dropped significantly after 48 hours of accelerated stress testing. There was a large drop in OCV, which coincided with a very large increase in hydrogen crossover implying that the mechanical integrity of the membrane was compromised as large quantities of hydrogen were being oxidised at the cathode. To add, the high frequency resistance also greatly increased after 48 hours, indicating the resistance in the membrane had grown. Overall, the membrane suffered large OCV drops and ohmic losses due to the repetitive humidity cycles.

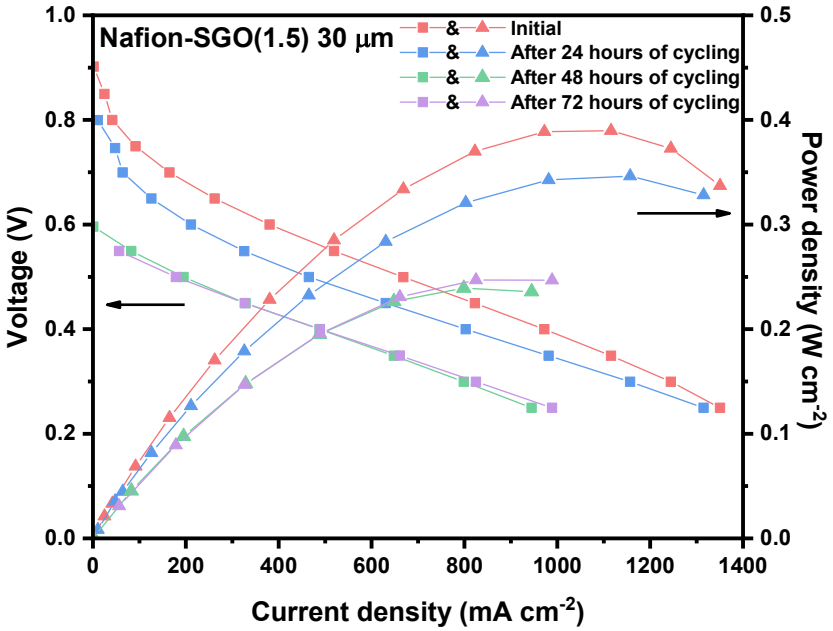



Figure 6-10: Polarisation and power curves of Nafion-SGO(1.5) during accelerated stress testing.

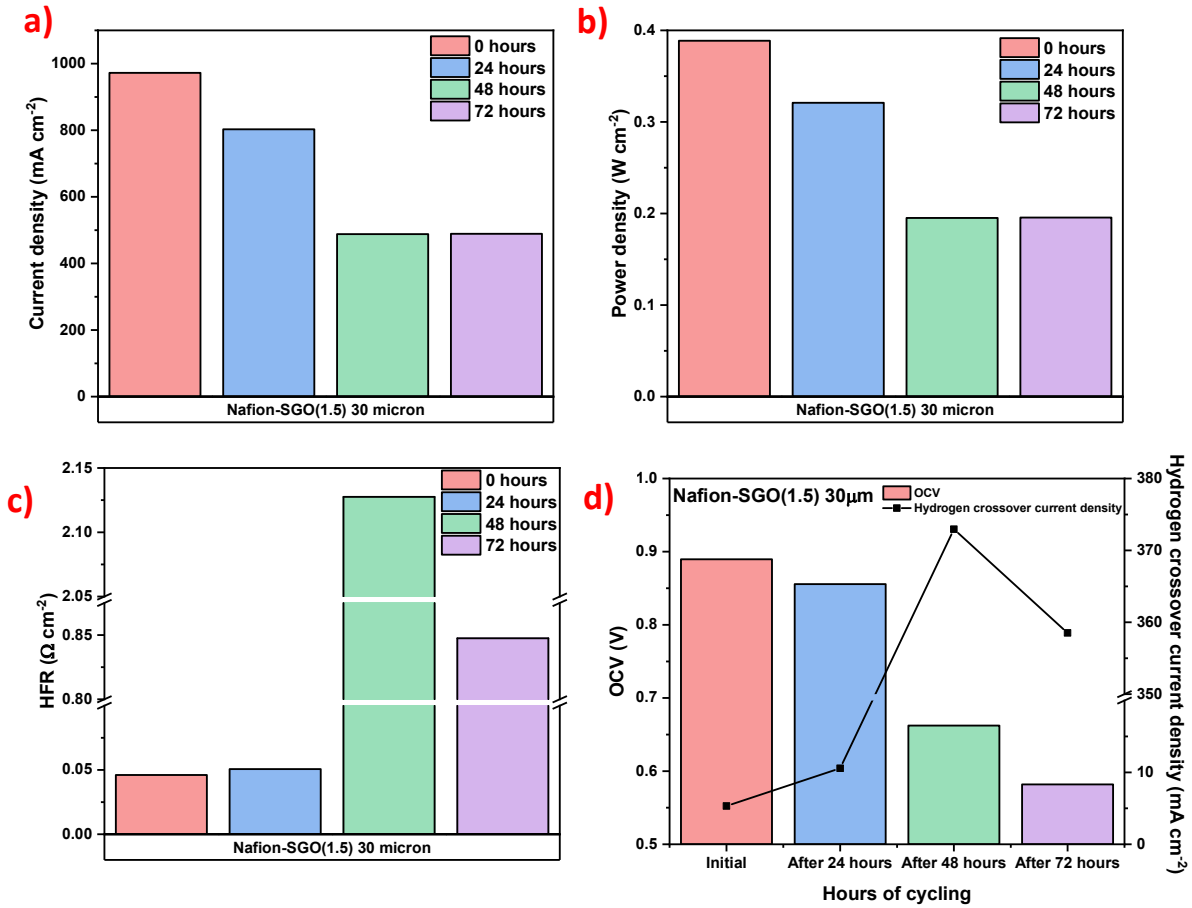



Figure 6-11: Results of Nafion-SGO(1.5): a) current density at 400 mV, b) power density at 400 mV, c) HFR and, d) hydrogen crossover current density and OCV during accelerated stress testing.

Multilayer counterparts with the same sulphonated filler were also tested, as shown in Figure 6-12 and Figure 6-13. Compared to the single layer membranes, the multilayer samples were able to operate for an extra 24 hours of humidity cycling, until their OCV dropped below 0.6 V. The peak power, peak current and OCV dropped with each consecutive day of operation, with the hydrogen crossover increasing. The use of a multilayer structure slowed the degradation due to essentially having three layers present, as the additional layers inhibit hydrogen crossover, if there was no delamination.

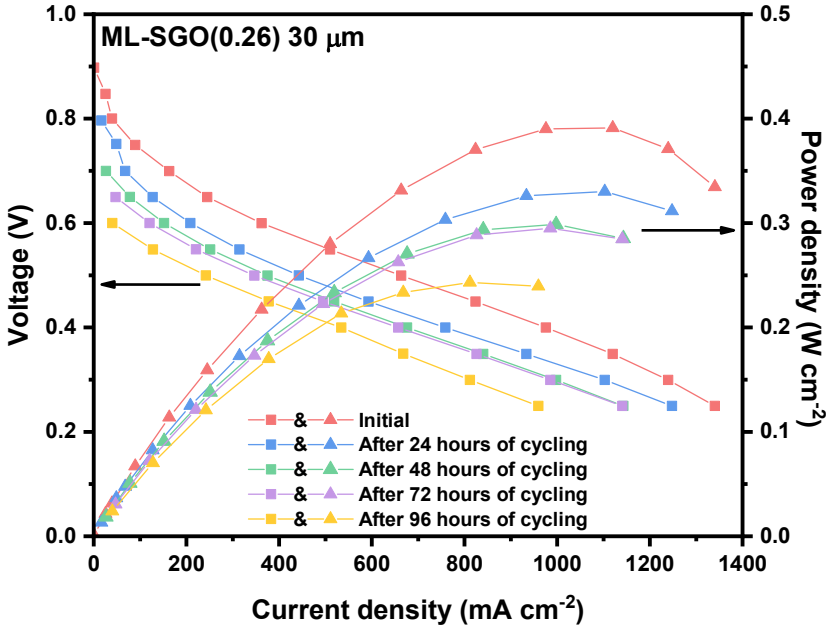



Figure 6-12: Polarisation and power curves of ML-SGO(0.26) during accelerated stress testing.

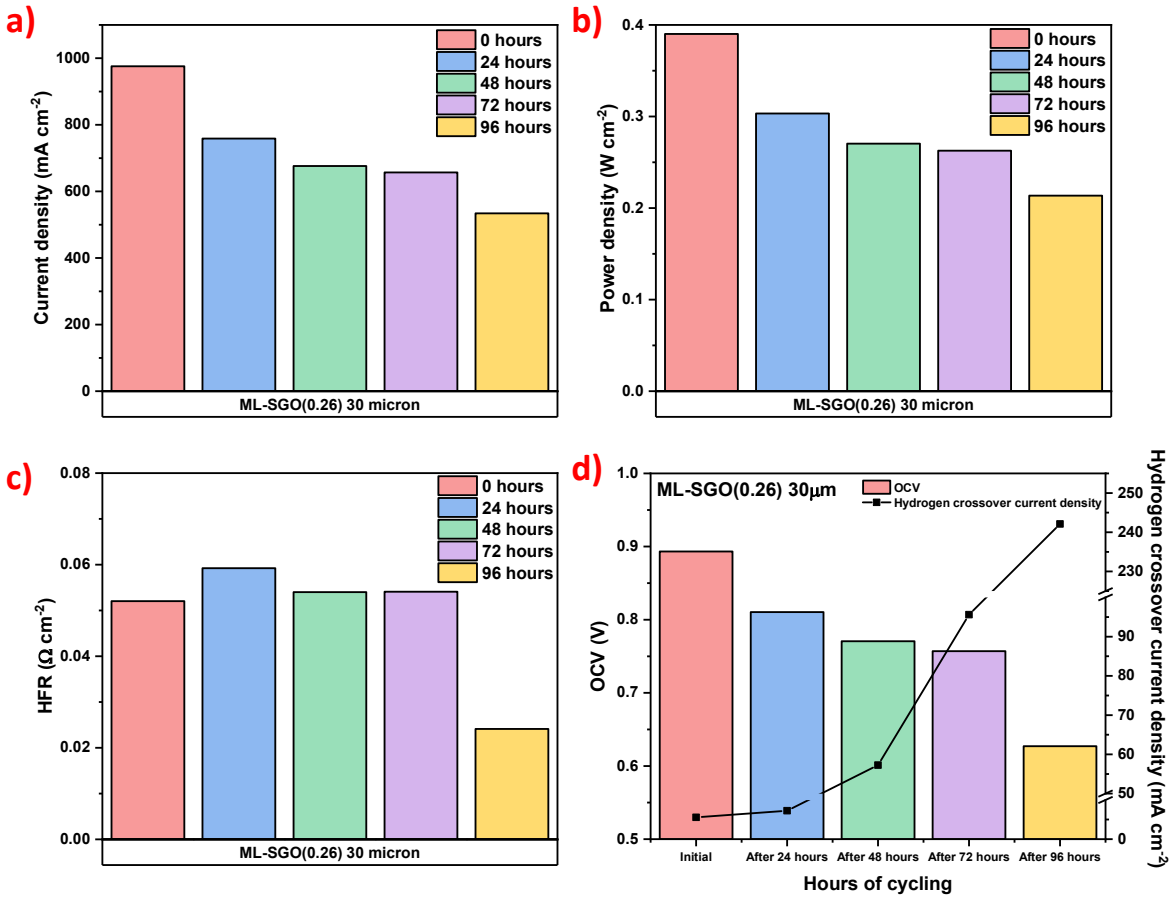



Figure 6-13: Results of ML-SGO(0.26): a) current density at 400 mV, b) power density at 400 mV, c) HFR and, d) hydrogen crossover current density and OCV during accelerated stress testing.

Table 6-4 summarises the test results of membranes with sulphonated GO and unmodified GO. It was observed that the use of SGO did little to change the maximum current and power density. However, the HFR was reduced with the addition of SGO, implying an improvement in the dispersion of the filler, specifically within the interface between the filler and polymer.

On the other hand, the performance of the multilayer membrane with SGO was reduced, and this could be the consequence of flooding at the cathode because of insufficient removal of water. Nevertheless, since the quantity of GO and SGO used in the multilayer was less than that in the single composite, it can be deduced that it was the result of something else.

One explanation is that the multilayer membrane with SGO can increase the amount of water within the membrane due to the sulphonic groups of GO but the multilayer structure makes exclusion of water tougher (such as water being trapped in between the layers), resulting in greater concentration losses.

Table 6-4: Influence of sulphonation on membrane performance.

| Sample | Maximum current density (mA $cm^{-2}$) | Maximum power density (W $cm^{-2}$) | HFR ($\Omega$ $cm^{-2}$) |
|---|---|---|---|
| Nafion-GO(1.5) | 1380 | 0.391 | 0.062 |
| Nafion-SGO(1.5) | 1350 | 0.390 | 0.042 |
| ML-GO(0.26) | 1588 | 0.471 | 0.050 |
| ML-SGO(0.26) | 1340 | 0.391 | 0.052 |

### 6.2.3 Single and multilayer membranes with synthesised sulphonated GO with a Nafion/Cerium oxide interlayer

To improve the longevity of the membranes during humidity cycling, cerium oxide was applied on both electrodes of the GDE prior to hot pressing. Figure 6-14 and Figure 6-15 present the polarisation and power curves, current and power densities at 400 mV, HFR and hydrogen crossover and OCV achieved by the single layer Nafion membrane with sulphonated graphene oxide with cerium oxide.

What was observed was that the sample lasted much longer, being able to produce an OCV above 0.6 V (the value where the test would be stopped) for one week. The polarisation curves from each day varied in terms of current and power density, but these variations did not show a pattern. What could have been occurring was that the loadings of the cerium oxide applied to the electrodes were too high, especially at the cathode side, as that is where the main mass transport losses occur. More water was produced at higher current densities and the presence of the cerium oxide could be blocking this area. The production of water and constant humidity cycling each day could result in migration of the cerium oxide. Migration of platinum catalyst nanoparticles from the catalyst layer into the membrane to form a platinum band has been observed in fuel cell testing[292], and migration of cerium oxide has also been observed[293–295]. Furthermore, the interlayer would result in an increase in the mean proton transport length in the catalyst layer, and thus decrease proton conductivity[296–298]. Also, the GDEs utilised have a "post coat" layer of Nafion to improve water management and adhesion to the membrane, which could be compromised with the addition of the interlayer.

Additionally, the presence of the Nafion/cerium oxide layer could be preventing the complete conditioning of the membrane prior to testing. This would result in an increase in current and

power density over several days. The presence of cerium oxide allowed the membrane sample to produce a consistent OCV value, being above 0.8 V every day. Furthermore, the hydrogen crossover current density was consistently around 9 mA $cm^{-2}$, showing that the cerium oxide was scavenging the radicals that were produced during the hydrogen crossover test. The application of cerium oxide has been shown to reduce hydrogen crossover in OCV holding tests, but also reduce cell performance[189,229,299,300].

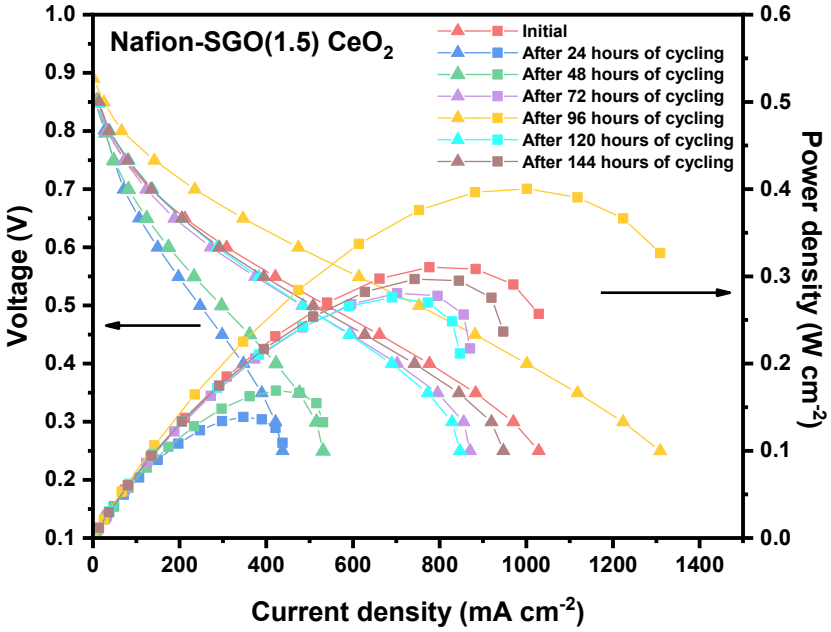



Figure 6-14: Polarisation and power curves of Nafion-SGO(1.5) with cerium oxide during accelerated stress testing.

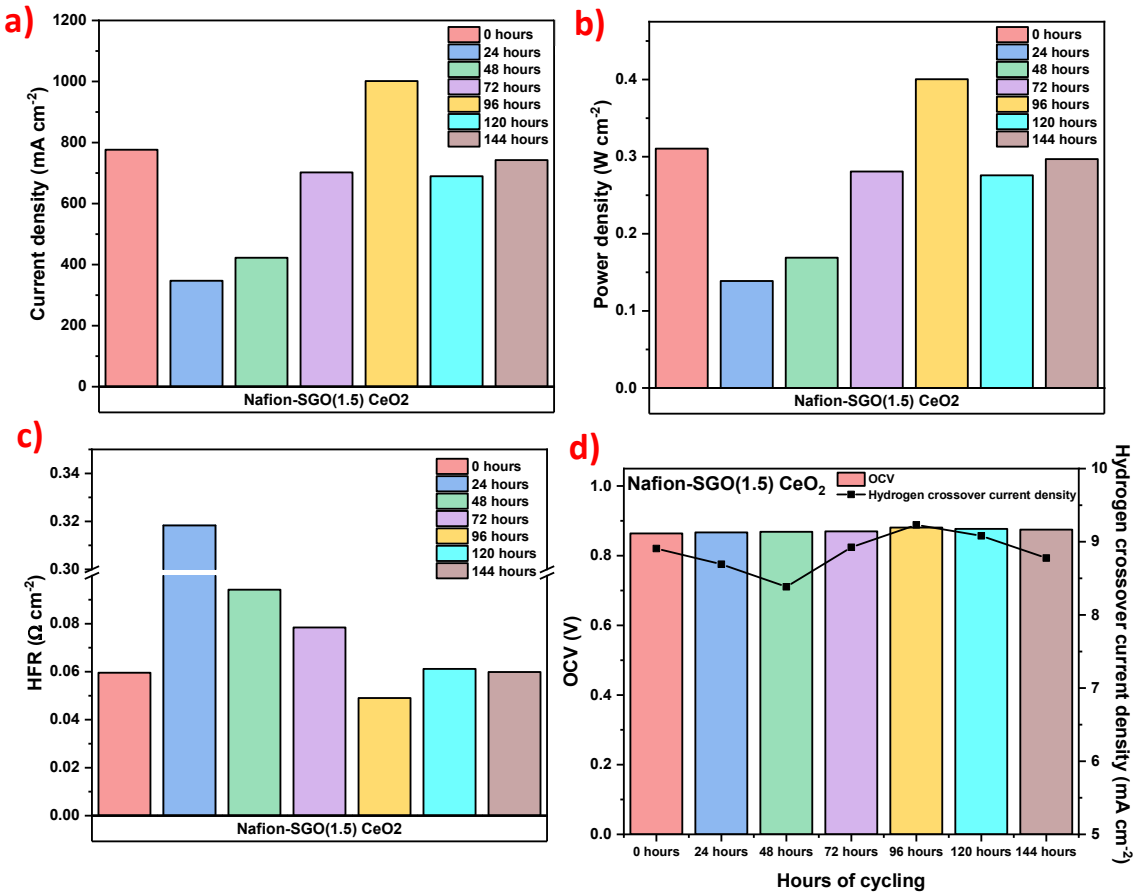



Figure 6-15: Results of Nafion-SGO(1.5) with cerium oxide: a) current density at 400 mV, b) power density at 400 mV, c) HFR and, d) hydrogen crossover current density and OCV during accelerated stress testing.

Figure 6-16 and Figure 6-17 show the fuel cell results for the multilayer membrane with the addition of cerium oxide. This sample shows a similar trend to the single layer membrane, with a drop in polarisation, current density, and power density after the first 24 hours of operation. The current and power density then improved, and the sample began to produce values similar to its initial values before the accelerated stress test, suggesting that the sample was not fully conditioned. Furthermore, the loading of cerium oxide should be optimised to a quantity that will not interfere with the mass transport process during high current density operation.

The OCV remained consistent each day for six days, producing an OCV value close to 0.9 V. The hydrogen crossover current density increased to 7.5 mA $cm^{-2}$ with an initial value of just below 5 mA $cm^{-2}$. The use of cerium oxide allowed the membrane to achieve consistent OCV and low hydrogen crossover even at an operating temperature of 100°C and low relative humidity.

This is in comparison to Nafion 211 without cerium oxide that was operated at 90°C, whose results are included in summary tables Table 6-5, Table 6-6, Table 6-7, Table 6-8, and Table 6-9. Nafion 211 was chosen instead of recast Nafion as Nafion 211 is an example of a polyelectrolyte membrane used in industry, instead of recast Nafion. After 96 hours, the sample experienced a hydrogen crossover current density just below 30 mA $cm^{-2}$, which is more than 3 times the hydrogen crossover current density produced by the samples with cerium oxide.

However, the Nafion 211 produced a much greater current and power density, which could be partly contributed to the slightly lower operating temperature of 90°C. Overall, further improvements are recommended in order for these sample to be competitive.

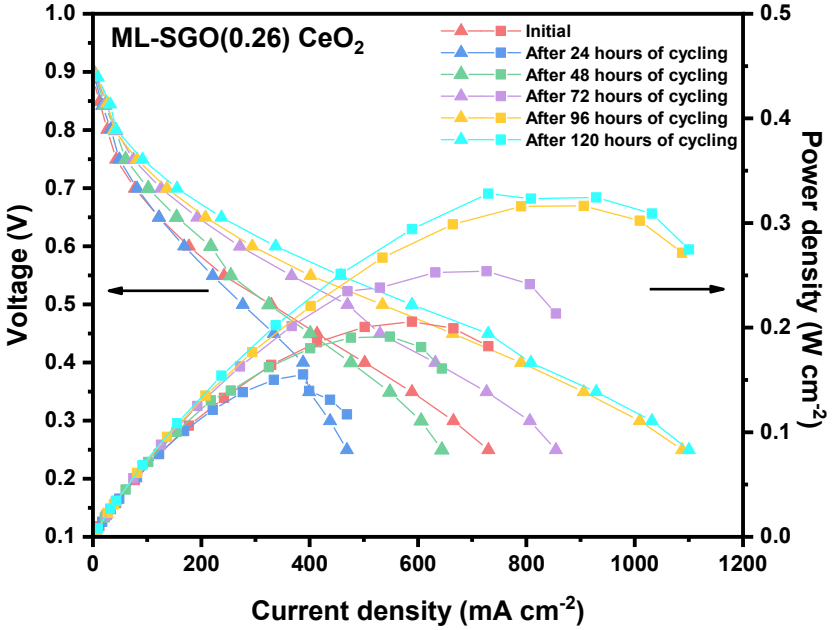



Figure 6-16: Polarisation and power curves of ML-SGO(0.26) with cerium oxide during accelerated stress testing.

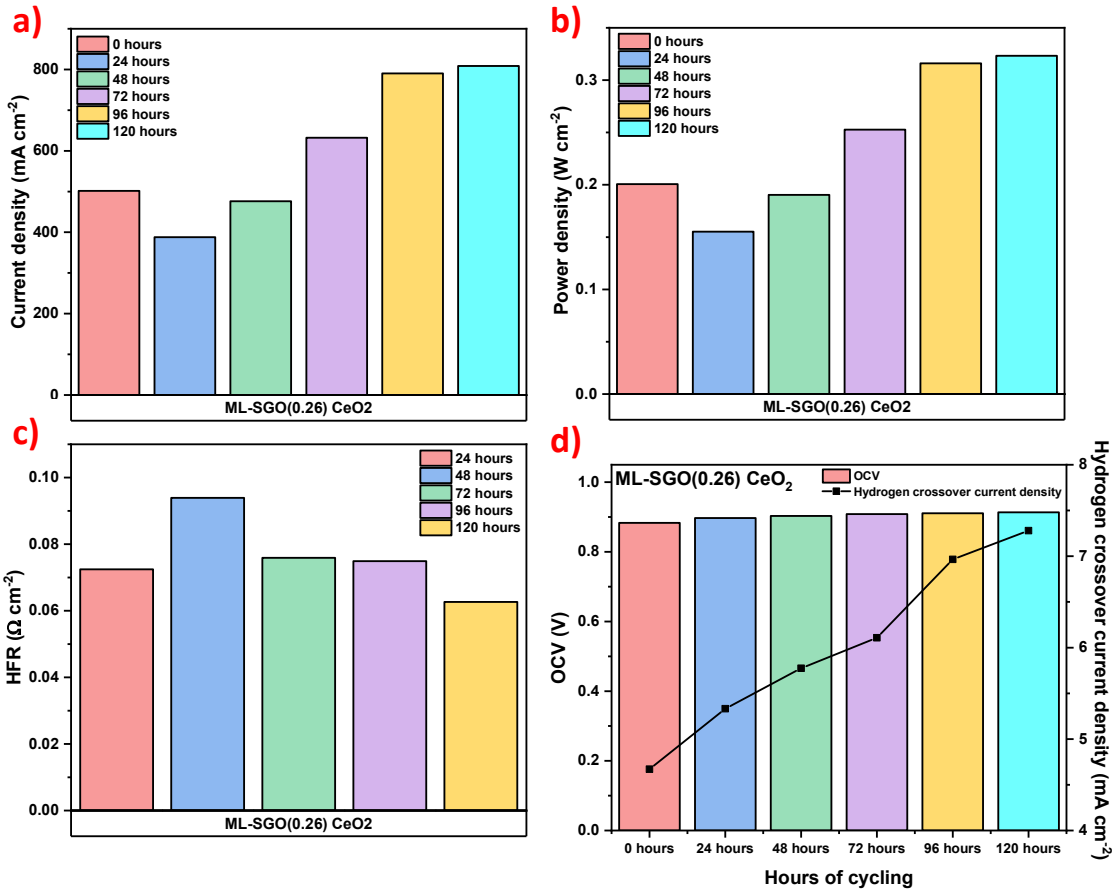



Figure 6-17: Results of ML-SGO(0.26) with cerium oxide: a) current density at 400 mV, b) power density at 400 mV, c) HFR and, d) hydrogen crossover current density and OCV during accelerated stress testing.

Table 6-5: Summary of AST testing; current density.

| Sample | Thickness (μm) | Temperature (°C) | Current density at 400 mV (mA $cm^{-2}$) | | | | | | |
|---|---|---|---|---|---|---|---|---|---|
| | | | 0 hours | 24 hours | 48 hours | 72 hours | 96 hours | 120 hours | 144 hours |
| Nafion-SGO(1.5) | 30 | 100 | 972 | 803 | 488 | 489 | X | X | X |
| ML-SGO(0.26) | 30 | 100 | 976 | 759 | 676 | 657 | 534 | X | X |
| Nafion-SGO(1.5) $CeO_2$ | 30 | 100 | 776 | 347 | 423 | 702 | 1001 | 690 | 742 |
| ML-SGO(1.5) $CeO_2$ | 30 | 100 | 502 | 388 | 476 | 632 | 790 | 809 | X |
| Nafion 211 | 25 | 90 | 2199 | 2266 | 2222 | 2179 | 2140 | X | X |

Table 6-6: Summary of AST testing; power density.

| Sample | Thickness (μm) | Temperature (°C) | Power density at 400 mV (W $cm^{-2}$) | | | | | | |
|---|---|---|---|---|---|---|---|---|---|
| | | | 0 hours | 24 hours | 48 hours | 72 hours | 96 hours | 120 hours | 144 hours |
| Nafion-SGO(1.5) | 30 | 100 | 0.39 | 0.32 | 0.20 | 0.20 | X | X | X |
| ML-SGO(0.26) | 30 | 100 | 0.39 | 0.30 | 0.27 | 0.26 | 0.21 | X | X |
| Nafion-SGO(1.5) $CeO_2$ | 30 | 100 | 0.31 | 0.14 | 0.17 | 0.28 | 0.40 | 0.28 | 0.30 |
| ML-SGO(1.5) $CeO_2$ | 30 | 100 | 0.20 | 0.16 | 0.19 | 0.25 | 0.32 | 0.32 | X |
| Nafion 211 | 25 | 90 | 0.88 | 0.91 | 0.89 | 0.87 | 0.86 | X | X |

Table 6-7: Summary of AST testing; HFR.

| Sample | Thickness (μm) | Temperature (°C) | HFR ($\Omega$ cm$^{-2}$) | | | | | | |
|---|---|---|---|---|---|---|---|---|---|
| | | | 0 hours | 24 hours | 48 hours | 72 hours | 96 hours | 120 hours | 144 hours |
| Nafion-SGO(1.5) | 30 | 100 | 0.046 | 0.051 | 2.128 | 0.847 | X | X | X |
| ML-SGO(0.26) | 30 | 100 | 0.052 | 0.059 | 0.054 | 0.054 | 0.024 | X | X |
| Nafion-SGO(1.5) $CeO_2$ | 30 | 100 | 0.060 | 0.318 | 0.094 | 0.078 | 0.049 | 0.061 | 0.060 |
| ML-SGO(1.5) $CeO_2$ | 30 | 100 | X | 0.072 | 0.094 | 0.076 | 0.075 | 0.063 | X |
| Nafion 211 | 25 | 90 | X | X | X | X | X | X | X |

Table 6-8: Summary of AST testing; hydrogen crossover current density.

| Sample | Thickness (μm) | Temperature (°C) | Hydrogen crossover current density (mA cm$^{-2}$) | | | | | | |
|---|---|---|---|---|---|---|---|---|---|
| | | | 0 hours | 24 hours | 48 hours | 72 hours | 96 hours | 120 hours | 144 hours |
| Nafion-SGO(1.5) | 30 | 100 | 5.33 | 10.58 | 372.94 | 358.53 | X | X | X |
| ML-SGO(0.26) | 30 | 100 | 5.56 | 7.26 | 57.27 | 95.61 | 242.10 | X | X |
| Nafion-SGO(1.5) $CeO_2$ | 30 | 100 | 8.91 | 8.69 | 8.34 | 8.92 | 9.23 | 9.08 | 8.78 |
| ML-SGO(1.5) $CeO_2$ | 30 | 100 | 4.67 | 5.33 | 5.77 | 6.11 | 6.97 | 7.28 | X |
| Nafion 211 | 25 | 90 | 6.60 | 7.36 | 9.08 | 12.84 | 29.83 | X | X |

Table 6-9: Summary of AST testing; OCV.

| Sample | Thickness (μm) | Temperature (°C) | OCV (V) | | | | | | |
|---|---|---|---|---|---|---|---|---|---|
| | | | 0 hours | 24 hours | 48 hours | 72 hours | 96 hours | 120 hours | 144 hours |
| Nafion-SGO(1.5) | 30 | 100 | 0.89 | 0.86 | 0.66 | 0.58 | X | X | X |
| ML-SGO(0.26) | 30 | 100 | 0.89 | 0.81 | 0.77 | 0.76 | 0.63 | X | X |
| Nafion-SGO(1.5) $CeO_2$ | 30 | 100 | 0.86 | 0.87 | 0.87 | 0.87 | 0.88 | 0.88 | 0.87 |
| ML-SGO(1.5) $CeO_2$ | 30 | 100 | 0.88 | 0.90 | 0.90 | 0.91 | 0.91 | 0.91 | X |
| Nafion 211 | 25 | 90 | 0.94 | 0.93 | 0.93 | 0.93 | 0.92 | X | X |

### 6.2.4 Progress assessment and best practices

The use of GO and cerium oxide significantly minimised hydrogen crossover during the AST and it is suggested that both are used as a filler for this purpose. However, the AST resulted in some of the membranes experiencing mechanical issues shown in large HFR.

Single layer membranes should be taken forward and reduced in thickness even further via the use of spraying for example. Progress in multilayer membranes should be focused on improving the adhesion between each layer.

It is recommended to increase the conditioning time for samples that utilise a Nafion and cerium oxide interlayer. Additionally, the loading of cerium oxide should be optimised both in the cathode and possibly at the anode too if required. Another suggestion involves incorporating the cerium oxide into the membrane or anchoring it onto the GO.

## 6.3 Conclusion

Membranes with parameters of 30 μm and 1.5/0.26 wt.% GO filler were prepared and tested in-situ with GO and SGO synthesised in-house. Additionally, the durability of the membranes was observed via an accelerated stress test.

There were some instances of high interfacial resistances. The thinner the membrane, the more likely there would be potential damage due to operating at intermediate temperatures and from the hydrating and drying process. Thus, use of multilayer membranes would require further development to prevent this effect. Sulphonation of graphene oxide did not produce a large difference in performance and hence further investigation is needed.

The use of cerium oxide applied on the electrode greatly reduced hydrogen crossover and allowed both the single layer and multilayer MEA to produce an OCV above 0.8 V and

experience a hydrogen crossover current density of below 10 mA $cm^{-2}$ after six days of humidity cycling. This was in comparison to samples without cerium oxide, which produced significantly larger hydrogen crossover current densities and whose OCV dropped below 0.6 V faster.

Further work in this area would involve optimising the loading of cerium oxide to prevent the irregular maximum current densities due to interference at the triple phase boundary and the water removal process. Furthermore, cerium oxide could be incorporated in the membrane layer itself, particularly for the multilayer membrane. In this case the Nafion layer on the cathode side would be doped with cerium oxide. Finally, the conditioning process should be increased to accommodate the addition of the Nafion/cerium oxide layer.

# 7 Conclusion and future directions

The aim of this thesis was to improve the durability of membranes used in PEFCs at intermediate temperature operation for potential automotive applications. Specifically, the use of graphene oxide was studied as a filler, hydrogen crossover. Furthermore, the architecture of the membrane, such as single and multilayer, was investigated.

Successful incorporation of GO into Nafion was confirmed via characterisation techniques such as ESEM. Furthermore, the introduction of GO increased water uptake from 16.84% for recast Nafion to 23.74% and 25.02% for Nafion-GO(1.5) and Nafion-GO(6), respectively.

Thinner membranes produced a greater current and power density at the cost of increased hydrogen crossover. The addition of GO reduced the maximum current and power output. This was due to the agglomeration of GO which produced regions of low proton conductivity. However, GO with higher oxygen functional group content (as identified through XPS) did not display this behaviour. Thus, the combination of thinner membranes with GO can potentially achieve high power output with reduced hydrogen crossover at intermediate temperatures. At an operating temperature of 120°C, Nafion produced a hydrogen crossover current density of 10.92 mA $cm^{-2}$, in comparison to Nafion-GO(1.5) which produced 5.94 mA $cm^{-2}$ and Nafion-GO(6) which achieved 2.62 mA $cm^{-2}$.

Further development in the production of thinner membranes could include the use of ultrasonic spraying onto a support to allow the fabrication of much thinner membranes. This would allow for greater fuel cell performance, reduced ohmic losses, with the support providing mechanical integrity. GO can be used in tandem to prevent the expected high levels of hydrogen crossover. This can be taken even further by preparing membranes that are just a few nanometres thick, generally consisting of defect-free 2D crystals that have been investigated due to their unique

sieving properties. It should be clarified that the mechanical support should not create a detrimental effect on fuel cell performance and is only present to prevent thin membranes from being damaged.

Multilayer membranes with three individual layers were successfully produced and tested in-situ. The use of multilayer membranes with GO also produced lower hydrogen crossover current density values of 5.23 mA $cm^{-2}$ for ML-GO(0.26) and 4.85 mA $cm^{-2}$ for ML-GO(1.05). However, there were occasions of delamination. An improvement would involve the use of crosslinking agents between each individual layer during the casting process, which would prevent water from being trapped between individual layers, mitigating swelling and delamination. Alternatively, single layer membranes and multilayer membranes can undergo a post-fabrication crosslinking process by submerging the membrane into an aqueous solution containing the crosslinking agent. Either way, a systematic study on crosslinking is recommended.

The durability of the prepared membranes was assessed through two durability tests, a 24-hour OCV holding test and an accelerated stress test involving humidity cycling. Single layer Nafion-GO(4.5) membranes experienced less thinning and OCV decay (0.83 mV $h^{-1}$) at 120°C in comparison to recast Nafion (5.38 mV $h^{-1}$).

The use of radical scavenging cerium oxide applied as a layer onto the gas diffusion electrode produced promising results in the accelerated stress tests, achieving lower hydrogen crossover current density than with pure Nafion 211 after a period of accelerated stress testing. Nafion 211 produced a hydrogen crossover current density value of 29.83 mA $cm^{-2}$ after four days. This is in comparison to Nafion-SGO(1.5) with cerium oxide that produced a value of 8.78 mA $cm^{-2}$ after six days, and ML-SGO(0.26) with cerium oxide that achieved 7.28 mA $cm^{-2}$ after

five days. Further development, such as optimisation of the loading and the different combinations at the anode and cathode, will be required. A suggestion would involve incorporating the cerium oxide nanoparticles into the layer closest to the cathode, to prevent potential migration, as shown in Figure 7-1.

Alternative propositions include anchoring the cerium oxide onto the GO to prevent particle migration during fuel cell operation, or optimising cerium oxide content in the catalyst layer to improve radical scavenging, without interfering in electrochemical reactions or prevent full membrane conditioning. Additional techniques such as analysis of fuel cell product water could provide greater knowledge on the extent of degradation during durability testing. The idea of a "self-healing" membrane, that is able to either prevent or mitigate membrane degradation during fuel cell operation is an ambitious one that should be investigated.

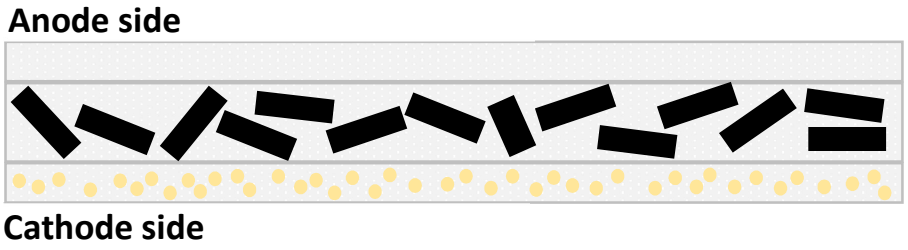



Figure 7-1: Schematic of an alternative multilayer design, with GO in the middle layer and cerium oxide nanoparticles in the cathode side layer.

Finally, the idea of fabricating an entirely "green" membrane by combining non-PFSA polymers such as nanocellulose, with natural fillers such as clays, and green solvents such as water and ethanol should be explored to provide an alternative to PFSA membranes.

# LIST OF REFERENCES


1. Lashof, D. A. & Ahuja, D. R. Relative contributions of greenhouse gas emissions to global warming. *Nat. 1990 3446266* **344**, 529–531 (1990).

2. Dignon, J. NOx and SOx emissions from fossil fuels: A global distribution. *Atmos. Environ. Part A. Gen. Top.* **26**, 1157–1163 (1992).

3. Lamb, W. F., Wiedmann, T., Pongratz, J., Andrew, R., Crippa, M., Olivier, J. G. J., Wiedenhofer, D., Mattioli, G., Khourdajie, A. Al, House, J., Pachauri, S., Figueroa, M., Saheb, Y., Slade, R., Hubacek, K., Sun, L., Ribeiro, S. K., Khennas, S., De La Rue Du Can, S., *et al.* A review of trends and drivers of greenhouse gas emissions by sector from 1990 to 2018. *Environ. Res. Lett.* **16**, 073005 (2021).

4. Sanchez, L. F. & Stern, D. I. Drivers of industrial and non-industrial greenhouse gas emissions. *Ecol. Econ.* **124**, 17–24 (2016).

5. Ritchie, H. & Roser, M. Sector by sector: where do global greenhouse gas emissions come from? *Our World Data* (2023).

6. Intergovernmental Panel on Climate Change. *Synthesis Report. A Report of the Intergovernmental Panel on Climate Change. Contribution of Working Groups I, II and III to the Sixth Assessment Report of the Intergovernmental Panel on Climate Change [Core Writing Team, H. Lee and J. Romero (Eds.)]*. *European University Institute* (2023).

7. Clémençon, R. The Two Sides of the Paris Climate Agreement: Dismal Failure or Historic Breakthrough? *J. Environ. Dev.* **25**, 3–24 (2016).

8. Wang, Y., Liu, Y. & Gu, B. COP26: Progress, Challenges, and Outlook. *Adv. Atmos. Sci.* **39**, 1209–1216 (2022).

9. Peters, R. L. Effects of global warming on forests. *For. Ecol. Manage.* **35**, 13–33 (1990).

10. Botkin, D. B., Saxe, H., Araújo, M. B., Betts, R., Bradshaw, R. H. W., Cedhagen, T., Chesson, P., Dawson, T. P., Etterson, J. R., Faith, D. P., Ferrier, S., Guisan, A., Hansen, A. S., Hilbert, D. W., Loehle, C., Margules, C., New, M., Sobel, M. J. & Stockwell, D. R. B. Forecasting the Effects of Global Warming on Biodiversity. *Bioscience* **57**, 227–236 (2007).

11. Kurane, I. The Effect of Global Warming on Infectious Diseases. *Osong Public Heal. Res. Perspect.* **1**, 4–9 (2010).

12. McCarthy, M. P., Best, M. J. & Betts, R. A. Climate change in cities due to global warming and urban effects. *Geophys. Res. Lett.* **37**, (2010).

13. Ding, Y., Zhang, S., Zhao, L., Li, Z. & Kang, S. Global warming weakening the inherent stability of glaciers and permafrost. *Sci. Bull.* **64**, 245–253 (2019).

14. Ekins, P., Summerton, P., Thoung, C. & Lee, D. A Major Environmental Tax Reform for the UK: Results for the Economy, Employment and the Environment. *Environ.*

*Resour. Econ.* **50**, 447–474 (2011).

15. Holman, C., Harrison, R. & Querol, X. Review of the efficacy of low emission zones to improve urban air quality in European cities. *Atmos. Environ.* **111**, 161–169 (2015).

16. Jones, A. M., Harrison, R. M., Barratt, B. & Fuller, G. A large reduction in airborne particle number concentrations at the time of the introduction of "sulphur free" diesel and the London Low Emission Zone. *Atmos. Environ.* **50**, 129–138 (2012).

17. Shaheen, S. A. & Lipman, T. E. Reducing greenhouse emissions and fuel consumption: Sustainable Approaches for Surface Transportation. *IATSS Res.* **31**, 6–20 (2007).

18. Kannan, N. & Vakeesan, D. Solar energy for future world: - A review. *Renew. Sustain. Energy Rev.* **62**, 1092–1105 (2016).

19. Joselin Herbert, G. M., Iniyan, S., Sreevalsan, E. & Rajapandian, S. A review of wind energy technologies. *Renew. Sustain. Energy Rev.* **11**, 1117–1145 (2007).

20. Yüksel, I. Hydropower for sustainable water and energy development. *Renew. Sustain. Energy Rev.* **14**, 462–469 (2010).

21. Yang, Y., Bremner, S., Menictas, C. & Kay, M. Battery energy storage system size determination in renewable energy systems: A review. *Renew. Sustain. Energy Rev.* **91**, 109–125 (2018).

22. Li, M., Lu, J., Chen, Z. & Amine, K. 30 Years of Lithium-Ion Batteries. *Adv. Mater.* **30**, 1800561 (2018).

23. Ajanovic, A. The future of electric vehicles: prospects and impediments. *Wiley Interdiscip. Rev. Energy Environ.* **4**, 521–536 (2015).

24. Hardt, C. & Bogenberger, K. Usage of e-Scooters in Urban Environments. *Transp. Res. Procedia* **37**, 155–162 (2019).

25. Mahmoudzadeh Andwari, A., Pesiridis, A., Rajoo, S., Martinez-Botas, R. & Esfahanian, V. A review of Battery Electric Vehicle technology and readiness levels. *Renew. Sustain. Energy Rev.* **78**, 414–430 (2017).

26. Sandy Thomas, C. E. "How green are electric vehicles?" *Int. J. Hydrogen Energy* **37**, 6053–6062 (2012).

27. Shiau, C. S. N., Samaras, C., Hauffe, R. & Michalek, J. J. Impact of battery weight and charging patterns on the economic and environmental benefits of plug-in hybrid vehicles. *Energy Policy* **37**, 2653–2663 (2009).

28. Al-Mufachi, N. A. & Shah, N. The role of hydrogen and fuel cell technology in providing security for the UK energy system. *Energy Policy* **171**, 113286 (2022).

29. Edwards, R. L., Font-Palma, C. & Howe, J. The status of hydrogen technologies in the UK: A multi-disciplinary review. *Sustain. Energy Technol. Assessments* **43**, 100901 (2021).

30. Manoharan, Y., Hosseini, S. E., Butler, B., Alzhahrani, H., Senior, B. T. F., Ashuri, T. & Krohn, J. Hydrogen fuel cell vehicles; Current status and future prospect. *Appl. Sci.* **9**, 2296 (2019).

31. Lee, D. Y., Elgowainy, A., Kotz, A., Vijayagopal, R. & Marcinkoski, J. Life-cycle implications of hydrogen fuel cell electric vehicle technology for medium- and heavy-duty trucks. *J. Power Sources* **393**, 217–229 (2018).

32. Camacho, M. de las N., Jurburg, D. & Tanco, M. Hydrogen fuel cell heavy-duty trucks: Review of main research topics. *Int. J. Hydrogen Energy* **47**, 29505–29525 (2022).

33. Stockford, C., Brandon, N., Irvine, J., Mays, T., Metcalfe, I., Book, D., Ekins, P., Kucernak, A., Molkov, V., Steinberger-Wilckens, R., Shah, N., Dodds, P., Dueso, C., Samsatli, S. & Thompson, C. H2FC SUPERGEN: An overview of the Hydrogen and Fuel Cell research across the UK. *Int. J. Hydrogen Energy* **40**, 5534–5543 (2015).

34. Matsumura, Y. & Nakamori, T. Steam reforming of methane over nickel catalysts at low reaction temperature. *Appl. Catal. A Gen.* **258**, 107–114 (2004).

35. Newsome, D. S. The Water-Gas Shift Reaction. *Catal. Rev. Sci. Eng.* **21**, 275–318 (1980).

36. Dawood, F., Anda, M. & Shafiullah, G. M. Hydrogen production for energy: An overview. *Int. J. Hydrogen Energy* **45**, 3847–3869 (2020).

37. Hermesmann, M. & Müller, T. E. Green, Turquoise, Blue, or Grey? Environmentally friendly Hydrogen Production in Transforming Energy Systems. *Prog. Energy Combust. Sci.* **90**, (2022).

38. Velazquez Abad, A. & Dodds, P. E. Green hydrogen characterisation initiatives: Definitions, standards, guarantees of origin, and challenges. *Energy Policy* **138**, 111300 (2020).

39. Dixon, J., Bell, K. & Brush, S. Which way to net zero? a comparative analysis of seven UK 2050 decarbonisation pathways. *Renew. Sustain. Energy Transit.* **2**, 100016 (2022).

40. Hammond, G. P. The UK industrial decarbonisation strategy revisited. *Proc. Inst. Civ. Eng. - Energy* **175**, 30–44 (2022).

41. Pye, S., Li, F. G. N., Price, J. & Fais, B. Achieving net-zero emissions through the reframing of UK national targets in the post-Paris Agreement era. *Nat. Energy* **2**, 17024 (2017).

42. van der Spek, M., Banet, C., Bauer, C., Gabrielli, P., Goldthorpe, W., Mazzotti, M., Munkejord, S. T., Røkke, N. A., Shah, N., Sunny, N., Sutter, D., Trusler, J. M. & Gazzani, M. Perspective on the hydrogen economy as a pathway to reach net-zero CO2 emissions in Europe. *Energy Environ. Sci.* **15**, 1034–1077 (2022).

43. Vielstich, W., Gasteiger, H. A. & Yokokawa, H. *Handbook of Fuel Cells: Advances in Electrocatalysis, Materials, Diagnostics and Durability, Volumes 5 and 6*. (John Wiley & Sons, 2009).

44. Carrette, L., Friedrich, K. A. & Stimming, U. Fuel Cells: Principles, Types, Fuels, and Applications. *CHEMPHYSCHEM* **1**, 162–193 (2000).

45. Kamarudin, S. K., Daud, W. R. W., Ho, S. L. & Hasran, U. A. Overview on the challenges and developments of micro-direct methanol fuel cells (DMFC). *J. Power Sources* **163**, 743–754 (2007).

46. McLean, G. F., Niet, T., Prince-Richard, S. & Djilali, N. An assessment of alkaline fuel cell technology. *Int. J. Hydrogen Energy* **27**, 507–526 (2002).

47. Dokiya, M. SOFC system and technology. *Solid State Ionics* **152**–**153**, 383–392 (2002).

48. Stambouli, A. B. & Traversa, E. Solid oxide fuel cells (SOFCs): a review of an environmentally clean and efficient source of energy. *Renew. Sustain. Energy Rev.* **6**, 433–455 (2002).

49. Kamarudin, S. K., Achmad, F. & Daud, W. R. W. Overview on the application of direct methanol fuel cell (DMFC) for portable electronic devices. *Int. J. Hydrogen Energy* **34**, 6902–6916 (2009).

50. Araya, S. S., Zhou, F., Liso, V., Sahlin, S. L., Vang, J. R., Thomas, S., Gao, X., Jeppesen, C. & Kær, S. K. A comprehensive review of PBI-based high temperature PEM fuel cells. *Int. J. Hydrogen Energy* **41**, 21310–21344 (2016).

51. Mekhilef, S., Saidur, R. & Safari, A. Comparative study of different fuel cell technologies. *Renew. Sustain. Energy Rev.* **16**, 981–989 (2012).

52. Wang, Y., Chen, K. S., Mishler, J., Cho, S. C. & Adroher, X. C. A review of polymer electrolyte membrane fuel cells: Technology, applications, and needs on fundamental research. *Appl. Energy* **88**, 981–1007 (2011).

53. Blum, L., Meulenberg, W. A., Nabielek, H. & Steinberger-Wilckens, R. Worldwide SOFC Technology Overview and Benchmark. *Int. J. Appl. Ceram. Technol.* **2**, 482–492 (2005).

54. Dicks, A. L. Molten carbonate fuel cells. *Curr. Opin. Solid State Mater. Sci.* **8**, 379–383 (2004).

55. Wei, C., Rao, R. R., Peng, J., Huang, B., Stephens, I. E. L., Risch, M., Xu, Z. J. & Shao-Horn, Y. Recommended Practices and Benchmark Activity for Hydrogen and Oxygen Electrocatalysis in Water Splitting and Fuel Cells. *Adv. Mater.* **31**, 1806296 (2019).

56. Reimer, U., Lehnert, W., Holade, Y. & Kokoh, B. Irreversible losses in fuel cells. *Fuel Cells Hydrog. From Fundam. to Appl. Res.* 15–40 (2018).

57. Mann, R. F., Amphlett, J. C., Peppley, B. A. & Thurgood, C. P. Application of Butler–Volmer equations in the modelling of activation polarization for PEM fuel cells. *J. Power Sources* **161**, 775–781 (2006).

58. Niya, S. M. R. & Hoorfar, M. Process modeling of the ohmic loss in proton exchange membrane fuel cells. *Electrochim. Acta* **120**, 193–203 (2014).

59. Berg, P., Promislow, K., St. Pierre, J., Stumper, J. & Wetton, B. Water Management in PEM Fuel Cells. *J. Electrochem. Soc.* **151**, A341 (2004).

60. Zhang, J., Zhang, H., Wu, J. & Zhang, J. Chapter 1 - PEM Fuel Cell Fundamentals. in *PEM Fuel Cell Testing and Diagnosis* 1–42 (Elsevier B.V, 2013).

61. Middelman, E., Kout, W., Vogelaar, B., Lenssen, J. & de Waal, E. Bipolar plates for

PEM fuel cells. *J. Power Sources* **118**, 44–46 (2003).

62. Park, S., Lee, J.-W. & Popov, B. N. A review of gas diffusion layer in PEM fuel cells: Materials and designs. *Int. J. Hydrogen Energy* **37**, 5850–5865 (2012).

63. Litster, S. & McLean, G. PEM fuel cell electrodes. *J. Power Sources* **130**, 61–76 (2004).

64. Beuscher, U., Cleghorn, S. J. C. & Johnson, W. B. Challenges for PEM fuel cell membranes. *Int. J. Energy Res.* **29**, 1103–1112 (2005).

65. Yu, X., Zhou, B. & Sobiesiak, A. Water and thermal management for Ballard PEM fuel cell stack. *J. Power Sources* **147**, 184–195 (2005).

66. Corbo, P., Migliardini, F. & Veneri, O. Performance investigation of 2.4kW PEM fuel cell stack in vehicles. *Int. J. Hydrogen Energy* **32**, 4340–4349 (2007).

67. Chan, C. C. The State of the Art of Electric, Hybrid, and Fuel Cell Vehicles. *Proc. IEEE* **95**, 704–718 (2007).

68. Ling-Chin, J., Giampieri, A., Wilks, M., Lau, S. W., Bacon, E., Sheppard, I., Smallbone, A. J. & Roskilly, A. P. Technology roadmap for hydrogen-fuelled transportation in the UK. *Int. J. Hydrogen Energy* **52**, 705–733 (2024).

69. Gharibeh, H. F., Yazdankhah, A. S. & Azizian, M. R. Energy management of fuel cell electric vehicles based on working condition identification of energy storage systems, vehicle driving performance, and dynamic power factor. *J. Energy Storage* **31**, 101760 (2020).

70. Oriani, R. A. Hydrogen embrittlement of steels. *Annu. Rev. Mater. Res.* 327–57 (1978).

71. Dwivedi, S. K. & Vishwakarma, M. Hydrogen embrittlement in different materials: A review. *Int. J. Hydrogen Energy* **43**, 21603–21616 (2018).

72. Caponi, R., Monforti Ferrario, A., Del Zotto, L. & Bocci, E. Hydrogen refueling stations and fuel cell buses four year operational analysis under real-world conditions. *Int. J. Hydrogen Energy* **48**, 20957–20970 (2023).

73. Genovese, M. & Fragiacomo, P. Hydrogen refueling station: Overview of the technological status and research enhancement. *J. Energy Storage* **61**, 106758 (2023).

74. Messaoudani, Z. labidine, Rigas, F., Binti Hamid, M. D. & Che Hassan, C. R. Hazards, safety and knowledge gaps on hydrogen transmission via natural gas grid: A critical review. *Int. J. Hydrogen Energy* **41**, 17511–17525 (2016).

75. Abohamzeh, E., Salehi, F., Sheikholeslami, M., Abbassi, R. & Khan, F. Review of hydrogen safety during storage, transmission, and applications processes. *J. Loss Prev. Process Ind.* **72**, 104569 (2021).

76. Najjar, Y. S. H. Hydrogen safety: The road toward green technology. *Int. J. Hydrogen Energy* **38**, 10716–10728 (2013).

77. Sealy, C. The problem with platinum. *Mater. Today* **11**, 65–68 (2008).

78. Holton, O. T. & Stevenson, J. W. The role of platinum in proton exchange membrane

fuel cells. *Platin. Met. Rev.* **57**, 259–271 (2013).

79. Yang, C. J. An impending platinum crisis and its implications for the future of the automobile. *Energy Policy* **37**, 1805–1808 (2009).

80. Ogungbemi, E., Ijaodola, O., Khatib, F. N., Wilberforce, T., El Hassan, Z., Thompson, J., Ramadan, M. & Olabi, A. G. Fuel cell membranes – Pros and cons. *Energy* **172**, 155–172 (2019).

81. Minke, C., Suermann, M., Bensmann, B. & Hanke-Rauschenbach, R. Is iridium demand a potential bottleneck in the realization of large-scale PEM water electrolysis? *Int. J. Hydrogen Energy* **46**, 23581–23590 (2021).

82. Wang, C., Lan, F., He, Z., Xie, X., Zhao, Y., Hou, H., Guo, L., Murugadoss, V., Liu, H., Shao, Q., Gao, Q., Ding, T., Wei, R. & Guo, Z. Iridium-Based Catalysts for Solid Polymer Electrolyte Electrocatalytic Water Splitting. *ChemSusChem* **12**, 1576–1590 (2019).

83. Wang, C., Wang, S., Peng, L., Zhang, J., Shao, Z., Huang, J., Sun, C., Ouyang, M. & He, X. Recent Progress on the Key Materials and Components for Proton Exchange Membrane Fuel Cells in Vehicle Applications. *Energies 2016, Vol. 9, Page 603* **9**, 603 (2016).

84. Nunes, S. P. & Peinemann, K.-V. *Membrane Technology: In the Chemical Industry*. (John Wiley & Sons, 2006).

85. Nunes, S. P., Culfaz-Emecen, P. Z., Ramon, G. Z., Visser, T., Koops, G. H., Jin, W. & Ulbricht, M. Thinking the future of membranes: Perspectives for advanced and new membrane materials and manufacturing processes. *J. Memb. Sci.* **598**, 117761 (2020).

86. Lakshminarayanaiah, N. Transport Phenomena in Artificial Membranes. *Chem. Rev.* **65**, 491–565 (1965).

87. Wijmans, J. G. & Baker, R. W. The solution-diffusion model: a review. *J. Memb. Sci.* **107**, 1–21 (1995).

88. Banerjee, S. & Curtin, D. E. Nafion® perfluorinated membranes in fuel cells. *J. Fluor. Chem.* **125**, 1211–1216 (2004).

89. Eldin, M. S. M., Elzatahry, A. A., El-Khatib, K. M., Hassan, E. A., El-Sabbah, M. M. & Abu-Saied, M. A. Novel grafted nafion membranes for proton-exchange membrane fuel cell applications. *J. Appl. Polym. Sci.* **119**, 120–133 (2011).

90. Mauritz, K. A. & Moore, R. B. State of Understanding of Nafion. *Chem. Rev.* **104**, 4535–4586 (2004).

91. Karimi, M. B., Mohammadi, F. & Hooshyari, K. Recent approaches to improve Nafion performance for fuel cell applications: A review. *Int. J. Hydrogen Energy* **44**, 28919–28938 (2019).

92. El-kharouf, A., Chandan, A., Hattenberger, M. & Pollet, B. G. Proton exchange membrane fuel cell degradation and testing: review. *J. Energy Inst.* **85**, 188–200 (2012).

93. Gierke, T. D. & Hsu, W. Y. The Cluster—Network Model of Ion Clustering in Perfluorosulfonated Membranes. in *Perfluorinated Ionomer Membranes* vol. 180 13–283 (American Chemical Society (ACS), 1982).

94. Saito, M., Hayamizu, K. & Okada, T. Temperature dependence of ion and water transport in perfluorinated ionomer membranes for fuel cells. *J. Phys. Chem. B* **109**, 3112–3119 (2005).

95. Agmon, N. The Grotthuss mechanism. *Chem. Phys. Lett.* **244**, 456–462 (1995).

96. Ludueña, G. A., Kühne, T. D. & Sebastiani, D. Mixed Grotthuss and Vehicle Transport Mechanism in Proton Conducting Polymers from Ab initio Molecular Dynamics Simulations. *Chem. Mater.* **23**, 1424–1429 (2011).

97. Carbone, A., Castriciano, M. A., Scolaro, L. M. & Gatto, I. Novel Polymeric Composite TPPS/s-PEEK Membranes for Low Relative Humidity PEFC. *Polym. 2020, Vol. 12, Page 1431* **12**, 1431 (2020).

98. Miller, E. L., Thompson, S. T., Randolph, K., Hulvey, Z., Rustagi, N. & Satyapal, S. US Department of Energy hydrogen and fuel cell technologies perspectives. *MRS Bull.* **45**, 57–64 (2020).

99. U.S. Department of Energy. DOE Technical Targets for Polymer Electrolyte Membrane Fuel Cell Components, Department of Energy, Hydrogen and Fuel Cell Technologies Office. 1–8 at (2020).

100. Gittleman, C. S., Kongkanand, A., Masten, D. & Gu, W. Materials research and development focus areas for low cost automotive proton-exchange membrane fuel cells. *Curr. Opin. Electrochem.* **18**, 81–89 (2019).

101. Banerjee, S. & Curtin, D. E. Nafion®perfluorinated membranes in fuel cells. *J. Fluor. Chem.* **125**, 1211–1216 (2004).

102. Ahmad, S., Nawaz, T., Ali, A., Orhan, M. F., Samreen, A. & Kannan, A. M. An overview of proton exchange membranes for fuel cells: Materials and manufacturing. *Int. J. Hydrogen Energy* **47**, 19086–19131 (2022).

103. Park, J.-S., Shin, M.-S. & Kim, C.-S. Proton exchange membranes for fuel cell operation at low relative humidity and intermediate temperature: An updated review. *Curr. Opin. Electrochem.* **5**, 43–55 (2017).

104. Chandan, A., Hattenberger, M., El-kharouf, A., Du, S., Dhir, A., Self, V., Pollet, B. G., Ingram, A. & Bujalski, W. High temperature (HT) polymer electrolyte membrane fuel cells (PEMFC) – A review. *J. Power Sources* **231**, 264–278 (2013).

105. Marrony, M., Barrera, R., Quenet, S., Ginocchio, S., Montelatici, L. & Aslanides, A. Durability study and lifetime prediction of baseline proton exchange membrane fuel cell under severe operating conditions. *J. Power Sources* **182**, 469–475 (2008).

106. Jung, H. Y. & Kim, J. W. Role of the glass transition temperature of Nafion 117 membrane in the preparation of the membrane electrode assembly in a direct methanol fuel cell (DMFC). *Int. J. Hydrogen Energy* **37**, 12580–12585 (2012).

107. Jean-Fulcrand, A., Masen, M. A., Bremner, T. & Wong, J. S. S. High temperature

tribological properties of polybenzimidazole (PBI). *Polymer (Guildf).* **128**, 159–168 (2017).

108. Li, Q., He, R., Jensen, J. O. & Bjerrum, N. J. PBI-based polymer membranes for high temperature fuel cells - Preparation, characterization and fuel cell demonstration. *Fuel Cells* **4**, 147–159 (2004).

109. Qi, Z. & Kaufman, A. Activation of low temperature PEM fuel cells. *J. Power Sources* **111**, 181–184 (2002).

110. Li, H., Tang, Y., Wang, Z., Shi, Z., Wu, S., Song, D., Zhang, J., Fatih, K., Zhang, J., Wang, H., Liu, Z., Abouatallah, R. & Mazza, A. A review of water flooding issues in the proton exchange membrane fuel cell. *J. Power Sources* **178**, 103–117 (2008).

111. Fernihough, O., Ismail, M. S. & El-kharouf, A. Intermediate Temperature PEFC's with Nafion® 211 Membrane Electrolytes: An Experimental and Numerical Study. *Membranes* vol. 12 (2022).

112. Dupuis, A.-C. Proton exchange membranes for fuel cells operated at medium temperatures: Materials and experimental techniques. *Prog. Mater. Sci.* **56**, 289–327 (2011).

113. Subianto, S. Recent advances in polybenzimidazole/phosphoric acid membranes for high-temperature fuel cells. *Polym. Int.* **63**, 1134–1144 (2014).

114. Li, Q., Jensen, J. O., Savinell, R. F. & Bjerrum, N. J. High temperature proton exchange membranes based on polybenzimidazoles for fuel cells. *Prog. Polym. Sci.* **34**, 449–477 (2009).

115. Alberti, G., Casciola, M., Massinelli, L. & Bauer, B. Polymeric proton conducting membranes for medium temperature fuel cells (110–160°C). *J. Memb. Sci.* **185**, 73–81 (2001).

116. Kaliaguine, S., Mikhailenko, S. D., Wang, K. P., Xing, P., Robertson, G. & Guiver, M. Properties of SPEEK based PEMs for fuel cell application. *Catal. Today* **82**, 213–222 (2003).

117. Zhang, J., Xie, Z., Zhang, J., Tang, Y., Song, C., Navessin, T., Shi, Z., Song, D., Wang, H., Wilkinson, D. P., Liu, Z.-S. & Holdcroft, S. High temperature PEM fuel cells. *J. Power Sources* **160**, 872–891 (2006).

118. Søndergaard, T., Cleemann, L. N., Becker, H., Aili, D., Steenberg, T., Hjuler, H. A., Seerup, L., Li, Q. & Jensen, J. O. Long-term durability of HT-PEM fuel cells based on thermally cross-linked polybenzimidazole. *J. Power Sources* **342**, 570–578 (2017).

119. Waller, M. G., Walluk, M. R. & Trabold, T. A. Performance of high temperature PEM fuel cell materials. Part 1: Effects of temperature, pressure and anode dilution. *Int. J. Hydrogen Energy* **41**, 2944–2954 (2016).

120. Guo, Z., Perez-Page, M., Chen, J., Ji, Z. & Holmes, S. M. Recent advances in phosphoric acid–based membranes for high–temperature proton exchange membrane fuel cells. *J. Energy Chem.* **63**, 393–429 (2021).

121. Meier, J. C., Galeano, C., Katsounaros, I., Topalov, A. A., Kostka, A., Schüth, F. &

Mayrhofer, K. J. J. Degradation Mechanisms of Pt/C Fuel Cell Catalysts under Simulated Start–Stop Conditions. *ACS Catal.* **2**, 832–843 (2012).

122. Zhang, T., Wang, P., Chen, H. & Pei, P. A review of automotive proton exchange membrane fuel cell degradation under start-stop operating condition. *Appl. Energy* **223**, 249–262 (2018).

123. Tang, Q., Li, B., Yang, D., Ming, P., Zhang, C. & Wang, Y. Review of hydrogen crossover through the polymer electrolyte membrane. *Int. J. Hydrogen Energy* **46**, 22040–22061 (2021).

124. Zhao, N., Chu, Y., Xie, Z., Eggen, K., Girard, F. & Shi, Z. Effects of Fuel Cell Operating Conditions on Proton Exchange Membrane Durability at Open-Circuit Voltage. *Fuel Cells* **20**, 176–184 (2020).

125. Okonkwo, P. C., Ben Belgacem, I., Emori, W. & Uzoma, P. C. Nafion degradation mechanisms in proton exchange membrane fuel cell (PEMFC) system: A review. *Int. J. Hydrogen Energy* **46**, 27956–27973 (2021).

126. Lü, W., Liu, Z., Wang, C., Mao, Z. & Zhang, M. The effects of pinholes on proton exchange membrane fuel cell performance. *Int. J. Energy Res.* **35**, 24–30 (2011).

127. Baik, K. D., Hong, B. K. & Kim, M. S. Novel technique for measuring oxygen crossover through the membrane in polymer electrolyte membrane fuel cells. *Int. J. Hydrogen Energy* **38**, 8927–8933 (2013).

128. Kocha, S. S., Yang, J. D. & Yi, J. S. Characterization of gas crossover and its implications in PEM fuel cells. *AIChE J.* **52**, 1916–1925 (2006).

129. Hutapea, Y. A., Nishihara, M., Gautama, Z. A. R., Mufundirwa, A., Lyth, S. M., Sugiyama, T., Nagayama, M., Sasaki, K. & Hayashi, A. Reduction of oxygen transport resistance in PEFC cathode through blending a high oxygen permeable polymer. *J. Power Sources* **556**, 232500 (2023).

130. Gautama, Z. A. R., Hutapea, Y. A., Hwang, B., Matsuda, J., Mufundirwa, A., Sugiyama, T., Ariyoshi, M., Fujikawa, S., Lyth, S. M., Hayashi, A., Sasaki, K. & Nishihara, M. Suppression of radical attack in polymer electrolyte membranes using a vinyl polymer blend interlayer with low oxygen permeability. *J. Memb. Sci.* **658**, 120734 (2022).

131. Nakayama, S. F., Yoshikane, M., Onoda, Y., Nishihama, Y., Iwai-Shimada, M., Takagi, M., Kobayashi, Y. & Isobe, T. Worldwide trends in tracing poly- and perfluoroalkyl substances (PFAS) in the environment. *TrAC Trends Anal. Chem.* **121**, 115410 (2019).

132. Umezawa, K., Oshima, T., Yoshizawa-Fujita, M., Takeoka, Y. & Rikukawa, M. Synthesis of hydrophilic-hydrophobic block copolymer ionomers based on polyphenylenes. *ACS Macro Lett.* **1**, 969–972 (2012).

133. Gebert, M. AQUIVION$^{TM}$ - The Short-Side-Chain and Low-EW PFSA for Next Generation PEFCs Expands Production and Utilization. *18th World Hydrog. Energy Conf. 2010, WHEC 2010, Proc.* **1**, 59–63 (2010).

134. Bakangura, E., Wu, L., Ge, L., Yang, Z. & Xu, T. Mixed matrix proton exchange

membranes for fuel cells: state of the art and perspectives Mixed matrix proton exchange membranes for fuel cells: state of the art and perspectives. *Prog. Polym. Sci.* **57**, 103–152 (2015).

135. Branco, C. M., Sharma, S., de Camargo Forte, M. M. & Steinberger-Wilckens, R. New approaches towards novel composite and multilayer membranes for intermediate temperature-polymer electrolyte fuel cells and direct methanol fuel cells. *J. Power Sources* **316**, 139–159 (2016).

136. Zarrin, H., Higgins, D., Jun, Y., Chen, Z. & Fowler, M. Functionalized graphene oxide nanocomposite membrane for low humidity and high temperature proton exchange membrane fuel cells. *J. Phys. Chem. C* **115**, 20774–20781 (2011).

137. Novoselov, K. S., Geim, A. K., Morozov, S. V, Jiang, D., Zhang, Y., Dubonos, S. V, Grigorieva, I. V & Firsov, A. A. Electric Field Effect in Atomically Thin Carbon Films. *Science* **306**, 666–669 (2004).

138. Georgakilas, V., Tiwari, J. N., Kemp, K. C., Perman, J. A., Bourlinos, A. B., Kim, K. S. & Zboril, R. Noncovalent Functionalization of Graphene and Graphene Oxide for Energy Materials, Biosensing, Catalytic, and Biomedical Applications. *Chem. Rev.* **116**, 5464–5519 (2016).

139. Pumera, M. Graphene-based nanomaterials for energy storage. *Energy Environ. Sci.* **4**, 668–674 (2011).

140. Olabi, A. G., Abdelkareem, M. A., Wilberforce, T. & Sayed, E. T. Application of graphene in energy storage device – A review. *Renew. Sustain. Energy Rev.* **135**, 110026 (2021).

141. Choi, W., Lahiri, I., Seelaboyina, R. & Kang, Y. S. Synthesis of Graphene and Its Applications: A Review. *Crit. Rev. Solid State Mater. Sci.* **35**, 52–71 (2010).

142. Novoselov, K. S., Fal′ko, V. I., Colombo, L., Gellert, P. R., Schwab, M. G. & Kim, K. A roadmap for graphene. *Nature* **490**, 192–200 (2012).

143. Randviir, E. P., Brownson, D. A. C. & Banks, C. E. A decade of graphene research: production, applications and outlook. *Mater. Today* **17**, 426–432 (2014).

144. Phiri, J., Gane, P. & Maloney, T. C. General overview of graphene: Production, properties and application in polymer composites. *Mater. Sci. Eng. B* **215**, 9–28 (2017).

145. Chung, C., Kim, Y.-K., Shin, D., Ryoo, S.-R., Hong, B. H. & Min, D.-H. Biomedical Applications of Graphene and Graphene Oxide. *Acc. Chem. Res.* **46**, 2211–2224 (2013).

146. Farooqui, U. R., Ahmad, A. L. & Hamid, N. A. Graphene oxide: A promising membrane material for fuel cells. *Renew. Sustain. Energy Rev.* **82**, 714–733 (2018).

147. Erickson, K., Erni, R., Lee, Z., Alem, N., Gannett, W. & Zettl, A. Determination of the Local Chemical Structure of Graphene Oxide and Reduced Graphene Oxide. *Adv. Mater.* **22**, 4467–4472 (2010).

148. Mkhoyan, K. A., Contryman, A. W., Silcox, J., Stewart, D. A., Eda, G., Mattevi, C., Miller, S. & Chhowalla, M. Atomic and Electronic Structure of Graphene-Oxide. *Nano*

*Lett.* **9**, 1058–1063 (2009).

149. Krishnamoorthy, K., Veerapandian, M., Yun, K. & Kim, S.-J. The chemical and structural analysis of graphene oxide with different degrees of oxidation. *Carbon N. Y.* **53**, 38–49 (2013).

150. Chen, L., Shi, G., Shen, J., Peng, B., Zhang, B., Wang, Y., Bian, F., Wang, J., Li, D., Qian, Z., Xu, G., Liu, G., Zeng, J., Zhang, L., Yang, Y., Zhou, G., Wu, M., Jin, W., Li, J., *et al.* Ion sieving in graphene oxide membranes via cationic control of interlayer spacing. *Nature* **550**, 380–383 (2017).

151. Chang, D. W. & Baek, J.-B. Charge transport in graphene oxide. *Nano Today* **17**, 38–53 (2017).

152. Aliyev, E., Filiz, V., Khan, M. M., Lee, Y. J., Abetz, C. & Abetz, V. Structural Characterization of Graphene Oxide : Surface Functional Groups and Fractionated Oxidative Debris. (2019).

153. Neklyudov, V. V, Khafizov, N. R., Sedov, I. A. & Dimiev, A. M. New insights into the solubility of graphene oxide in water and alcohols. *Phys. Chem. Chem. Phys.* **19**, 17000–17008 (2017).

154. Kumar, N., Salehiyan, R., Chauke, V., Joseph Botlhoko, O., Setshedi, K., Scriba, M., Masukume, M. & Sinha Ray, S. Top-down synthesis of graphene: A comprehensive review. *FlatChem* **27**, 100224 (2021).

155. Tang, L., Li, X., Ji, R., Teng, K. S., Tai, G., Ye, J., Wei, C. & Lau, S. P. Bottom-up synthesis of large-scale graphene oxide nanosheets. *J. Mater. Chem.* **22**, 5676–5683 (2012).

156. Hummers, W. S. J. & Offeman, R. E. Preparation of Graphitic Oxide. *J. Am. Chem. Soc.* **80**, 1339 (1958).

157. Staudenmaier, L. Verfahren zur Darstellung der Graphitsäure. *Berichte der Dtsch. Chem. Gesellschaft* **31**, 1481–1487 (1898).

158. Hofmann, U. & König, E. Untersuchungen über Graphitoxyd. *Zeitschrift für Anorg. und Allg. Chemie* **234**, 311–336 (1937).

159. Poh, H. L., Šaněk, F., Ambrosi, A., Zhao, G., Sofer, Z. & Pumera, M. Graphenes prepared by Staudenmaier, Hofmann and Hummers methods with consequent thermal exfoliation exhibit very different electrochemical properties. *Nanoscale* **4**, 3515–3522 (2012).

160. Compton, O. C. & Nguyen, S. T. Graphene Oxide, Highly Reduced Graphene Oxide, and Graphene: Versatile Building Blocks for Carbon-Based Materials. *Small* **6**, 711–723 (2010).

161. Kumar, R., Xu, C. & Scott, K. Graphite oxide/Nafion composite membranes for polymer electrolyte fuel cells. *RSC Adv.* **2**, 8777 (2012).

162. Kumar, R., Mamlouk, M. & Scott, K. Sulfonated polyether ether ketone-sulfonated graphene oxide composite membranes for polymer electrolyte fuel cells. *RSC Adv.* **4**, 617–623 (2014).

163. He, Y., Wang, J., Zhang, H., Zhang, T., Zhang, B., Cao, S. & Liu, J. Polydopamine-modified graphene oxide nanocomposite membrane for proton exchange membrane fuel cell under anhydrous conditions. *J. Mater. Chem. A* **2**, 9548–9558 (2014).

164. Liu, Y., Wang, J., Zhang, H., Ma, C., Liu, J., Cao, S. & Zhang, X. Enhancement of proton conductivity of chitosan membrane enabled by sulfonated graphene oxide under both hydrated and anhydrous conditions. *J. Power Sources* **269**, 898–911 (2014).

165. Bai, H., Li, Y., Zhang, H., Chen, H., Wu, W., Wang, J. & Liu, J. Anhydrous proton exchange membranes comprising of chitosan and phosphorylated graphene oxide for elevated temperature fuel cells. *J. Memb. Sci.* **495**, 48–60 (2015).

166. Beydaghi, H., Javanbakht, M. & Kowsari, E. Synthesis and characterization of poly(vinyl alcohol)/Sulfonated graphene oxide nanocomposite membranes for use in proton exchange membrane fuel cells (PEMFCs). *Ind. Eng. Chem. Res.* **53**, 16621–16632 (2014).

167. Cai, Y., Yue, Z. & Xu, S. A novel polybenzimidazole composite modified by sulfonated graphene oxide for high temperature proton exchange membrane fuel cells in anhydrous atmosphere. *J. Appl. Polym. Sci.* **134**, 1–8 (2017).

168. Peng, K.-J. J., Lai, J.-Y. Y. & Liu, Y.-L. L. Nanohybrids of graphene oxide chemically-bonded with Nafion: Preparation and application for proton exchange membrane fuel cells. *J. Memb. Sci.* **514**, 86–94 (2016).

169. Lim, M. Y. & Kim, K. Sulfonated poly(arylene ether sulfone) and perfluorosulfonic acid composite membranes containing perfluoropolyether grafted graphene oxide for polymer electrolyte membrane fuel cell applications. *Polymers (Basel).* **10**, (2018).

170. Kim, K., Heo, P., Ko, T., Kim, K., Kim, S.-K., Pak, C. & Lee, J.-C. Poly(arlyene ether sulfone) based semi-interpenetrating polymer network membranes containing cross-linked poly(vinyl phosphonic acid) chains for fuel cell applications at high temperature and low humidity conditions. *J. Power Sources* **293**, 539–547 (2015).

171. Lee, D. C. C., Yang, H. N. N., Park, S. H. H. & Kim, W. J. J. Nafion/graphene oxide composite membranes for low humidifying polymer electrolyte membrane fuel cell. *J. Memb. Sci.* **452**, 20–28 (2014).

172. Watanabe, M., Uchida, H., Seki, Y., Emori, M. & Stonehart, P. Self-Humidifying Polymer Electrolyte Membranes for Fuel Cells. *J. Electrochem. Soc.* **143**, 3847–3852 (1996).

173. Lee, D. C., Yang, H. N., Park, S. H., Park, K. W. & Kim, W. J. Self-humidifying Pt–graphene/SiO2 composite membrane for polymer electrolyte membrane fuel cell. *J. Memb. Sci.* **474**, 254–262 (2015).

174. Yang, H. N., Lee, W. H., Choi, B. S. & Kim, W. J. Preparation of Nafion/Pt-containing TiO2/graphene oxide composite membranes for self-humidifying proton exchange membrane fuel cell. *J. Memb. Sci.* **504**, 20–28 (2016).

175. Beydaghi, H. & Javanbakht, M. Aligned Nanocomposite Membranes Containing Sulfonated Graphene Oxide with Superior Ionic Conductivity for Direct Methanol Fuel Cell Application. *Ind. Eng. Chem. Res.* **54**, 7028–7037 (2015).

176. Ma, W.-T., Kumar, S. R., Hsu, C.-T., Shih, C.-M., Tsai, S.-W., Yang, C.-C., Liu, Y.-L. & Lue, S. J. Magnetic field-assisted alignment of graphene oxide nanosheets in a polymer matrix to enhance ionic conduction. *J. Memb. Sci.* **563**, 259–269 (2018).

177. Lue, S. J., Chen, J. Y. & Yang, J. M. Crystallinity and stability of poly(vinyl alcohol)-fumed silica mixed matrix membranes. *J. Macromol. Sci. Part B Phys.* **47**, 39–51 (2008).

178. Vinothkannan, M., Kim, A. R., Gnana Kumar, G. & Yoo, D. J. Sulfonated graphene oxide/Nafion composite membranes for high temperature and low humidity proton exchange membrane fuel cells. *RSC Adv.* **8**, 7494–7508 (2018).

179. Yang, L., Tang, B. & Wu, P. Metal-organic framework-graphene oxide composites: A facile method to highly improve the proton conductivity of PEMs operated under low humidity. *J. Mater. Chem. A* **3**, 15838–15842 (2015).

180. Branco, C. M. Multilayer membranes for intermediate temperature polymer electrolyte fuel cells. *PhD Thesis* (2017).

181. Decher, G. Fuzzy nanoassemblies: Toward layered polymeric multicomposites. *Science* **277**, 1232–1237 (1997).

182. Sha Wang, L., Nan Lai, A., Xiao Lin, C., Gen Zhang, Q., Mei Zhu, A. & Lin Liu, Q. Orderly sandwich-shaped graphene oxide/Nafion composite membranes for direct methanol fuel cells. *J. Memb. Sci.* **492**, 58–66 (2015).

183. Paredes, J. I., Rodil, S. V., Alonso, A. M. & Tascón, J. M. D. Graphene Oxide Dispersions in Organic Solvents Partners. *Langmuir* **121**, 1–2 (2008).

184. Bayer, T., Bishop, S. R., Nishihara, M., Sasaki, K. & Lyth, S. M. Characterization of a graphene oxide membrane fuel cell. *J. Power Sources* **272**, 239–247 (2014).

185. Bayer, T., Cunning, B. V, Selyanchyn, R., Daio, T., Nishihara, M., Fujikawa, S., Sasaki, K. & Lyth, S. M. Alkaline anion exchange membranes based on KOH-treated multilayer graphene oxide. *J. Memb. Sci.* **508**, 51–61 (2016).

186. Lin, C. W. W. & Lu, Y. S. S. Highly ordered graphene oxide paper laminated with a Nafion membrane for direct methanol fuel cells. *J. Power Sources* **237**, 187–194 (2013).

187. Lue, S. J., Pai, Y.-L. L., Shih, C.-M. M., Wu, M.-C. C. & Lai, S.-M. M. Novel bilayer well-aligned Nafion/graphene oxide composite membranes prepared using spin coating method for direct liquid fuel cells. *J. Memb. Sci.* **493**, 212–223 (2015).

188. Klingele, M., Breitwieser, M., Zengerle, R. & Thiele, S. Direct deposition of proton exchange membranes enabling high performance hydrogen fuel cells. *J. Mater. Chem. A* **3**, 11239–11245 (2015).

189. Breitwieser, M., Bayer, T., Büchler, A., Zengerle, R., Lyth, S. M. & Thiele, S. A fully spray-coated fuel cell membrane electrode assembly using Aquivion ionomer with a graphene oxide/cerium oxide interlayer. *J. Power Sources* **351**, 145–150 (2017).

190. Nunes, S. P., Ruffmann, B., Rikowski, E., Vetter, S. & Richau, K. Inorganic modification of proton conductive polymer membranes for direct methanol fuel cells. *J.*

*Memb. Sci.* **203**, 215–225 (2002).

191. Di Noto, V., Gliubizzi, R., Negro, E., Vittadello, M. & Pace, G. Hybrid inorganic–organic proton conducting membranes based on Nafion and 5 wt.% of MxOy (M = Ti, Zr, Hf, Ta and W): Part I. Synthesis, properties and vibrational studies. *Electrochim. Acta* **53**, 1618–1627 (2007).

192. Di Noto, V., Lavina, S., Negro, E., Vittadello, M., Conti, F., Piga, M. & Pace, G. Hybrid inorganic–organic proton conducting membranes based on Nafion and 5 wt% of MxOy (M = Ti, Zr, Hf, Ta and W). Part II: Relaxation phenomena and conductivity mechanism. *J. Power Sources* **187**, 57–66 (2009).

193. Pineda-Delgado, J. L., Gutierrez B, C. K., Rivas, S., Arjona, N., Arriaga, L. G. & Chávez-Ramirez, A. U. Synthesis and evaluation of $HfO_2$ as a prospective filler in inorganic–organic hybrid membranes based on Nafion for PEM fuel cells. *Nanotechnology* **30**, 105707 (2019).

194. T. Adjemian, K., Dominey, R., Krishnan, L., Ota, H., Majsztrik, P., Zhang, T., Mann, J., Kirby, B., Gatto, L., Velo-Simpson, M., Leahy, J., Srinivasan, S., B. Benziger, J. & B. Bocarsly, A. Function and Characterization of Metal Oxide−Nafion Composite Membranes for Elevated-Temperature H2/O2 PEM Fuel Cells. *Chem. Mater.* **18**, 2238–2248 (2006).

195. Giffin, G. A., Piga, M., Lavina, S., Navarra, M. A., D'Epifanio, A., Scrosati, B. & Di Noto, V. Characterization of sulfated-zirconia/Nafion® composite membranes for proton exchange membrane fuel cells. *J. Power Sources* **198**, 66–75 (2012).

196. D'Epifanio, A., Assunta Navarra, M., Christoph Weise, F., Mecheri, B., Farrington, J., Licoccia, S. & Greenbaum, S. Composite Nafion/Sulfated Zirconia Membranes: Effect of the Filler Surface Properties on Proton Transport Characteristics. *Chem. Mater.* **22**, 813–821 (2009).

197. Saccà, A., Gatto, I., Carbone, A., Pedicini, R. & Passalacqua, E. ZrO2–Nafion composite membranes for polymer electrolyte fuel cells (PEFCs) at intermediate temperature. *J. Power Sources* **163**, 47–51 (2006).

198. Saccà, A., Carbone, A., Gatto, I., Pedicini, R., Freni, A., Patti, A. & Passalacqua, E. Composites Nafion-titania membranes for Polymer Electrolyte Fuel Cell (PEFC) applications at low relative humidity levels: Chemical physical properties and electrochemical performance. *Polym. Test.* **56**, 10–18 (2016).

199. Saccà, A., Carbone, A., Passalacqua, E., D'Epifanio, A., Licoccia, S., Traversa, E., Sala, E., Traini, F. & Ornelas, R. Nafion–TiO2 hybrid membranes for medium temperature polymer electrolyte fuel cells (PEFCs). *J. Power Sources* **152**, 16–21 (2005).

200. Alberti, G., Casciola, M., Capitani, D., Donnadio, A., Narducci, R., Pica, M. & Sganappa, M. Novel Nafion–zirconium phosphate nanocomposite membranes with enhanced stability of proton conductivity at medium temperature and high relative humidity. *Electrochim. Acta* **52**, 8125–8132 (2007).

201. Sahu, A. K., Selvarani, G., Pitchumani, S., Sridhar, P. & Shukla, A. K. A Sol-Gel Modified Alternative Nafion-Silica Composite Membrane for Polymer Electrolyte Fuel

Cells. *J. Electrochem. Soc.* **154**, B123--B132 (2007).

202. Costamagna, P., Yang, C., Bocarsly, A. B. & Srinivasan, S. Nafion® 115/zirconium phosphate composite membranes for operation of PEMFCs above 100 °C. *Electrochim. Acta* **47**, 1023–1033 (2002).

203. Xu, G., Wu, Z., Wei, Z., Zhang, W., Wu, J., Li, Y., Li, J., Qu, K. & Cai, W. Non-destructive fabrication of Nafion/silica composite membrane via swelling-filling modification strategy for high temperature and low humidity PEM fuel cell. *Renew. Energy* **153**, 935–939 (2020).

204. Xu, G., Wei, Z., Li, S., Li, J., Yang, Z. & Grigoriev, S. A. In-situ sulfonation of targeted silica-filled Nafion for high-temperature PEM fuel cell application. *Int. J. Hydrogen Energy* **44**, 29711–29716 (2019).

205. Oh, K., Kwon, O., Son, B., Lee, D. H. & Shanmugam, S. Nafion-sulfonated silica composite membrane for proton exchange membrane fuel cells under operating low humidity condition. *J. Memb. Sci.* **583**, 103–109 (2019).

206. Amjadi, M., Rowshanzamir, S., Peighambardoust, S. J. & Hosseini, M. G. Investigation of physical properties and cell performance of Nafion/TiO2 nanocomposite membranes for high temperature PEM fuel cells. *Int. J. Hydrogen Energy* **35**, 9252–9260 (2010).

207. Matos, B. R., Santiago, E. I., Rey, J. F. Q., Ferlauto, A. S., Traversa, E., Linardi, M. & Fonseca, F. C. Nafion-based composite electrolytes for proton exchange membrane fuel cells operating above 120 °C with titania nanoparticles and nanotubes as fillers. *J. Power Sources* **196**, 1061–1068 (2011).

208. Zhengbang, W., Tang, H. & Mu, P. Self-assembly of durable Nafion/TiO2 nanowire electrolyte membranes for elevated-temperature PEM fuel cells. *J. Memb. Sci.* **369**, 250–257 (2011).

209. Ketpang, K., Shanmugam, S., Suwanboon, C., Chanunpanich, N. & Lee, D. Efficient water management of composite membranes operated in polymer electrolyte membrane fuel cells under low relative humidity. *J. Memb. Sci.* **493**, 285–298 (2015).

210. Jun, Y., Zarrin, H., Fowler, M. & Chen, Z. Functionalized titania nanotube composite membranes for high temperature proton exchange membrane fuel cells. *Int. J. Hydrogen Energy* **36**, 6073–6081 (2011).

211. Ketpang, K., Son, B., Lee, D. & Shanmugam, S. Porous zirconium oxide nanotube modified Nafion composite membrane for polymer electrolyte membrane fuel cells operated under dry conditions. *J. Memb. Sci.* **488**, 154–165 (2015).

212. Shaari, N., Siti, |, Kamarudin, K. & Kamarudin, S. K. Recent advances in additive-enhanced polymer electrolyte membrane properties in fuel cell applications: An overview. *Int. J. Energy Res.* **43**, 2756–2794 (2019).

213. Devrim, Y., Erkan, S., Baç, N. & Eroğlu, I. Preparation and characterization of sulfonated polysulfone/titanium dioxide composite membranes for proton exchange membrane fuel cells. *Int. J. Hydrogen Energy* **34**, 3467–3475 (2009).

214. Carbone, A., Pedicini, R., Saccà, A., Gatto, I. & Passalacqua, E. Composite S-PEEK

membranes for medium temperature polymer electrolyte fuel cells. *J. Power Sources* **178**, 661–666 (2008).

215. Carbone, A., Saccà, A., Gatto, I., Pedicini, R. & Passalacqua, E. Investigation on composite S-PEEK/H-BETA MEAs for medium temperature PEFC. *Int. J. Hydrogen Energy* **33**, 3153–3158 (2008).

216. Sambandam, S. & Ramani, V. SPEEK/functionalized silica composite membranes for polymer electrolyte fuel cells. *J. Power Sources* **170**, 259–267 (2007).

217. Joseph Helen Therese, J. B. A., Gayathri, R., Selvakumar, K., Ramesh Prabhu, M. & Sivakumar, P. Incorporation of sulfonated silica nano particles into polymer blend membrane for PEM fuel cell applications. *Mater. Res. Express* **6**, 115336 (2019).

218. Elakkiya, S., Arthanareeswaran, G., Ismail, A. F., Das, D. B. & Suganya, R. Polyaniline coated sulfonated TiO2 nanoparticles for effective application in proton conductive polymer membrane fuel cell. *Eur. Polym. J.* **112**, 696–703 (2019).

219. Özdemir, Y., Üregen, N. & Devrim, Y. Polybenzimidazole based nanocomposite membranes with enhanced proton conductivity for high temperature PEM fuel cells. *Int. J. Hydrogen Energy* **42**, 2648–2657 (2017).

220. Lee, S., Seo, K., Ghorpade, R. V, Nam, K. H. & Han, H. High temperature anhydrous proton exchange membranes based on chemically-functionalized titanium/polybenzimidazole composites for fuel cells. *Mater. Lett.* **263**, 127167 (2020).

221. Ooi, Y. X., Ya, K. Z., Maegawa, K., Tan, W. K., Kawamura, G., Muto, H. & Matsuda, A. CHS-WSiA doped hexafluoropropylidene-containing polybenzimidazole composite membranes for medium temperature dry fuel cells. *Int. J. Hydrogen Energy* **44**, 32201–32209 (2019).

222. Devrim, Y., Devrim, H. & Eroglu, I. Polybenzimidazole/SiO2 hybrid membranes for high temperature proton exchange membrane fuel cells. *Int. J. Hydrogen Energy* **41**, 10044–10052 (2016).

223. Zou, Y. C., Mogg, L., Clark, N., Bacaksiz, C., Milovanovic, S., Sreepal, V., Hao, G. P., Wang, Y. C., Hopkinson, D. G., Gorbachev, R., Shaw, S., Novoselov, K. S., Raveendran-Nair, R., Peeters, F. M., Lozada-Hidalgo, M. & Haigh, S. J. Ion exchange in atomically thin clays and micas. *Nat. Mater.* **20**, 1677–1682 (2021).

224. Plackett, D., Siu, A., Li, Q., Pan, C., Jensen, J. O., Nielsen, S. F., Permyakova, A. A. & Bjerrum, N. J. High-temperature proton exchange membranes based on polybenzimidazole and clay composites for fuel cells. *J. Memb. Sci.* **383**, 78–87 (2011).

225. Aili, D., Zhang, J., Dalsgaard Jakobsen, M. T., Zhu, H., Yang, T., Liu, J., Forsyth, M., Pan, C., Jensen, J. O., Cleemann, L. N., Jiang, S. P. & Li, Q. Exceptional durability enhancement of PA/PBI based polymer electrolyte membrane fuel cells for high temperature operation at 200°C. *J. Mater. Chem. A* **4**, 4019–4024 (2016).

226. Pearman, B. P., Mohajeri, N., Brooker, R. P., Rodgers, M. P., Slattery, D. K., Hampton, M. D., Cullen, D. A. & Seal, S. The degradation mitigation effect of cerium oxide in polymer electrolyte membranes in extended fuel cell durability tests. *J. Power Sources* **225**, 75–83 (2013).

227. Pearman, B. P., Mohajeri, N., Slattery, D. K., Hampton, M. D., Seal, S. & Cullen, D. A. The chemical behavior and degradation mitigation effect of cerium oxide nanoparticles in perfluorosulfonic acid polymer electrolyte membranes. *Polym. Degrad. Stab.* **98**, 1766–1772 (2013).

228. Lee, H., Han, M., Choi, Y.-W. & Bae, B. Hydrocarbon-based polymer electrolyte cerium composite membranes for improved proton exchange membrane fuel cell durability. *J. Power Sources* **295**, 221–227 (2015).

229. Sahin, A., Tasdemir, H. M. & Ar, İ. Improved performance and durability of sulfonated polyether ether ketone/cerium phosphate composite membrane for proton exchange membrane fuel cells. *Ionics (Kiel).* **25**, 5163–5175 (2019).

230. Rodgers, M. P., Pearman, B. P., Bonville, L. J., Cullen, D. A., Mohajeri, N. & Slattery, D. K. Evaluation of the Effect of Impregnated Platinum on PFSA Degradation for PEM Fuel Cells. *J. Electrochem. Soc.* **160**, F1123--F1128 (2013).

231. Xu, C., Liu, X., Cheng, J. & Scott, K. A polybenzimidazole/sulfonated graphite oxide composite membrane for high temperature polymer electrolyte membrane fuel cells. *J. Mater. Chem.* **274**, 922–927 (2011).

232. Choi, P., Li, B., Agarwal, R., Pearman, B. P., Mohajeri, N., Rodgers, M., Slattery, D., Bonville, L., Kunz, H. R. & Fenton, J. M. Effect of Equivalent Weight of Phosphotungstic Acid-Incorporated Composite Membranes on the High Temperature Operation of PEM Fuel Cells. *ECS Trans.* **16**, 2157–2164 (2008).

233. Ramani, V., Kunz, H. R. & Fenton, J. M. Investigation of Nafion®/HPA composite membranes for high temperature/low relative humidity PEMFC operation. *J. Memb. Sci.* **232**, 31–44 (2004).

234. Ramani, V., Kunz, H. R. & Fenton, J. M. Stabilized composite membranes and membrane electrode assemblies for elevated temperature/low relative humidity PEFC operation. *J. Power Sources* **152**, 182–188 (2005).

235. Lei, Z., Chen, B., Koo, Y. M. & Macfarlane, D. R. Introduction: Ionic Liquids. *Chem. Rev.* **117**, 6633–6635 (2017).

236. Alashkar, A., Al-Othman, A., Tawalbeh, M. & Qasim, M. A Critical Review on the Use of Ionic Liquids in Proton Exchange Membrane Fuel Cells. *Membranes (Basel).* **12**, 178 (2022).

237. Lee, J. S., Nohira, T. & Hagiwara, R. Novel composite electrolyte membranes consisting of fluorohydrogenate ionic liquid and polymers for the unhumidified intermediate temperature fuel cell. *J. Power Sources* **171**, 535–539 (2007).

238. Lee, S.-Y. & Yasuda, T. Fabrication of protic ionic liquid/sulfonated polyimide composite membranes for non-humidified fuel cells. *J. Power Sources* **195**, 5909–5914 (2010).

239. Yi, S., Zhang, F., Li, W., Huang, C., Zhang, H. & Pan, M. Anhydrous elevated-temperature polymer electrolyte membranes based on ionic liquids. *J. Memb. Sci.* **366**, 349–355 (2011).

240. Malik, R. S., Verma, P. & Choudhary, V. A study of new anhydrous, conducting

membranes based on composites of aprotic ionic liquid and cross-linked SPEEK for fuel cell application. *Electrochim. Acta* **152**, 352–359 (2015).

241. Yasuda, T., Nakamura, S. I., Honda, Y., Kinugawa, K., Lee, S. Y. & Watanabe, M. Effects of polymer structure on properties of sulfonated polyimide/protic ionic liquid composite membranes for nonhumidified fuel cell applications. *ACS Appl. Mater. Interfaces* **4**, 1783–1790 (2012).

242. Chen, J., Yao, B., Li, C. & Shi, G. An improved Hummers method for eco-friendly synthesis of graphene oxide. *Carbon N. Y.* **64**, 225–229 (2013).

243. XIII. On the atomic weight of graphite. *Philos. Trans. R. Soc. London* **149**, 249–259 (1859).

244. Marcano, D. C., Kosynkin, D. V, Berlin, J. M., Sinitskii, A., Sun, Z., Slesarev, A. S., Alemany, L. B., Lu, W. & Tour, J. M. Improved Synthesis of Graphene Oxide. *ACS Nano* **12**, 2078 (2010).

245. Guerrero-Contreras, J. & Caballero-Briones, F. Graphene oxide powders with different oxidation degree, prepared by synthesis variations of the Hummers method. *Mater. Chem. Phys.* **153**, 209–220 (2015).

246. Nair, R. R., Wu, H. A., Jayaram, P. N., Grigorieva, I. V & Geim, A. K. Unimpeded permeation of water through helium-leak-tight graphene-based membranes. *Science* **335**, 442–444 (2012).

247. Chandan, A., Harding, C., Singh, P., Du, S., Rees, N., Ingram, A., Steinberger-Wilckens, R., Self, V. & Richmond, J. Graphene Oxide as a Support Material for HT-PEFCs. in *4th European PEFC and H2 Forum* (2013).

248. Xu, J. J., Liu, Q. C., Yu, Y., Wang, J., Yan, J. M. & Zhang, X. B. In Situ Construction of Stable Tissue-Directed/Reinforced Bifunctional Separator/Protection Film on Lithium Anode for Lithium–Oxygen Batteries. *Adv. Mater.* **29**, 1–6 (2017).

249. Gao, S., Wang, K., Wang, R., Jiang, M., Han, J., Gu, T., Cheng, S. & Jiang, K. Poly(vinylidene fluoride)-based hybrid gel polymer electrolytes for additive-free lithium sulfur batteries. *J. Mater. Chem. A* **5**, 17889–17895 (2017).

250. Ni'mah, Y. L., Cheng, M.-Y., Cheng, J. H., Rick, J. & Hwang, B.-J. Solid-state polymer nanocomposite electrolyte of TiO2/PEO/NaClO4 for sodium ion batteries. *J. Power Sources* **278**, 375–381 (2015).

251. Nunes-Pereira, J., Martins, P., Cardoso, V. F., Costa, C. M. & Lanceros-Méndez, S. A green solvent strategy for the development of piezoelectric poly(vinylidene fluoride–trifluoroethylene) films for sensors and actuators applications. *Mater. Des.* **104**, 183–189 (2016).

252. Wang, T., Zhang, Y., Liu, Q., Cheng, W., Wang, X., Pan, L., Xu, B. & Xu, H. A Self-Healable, Highly Stretchable, and Solution Processable Conductive Polymer Composite for Ultrasensitive Strain and Pressure Sensing. *Adv. Funct. Mater.* **28**, 1–12 (2018).

253. Dong, B., Zhang, L. & Wu, Y. Highly conductive natural rubber–graphene hybrid films prepared by solution casting and in situ reduction for solvent-sensing application.

*J. Mater. Sci.* **51**, 10561–10573 (2016).

254. Ma, C. H., Yu, T. L., Lin, H. L., Huang, Y. T., Chen, Y. L., Jeng, U. S., Lai, Y. H. & Sun, Y. Sen. Morphology and properties of Nafion membranes prepared by solution casting. *Polymer (Guildf).* **50**, 1764–1777 (2009).

255. Wang, L., Yi, B. L., Zhang, H. M., Liu, Y. H., Xing, D. M., Shao, Z. G. & Cai, Y. H. Novel multilayer Nafion/SPI/Nafion composite membrane for PEMFCs. *J. Power Sources* **164**, 80–85 (2007).

256. Deligöz, H., Yilmaztürk, S., Karaca, T., Özdemir, H., Koç, S. N., Öksüzömer, F., Durmuş, A. & Gürkaynak, M. A. Self-assembled polyelectrolyte multilayered films on Nafion with lowered methanol cross-over for DMFC applications. *J. Memb. Sci.* **326**, 643–649 (2009).

257. Vyazovkin, S., Burnham, A. K., Favergeon, L., Koga, N., Moukhina, E., Pérez-Maqueda, L. A. & Sbirrazzuoli, N. ICTAC Kinetics Committee recommendations for analysis of multi-step kinetics. *Thermochim. Acta* **689**, 178597 (2020).

258. Smith, B. C. *Fundamentals of Fourier Transform Infrared Spectroscopy*. (CRC Press, 2011).

259. Isaacs, M. A., Davies-Jones, J., Davies, P. R., Guan, S., Lee, R., Morgan, D. J. & Palgrave, R. Advanced XPS characterization: XPS-based multi-technique analyses for comprehensive understanding of functional materials. *Mater. Chem. Front.* **5**, 7931–7963 (2021).

260. Zhang, X., Zhang, T., Chen, H. & Cao, Y. A review of online electrochemical diagnostic methods of on-board proton exchange membrane fuel cells. *Appl. Energy* **286**, 116481 (2021).

261. Cooper, K. R. *Experimental Methods and Data Analyses for Polymer Electrolyte Fuel Cells*. (Scribner Associates, 2005).

262. Gengenbach, T. R., Major, G. H., Linford, M. R. & Easton, C. D. Practical guides for x-ray photoelectron spectroscopy (XPS): Interpreting the carbon 1s spectrum. *J. Vac. Sci. Technol. A Vacuum, Surfaces, Film.* **39**, 13204 (2021).

263. Elessawy, N. A., Gouda, M. H., Ali, S. M., Salerno, M. & Eldin, M. S. M. Effective elimination of contaminant antibiotics using high-surface-area magnetic-functionalized graphene nanocomposites developed from plastic waste. *Materials (Basel).* **13**, 1517 (2020).

264. Basha, I. K., Abd El-Monaem, E. M., Khalifa, R. E., Omer, A. M. & Eltaweil, A. S. Sulfonated graphene oxide impregnated cellulose acetate floated beads for adsorption of methylene blue dye: optimization using response surface methodology. *Sci. Rep.* **12**, 1–17 (2022).

265. Friedman, A. K., Shi, W., Losovyj, Y., Siedle, A. R. & Baker, L. A. Mapping Microscale Chemical Heterogeneity in Nafion Membranes with X-ray Photoelectron Spectroscopy. *J. Electrochem. Soc.* **165**, H733–H741 (2018).

266. Chen, Z., Patel, R., Berry, J., Keyes, C., Satterfield, C., Simmons, C., Neeson, A., Cao, X. & Wu, Q. Development of Screen-Printable Nafion Dispersion for Electrochemical

Sensor. *Appl. Sci.* **12**, 6533 (2022).

267. Lee, A. Y., Yang, K., Anh, N. D., Park, C., Lee, S. M., Lee, T. G. & Jeong, M. S. Raman study of D* band in graphene oxide and its correlation with reduction. *Appl. Surf. Sci.* **536**, 147990 (2021).

268. Scardaci, V. & Compagnini, G. Raman Spectroscopy Investigation of Graphene Oxide Reduction by Laser Scribing. *C* **7**, 48 (2021).

269. Sudesh, Kumar, N., Das, S., Bernhard, C. & Varma, G. D. Effect of graphene oxide doping on superconducting properties of bulk MgB2. *Supercond. Sci. Technol.* **26**, 095008 (2013).

270. Al-Gaashani, R., Najjar, A., Zakaria, Y., Mansour, S. & Atieh, M. A. XPS and structural studies of high quality graphene oxide and reduced graphene oxide prepared by different chemical oxidation methods. *Ceram. Int.* **45**, 14439–14448 (2019).

271. Aliyev, E., Shishatskiy, S., Abetz, C., Lee, Y. J., Neumann, S., Emmler, T. & Filiz, V. SI-ATRP Polymer-Functionalized Graphene Oxide for Water Vapor Separation. *Adv. Mater. Interfaces* **7**, 2000443 (2020).

272. Mampallil, D. & Eral, H. B. A review on suppression and utilization of the coffee-ring effect. *Adv. Colloid Interface Sci.* **252**, 38–54 (2018).

273. Yunker, P. J., Still, T., Lohr, M. A. & Yodh, A. G. Suppression of the coffee-ring effect by shape-dependent capillary interactions. *Nature* **476**, 308–311 (2011).

274. Zhang, F., Zhang, Z., Liu, Y., Lu, H. & Leng, J. The quintuple-shape memory effect in electrospun nanofiber membranes. *Smart Mater. Struct.* **22**, 085020 (2013).

275. Khaleghi-Abbasabadi, M. & Azarifar, D. Magnetic Fe 3 O 4 -supported sulfonic acid-functionalized graphene oxide (Fe 3 O 4 @GO-naphthalene-SO 3 H): a novel and recyclable nanocatalyst for green one-pot synthesis of 5-oxo-dihydropyrano[3,2-c]chromenes and 2-amino-3-cyano-1,4,5,6-tetrahydropyrano[3,2-c]quinolin-5-ones. *Res. Chem. Intermed.* **45**, 2095–2118 (2019).

276. Ludvigsson, M., Lindgren, J. & Tegenfeldt, J. Crystallinity in Cast Nafion. *J. Electrochem. Soc.* **147**, 1303 (2000).

277. Fernandez Bordín, S. P., Andrada, H. E., Carreras, A. C., Castellano, G. E., Oliveira, R. G. & Galván Josa, V. M. Nafion membrane channel structure studied by small-angle X-ray scattering and Monte Carlo simulations. *Polymer (Guildf).* **155**, 58–63 (2018).

278. Aragaw, B. A., Su, W. N., Rick, J. & Hwang, B. J. Highly efficient synthesis of reduced graphene oxide–Nafion nanocomposites with strong coupling for enhanced proton and electron conduction. *RSC Adv.* **3**, 23212–23221 (2013).

279. Sahu, A. K., Ketpang, K., Shanmugam, S., Kwon, O., Lee, S. & Kim, H. Sulfonated Graphene-Nafion Composite Membranes for Polymer Electrolyte Fuel Cells Operating under Reduced Relative Humidity. *J. Phys. Chem. C* **120**, 15855–15866 (2016).

280. Gagliardi, G. G., El-Kharouf, A. & Borello, D. Assessment of innovative graphene oxide composite membranes for the improvement of direct methanol fuel cells performance. *Fuel* **345**, 128252 (2023).

281. Gagliardi, G. G., Palone, O., Paris, E. & Borello, D. An efficient composite membrane to improve the performance of PEM reversible fuel cells. *Fuel* **357**, 129993 (2024).

282. Shao, Z. G., Joghee, P. & Hsing, I. M. Preparation and characterization of hybrid Nafion–silica membrane doped with phosphotungstic acid for high temperature operation of proton exchange membrane fuel cells. *J. Memb. Sci.* **229**, 43–51 (2004).

283. Kumar, S., Garg, A. & Chowdhuri, A. Sonication effect on graphene oxide (GO) membranes for water purification applications. *Mater. Res. Express* **6**, 085620 (2019).

284. Schalenbach, M., Hoefner, T., Paciok, P., Carmo, M., Lueke, W. & Stolten, D. Gas Permeation through Nafion. Part 1: Measurements. *J. Phys. Chem. C* **119**, 25145–25155 (2015).

285. Catalano, J., Myezwa, T., De Angelis, M. G., Baschetti, M. G. & Sarti, G. C. The effect of relative humidity on the gas permeability and swelling in PFSI membranes. *Int. J. Hydrogen Energy* **37**, 6308–6316 (2012).

286. Mukaddam, M., Litwiller, E. & Pinnau, I. Gas Sorption, Diffusion, and Permeation in Nafion. *Macromolecules* **49**, 280–286 (2016).

287. Ibrahim, A., Hossain, O., Chaggar, J., Steinberger-Wilckens, R. & El-Kharouf, A. GO-nafion composite membrane development for enabling intermediate temperature operation of polymer electrolyte fuel cell. *Int. J. Hydrogen Energy* **45**, 5526–5534 (2020).

288. Springer, T. E., Zawodzinski, T. A. & Gottesfeld, S. Polymer Electrolyte Fuel Cell Model. *J. Electrochem. Soc.* **138**, 2334–2342 (1991).

289. Mishra, A. K., Kim, N. H., Jung, D. & Lee, J. H. Enhanced mechanical properties and proton conductivity of Nafion-SPEEK-GO composite membranes for fuel cell applications. *J. Memb. Sci.* **458**, 128–135 (2014).

290. Kim, Y., Ketpang, K., Jaritphun, S., Park, J. S. & Shanmugam, S. A polyoxometalate coupled graphene oxide-Nafion composite membrane for fuel cells operating at low relative humidity. *J. Mater. Chem. A* **3**, 8148–8155 (2015).

291. Chong, J. Y., Wang, B., Mattevi, C. & Li, K. Dynamic microstructure of graphene oxide membranes and the permeation flux. *J. Memb. Sci.* **549**, 385–392 (2018).

292. Macauley, N., Wong, K. H., Watson, M. & Kjeang, E. Favorable effect of in-situ generated platinum in the membrane on fuel cell membrane durability. *J. Power Sources* **299**, 139–148 (2015).

293. Stewart, S. M., Spernjak, D., Borup, R., Datye, A. & Garzon, F. Cerium migration through hydrogen fuel cells during accelerated stress testing. *ECS Electrochem. Lett.* **3**, (2014).

294. Lim, C., Alavijeh, A. S., Lauritzen, M., Kolodziej, J., Knights, S. & Kjeang, E. Fuel Cell Durability Enhancement with Cerium Oxide under Combined Chemical and Mechanical Membrane Degradation. *ECS Electrochem. Lett.* **4**, F29--F31 (2015).

295. Baker, A. M., Mukundan, R., Spernjak, D., Judge, E. J., Advani, S. G., Prasad, A. K. & Borup, R. L. Cerium Migration during PEM Fuel Cell Accelerated Stress Testing. *J.*

*Electrochem. Soc.* **163**, F1023--F1031 (2016).

296. Cheng, T. T. H., Wessel, S. & Knights, S. Interactive Effects of Membrane Additives on PEMFC Catalyst Layer Degradation. *J. Electrochem. Soc.* **160**, F27–F33 (2013).

297. Banham, D., Ye, S., Cheng, T., Knights, S., Stewart, S. M., Wilson, M. & Garzon, F. Effect of CeOx Crystallite Size on the Chemical Stability of CeOx Nanoparticles. *J. Electrochem. Soc.* **161**, F1075–F1080 (2014).

298. Banham, D., Ye, S., Knights, S., Stewart, S. M., Wilson, M. & Garzon, F. UV-visible spectroscopy method for screening the chemical stability of potential antioxidants for proton exchange membrane fuel cells. *J. Power Sources* **281**, 238–242 (2015).

299. Wang, P., Cai, C., Tan, J. & Pan, M. Effect of the CeO2 nanoparticles in microporous layers on the durability of proton exchange membrane fuel cells. *Int. J. Hydrogen Energy* **46**, 34867–34873 (2021).

300. Lin, R., Cao, C., Zhang, H., Huang, H. & Ma, J. Electro-catalytic activity of enhanced CO tolerant cerium-promoted Pt/C catalyst for PEM fuel cell anode. *Int. J. Hydrogen Energy* **37**, 4648–4656 (2012).